Technische Universität München
TUM School of Engineering and Design

Helicopter Main Rotor Efficiency Improvement Through Active Blade Camber Morphing

Dominik Komp

Vollständiger Abdruck der von der TUM School of Engineering and Design der Technischen Universität München zur Erlangung eines

Doktors der Ingenieurwissenschaften (Dr.-Ing.)

genehmigten Dissertation.

Vorsitz: Prof. Dr. Ilkay Yavrucuk

Prüfende der Dissertation:

1. Prof. Dr.-Ing. Manfred Hajek
2. Prof. Dr. Jürgen Rauleder

Die Dissertation wurde am 11.06.2024 bei der Technischen Universität München eingereicht und durch die TUM School of Engineering and Design am 06.11.2024 angenommen.

Abstract

The main rotor of a helicopter operates in a complex aerodynamic environment with constantly changing flow conditions and highly unsteady aerodynamics. Ensuring efficient operation under these conditions becomes even more challenging when considering the variety of requirements the rotor must meet, such as the flight envelope capacity, the permissible level of vibration and noise emission, and the safety. Improving the efficiency of helicopter main rotors has been a continuous effort and is still an ongoing process. Typically, static blade design, including complex blade tip geometries, has been the subject of such optimizations. However, due to the significant variability and unsteadiness in the aerodynamics of a helicopter rotor blade, some degree of efficiency improvement can only be achieved by using an active mechanism capable of adjusting the rotor blades during operation.

In the present study, a continuous (camber) morphing of the rear part of the rotor blade was investigated based on a comprehensive analysis model of a full-scale, four-bladed, hingeless Bo 105 main rotor. To calculate the aerodynamic forces, a free-vortex wake method in conjunction with airfoil table-based lifting-line theory was employed. The resulting elastic deformation of the rotor blades was solved in a coupled manner using the Euler-Bernoulli beam theory.

A computational investigation was conducted to examine the potential benefits of active camber control. This comprised a static configuration change of the camber deflection to adapt the rotor to different flight conditions, and, specifically for high-speed flight, a highly dynamic actuation with complex variation of the airfoil geometry over one revolution. The objective of this study was to gain a better understanding of this technology in order to make a more reliable estimate of the potential rotor power savings. Moreover, the purpose was to identify the most effective manner in which such systems can be utilized and to determine the correlation between active camber control and the design of the baseline rotor.

It was found that the effectiveness of such systems is highly dependent on the required speed range of the helicopter in terms of edge-wise flight of the main rotor. When a wide range of advance ratios is required, three main principles of enhancing the efficiency were observed, each offering significant potential to improve rotor performance. On the one hand, power gains resulted from the need to strongly orient the rotor design towards the requirements in high-speed flight in order to achieve acceptable rotor behavior in this complex flight condition. This opens up the potential to improve hover and low-speed rotor efficiency, primarily through static deflection of the airfoil geometry. The resulting effect is analogous to the introduction of additional blade

twist, which results in a redistribution of aerodynamic loads to further inboard radial stations. The second source of potential performance gains can be attributed to the phenomenon of unfavorable rotor thrust distribution in high-speed flight. A complex, mainly azimuthal redistribution of aerodynamic loads based on a periodic, multi-harmonic camber deflection schedule resulted in a noticeable rotor efficiency enhancement.

The third principle for improving rotor efficiency is an indirect effect based on the baseline rotor design and the ability to address multiple objectives with this active mechanism. It allows rotor performance improvements over the entire flight envelope, from hover to high-speed forward flight. The idea is to overcome limitations in the rotor design towards more efficient designs by actively compensating detrimental effects in non-performance-related aspects, such as oscillatory loads and stall margin. Accordingly, the active-camber mechanism was employed to restore the original characteristics of the passive rotor prior to modifying the rotor design, while simultaneously achieving a higher efficiency of the rotor system.

Such indirect gains associated with the passive rotor design resulted in an amplification of the direct active-camber-related power savings by over 50%. When operating at $C_T/\sigma = 0.089$, the combination of direct and indirect gains resulted in an efficiency improvement of more than 8% at hover, more than 5% at low to medium speed, and more than 6% at high-speed flight of $\mu = 0.3$. Moreover, the achieved power gains were further enhanced, for instance, at higher thrust coefficients, by increasing the advance ratio, and especially by relaxing the requirement to maintain the full original stall margin. Conversely, an improvement in the baseline rotor efficiency resulted mostly in a moderate reduction in terms of direct gains from active camber. However, based on the present results, this effect is considered to be limited due to the fact that any advantage in the baseline rotor efficiency resulted in an increase in the rotor oscillatory loads.

In terms of secondary effects on the overall rotorcraft design, it was assumed that the additional weight resulting from the implementation of such systems would likely be offset by potential weight savings. These weight savings could be realized, for example, in the drivetrain and engine of the rotorcraft (less peak power required), by carrying less fuel, and by reducing the number of anti-vibration measures.

Acknowledgments

I would like to express my sincere gratitude to all those who have supported and guided me throughout this project.

First and foremost, I would like to thank Prof. Dr.-Ing. Manfred Hajek, my advisor, for his invaluable guidance and encouragement throughout this process. His strong support, insightful feedback, and the establishment of an excellent working environment were crucial in shaping this work. Likewise, I would like to express my gratitude to Prof. Dr. Juergen Rauleder, one of the initiators of the research project from which this work emerged, for his mentorship. His continuous support, commitment, and valuable advice have been essential throughout this journey.

My deepest gratitude also goes to my office colleagues and team members, Amine Abdelmoula and Sumeet Kumar. Their unwavering support, camaraderie, encouragement, and our deep discussions have been extraordinarily important in moving this work forward.

I extend my heartfelt thanks to all my colleagues at our institute for their cooperative spirit, their helpful feedback, and the enjoyable time we spent working together. Special thanks go to Martina Thieme for her great support, her cheerful demeanor, and her essential contribution to the warm atmosphere in our institute. I am also deeply grateful to Prof. Dr. Ilkay Yavrucuk, who has done an excellent job of maintaining the cordial, appreciative, and productive culture. Additionally, I extend special thanks to Jonas Koch for his exceptional helpfulness and technical support. I have also been extremely fortunate with all my office colleagues, in addition to those already mentioned, especially Tim Mehling and Ongun Hazar Aslandogan, and on a partial but regular basis, Prof. Dr. Milan Vrdoljak.

I would also like to thank Prof. Dr. Ben Woods for his initiative and excellent guidance in the SABRE project, from which this work originated, and the entire research group for the continuous exchange and pleasant collaboration. I would also like to acknowledge that this SABRE project was funded by the European Union's Horizon 2020 research and innovation program (Grant Agreement No. 723491).

My grateful thanks also go to Oliver Dieterich for helpful discussions and advice on specific technical aspects of this research. Many thanks to Dr. Wayne Johnson for a very helpful workshop on performing comprehensive helicopter analysis, for his immediate responses to complex problems, and for providing an academic license of his CAMRAD II software that made this work pos-

sible. My sincere thanks also go to Prof. Dr. Jayant Sirohi for his knowledge transfer during his visits to our institute and his contribution to the idea of the specific active-camber concept that is the subject of this investigation. I would also like to thank Dr. Oliver Oberinger for his support in guiding me through my first steps in the field of comprehensive rotor analysis.

Lastly, I am deeply grateful to all those who are close to me for their constant support and understanding.

Thank you all.

Contents

Abbreviations and Symbols

Symbols

b_{lo}	lower bounds for optimization variables
b_{up}	upper bounds for optimization variables
c	blade chord length, m
c_{tip}	blade chord length at the blade tip, m
c_{root}	blade chord length at the (aerodynamic) blade root ($r = 0.22$), m
c_{ref}	blade chord length at the $r = 0.75$, m
C_l	lift coefficient
$C_{l,\text{max}}$	maximum lift coefficient
C_d	drag coefficient
C_m	moment coefficient
C_x	rotor sectional drag coefficient (shaft axis)
C_T	rotor thrust coefficient (shaft axis)
D	rotor drag force (wind axis), N
e	exponent of the individual terms in the cost function
EI_x	blade flap (out-of-plane) bending stiffness, Nm^2
EI_z	blade lag (inplane) bending stiffness, Nm^2
EA	blade axial stiffness, N
f_i	individual objectives in the cost function
$F_{\text{pl},0}$	mean pitch-link loads, N
$F_{\text{pl,pp}}$	peak-to-peak pitch-link loads, N
F_x	hub force in x-direction (shaft axis), N
F_y	hub force in y-direction (shaft axis), N
F_z	hub force in z-direction (shaft axis, N), blade section thrust (shaft axis, kN/m)
F_{pp}	peak-to-peak hub forces, N
GJ	torsion stiffness

I_θ	blade section mass moment of inertia, kg·m^2
L	rotor lift force (wind axis), N
m	mass per length, kg/m
m_b	mass of the rotor blade
M	Mach number
M_x	rotor hub roll moment (shaft axis, right wing up positive), Nm
M_y	rotor hub pitch moment (shaft axis, nose up positive), Nm
M_z	rotor shaft torque (shaft axis, negative for power absorbed by the rotor), Nm
$\overline{M_z}$	mean rotor shaft torque (shaft axis), Nm
M_{pp}	peak-to-peak hub moments, Nm
n	control frequency in terms of rotor harmonics, Ω
N_b	number of rotor blades
N_o	number of objectives considered in the cost function
N_{panels}	number of far wake trailed vorticity panels
N_r	number of sample points along the blade radius
o_i	specific optimization target
P	rotor power
P_a	active rotor power
P_p	passive rotor power
P_{ref}	Bo 105 rotor power
P_D	rotor parasite power (related to rotor drag D)
q	dynamic pressure, $0.5\rho v^2$
R	rotor radius, m
r	radial position, y/R
r_1	radial position of inboard edge of the active-camber section, $1/R$
r_2	radial position of outboard edge of the active-camber section, $1/R$
r_c	radial position of the active-camber section center, $1/R$
r_{cut}	blade root cutout, $1/R$
s	radial length of the active-camber section, $1/R$
S_{Bo105}	configuration with original Bo 105 structural properties
S_{mod}	configuration with modified structural properties
SM	stall margin
SM_o	inverted stall margin used in the objective function (minimization problem)
T	rotor thrust (shaft axis), kN
t	taper ratio

t_b	thickness of the rotor blade
w_P	weighting factor for the rotor power (cost function)
w_L	weighting factor for the peak-to-peak pitch-link and hub loads (cost function)
w_{SM}	weighting factor for the stall margin (cost function)
v	flight speed of the rotorcraft relative to the air, m/s
v_i	induced velocity, m/s
v_{tip}	blade tip velocity, m/s
w_i	weighting coefficients
x	rotor blade coordinate in chord-wise direction, m
$\vec{x}$	optimization variables (active-camber control inputs)
x_{CG}	blade center of gravity offset from elastic axis (chordwise), m
x_b	blade lag displacement, m
x_c	blade tension center offset from elastic axis (chordwise), m
y	rotor blade coordinate in radial direction, m
z_b	blade flap displacement relative to the precone virtual line, m
α	blade section angle of attack, deg
α_s	rotor shaft tilt (wind axis, negative forward), deg
δ	active-camber deflection (positive downward), deg
δ_{r_1}	active-camber deflection at r_1, deg
δ_{r_2}	active-camber deflection at r_2, deg
$\delta_{0\text{P}}$	static/mean camber deflection, deg
δ_{r_c}	active-camber deflection at r_c, deg
$\delta_{n\text{P}}$	active-camber control amplitude (n-th rotor harmonic), deg
δ_{ref}	reference control input to specify spanwise variation of camber deflection, deg
Δ	difference operator
ϵ_β	flap hinge distance
λ	scaling factor
μ	advance ratio, $V_\infty/\Omega R$
Ω	rotational speed of the rotor, rad/s
Ω_{ref}	nominal rotational speed of the rotor, rad/s
ϕ	section inflow angle, deg
$\phi_{n\text{P}}$	active-camber control phase (n-th rotor harmonic), deg
Π	cost function to be minimized during the optimization
ψ	rotor azimuth (counter-clockwise), deg
ρ	air density, kg/m^3

σ	rotor solidity, $Nc/\pi R$
τ_R	metric to quantify the modification of the rotor in relative terms, %
θ	blade sectional pitch, deg
θ_e	blade elastic twist, deg
θ_tw	blade built-in twist, deg
θ_root	blade pitch angle at the blade root, deg
θ_tip	blade pitch angle at the blade tip, deg
θ_0	collective pitch angle, deg
θ_{1c}	lateral cyclic pitch angle, deg
θ_{1s}	longitudinal cyclic pitch angle, deg
ϑ	metric to quantify spanwise variation of camber deflection, %

Subscripts

a	active rotor
p	passive rotor
P	power
pl	pitch link
pp	peak-to-peak
hpp	half peak-to-peak
ref	reference
max	maximum
min	minimum
n	rotor harmonic
L	loads, representative of all peak-to-peak rotor hub loads (forces and moments)
SM	stall margin
P	rotor power
root	blade root (r=0.22)
tip	blade tip (r=1)
x, y, z	Cartesian Coordinates

Abbreviations

2D, 3D	two-dimensional, three-dimensional
BVI	blade-vortex interaction
CAMRAD	comprehensive analysis model of rotorcraft aerodynamics and dynamics
CFD	computational fluid dynamics
CG	center of gravity
CSD	computational structure dynamics
DLR	German Aerospace Center
EDLIN	Equations Differentielles Lineaires
Exp	experiment
HHC	higher-harmonic control
IBC	individual blade control
ISA	international standard atmosphere
MTOW	maximum takeoff weight
NASA	National Aeronautics and Space Administration
ONERA	Office national d'études et de recherches aérospatiales
RANS	Reynolds-averaged Navier-Stokes
RPM	revolutions per minute
WM	wake modeling

List of Figures

List of Tables

1 Introduction

Helicopter main rotor blades experience a wide range of different flow conditions and a high degree of aerodynamic unsteadiness. This variability is related to different flight conditions during a mission, such as hovering flight and high-speed forward flight. Additionally, as the forward speed increases, the rotor blades experience a significant change in oncoming flow velocity over the course of one rotor revolution. While high Mach numbers are encountered on the advancing side, moderate Mach numbers are encountered outboard on the retreating side of the rotor disk. Towards the blade root on the retreating side, the oncoming flow velocity decreases linearly and reaches negative values in the so-called reverse flow regime. Rotor primary control, usually based on a swashplate mechanism, is used to balance the rotor under these unevenly distributed aerodynamic conditions by adjusting the blade pitch position along the rotor azimuth. This directly affects the local angles of attack and aerodynamic forces during a rotor revolution.

For a typical forward flight scenario, this results in small angles of attack on the advancing side (high Mach numbers) and large angles of attack on the retreating side (low Mach numbers). While this is an effective way to keep the main rotor in balance and to ensure the controllability of the rotorcraft, it is limited in its ability to provide efficient operation. Consequently, as forward speeds increase, the aerodynamic forces are distributed more and more unevenly across the rotor disk, and a passive rotor is unable to sufficiently counteract this effect. Furthermore, a static airfoil can only be a compromise for these varying flow conditions.

Increasing the efficiency of rotorcrafts is an important step in reducing CO2 emissions, increasing endurance and range, and reducing operating costs. Therefore, active rotor concepts have been proposed to simultaneously enable main rotor controllability and improve aerodynamic performance. A straightforward approach to this is a concept known as individual blade control (IBC), which allows not only 1/rev actuation but also higher harmonic control. This method does not involve active deformation of the rotor blade. Instead, the pitch position of the entire blade is adjusted to better anticipate the demand at each azimuth position. Another approach is the active-twist concept, which actively changes the blade twist during flight. However, neither of the aforementioned concepts involves modifying the blade's two-dimensional (2D) cross-sectional geometry at a given radial position. To this end, active trailing-edge flaps, active leading-edge morphing, or active-camber concepts have been proposed. In addition to modifying the cross-sectional geometry, these concepts also permit a more targeted application within a specific range along the rotor blade.

To date, active rotors, particularly active-camber concepts, have not become established in conventional helicopters due to the high complexity of such systems. The development of such systems is expected to be difficult and costly, and involves an elaborate certification process. Furthermore, the integration of such systems adds weight and additional components to the helicopter system, which may fail during operation and require maintenance. Additionally, the implementation of these systems presents several challenges that have not been satisfactorily resolved for real-world applications. For instance, the competing requirements of having an elastic skin to allow a deformation of the airfoil while providing sufficient stiffness to resist the aerodynamic and centrifugal forces present a significant challenge. Nevertheless, although these challenges must be addressed when considering the integration of such systems, they are deemed negotiable from a technical perspective. This is supported by preliminary experimental studies in the field of active rotors, as discussed in the following. Consequently, the ultimate decision to pursue this technology will be based on economic considerations. However, in order to make an informed decision, it is essential to have a comprehensive understanding of the features, benefits, and capabilities of such systems. This understanding will allow a balanced assessment of the potential benefits and costs associated with implementing active camber morphing.

With regard to this latter aspect, a lack of knowledge and research was identified at the outset of this study, resulting in an incomplete understanding of the operational characteristics and beneficial application of active camber. Consequently, the information in the literature is insufficient to fully evaluate the capability and most appropriate application of active camber. In addition to the benefits of this technology, the limitations and constraints are also of great interest in assessing the value of developing such systems. At this point, the current work aims to contribute to and provide a better understanding of the complex but promising active-camber concept. The study examines the ability of this mechanism to improve rotor efficiency while maintaining critical operational aspects within acceptable limits. Additionally, it attempts to provide guidance for the development process of an active-camber system in order to fully exploit its ability to improve rotor efficiency. Before discussing the objectives of this study in more detail, a comprehensive overview of existing research on active rotor concepts is provided.

1.1 Previous Research on Active Rotors

Over the past decades, numerous active rotor concepts have been proposed, studied, and tested. These studies have often focused on load and vibration reduction, as well as rotor power reduction. In addition, noise reduction and flight envelope extension in terms of dynamic stall alleviation and thrust increase have also been analyzed. Finally, replacing the conventional swashplate mechanism for the primary control of the rotor was another objective in some of the studies.

Higher harmonic blade pitch control (HHC) and individual blade control (IBC) are common active rotor concepts that have been extensively studied in research projects [1–11]. With a conventional swashplate mechanism, blade pitch control is only available in the first harmonic. It

adequately enables rotor balancing for each flight condition. However, it was found that greater flexibility in adjusting the blade pitch along the rotor azimuth was beneficial for some of the above mentioned objectives. This was usually achieved by superimposing a 2/rev or higher harmonic pitch control signal on top of the 1/rev primary control, for example by replacing the pitch links with actuators.

Extensive wind tunnel testing was conducted in the NASA Ames 40- by 80-foot wind tunnel [1] on a full-scale Bo 105 main rotor. It showed that IBC is suited to simultaneously reduce blade vortex interaction (BVI), noise, and helicopter vibrations. Hydraulic servo-actuators replaced the pitch links of the rotor to enable individual control of all rotor blades. Furthermore, up to 7% rotor performance improvements were reported for 2/rev actuation at a high-speed flight of $\mu =$ 0.45 using this technology. However, half of the reported power savings had to be invested in the hydraulic system to achieve this actuation. In addition, this μ was higher than the actual speed limit of the investigated Bo 105 helicopter. For $\mu = 0.3$ (close to cruise speed), no performance gains were found based on the limited number of 2/rev actuation amplitudes examined in this study. Similar results were obtained in an earlier study of a scaled CH-47D rotor model [2]. It reported power gains at high-speed flight ($\mu = 0.35$) of about 3% to 5%. Based on a computational study, the same author showed in [3] the ability to use IBC to suppress blade stall. However, stall and rotor performance could not be improved simultaneously. Any benefit in one area had a detrimental effect on the other.

The result of testing IBC in real flight on a CH-53G helicopter is presented in [4, 5]. In a high-speed flight of 130kts, 6% power reduction was achieved with 2/rev actuation. At the same time, the pitch-link loads decreased. In addition, even with a small IBC authority, 60% vibration reduction and 3dB noise reduction could be achieved. Moreover, an approach was proposed to significantly reduce the required power of the IBC actuators by allowing power recovery over one rotor revolution.

Another experimental study of an IBC system was conducted in the National Full-Scale Aerodynamics Complex 40- by 80-foot wind tunnel using a UH-60A main rotor [6]. In addition to reductions in the hub loads, pitch-link loads, and noise, a 5% reduction in rotor power was achieved ($\mu = 0.4$). The same tests were used for a comparison with a computational study in [7, 8] including CAMRAD II and OVERFLOW-based analyses. With CAMRAD II, the rotor power savings could be well predicted up to $\mu = 0.35$. For higher advance ratios, only a coupled CAMRAD II/OVERFLOW simulation correlated well with the measured data. Optimal rotor power savings were based on a 2/rev actuation with an amplitude of 2° and a phasing of $\phi = 225°$, i.e., peaks in blade pitch at $\psi = 112.5°$ and $\psi = 292.5°$. This unloaded the fore and aft region of the rotor disk and alleviated the negative thrust on the advancing side.

While IBC is usually based on actuators replacing the pitch links, a multiple swashplate concept was proposed for multi-harmonic IBC [9] and has been tested on a scaled model in the DNW-LLF wind tunnel. The BVI noise level, rotor vibrations, and rotor power were successfully reduced. With $\mu = 0.345$, a power reduction of about 5.6% was achieved using a 2/rev actuation (1° ampli-

tude, 240° phase shift).

Active twist is another concept that aims to improve the rotor behavior according to the above-presented objectives. Instead of adjusting the entire blade pitch, as is done with IBC, this method attempts to modify the blade pitch along the blade span by actively adjusting the rotor blade twist [12–18]. This can be done either by changing the twist for different flight speeds or by periodically adjusting the twist per rotor azimuth.

In [12], the NASA/Army/MIT Active Twist Rotor was experimentally tested in the Langley Transonic Dynamics Tunnel. This scaled model was based on piezoelectric active fiber composite actuators. High load reductions were reported, especially when using a 3/rev actuation. The same test setup was investigated in [13, 14] using a comprehensive analysis (CAMRAD II) to conduct a parametric study in which various baseline blade design aspects were changed, i.e., blade tip sweep, droop, built-in twist θ_{tw}, and taper. In terms of rotor power and hub vibration improvements, values of $\theta_{\text{tw}} = -10°$, blade tip (outer 5%) sweep of 30°, droop of 10°, and taper ratio ($c_{0.95R}/c_{\text{tip}}$) of 2.5:1 were suggested. Also [19] investigated this setup computationally. It was found that 2/rev actuation was able to improve rotor performance when using a 210° phase shift. This resulted in a reduction of the blade twist at $\psi = 110°$ and $\psi = 290°$ and an increase of the outboard blade pitch on the advancing and retreating sides. A rotor lift-to-drag ratio increase of more than 10% was reported for active twist at $\mu = 0.45$ and about 2% at $\mu = 0.3$ ($C_T/\sigma = 0.075$). In terms of achieving net rotor power gains, these improvements are approximately halved due to the neglect of parasitic drag in the definition of the equivalent rotor lift-to-drag ratio (L/D_e with $D_e = (P_i + P_0)/V$, as opposed to the aircraft lift-to-drag ratio).

An approach to change the blade twist for different advance ratios was investigated computationally in [15]. Through extension−torsion coupling in combination with a variation of the rotor rotational speed, the blade twist was adapted to different flight conditions.

While IBC and active twist only affect the rotor blades' global or local pitch angle, another group of active rotor concepts aims to change the cross-sectional geometry of the rotor blades. These concepts are part of the on-blade control mechanisms. The morphing of the cross-sectional geometry can be achieved in either a discrete or a continuous manner. The former group of concepts comprises discrete leading-edge slats, trailing-edge flaps, or gurney flaps, which are described by a rigid body motion relative to the main body of the rotor blade. A further distinction within these discrete concepts can be made by how the actuated part is separated from the main body, i.e., with or without a gap.

Of the mechanisms just mentioned, trailing-edge flaps have been the most extensively studied [19–34]. Although not widely used in existing helicopters, servo trailing-edge flaps have been used since the late 1940s for rotor primary control [20, 21]. Based on 1/rev actuation, the blade pitch position is adjusted by changing the aerodynamic pitching moment via trailing-edge flap control. However, to improve the aforementioned objectives, such as rotor performance and vibration, a trailing-edge flap actuation superimposed on a swashplate-based primary control has typically

been investigated.

Flight testing of a piezoelectrically driven trailing-edge flap was presented in [22–24] based on a hingeless BK117/EC145 helicopter. It was implemented between 63%R and 85%R. A simultaneous reduction of noise and vibration was achieved. From an actuation power perspective, it was recommended not to extend the chordwise range to more than 15%c. Instead, a larger expansion in radial direction was suggested. By reducing the tuning mass and eliminating the pendulum absorber, it was possible to overcompensate for the additional weight resulting from the implementation of the active trailing-edge flap mechanism. Flight tests of a trailing-edge flap system on an AW139 helicopter have also been reported [25]. These tests were also based on an implementation of the flap in the rear 15%c of the rotor blade. With this trailing-edge flap implementation, an actuation amplitude of 3° was possible.

In addition to flight tests, several wind tunnel tests have been conducted on active trailing-edge flaps [26, 27]. While the former study was based on BVI noise reduction and vibration reduction, the latter study also investigated the rotor performance at flight speeds up to 155kt ($\mu = 0.375$) on a MD900 main rotor ($C_T/\sigma = 0.075$). Noise reductions of 6dB and vibratory hub load reductions of about 80% were reported. A 3° amplitude was sufficient for these enhancements. However, power gains were only in the order of 1% in terms of rotor L/D_e at $\mu = 0.3$ (2/rev, 90° phase).

Furthermore, a significant number of computational studies of active trailing-edge flaps have been published. In [28], a hybrid optimization of the trailing-edge flap-related parameters and the rotor blade structural properties (i.e., stiffness and tuning mass) was performed numerically to reduce rotor hub vibrations with minimal actuation input. It was found that the hybrid optimization achieved vibration reductions similar to the retrofit design or sequential design, but the control effort was significantly reduced.

Using trailing-edge flaps for rotor performance enhancements was investigated in [19]. With an optimum trailing-edge flap location from 50%R to 90%R, approximately 1% (2% rotor L/D_e) power gain was found at cruise speed, and about 5% (10% rotor L/D_e) power gain at $\mu = 0.45$. In [30], a simultaneous reduction of vibration and rotor power was demonstrated at high advance ratios ($\mu = 0.35$ and $\mu = 0.4$) using a computational Bo 105 rotor model. When optimizing for rotor power only, power savings of 4% and 6.4% were reported for $\mu = 0.35$ and $\mu = 0.4$, respectively. The actuation was based on a combination of 2/rev to 5/rev actuation. However, it was accompanied by higher vibration levels. A simultaneous reduction in vibration and rotor power was only possible with a significant reduction in power gains.

Instead, 1−4/rev trailing-edge flap actuation on a UH-60A rotor was investigated in [35] using the RCAS comprehensive analysis code. In addition, a multi-harmonic deployment schedule was investigated. At an advance ratio of $\mu = 0.368$, up to 3.7% power gain was reported with 1/rev actuation. This was slightly higher than the gains found with the multi-harmonic deployment scheme. Furthermore, using the same computational framework, a 1/rev trailing-edge flap actuation was investigated in [31] with respect to the correlation between possible power savings

and the blade torsional stiffness. It was found that additional power gains induced by decreasing the blade torsional stiffness (GJ) resulted from the deterioration of the passive rotor efficiency by reducing GJ. Thus, in contrast to vibration reduction studies, reducing GJ was not deemed useful for improving the rotor performance when using an active trailing-edge flap.

As a continuation of this work, the influence of a gap between the rotor blade main body and the trailing-edge flap on the rotor performance was investigated in [32]. In addition, this study was complemented by using a high-fidelity coupled CSD-CFD analysis. It was found that spanwise gaps inboard and outboard were less significant and only reduced the rotor efficiency by about 1% compared to integral flaps. However, chordwise gaps reduced the rotor efficiency by 2% to 3%. As the spanwise extension of the TE flap increased, the performance penalty due to gaps decreased moderately.

Another study that investigated a simultaneous reduction in rotor performance and vibration is presented in [33] and was based on a UMARC comprehensive analysis model of the UH-60A rotor. Only a small trailing-edge flap with a spanwise extension of 10%R and a chordwise range of 15%c was investigated. It was placed at 65%R. Constant deflection combined with 1/rev and 2/rev trailing-edge flap control resulted in 2% and 4−5% power reductions at $\mu = 0.3$ and $\mu = 0.4$, respectively. The mechanism responsible for these power gains was identified as an unloading of the front and rear parts of the rotor disk and a reduction of the negative thrust on the advancing side. Actuation amplitudes of 5° to 10° were used for these power gains. When also optimizing for vibration reduction, a combination of 1−5/rev actuation inputs resulted in 1.5% power reduction and 50% vibration reduction. In hover, the rotor efficiency was improved by constant trailing-edge flap deflection, which induced a greater blade twist.

Again based on the UH-60A main rotor, a surrogate optimization-based investigation is presented in [34]. RCAS with uniform inflow wake modeling was used for the aeromechanics calculations. Contrary to previous studies on the same rotor, it reported 9.5% power savings at a $\mu = 0.3$ advance ratio. Lower power savings were obtained at higher advance ratios, again in contrast to other publications. At the same time, a significant reduction in hub vibration was reported. The actuation schedule was based on a superposition of up to 15 rotor harmonics. However, the discontinuous slope of the reported power gains over the advance ratio indicates that full convergence of the calculations was not achieved, as there was no indication of a physical reason to explain this behavior.

An alternative to the classic trailing-edge flap is the so-called Gurney flap or micro-tab. Instead of being initially aligned with the airfoil chord and actuated at an angle, they typically translate orthogonal to the airfoil chord and are placed close to the trailing edge. As a result, only a very small mechanism and a small amount of actuation are required to achieve a relevant effect. On the downside, this discontinuity results in a less-than-optimal streamlining shape, which negatively affects the efficiency of the airfoil. Nevertheless, it is a feasible way to influence the aerodynamic loads on the rotor disk. Investigations of this concept are presented in [36–40] Similar to this concept, microflaps have also been proposed [41]. They compare well with conventional

trailing-edge flaps but are much smaller and can be actuated up to 90°.

Unlike trailing-edge flaps, leading-edge flaps are applied in front of the airfoil. This concept has been studied in [19, 35, 42–44]. A specific conclusion in these works was that leading-edge flaps were particularly interesting for high-thrust scenarios. Under normal conditions, however, they were less effective than trailing-edge flaps in improving rotor performance.

In contrast to the discrete on-blade control mechanisms, a continuous change in the airfoil geometry has also been investigated. In the following, the term "active camber" is used to describe mechanisms that involve a continuous morphing of the camber line. This morphing can be applied either along the entire blade chord or only over a certain range, e.g. in the leading or trailing-edge region of the rotor blade. When applied to the leading edge, these concepts are also referred to as "variable droop leading edge". Otherwise, when applied to the trailing edge, these concepts are also referred to as continuous trailing-edge flaps. Only limited research is available regarding evaluating the performance of continuous approaches. In terms of leading-edge deflection, no relevant difference was found between the discrete leading-edge flap and the variable droop leading edge [19]. In [32], the investigation of the effect of having or not having a gap between the trailing-edge flap includes a configuration that is at least similar to a continuous trailing-edge flap. Compared to the discrete configuration with a gap, the seamless approach was more efficient.

Instead, several research efforts have aimed at developing such morphing concepts from a design and implementation point of view, e.g., in [45–57]. A well-known challenge of these concepts is the need for a flexible blade surface to facilitate camber morphing while providing sufficient resistance to aerodynamic and centrifugal forces. In addition, the actuation mechanism itself must operate reliably under high centrifugal forces and overcome significant aerodynamic and structural resistances. This results in a trade-off between the robustness of the mechanism and the additional weight due to increased material thickness and actuator dimensions, as well as the power required to actuate the mechanism. Nevertheless, the referenced research claims to have satisfactorily addressed these challenges, and these concepts have been deemed feasible for application to helicopter main rotors, although this has not yet been conclusively proven. Alternatively, the mechanism proposed by [53–55] avoids the need to stretch the blade surface by using a sliding mechanism. As a result, only bending of the blade surface is involved at the cost of a small discontinuity on the lower surface of the rotor blade.

Furthermore, some research has been done on the two-dimensional aerodynamics of morphing airfoil sections [45, 57, 58]. A comparison between a trailing-edge flap and an active-camber system showed advantages on the side of the continuous approach [45, 47]. In addition, different chordwise ranges were examined in [59], and it was found that further gains from morphing more than the aft 25% of the airfoil were not in good proportion to the potential benefits. The exact airfoil polars of the morphed geometries, especially the results of [58], are discussed further in the next chapter, as they were the basis for the aerodynamic calculations in the current work.

For completeness, other active rotor concepts and different approaches to improving rotor effi-

ciency are briefly discussed below. One approach that is mainly aimed at improving the hover performance is the variable chord extension concept as suggested in [60–62]. It has been proposed to adapt the rotor blade geometry to different flight speeds rather than dynamically actuating it over a rotor revolution. Moreover, an active oscillating jet concept was investigated, which blows air through small gaps in the blade surface to specifically affect the near-field aerodynamics. However, this concept was not considered to be very relevant for improving the performance of the rotor blade [19].

Variable speed rotors are not typically referred to as active rotors. However, they do provide active variability to better adapt the rotor aerodynamics to specific flight conditions to increase rotor efficiency [63]. An interesting aspect of this concept is that it can be combined with most of the active rotor concepts discussed above. For example, a study of combined active twist and variable rotor speed was presented in [64].

Overall, the active rotor concepts IBC, active twist, and trailing-edge flap were suggested to be particularly suitable for improving rotor efficiency at high speeds [19, 35, 37, 43, 65]. The mechanism for improving rotor performance at high speeds was similar for all of the previously mentioned active rotor concepts. Rotor power savings were attributed primarily to the distribution of thrust to the lateral sides of the rotor disk, thereby reducing the thrust peaks in the front and rear regions of the rotor disk and the negative thrust on the advancing side.

In addition to the research on active rotors, a brief overview of the previous work on passive rotor optimization is given. On the one hand, improving the aerodynamic efficiency of the rotor competes with any active concept because passive measures are usually easier to implement. On the other hand, the ultimate goal of an active rotor design would be an integral optimization that includes both active and passive rotor design aspects. Previous research on static rotor design optimization has mostly involved the discussion of complex rotor blade geometries [66–68]. Instead, [69] discussed criteria for evaluating the suitability of different airfoils for use on helicopter main rotors. In addition, some studies aimed at minimizing the rotor vibrations by optimizing the structural blade parameters [70, 71]. Other than blade airfoils, typical design parameters are the blade twist and the chord distribution across the blade span. With relatively small design changes regarding the above-mentioned parameters, the efficiency of a Bo 105 main rotor was improved by about 10% [66]. By using carbon fiber material in specific areas of the blade, the original torsional and bending stiffness was largely maintained.

The design of the rotor blade tip has also been intensively studied. A considerable number of different designs have been proposed, and according to [67], it is not possible at this point to declare any particular geometry as the best tip shape. In [68], it was found that sweeping the blade forward can also contribute to efficiency gains. This was due to the aeroelastic effect of canceling the nose-down elastic twist by moving the thrust forward of the pitch axis. It shows that the design optimization of passive rotor blades is an ongoing process with many parameters, multiple objectives, and complex interdependencies. Not only the aerodynamic efficiency but the whole aeroelastic system has to be evaluated to successfully improve the rotor design.

1.2 Research Objectives

Previous studies have been unable to provide an accurate answer to the potential of active camber to enhance the performance of a helicopter main rotor, particularly when considering more sophisticated control schemes and the impact of rotor design variables. Additionally, studies on similar concepts have been limited by either a lack of scope or an insufficient level of fidelity. Based on the evaluation of previous research, an active camber morphing in the rear part of the rotor blade appears to be a particularly capable solution. This is due to its high effectiveness in influencing the rotor aerodynamics in a targeted manner, similar to that of trailing-edge flaps. However, it is better streamlined and without discontinuity, which can induce separation of flow, thus increasing drag and reducing lift.

The objective of this study is to enhance the understanding of this technology in terms of the underlying physical phenomena and to identify potential benefits that have not been previously identified or studied. This entails investigating the interdependence with essential rotor design variables, which was not adequately addressed in previous research. This is also intended to provide guidance in optimizing the rotor designs when employing this system. Ultimately, a realistic estimation of the efficiency improvements achievable with this technology is aimed to be possible based on the following analysis. In more detailed terms, the following research questions are addressed:

1. **What are the attainable performance enhancements possible through the implementation of active camber control on the main rotor of a helicopter, and how can they be achieved?**
   In particular, discrete trailing-edge flaps have been the subject of previous research, including estimates of potential power savings. Although the results are expected to be similar between discrete and continuous morphing mechanisms, the difference in aerodynamic efficiency is expected to affect the results to some extent. Furthermore, only a small subset of possible applications has been studied. The effect of size and placement has not been sufficiently discussed. Additionally, a continuously applied spanwise variation of the actuation amplitude has not been investigated. This application is somewhat unique to active-camber systems, as it necessitates some flexibility in the blade surface to permit this type of actuation deployment. Furthermore, the majority of previous studies have concentrated on specific high-speed flight cases, rather than considering the full flight envelope.

   Moreover, previous studies have predominantly employed parametric studies of isolated harmonic inputs for actuation deployment, rather than performing an optimization of complex actuation schedules based on the superposition of multiple harmonics. In studies that were based on an advanced optimization approach, the level of aerodynamic fidelity was typically low, for instance, uniform inflow wake modeling. This work also attempts to clarify aspects that have been contradicted in some of the aforementioned literature, such as the effect of using multiple rotor harmonics for control or questionable trends in the correlation

of power gain and advance ratio.

Although this study was not explicitly aimed at reducing rotor loads and vibrations, the study focused on actuation deployments that did not exceed the baseline peak-to-peak loads. This approach was assumed to capture only results that are relevant to helicopter applications. Furthermore, the retreating-blade stall margin was also considered in the following investigations. Finally, operational aspects for the application of such systems on real rotors, including risk mitigation measures, were discussed.

2. **What underlying phenomena contribute to the rotor efficiency gains induced by active camber?**
   Previous research has yielded insights into the potential for improving rotor efficiency with the use of trailing-edge flaps. However, these studies have not yet provided a comprehensive understanding of the aeroelastic causal chain and the main drivers in enhancing the rotor efficiency. In particular, there is less information available in the literature for mechanisms that continuously morph the blade geometry, like active camber control. Such an understanding is important not only for drawing conclusions regarding active rotor design but also for evaluating the capability of the current modeling approach in capturing the primary effects caused by active camber actuation.

3. **How are the rotor power savings from active camber related to the baseline rotor design parameters?**
   The purpose of this investigation is to assess the generality of the results obtained with regard to the two research questions previously presented. This entails examining the relationship between active-camber-induced power gains and an efficiency improvement of the passive baseline rotor. Furthermore, this analysis is intended to identify design goals for the baseline rotor, which is to be used in conjunction with an active-camber system. This covers an exploration of the potential benefits that may result from a suitable modification of the baseline rotor parameters.

2 Methodology and Scientific Approach

The following is an outline of the approach to finding answers to the research questions presented earlier. A computational approach was deemed most appropriate for this type of analysis. An experimental study, on the other hand, was not feasible due to the complexity of such active-camber mechanisms, the infrastructure required to conduct full-scale experimental tests under high-speed flight conditions, and the significant amount of parameter variation envisaged in this investigation. To adequately model the contributing phenomena, a suitable representation of the rotor aerodynamics is essential. However, according to the literature, the rigid body motion and the elastic deformation of the rotor system are also indispensable for this investigation. In addition, the computational framework must be able to perform a trim calculation to ensure realistic operating conditions and comparability between different cases.

These capabilities are consolidated in so-called comprehensive rotor analysis codes, which combine the aforementioned disciplines. Various frameworks have been developed, typically covering aerodynamic wake modeling from low (e.g., uniform inflow) to medium (e.g., free-vortex wake) fidelity. To involve high-fidelity aerodynamic modeling (e.g., Reynolds-Averaged Navier-Stokes (RANS)-based computational fluid dynamics (CFD)), the typical approach is to couple an external aerodynamic solver to an existing comprehensive analysis framework. In this approach, the internal calculation of aerodynamic forces is replaced, for example, by a three-dimensional CFD calculation. In particular, for rotor power savings from an active rotor mechanism, previous work has shown that mid-fidelity wake modeling already provides good agreement with CFD simulations or wind tunnel test results. For vibration estimation, the capabilities of mid-fidelity methods were somewhat lower [8, 35]. Therefore, an established mid-fidelity comprehensive analysis code with free-vortex wake modeling was considered appropriate to model the aeroelastic behavior of an active-camber rotor with a focus on the rotor efficiency. It should also be noted that a comparable study would not have been feasible with CFD aerodynamic modeling due to the much higher computational resources required. In contrast, low-fidelity wake modeling was not considered suitable for evaluating the complex aerodynamic phenomena initiated by the active on-blade control.

Active camber is not an established technology for helicopter main rotors. Therefore, certain assumptions about the capabilities, limitations, and characteristics of such systems had to be made. To keep these assumptions to a minimum, a real concept developed at the University of Bristol called Fish Bone Active Camber (FishBAC) [45] was used in the present work to derive some key aspects (see Fig. 2.1). These include the geometries of the morphed airfoils, the actuation ranges

and frequencies, and some basic capabilities such as a differential actuation mode with different camber control along the blade span. This feature is achieved by independently controlling two actuators which are located inboard and outboard of the active-camber segment. It leads to a linear variation of camber deflection (i.e., trailing-edge deflection) between the two actuators.

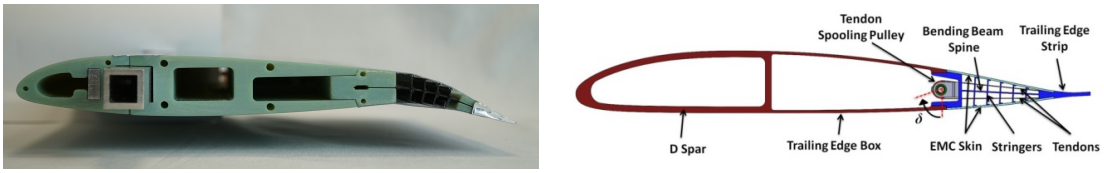

(a) Cross section of active-camber test article **(b)** Active-camber cross sectional details

Figure 2.1: FishBAC active-camber concept (Courtesy of Ben Woods, University of Bristol).

In the present work, a hingeless Bo 105 main rotor was selected as the baseline for the following investigations. It is a well-established and well-known helicopter rotor. Accordingly, the geometric and structural properties of the rotor are publicly available, and a relevant amount of experimental data and numerical studies on this rotor have been published. Also, the previously described FishBAC active camber mechanism was implemented on a section of the Bo 105 rotor blade using a NACA23012 airfoil. Another aspect of this rotor is its comparatively simple design involving rectangular blades and a linear blade twist. Some of the more advanced helicopter rotor blades have different airfoils along the rotor blade and complex rotor blade geometries. However, using one of these advanced rotors as a baseline for the current study was not feasible due to the lack of information on these rotor systems. Furthermore, the implementation and computational effort would have been significantly higher, and the analysis and interpretation of the results would have been even more difficult compared to a simpler rotor design. Nevertheless, in order to reduce the dependence of the following results on the choice of the baseline rotor, the influence of the baseline rotor design is investigated in the following work. Table 2.1 lists some of the most important parameters related to the Bo 105 main rotor.

Table 2.1: Bo 105 rotor parameters [72]

Parameter	**Symbol**	**Value**	**Unit**
Number of blades	N_b	4	-
Rotor rotational speed	Ω	44.4	rad/s
Blade tip speed	v_{tip}	218	m/s
Rotor radius	R	4.912	m
Rotor root cutout	r_{cut}	0.22	$1/R$
Blade chord length	c	0.27	m
Blade airfoil	-	NACA23012	-
Precone angle	-	2.5	deg
Maximum take-off weight	MTOW	2850	kg
Blade built-in twist (hub to tip)*	θ_{tw}	-8	deg

*Reference radial station for blade pitch position: $0.7R$.

While the focus of this study is on improving the efficiency of the helicopter main rotor using an active-camber system, good operability of the active rotor system was considered to be essential. This is to avoid approaching theoretical gains that are not useful in a realistic scenario. For this purpose, peak-to-peak rotor loads were taken into account. In addition, the stall margin was evaluated to ensure that the original flight envelope was maintained while using active camber. This resulted in a multi-objective optimization problem to be solved for each individual operational scenario. The following is a detailed description of the modeling and computational approach used to evaluate active-camber actuation on a helicopter main rotor.

2.1 Modeling of the Active Rotor

The present study was based on the Comprehensive Analytical Model of Rotorcraft Aerodynamics and Dynamics (CAMRAD) II to solve the aerodynamics, multi-body dynamics, and elasticity in a coupled and iterative manner, as further described in the following.

2.1.1 Rotor Structural Dynamics Model

A full-scale structural model of the four-bladed hingeless Bo 105 rotor was constructed with CAMRAD II including the swashplate mechanism for blade pitch control. The elastic deformation of the rotor blades was modeled using the Euler−Bernoulli beam theory for isotropic materials. It is generally considered to be a good approximation for slender beams that undergo moderate deformations [73]. In particular, this method effectively captures the low frequency modes of rotor blades. The equation of motion of a Euler–Bernoulli beam is generally described by

$$\rho A \frac{d^2 v}{dt^2} + EI \frac{d^4 v}{dx^4} = q(x,t) \tag{2.1}$$

In this equation, ρA represents the mass per unit length, EI the beam bending stiffness, and v the transverse deflection of a local beam section. The transverse load, q, that acts on the rotor blade is composed of aerodynamic, centrifugal, and Coriolis forces. This equation is solved by discretizing it using generalized coordinates and shape functions representing the elastic degrees of freedom of the beam. Numerical methods are required to solve this large system of equations that results from modeling a complex helicopter rotor.

Based on a convergence study, each rotor blade was discretized into seven elastic beam segments along the span (see Fig. 2.2). Seven shape functions were employed for each beam segment to represent the elastic deformation, with one function for axial deflection and two functions each for bending and torsion. This resulted in the use of 49 elastic degrees of freedom for each rotor blade.

The structural properties of the rotor blade, including stiffness, mass, and inertia, were supplied

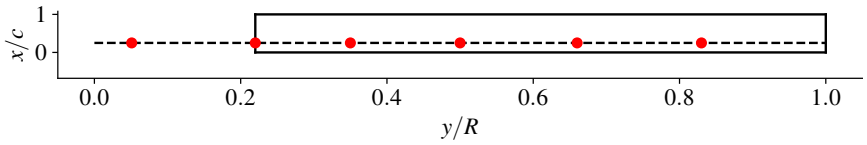

Figure 2.2: Structural discretization of the rotor blades.

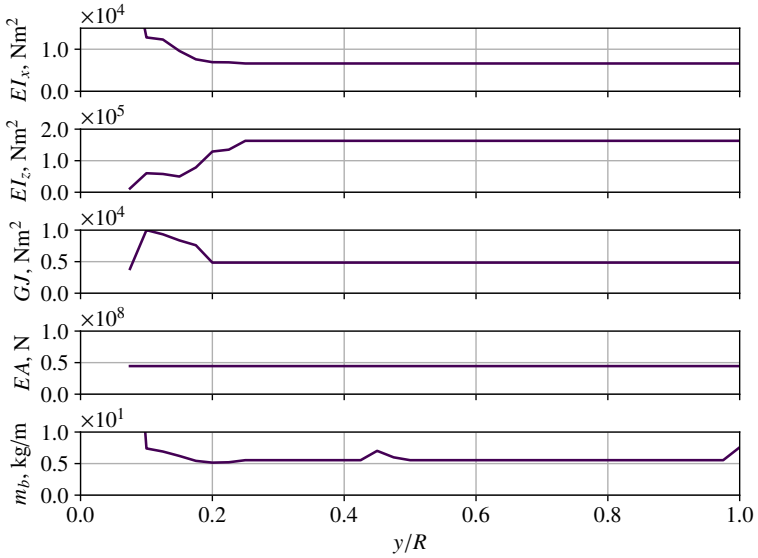

Figure 2.3: Rotor blade structural properties. Blade flap bending stiffness (EI_x), blade lag bending stiffness (EI_z), blade torsional stiffness (GJ), blade axial stiffness (EA), blade mass (m_b).

by the German Aerospace Center (DLR) [72]. Details can be found in Figure 2.3. These rotor blade structural properties of the baseline Bo 105 rotor were used throughout the present study for both the passive and active rotor unless otherwise indicated.

Based on the research objectives specified in Section 1.2, the baseline rotor design was modified to investigate interdependencies with active camber morphing (Chapter 4). This involved a variation of the blade geometry, including scaling of the airfoil cross-section. This raises the question of how to handle this aspect from a structural dynamics point of view.

It is common practice in blade design to pre-determine the structural properties of the blade and attempt to match these empirical values during the design process, e.g., by adjusting the number of composite layers in the blade skin or spars [74]. This reduces the risk of running into a problematic regime in this highly multidisciplinary design environment. In the present context, this approach translates into a scenario where the blade structural properties remain constant regardless of blade geometry modifications. However, the geometry changes must be small enough to justify this approach.

An alternative strategy is to assume that all relevant thicknesses vary proportionally with the chord length of the blade. For a filled rectangular cross-section, the bending and torsional stiff-

nesses would scale to the fourth power of the chord length, as per the second moment of area formulation. The blade mass per unit length would scale to the second power since only two dimensions (airfoil chord length and thickness) are involved. The mass moment of inertia would also scale to the second power because the distance of the mass from the center of rotation has a quadratic influence. The result of this scaling approach is summarized in Eq. 2.2 and Table 2.2.

$$\lambda = \frac{c_{\text{new}}}{c} = \frac{t_{b,\text{new}}}{t_b}. \tag{2.2}$$

Table 2.2: Scaling factors for rotor blade structural properties.

Variable	Symbol	Scaling Factor
Flap (out-of-plane) bending stiffness	EI_x	λ^4
Lag (inplane) bending stiffness	EI_z	λ^4
Torsion stiffness	GJ	λ^4
Axial stiffness	EA	λ^2
Mass/length	m	λ^2
Mass moment of inertia	I_θ	λ^2
Center of gravity offset	x_{CG}	λ
Tension center offset	x_c	λ

In this work, the first approach was used predominantly. However, in section 4.2.4 a comparison between the two approaches is presented to evaluate the impact of this modeling aspect. A real rotor design is expected to lie somewhere between these two approaches.

2.1.2 Rotor Aerodynamics Model

The rotor aerodynamic forces (lift and drag) and moments were calculated using a combination of airfoil table-based lifting-line theory and free-vortex wake analysis to estimate the nonuniform inflow. An overview of this method, implemented in the CAMRAD II framework, is given below, based on a detailed description in [73].

The combination of second-order lifting-line theory and vortex theory allows efficient computation of the main rotor aerodynamics. While saving a significant amount of computing power compared to a three-dimensional CFD calculation, three-dimensional effects such as tip losses and blade-vortex interaction (BVI), unsteady aerodynamic effects, and effects due to fluid viscosity and compressibility are still considered, but only locally or by applying simplified or empirical models. Therefore, it was considered most appropriate for the current research objectives. For the three-dimensional wake domain, vortex theory based on the Biot-Savart law, Kelvin's theorem, and Helmholtz's theorems were applied, assuming the flow to be inviscid, irrotational, and isentropic. Instead, the local aerodynamic forces were calculated based on high-fidelity RANS

CFD simulations, which, however, had to be solved only for discrete flow conditions in the steady, two-dimensional domain (further discussed in Sec. 2.1.5 and [58]). The results were stored in airfoil coefficient look-up tables to be used in the currently described computational framework.

Both the near-field and far-field solutions are coupled via the induced velocity, which is obtained from the wake modeling by integrating the Biot-Savart law over the vortex wake elements in the rotor wake. The induced velocity affects the aerodynamic angle of attack, which is used to pick the correct airfoil coefficients from the look-up table. For intermediate values that were not exactly covered by the airfoil coefficient look-up tables, a linear interpolation was applied. The two-dimensional airfoil coefficients are used to calculate the aerodynamic forces on the rotor blade, which in turn are used to calculate the bound circulation and, consequently, the rotor wake. Technically speaking, the wake strength is a result of the radial and azimuthal variation of the bound circulation. A spanwise change in the bound circulation produces trailed vorticity. A temporal change in the bound circulation produces shed vorticity. The geometry of the wake was calculated under consideration of the self-induced distortion by evaluating at each time step the induced velocity at each wake element based on the contribution of all wake elements (as also done to determine the induced velocity at the rotor disk). Numerical integration was then required to determine the wake geometry at the next time step.

To appropriately account for the three-dimensional effects according to Prandtl's lifting-line theory and the unsteady effects according to Theodorsen's lift deficiency function, a sufficient discretization of the wake model in space and time had to be applied. This was ensured based on a convergence study. With this, three-dimensional effects like tip losses were successfully considered, and no additional tip loss corrections were required when using this modeling approach. Time-wise, the wake problem was discretized in $\Delta\psi = 15°$ azimuth steps, i.e., 24 time steps per revolution. Space-wise, the rotor blade was discretized into 26 panels along the span. The non-uniform distribution of these panels is shown in Fig. 2.4. The aerodynamically active section ranged from $r = 0.22$ to the tip of the blade. Inboard, a root cutout was applied, and no aerodynamics were modeled in this region.

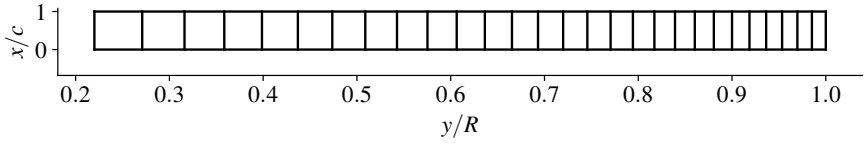

Figure 2.4: Aerodynamic discretization of the rotor blades.

The far wake was modeled using a rollup model with four (at high speed) to eight (at hover) trailed vortices. Two trailed vortices enclosed the aerodynamically active part of the rotor blade, i.e., they were placed at the most inboard ($0.22R$) and outboard ($1.00R$) radial stations. Two additional trailed vortices were placed at the inner and outer edges of the active-camber segment where high gradients in the bound circulation were expected. This approach was based on the suggestion in [73] to extend the classical far wake modeling approach with only one wake panel by assuming that a concentrated trailed vortex emanates from each geometric feature, i.e., edges of trailing-

edge flaps or rapid changes in blade chord length. In hover and low-speed flight, the number of vortex panels had to be further increased to avoid dependence of the results on the number and position of trailed vortices. A reassessment of this approach with respect to results in the current context is presented in Section 3.3.2. The vorticity distribution of trailed and shed vortices was based on the Scully vortex core model. According to [73], this model coincided well with measurements of a tip vortex. A Bagai-Leishman core radius growth model was applied to mimic the viscous diffusion of the vortex field. Depending on the forward flight velocity, the far wake was truncated after a certain number of rotor revolutions. In hover, the wake was modeled with 17 rotor revolutions to achieve full convergence. In high-speed flight, five rotor revolutions were sufficient as the entire wake was convected downstream of the rotor.

The ONERA-EDLIN unsteady aerodynamics model was used to estimate a correction for aerodynamic loads due to unsteadiness. It is based on the incompressible thin-airfoil theory, but several modifications have been made to make it more suitable for rotorcraft problems. Compared to the thin-airfoil theory, the ONERA-EDLIN theory also considers heave and pitch, as well as the time-varying free stream [75]. In addition, Küssner's coefficients are used to account for compressibility effects. All terms representing static loads are excluded from the original equations, as they are already adequately accounted for by the use of airfoil tables [75].

2.1.3 Trim Procedure and Numerical Settings

The CAMRAD II comprehensive analysis solver allows the use of a harmonic balance method to calculate steady-state trim conditions more efficiently than time integration approaches. This involves the use of larger time steps. However, it requires that a finite number of harmonics sufficiently represent the physical problem, since periodicity is enforced in the solution [73]. The Newton-Raphson method is employed to iteratively solve the trim problem. The required derivative matrix is evaluated by numerical perturbation.

In addition to the outer trim loop, several inner loops had to be solved, e.g., for structural dynamics, aerodynamic loads, and wake calculations. Most of these loops were controlled by tolerances to assess convergence with respect to the required accuracy of the calculation. In a few cases, however, the number of iterations had to be specified, and manual verification of convergence was required. Furthermore, for successful convergence, the Newton-Raphson method requires the specification of appropriate relaxation factors and an appropriate initial estimate of the solution. These convergence control parameters (such as the number of iterations, tolerances, and relaxation factors of all inner loops) had to be defined to be suitable for a wide range of different scenarios. Changing the numerical settings during the course of the study could reduce comparability and the ability to successfully determine the optimal solution. This was accomplished by evaluating the numerical settings for a sample of scenarios, including different operating conditions and active-camber control inputs. An important indication of appropriate convergence behavior is the independence of the final solution from the initial solution, i.e., a high-quality and

a medium-quality initial estimate. However, in the results part of the current work, a high-quality initial solution was always provided to support this independence from the initial estimate. This required careful management of the computed solutions to prevent the database from growing too large. This was achieved by ensuring that the solutions were substantially different from each other. The best initial solution available in the database was evaluated based on the minimum distance with respect to the active-camber actuation inputs and operating condition parameters by using a mean squared error approach. This required standardization of the control parameters by scaling to unit variance.

The above-described process of numerically evaluating a solution to the physical model of the helicopter rotor was generally successful for the most relevant range of operating conditions and active-camber control inputs. However, in the low-speed flight regime from $\mu = 0.05$ to $\mu = 0.10$, it is particularly difficult and elaborate to achieve a converged solution. This is due to the combination of low convection of the rotor wake and a complex wake geometry due to the growing asymmetry of the aerodynamics in this flight state. Since low-speed flight is generally less important in the present context, it has been excluded from most of the following investigations.

The current study focused only on the aeromechanics of the main rotor. Therefore, a wind tunnel trim with a fixed mounting of the rotor shaft was used instead of a free flight trim to reduce unnecessary complexity in the model, e.g., to avoid additional sources of error and computational effort. The (wind tunnel) trim strategy employed in this work is known as propulsive trim. This means that, in addition to the lift force of the rotor, also the propulsive force is part of the trim targets. This approach is necessary when comparing power requirements across different active-rotor scenarios due to the significant impact the propulsive force has on rotor power during high-speed flight. An identical propulsive force is not guaranteed when, for example, trimming to a specific pitch moment of the rotor. Only a small influence on rotor power is anticipated from changes in the side force. Therefore, the standard practice for setting the third trim variable is to specify a representative roll moment, as was done in this study. For any active-rotor actuation inputs in this work, the rotor was consistently trimmed to the original trim targets. The trim targets were specified in SI units and, therefore, were independent of changes in the baseline rotor parameters.

2.1.4 Active Camber Implementation and Parametrization

The previously mentioned FishBAC active-camber concept is investigated on a Bo 105 rotor blade which uses a NACA23012 airfoil. The computational modeling of the camber morphing was realized by providing specific airfoil tables, as described in the following section. The manner in which the camber deflection was quantified is described below. Only the aft 25% of the chord was actively morphed throughout the following work. This decision was motivated by considerations of the feasibility of the morphing mechanism and supported by the results of a study investigating the impact of this variable on the airfoil efficiency [59].

Figure 2.5 shows the region on the rotor blade where active camber morphing was applied. The variables r and s are introduced to specify the radial station of the center of the active camber segment and its size, respectively. Accordingly, r_1 and r_2 describe the inner and outer edges of the active-camber segment. Due to implementation limitations in the spanwise direction, it was assumed that such mechanisms could only be used up to $r_2 = 90\%R$. Further outboard, challenges arise due to the limited space available for the actuators, especially when dealing with highly tapered blade tip shapes. Additionally, the mechanism is subjected to increasing centrifugal and aerodynamic forces toward the tip of the blade.

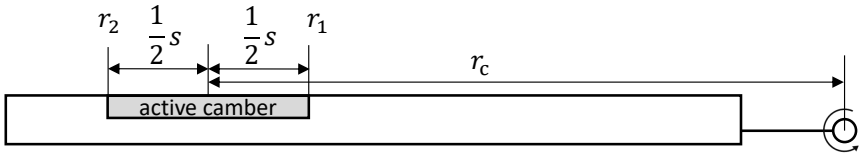

Figure 2.5: Active-camber size and location parameters.

Figure 2.6 shows the blade airfoil for different degrees of camber deflection. Furthermore, the parameter δ is introduced as the metric to describe the camber deflection. During aeromechanics calculations, the deflection of the active-camber section was prescribed, excluding any inertial effects caused by dynamic actuation and chordwise elastic deformation. Note that the chord line of the baseline airfoil, indicated by the dashed line in Fig. 2.6, was used to measure the angle of attack regardless of the degree of camber deflection. This means that the angle of attack is the same for all the airfoil shapes shown in the figure 2.6.

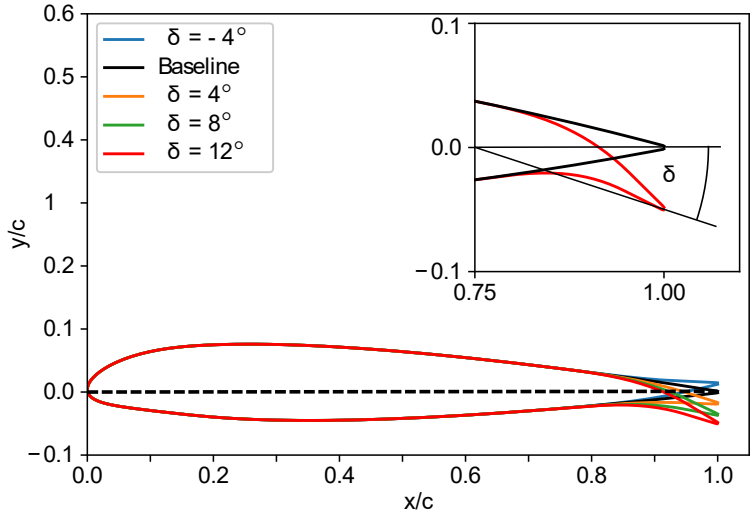

Figure 2.6: Active-camber airfoils and definition of camber morphing (δ) [76].

Periodic actuation that changes the camber deflection δ during a rotor revolution, as well as static camber morphing, were investigated. Trigonometric functions are well-suited to describe such cases and were applied through a Fourier series with the rotor frequency as the fundamental frequency. An amplitude-phase form is used in this work to describe the actuation inputs. For

isolated nP (n-periodic) harmonic actuation, the equation

$$\delta(\psi) = \delta_{0\mathrm{P}} + \delta_{n\mathrm{P}} \cdot \cos(n \cdot \psi - \phi_{n\mathrm{P}}) \tag{2.3}$$

describes the camber deflection as a function of the azimuth position ψ, where n is the integer multiple of the rotor rotational frequency. In this study, a 0/rev (0P) actuation corresponds to a constant mean deflection. An appropriate mean displacement was required to obtain favorable results, therefore it was adjusted with any type of harmonic actuation.

In the case of multi-harmonic (superimposed) control, the actuation signal is described by a Fourier series with a finite number of terms ($n_{\max}$)

$$\delta(\psi) = \delta_{0\mathrm{P}} + \sum_{n=1}^{n_{\max}} \delta_{n\mathrm{P}} \cdot \cos(n \cdot \psi - \phi_{n\mathrm{P}}). \tag{2.4}$$

This general expression also includes a single-harmonic actuation, i.e., when $n_{\min} = n_{\max}$. In this work, only values up to $n_{\max} = 5$ were considered. In the case of multi-harmonic actuation, $n_{\min} = 1$ was used throughout the work. Hence, $n_{\max}$ directly represents the number of harmonics that were superimposed. For 1/rev (1P) actuation, no difference exists between isolated and superimposed actuation since an appropriate mean deflection was always considered for each type of actuation input.

Additionally, a spanwise varying active camber actuation was studied in addition to the fundamental spanwise uniform deployment. The spanwise variation of camber morphing was specified in terms of ϑ. It is comparable to a linear blade twist that only exists in the region where camber morphing was applied. With $\vartheta > 0$, the original control input $\delta(\psi)$ was modified such that the inboard edge of the active-camber section, r_1, was actuated according to Eq. 2.5, and at the outboard edge, r_2, was actuated according to Eq. 2.7. Between these edges, camber morphing was subjected to a linear variation, resulting in the originally specified actuation input, $\delta(\psi)$, at the mid-span of the active-camber section, r_{mid}.

$$\delta_1(\psi) = (\delta(\psi) - \delta_{\mathrm{ref}}) \cdot (100\% + \vartheta) + \delta_{\mathrm{ref}} \tag{2.5}$$

$$\delta_{\mathrm{mid}}(\psi) = \delta(\psi) \tag{2.6}$$

$$\delta_2(\psi) = (\delta(\psi) - \delta_{\mathrm{ref}}) \cdot (100\% - \vartheta) + \delta_{\mathrm{ref}} \tag{2.7}$$

The variable $\delta(\psi)$ in Eqs. 2.5 to 2.7 was based on Eq. 2.4. Any spanwise variation of camber deflection was defined relative to a reference camber deflection, δ_{ref}. For each different combination of ϑ and δ_{ref}, a separate airfoil table had to be provided for the aeromechanics analysis, as explained in the following section.

Likewise to comparable studies in the literature, the actuation power to operate the active-camber mechanism was neglected in this work. This decision was supported by an estimate from a simplified model by the author, published in Ref. [77]. It yielded marginal actuation power requirements in comparison to the power savings possible with such a mechanism.

2.1.5 Aerodynamic Coefficients of the Morphed and Unmorphed Airfoils

As mentioned earlier, the methodology used to calculate aerodynamic forces requires an accurate data set of cross-sectional airfoil coefficients to generate well-converged and high-quality aeromechanics results. Typically, these airfoil coefficients are based on a range of angles of attack and Mach numbers. In this study, however, an additional degree of freedom had to be covered, namely the morphing of the NACA23012 airfoil.

Figure 2.7 provides an overview of the flow conditions that may occur locally on the rotor blade during a typical operation. It shows the Mach number and angle of attack range for three different advance ratios (μ). To ensure good reliability of the aeromechanical simulations, it is crucial that the airfoil table covers as much of this Mach number and angle of attack range as possible. Only in and near the reverse flow regime (at high speed on the retreating side) were empirical data acceptable.

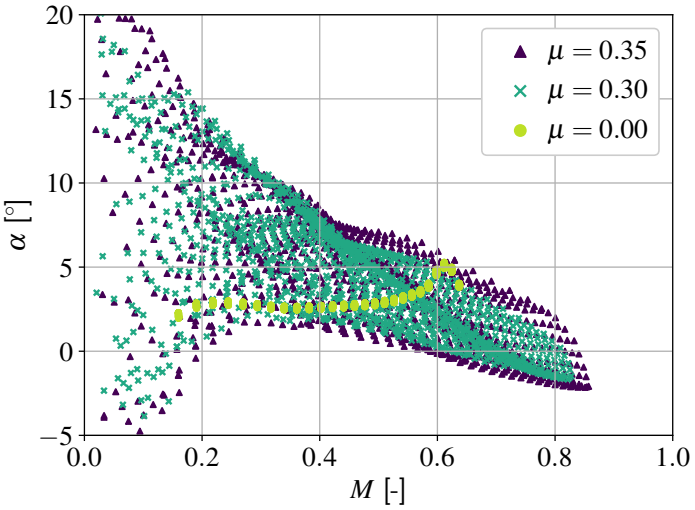

Figure 2.7: Flow conditions observed at the rotor blades of the Bo 105 passive rotor based on different advance ratios. Indicates the required range of conditions covered by the airfoil tables.

The airfoil coefficients used in this work were calculated using two-dimensional steady-state Navier-Stokes equation-based RANS CFD. This approach allows accurate modeling of viscosity and compressibility effects. The CFD solver employed was the DLR-TAU code, and the International Standard Atmosphere (ISA) at sea level was assumed for the simulations. The computations were validated with measurement data. A detailed description of this work can be found in [58]. This core data set covers the most important range of flow conditions. Nonetheless, for some camber deflections, the data set was incomplete, particularly in the boundary regions (low or high angles of attack). To compensate for the missing data, an interpolation method was applied, as described below. The underlying process is illustrated in Fig. 2.8. Each gray-shaded block in this flowchart represents data of a particular origin.

Three-dimensional multiquadratic radial basis function (RBF) interpolation (and extrapolation)

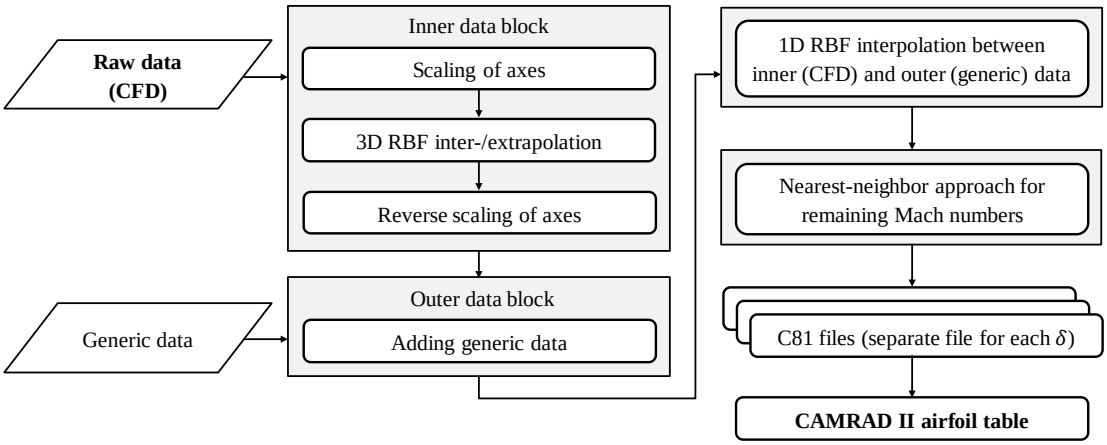

Figure 2.8: Flowchart of the process of generating the airfoil coefficient lookup table.

was used to complement the CFD-based aerodynamic coefficients. It is an established approach for high-dimensional interpolations of unstructured data [78]. The independent variables in this interpolation were camber deflection, Mach number, and angle of attack. The dependent variables were the airfoil coefficients (C_l, C_d, C_m). The purpose of the interpolation and extrapolation procedure was to provide physically meaningful data in regions between and near the existing CFD data. The CFD data was computed using small angle-of-attack intervals due to convergence requirements. Combined with small-scale numerical fluctuations in the solving process (random noise), the resulting data may contain exaggeratedly high gradients. This is a problem for most non-linear interpolation algorithms and can lead to overfitting of the data set. To overcome this issue, a small smoothing factor had to be applied. An alternative approach, which was similarly successful in the current context, is to map the CFD data onto a slightly coarser, uniformly spaced (1°) angle-of-attack interval using linear interpolation.

Another challenge in this interpolation task was that each axis was measured on a different scale. As a result, it is not possible to directly calculate the Euclidean distance, which is the criterion for assessing the influence of neighboring data points on the data point being evaluated. Therefore, in order to properly account for the influence of each dimension, it was necessary to center and scale each axis. Scaling was done by dividing each axis by its standard deviation. In effect, all variables were transformed into a Gaussian shape with a mean of zero and unit variance. Once the interpolation task was completed, the data needed to be inverse-transformed by multiplying the inverse of the scaling factors and adding the previously subtracted means.

A cross-validation study was performed to evaluate the robustness of the interpolation approach. For this purpose, the data set was randomly divided into training (60%) and test (40%) data sets. The training data was used to fit the RBF interpolation function, while the success of the interpolation was evaluated on the test data. It was shown that the Root Mean Square Error (RMSE) on the test data was sufficiently small throughout all train-test splits. Based on an exemplary train-test split, Figure 2.9 shows a good agreement between the RBF interpolation and the validation data when the data set was scaled. Note that the interpolation function also considered data points

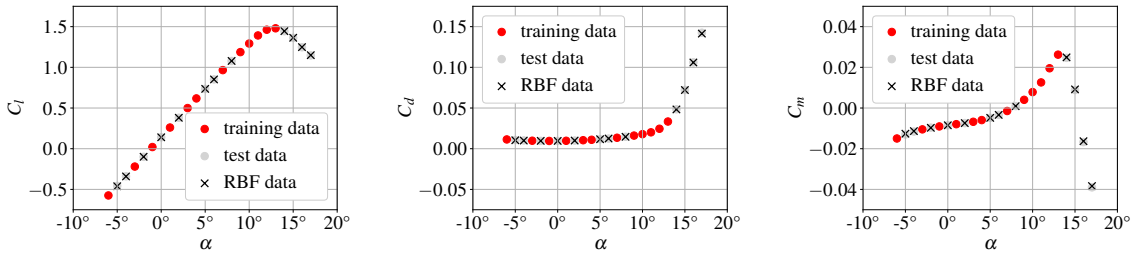

(a) C_l **(b)** C_d **(c)** C_m

Figure 2.9: Validation of the 3D RBF interpolation (α, M, δ) based on a random split of the data ($M = 0.4$, $\delta = 0°$). Only the α-dimension is shown.

with different Mach numbers and camber deflections, which are not visualized here.

While the CFD data generally covered an angle of attack range from $\alpha = -6°$ to $\alpha = 18°$, the range was extended to $\alpha = -7°$ to $\alpha = 19°$ using the previously described RBF interpolation function. This α range contained the most relevant Mach numbers (see Fig. 2.7), while extrapolation was applied only in a small range very close to the CFD data. In addition to extending the data in the α direction, RBF extrapolation was applied for high Mach numbers, M, and high camber deflections. Thus, the original Mach number range from $M = 0.2$ to $M = 0.8$ was extended to $M = 0.9$, and the camber deflection range from $\delta = -9.1°$ to $\delta = 13.5°$ was extended to $\delta = 15.7°$. For these conditions added with RBF extrapolation, it was difficult to obtain converged CFD solutions, and at the same time, the relevance of the data for the current study decreased significantly.

The resulting airfoil coefficients are shown for some example conditions in Figs. 2.10 and 2.11. The original CFD data are represented by the solid lines, and the data added by RBF interpolation and extrapolation are represented by the dashed lines. Figure 2.10 shows the airfoil coefficients versus the angle of attack for different Mach numbers. The trend is compared for two exemplary camber deflections. Instead, Fig. 2.11 shows the airfoil coefficients versus the angle of attack for different camber deflections based on an exemplary Mach number.

While the previous approach dealt with data processing in the regime specifically relevant to the following study, the full range of angles of attack from $\alpha = -180°$ to $\alpha = 180°$ must be provided to the CAMRAD II framework as a hard requirement. This allows the modeling of the reverse flow regime on the retreating side in high-speed flight, although it is not relevant for most rotor aeroelastic analyses due to the small forces and moments generated at such low flow speeds. Since poor extrapolation quality is expected for regions far from the CFD data, the commonly suggested approach is to use generic fill data to approximate the data for the missing regions [79].

To provide a smooth transition between this generic data and the CFD based data block (including the 3D RBF interpolated data), a simple 1D RBF interpolation could be applied between $\alpha = -7°$ and $\alpha = -40°$ and between $\alpha = 19°$ and $\alpha = 50°$, with the angle of attack being the only independent variable considered during the interpolation. This is because it was interpolated between two fully occupied regular grid datasets. This approach provided a smooth and kink-free transi-

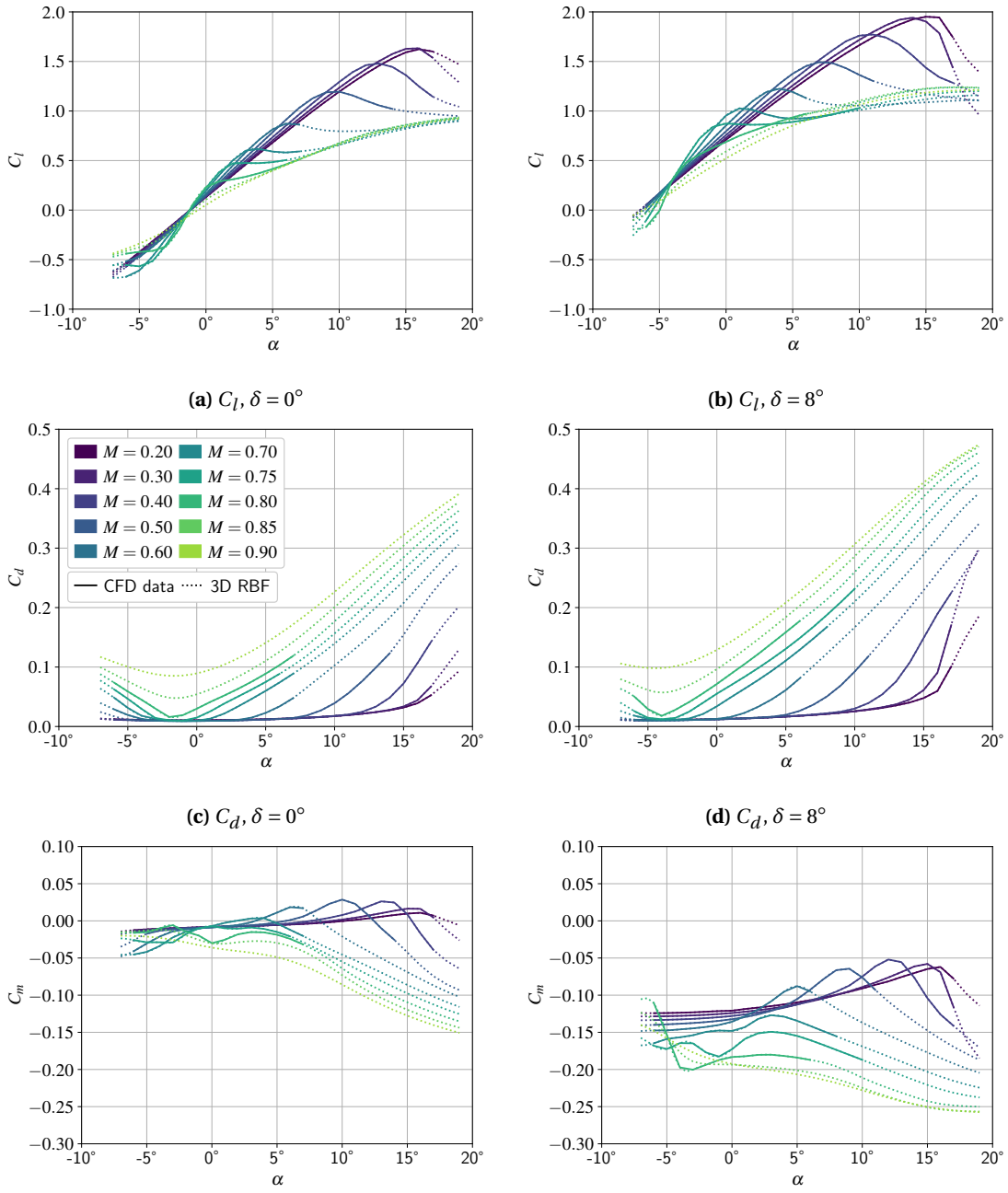

(a) C_l, $\delta = 0°$ **(b)** C_l, $\delta = 8°$

(c) C_d, $\delta = 0°$ **(d)** C_d, $\delta = 8°$

(e) C_m, $\delta = 0°$ **(f)** C_m, $\delta = 8°$

Figure 2.10: Airfoil coefficients for different Mach numbers (M) and two different camber deflections. CFD data and RBF interpolated data.

tion between these ranges while ensuring that there was no overshoot compared to quadratic or cubic interpolation. For the baseline NACA23012 airfoil, the result for the full range from $\alpha = -180°$ to $\alpha = 180°$ is shown in Fig. 2.12.

Finally, for Mach numbers $M = 0.0$, $M = 0.1$, and $M = 1.0$, the nearest neighbor search algorithm was used to complete the data set with respect to the required Mach number range. Hence, data

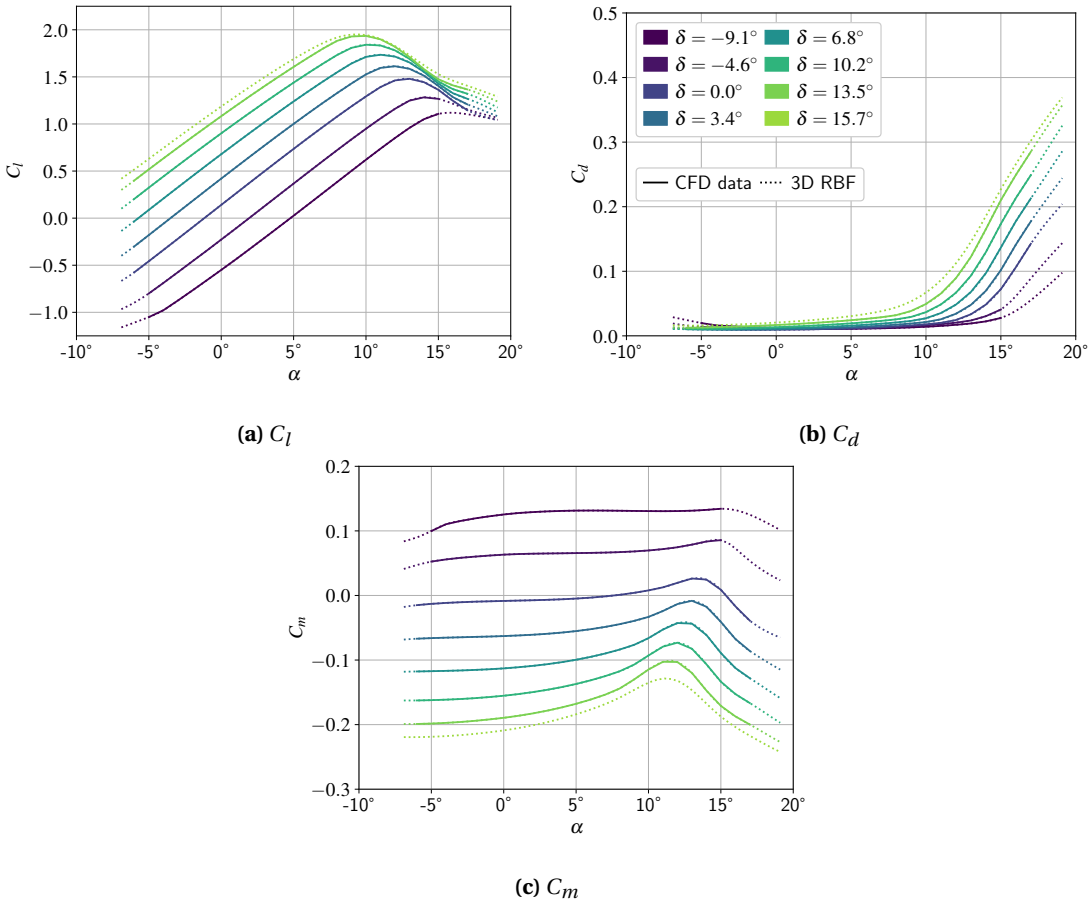

(a) C_l

(b) C_d

(c) C_m

Figure 2.11: Airfoil coefficients for different camber deflections (δ) based on $M = 0.4$. CFD data and RBF interpolated data.

from $M = 0.2$ was used for the low-speed range, while the data deposited for $M = 1.0$ was based on $M = 0.9$. The resulting data set was stored in an airfoil table file that was read by CAMRAD II during the aeromechanics calculations. All necessary values between the data points specified in this airfoil table were estimated based on linear interpolation. The sequence in which this interpolation was performed was first α, then M, and finally δ.

The procedure described above resulted in an airfoil table that was used for spanwise uniform camber control. That is, the camber deflection varied along the azimuth but not in the spanwise direction. However, a spanwise varying active camber control was also part of the subsequent investigations. Since this was not a feature directly provided by the CAMRAD II framework, it had to be achieved by manipulating the airfoil tables. As a result, each type of spanwise variation of camber deflection required an individual computation of a specific airfoil table, as described hereafter. For this purpose, airfoil coefficients had to be specified separately at four radial stations of the rotor blade. The original non-morphed NACA23012 airfoil coefficients were used at an infinitesimal distance inboard and outboard of the active camber segment to mimic a discrete transition from the non-morphed to the morphed part. In contrast, airfoil coefficients representing the respective degree of camber deflection were used at an infinitesimal distance inward of

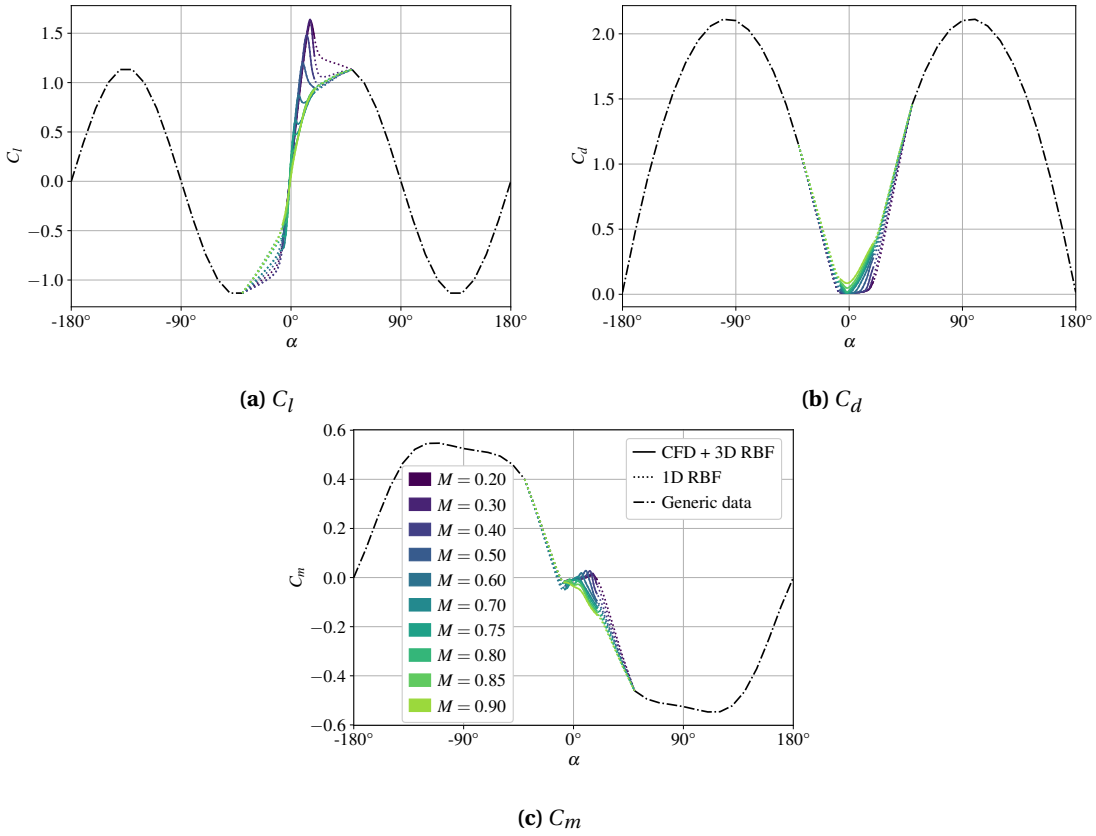

(a) C_l **(b)** C_d

(c) C_m

Figure 2.12: Final airfoil coefficients for $\delta = 0°$ covering the full range of possible α values.

the specified edges of the active camber segment. However, for a given camber deflection δ, the deposited airfoil coefficients at r_1 and r_2 were based on the camber deflections resulting from Eqs. 2.5 and 2.7, respectively. Since data points were generally not available for the camber deflections resulting from this transformation, the airfoil coefficients had to be determined based on the three-dimensional RBF interpolation described earlier. This approach did not require any manipulation of the aeromechanics framework itself, except for switching to a different airfoil table.

2.1.6 Stall Margin Estimation

In the current work, the retreating-blade stall margin was evaluated, e.g., to estimate the effect of camber morphing on the operational limits. The metric presented below was also used to consider the stall margin as an additional objective when optimizing the camber control inputs. The goal was to at least maintain the original forward speed limits and maneuverability of the rotorcraft. Since this resulted in scenarios where the retreating-blade stall margin was insignificant, it was not considered necessary to use an empirical dynamic stall model in the aeromechanics framework, especially since dynamic stall models depend on accurate determination of many empirical parameters, but achieve questionable reliability. [73]. Therefore, in this work, the local

stall margin for a blade cross-section was determined based on the previously presented steady airfoil characteristics, neglecting any unsteady aerodynamic effects. In [80], the stall margin was mathematically described as

$$SM = \left(1 - \frac{C_l}{C_{l,\max}}\right) \cdot 100\%. \tag{2.8}$$

In the current context, however, a simplified approach using $C_{l,\max} - C_l$ to evaluate the stall margin was considered sufficient and was therefore the preferred choice for most analyses. The lift coefficient C_l and the maximum lift coefficient $C_{l,\max}$ were evaluated based on the local Mach number and camber deflection.

In order to incorporate the stall margin as an objective in the optimization of active-camber control inputs, it was necessary to quantify it as a scalar value. Only the aerodynamically significant region was considered, excluding the reverse flow regime and nearby regions with nominal lift contribution. Furthermore, the region near the blade tip was neglected because the stall margin tends to infinity as the lift at the blade tip typically approaches zero. Therefore, at an azimuth position of $\psi = 270°$, the average stall margin was evaluated between $r = 0.5$ and $r = 0.9$. Furthermore, because of the use of an algorithm that minimizes the objective function, it was necessary to define the stall margin so that the condition improves as the value decreases. This required an inverse definition of the stall margin. When evaluating the average stall margin of a number of sample points (N_r) along the radius, the following expression results:

$$SM_o(\psi) = \left(\sum_{r=0.5}^{0.9} \frac{C_{l,\max}(r,\psi) - C_l(r,\psi)}{N_r}\right)^{-1} \tag{2.9}$$

While the local C_l was part of the simulation output, $C_{l,\max}$ had to be determined using the CFD-based airfoil coefficients data set. This process is illustrated for two airfoil geometries in Fig. 2.13. It shows that for small to moderate Mach numbers there is a distinct maximum of C_l ($C_{l,\max}$). In contrast, for higher Mach numbers, C_l always increased within the examined range of α. For most of the following investigations, only Mach numbers were analyzed where $C_{l,\max}$ could be unambiguously identified. In cases where $C_{l,\max}$ was undefined, the search for $C_{l,\max}$ was limited to values of $\alpha = 10°$. This allowed at least a qualitative assessment of whether the stall margin increased or decreased. The result of this approach is shown in Fig. 2.14. While $C_{l,\max}$ increased at higher camber deflections, it decreased at higher Mach numbers.

Note that when examining the variance between the maximum lift coefficient and the current lift coefficient, it is not possible to determine whether the data point represents a situation before or after the stall occurs. However, this information can be inferred from the context. If the data point represents a stall condition, then there must be a zero stall margin point at a previous azimuth position. Otherwise, the data point clearly indicates a situation that is not a stall condition. It should also be noted that no lift coefficients are defined in the absence of oncoming flow. Therefore, the presented approach to determine the stall margin cannot be applied. Although it exists in the reverse flow regime, it was considered an irrelevant scenario for a stall margin analysis.

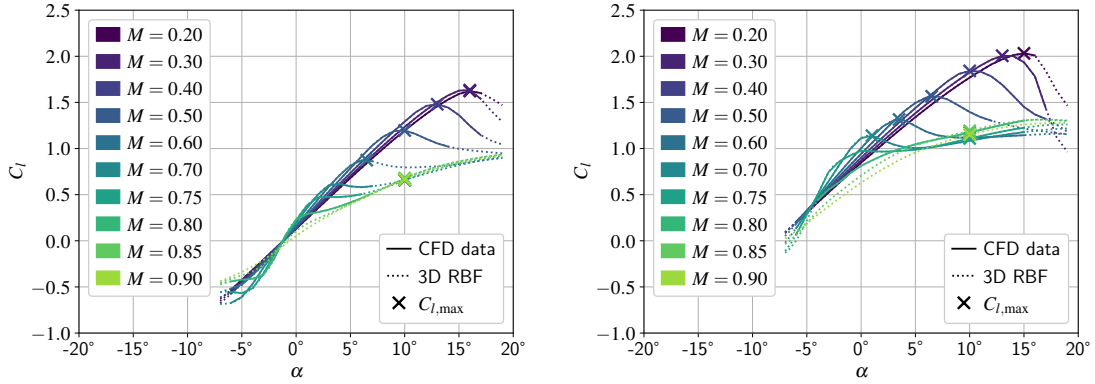

(a) C_l at $\delta = 0°$ **(b)** C_l at $\delta = 10°$

Figure 2.13: Maximum lift coefficient determination for different Mach numbers and camber deflections.

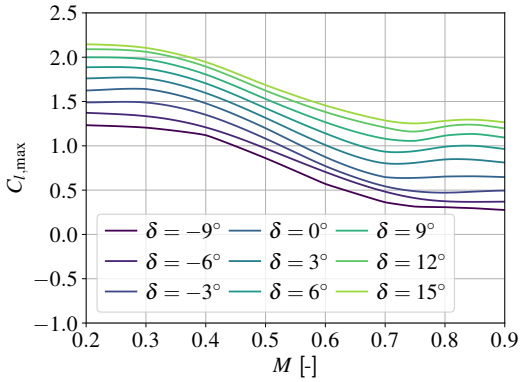

Figure 2.14: Maximum lift coefficients $C_{l,\max}$ (based on the aforementioned approach).

2.2 Model Validation and Trim Targets

The comprehensive analysis model described above was compared to wind tunnel [81, 82] and flight test data [83] to evaluate the accuracy of the modeling approach. While the referenced wind tunnel test campaign provided a more comprehensive data set, including individual blade control (IBC) test cases, the flight tests were used not only for validation but also as a reference to define the trim states of the active camber study. In addition, further comparisons of the essentially same computational framework and experimental data [84] were published in [77]. Therein, blade loads over azimuth were compared and showed reasonable conformity.

2.2.1 Validation of the Rotor Structural Model

Before comparing the entire computational framework with full-scale experimental data, the natural frequencies of the rotor blades were compared between the comprehensive analysis model and reference data from DLR [85] in the form of a Campbell diagram. As shown in Fig. 2.15,

the first ten natural frequencies of the rotor blades were in good agreement. Therefore, it was assumed that the rotor structural properties and rotor dynamics were adequately modeled.

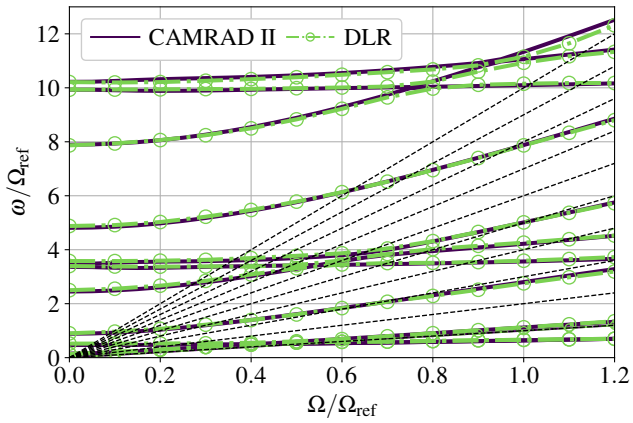

Figure 2.15: Rotor natural frequencies versus rotor rotational speed Ω. Reference data from [85].

2.2.2 Comparison to Wind Tunnel Measurements

The computational rotor model used in this work was compared to a subset of data from the wind tunnel test campaign of a full-scale Bo 105 rotor [81, 82]. The selected data points and corresponding trim conditions are listed in Table 2.3. These parameters were used to trim the computational model to ensure equivalent conditions.

Table 2.3: Trim conditions used in the validation study (experimental data from [81, 82]).

Year	Run No.	Point No.	μ	α_S [°]	RPM	L [N]	D [N]	M_x [Nm]
1994	15	5	0.01	0	428.1	20964	0	502
1994	45	16	0.1	-2.4	425.5	22330	-142	491
1993	30	23	0.2	-3	424.6	20537	-947	287
1994	26	48	0.3	-7.6	425.9	21948	-2945	879
1994	57	42	0.4	-9	425.0	21859	-3256	1902

Drag and lift in the wind axis system. Roll moment in the shaft axis system.

Figure 2.16 shows a comparison of the required rotor power. As the main focus of the following work was to reduce the required rotor power, the ability to predict the rotor power adequately was considered most important. In Fig. 2.16a, the measurements and the calculations are in good agreement for most of the advance ratios μ. Only at high speed, the deviations are a bit higher. It should be noted, however, that the wind tunnel tests showed a moderate inconsistency in the propulsive force. This particularly affects the power required in high-speed flight ($\mu = 0.35$), where the parasitic drag (D) becomes the main contributor to the required rotor power.

To demonstrate the ability to predict the power savings associated with higher harmonic active

rotor control, a comparison to IBC experiments is shown in Fig. 2.16b. All data points in this figure were generated at $\mu = 0.3$. Note that for each IBC control input, the trim state varied moderately (see Table 2.4). At first glance, the constant offset of about 10% in the rotor power does not satisfactorily confirm the validity of the model. The offset could be explained by the previously mentioned inconsistency in the experimental data regarding the measured drag force. The magnitude of this offset was only slightly higher than in the comparison without IBC (about 8% at $\mu = 0.3$). However, when neglecting the constant offset between experimental data and simulations, both the phase dependence and the absolute values of power reduction showed excellent accordance. Thus, it was assumed that the model was suitable for evaluating the relative power savings from higher harmonic control and for drawing conclusions about the effect of changing the actuation schedule.

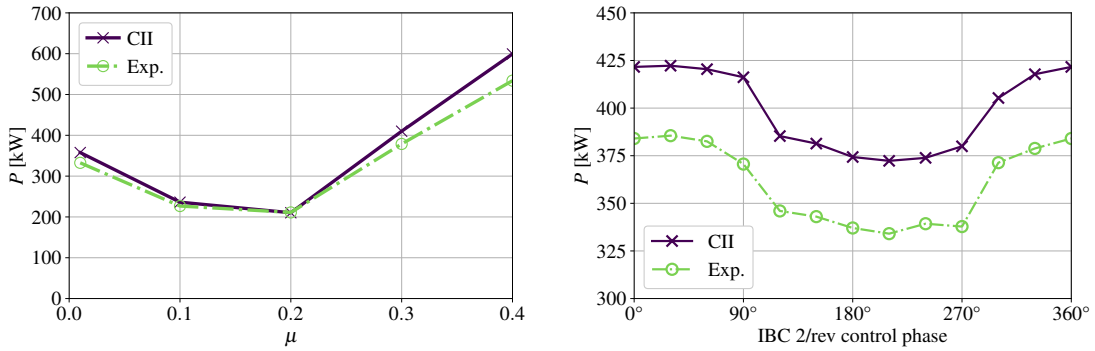

(a) Passive rotor

(b) 2/rev IBC actuation (1°)

Figure 2.16: Comparison of rotor power between wind tunnel tests (Exp.) and CAMRAD II (CII) computations.

For the cases shown Fig. 2.16a, control angles and loads are compared in Fig. 2.17. Regarding the rotor controls, good agreement between the experimental rotor tests and the computational model was obtained (see Fig. 2.17a). Only the trim calculation of the comprehensive analysis resulted in a constant negative offset of about −2° to the experimental data. This may be due to neglecting the trailing-edge tab when computing the aerodynamic coefficients with CFD. Otherwise, differences in the airfoil chord line or calibration issues could be responsible for this deviation. For the cyclic control, the agreement was excellent except for $\mu = 0.1$. Again, this could be explained by inconsistencies in the trim state specification of the rotor tests.

In Fig. 2.17b, the mean ($F_{\mathrm{p}l,0}$) and half peak-to-peak ($F_{\mathrm{p}l}$) pitch-link loads are compared between computations and experiments. In the following study, the pitch-link loads were considered as a secondary optimization objective to avoid exceeding the existing values of the passive rotor. With respect to $F_{\mathrm{p}l,0}$, only the overall magnitude showed good agreement. However, $F_{\mathrm{p}l,0}$ fluctuated strongly when comparing the experiments at different advanced ratios. This fluctuation was not observed in the simulations. Instead, the half peak-to-peak pitch link loads $F_{\mathrm{p}l}$ of the comprehensive analysis and the experiments showed excellent agreement.

In Figs. 2.17c and 2.17d show the half peak-to-peak hub loads and moments. With one exception,

Table 2.4: Trim conditions used in the IBC study (experimental data from [81, 82], year 1994).

IBC Phase [°]	Run No.	Point No.	μ	α_S [°]	RPM	L [N]	D [N]	M_x [Nm]
0	26	23	0.3	-7.6	424.9	21930	-2922	1041
30	26	18	0.3	-7.6	425.3	21894	-2891	1309
60	26	17	0.3	-7.6	425.6	22103	-2865	1329
90	26	13	0.3	-7.6	424.6	21916	-2905	1229
120	23	28	0.3	-7.6	424.6	21520	-2633	1039
150	23	24	0.3	-7.6	424.7	21209	-2678	1185
180	23	20	0.3	-7.6	425.1	21258	-2611	1185
210	23	18	0.3	-7.6	424.8	21116	-2616	933
240	23	16	0.3	-7.6	424.8	21311	-2589	980
270	23	11	0.3	-7.6	425.3	21276	-2611	1050
300	26	29	0.3	-7.6	424.8	21761	-2856	1020
330	26	24	0.3	-7.6	424.9	22321	-2869	1144
360	26	23	0.3	-7.6	424.9	21930	-2922	1041

Drag and lift in wind axis system. Roll moment in shaft axis system.

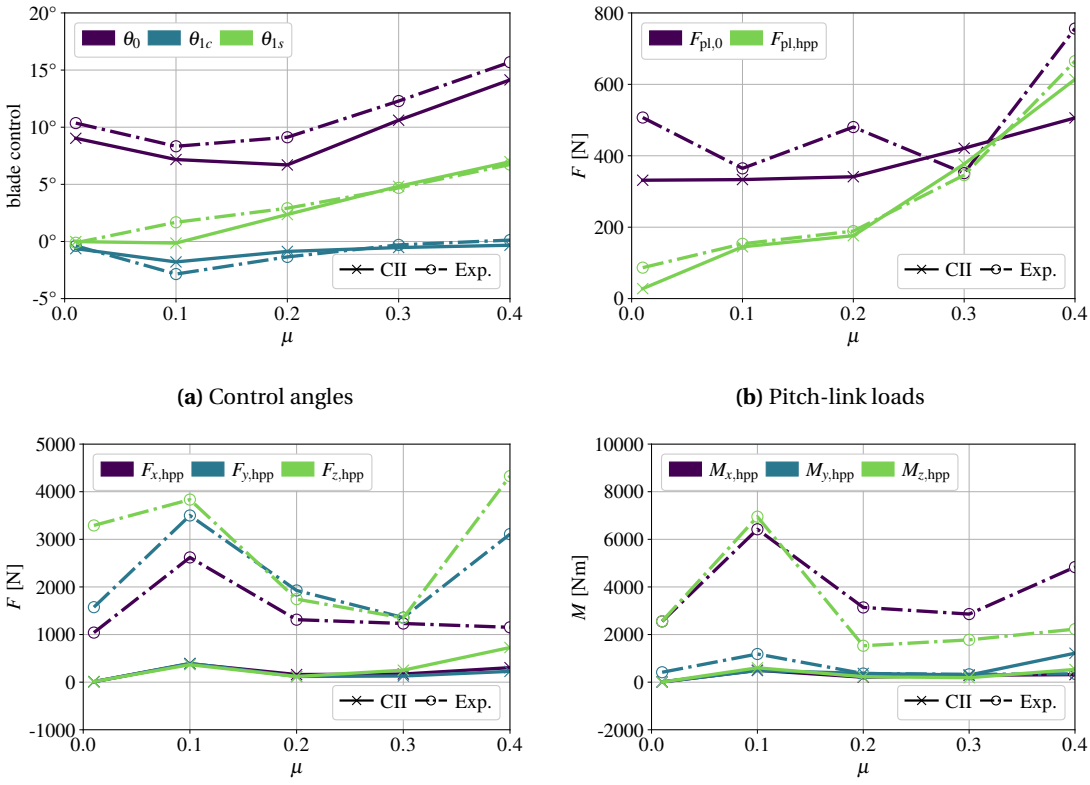

(a) Control angles

(b) Pitch-link loads

(c) Hub forces (half peak-to-peak)

(d) Hub moments (half peak-to-peak)

Figure 2.17: Comparison of rotor controls and rotor loads between wind tunnel tests and CAMRAD II (CII) computations (passive rotor).

the experimental loads were significantly higher than the comprehensive analysis results. Only M_y was in the range of the simulations. However, in another section of the report, conflicting results were given for some of the data points, suggesting that the measurements for M_y were also in the same range as the other hub moments. In order to classify the difference in these loads between simulations and experiments, it has to be considered that the base level of the half peak-to-peak loads in the axisymmetric hovering flight was extraordinarily high. Even for some forward flight conditions, the vibratory loads were smaller than in hovering flight, indicating a major imbalance of the system, calibration issues, or other types of problems in the experiments. Also, the perfectly stiff support structure (rotor shaft and rotor shaft position) in the computational model could be a reason for this deviation compared to the experiments. Therefore, it was assumed that these load measurements were not fully reliable and comparable, and no substantive conclusions were drawn from this comparison. Only the trend that the peak-to-peak loads were highest in low-speed ($\mu = 0.1$) and high-speed ($\mu = 0.35$) flight was similar between experiments and computations.

2.2.3 Comparison to Flight Tests

Flight tests were used to extract trim targets for the active rotor study. The goal was to perform the study under the most realistic operating conditions. Wind tunnel tests, on the other hand, also allow for flight states characterized by system imbalance, representing a non-existent stationary flight regime (e.g., a high advance ratio according to the oncoming velocity, but an insufficient propulsive force to maintain such a flight state). For this purpose, the Bo 105 flight test campaign documented in [83] was used. Since the main focus of the active rotor study was on power consumption, it was essential to apply a so-called propulsive trim definition. This means that the propulsive force (usually given as a negative drag force) was used as one of the trim targets instead of the pitching moment. This drag force (D), also known as parasitic drag, is the major source of power consumption in high-speed flight. It is directly opposed to the propulsive force the rotor must generate to overcome this drag. Hence, the parasitic power (P_D) is defined as

$$P_D = v \cdot D \tag{2.10}$$

with flight velocity v. Therefore, for a fair comparison of power requirements between different active rotor cases, the propulsive force must be identical. Since the propulsive force of the rotor was not given in [83], it was calculated using the fuselage drag polars from [86]. Only the lift (L), roll moment (M_x), and shaft tilt (α_s) were extracted from [83]. The exact values are detailed in Table 2.5. It also lists the required trim controls (θ_0, θ_{1c}, and θ_{1s}) for the baseline rotor as a result of trim calculations using the above-mentioned aeromechanics framework. Since active rotor inputs affected the rotor aerodynamics, it was necessary to re-trim the rotor for camber actuation studies. That is, the rotor controls were iteratively adjusted to meet the predefined trim targets. A thrust of $T = 27520$ N was used, which corresponded to a $C_T/\sigma = 0.0886$ for this Bo 105 rotor.

Table 2.5: Trim conditions used during the active-camber study.

		Trim targets			Trim controls		
μ	α_s[°]	L [N]	M_x [Nm]	D [N]	θ_0[°]	θ_{1c}[°]	θ_{1s}[°]
0.00	0	27520	1400	0	10.8	-0.41	-0.18
0.10	-2	27520	600	-289	8.6	-2.50	0.84
0.15	-3	27520	500	-652	8.1	-1.64	1.25
0.20	-4	27520	600	-1149	8.4	-1.09	2.10
0.25	-5	27520	700	-1802	9.3	-0.77	3.22
0.30	-6	27520	1000	-2609	11.0	-0.72	4.87
0.35	-7.3	27520	1400	-3572	13.2	-0.76	6.78

Drag and lift in wind axis system. Roll moment in shaft axis system.

In order to verify that all values were appropriately implemented and to validate the model with an additional data set, the comprehensive analysis results in Fig. 2.18 were compared with the power and rotor control data available in Ref. [83]. In terms of rotor power, computations and flight tests show very good agreement over the entire flight envelope. This includes the high-speed flight cases, which were less consistent with the wind tunnel tests. Similar to the comparison with the wind tunnel tests, the collective control again showed a constant underestimation of about 2°. The cyclic controls were in good agreement.

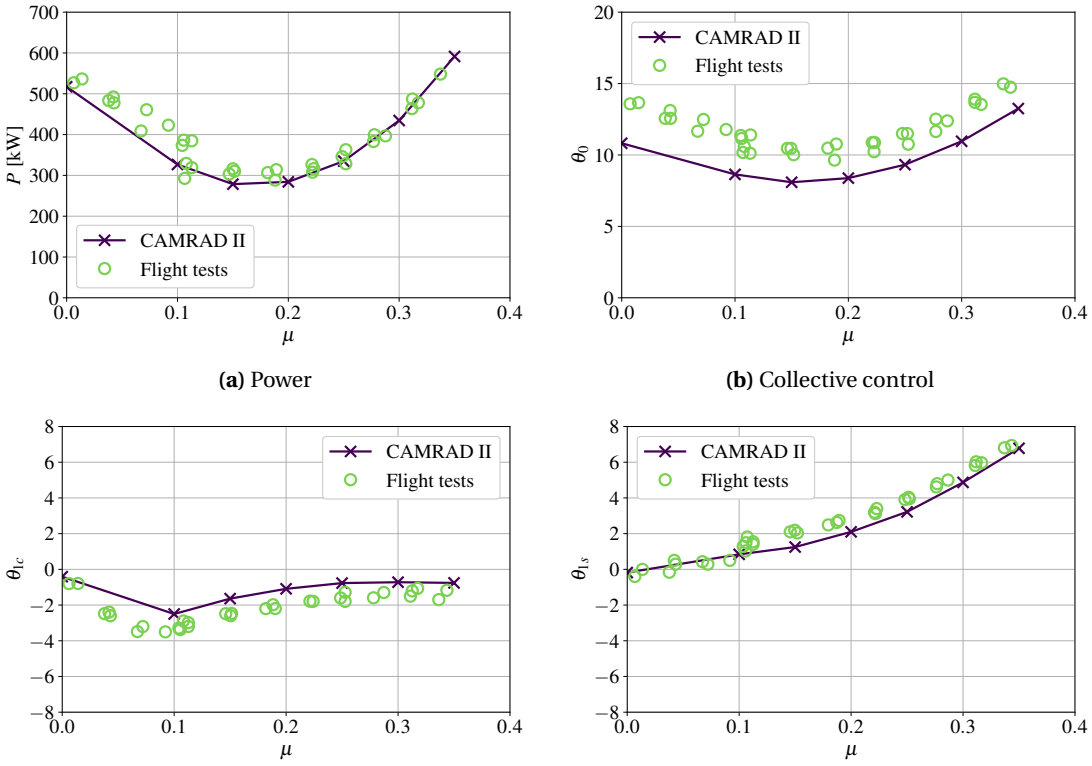

(a) Power

(b) Collective control

(c) Lateral cyclic control

(d) Longitudinal cyclic control

Figure 2.18: Comparison of rotor power and controls between flight tests and CAMRAD II computations.

Overall, the comparisons between the computational model and experimental data showed satisfactory agreement, suggesting that the model is suitable for assessing trends in the effect of an active rotor mechanism on rotor power and for evaluating the underlying aeroelastic phenomena associated with this performance increase.

2.3 Optimization of Active Rotor Control Parameters

In the present work, the active camber control inputs were determined based on an optimization approach as presented in the following. Due to the wide range of different configurations, operating conditions, and boundary conditions of the optimization problem, a large number of individual optimizations had to be performed. Due to the computational complexity of a single comprehensive analysis simulation, a sophisticated optimization procedure was used to efficiently determine the most beneficial use of the active mechanism. In addition, two other challenges had to be overcome during the optimization process. First, it was known from a preliminary parametric study that the solution space always contained a large, unspecified number of local optima. Second, the simulation results were not completely noise-free, e.g., a small dependence on the initial solution, although measures were taken to minimize this effect.

There are several strategies and concepts for solving optimization problems. To avoid getting stuck at a local minimum and to deal with noise in the results of the objective function, a stochastic approach is required, which introduces randomness into the search process, instead of a gradient-based, deterministic approach [87]. For computationally expensive models that need to be evaluated during optimization, surrogate-based methods (also known as metamodels or response surfaces) are considered the most efficient. In such model-based approaches, a surrogate model guides the optimization process [87]. It is intended to approximate the objective function while being substantially less computationally expensive [88]. Hence, it provides an inexpensive way to explore the design space for promising candidate points. This minimizes the number of objective function evaluations while searching for the global optimum, which saves a significant amount of computation, especially when the objective function involves aeromechanical calculations [89, 90].

2.3.1 Surrogate Optimization Approach

In this work, the Python-based implementation of the synchronous SOP algorithm [91] was used, which is available in the form of the Surrogate Optimization Toolbox (pySOT) [88]. It meets the requirements described above. Alternative approaches such as genetic algorithm, simulated annealing, or particle swarm required more objective function evaluations than the surrogate model approach [91]. The main aspects of the chosen method are summarized below.

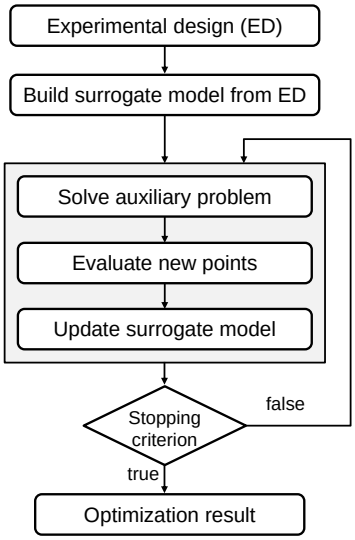

Figure 2.19: Procedure of synchronous surrogate optimization based on the parallel surrogate global optimization with Pareto center selection (SOP) [88].

The surrogate optimization approach essentially consists of three components: the process manager or optimization strategy, the experimental design method, and the surrogate model. The so-called SOP optimization strategy used in this work is described in [91] and [88]. The procedure is shown in Fig. 2.19 and explained in more detail below.

The first step is to compute an initial set of design points to be used to fit the initial surrogate model. This is done using a symmetric Latin hypercube experimental design method as proposed in [92]. It aims to generate a high-quality initial surrogate model with the least number of computations required and is significantly less computationally expensive compared to a full factorial design [88]. The surrogate model used in this work is referred to as the Gaussian process regression model (also known as kriging) based on an implementation of scikit-learn (GPRegressor) [93] as proposed by [94]. This is a derivative-free, supervised machine learning type of algorithm. Unlike radial basis functions (RBF), it can simultaneously predict the value of the objective function and its variance. This allows conclusions to be drawn about the uncertainty of a prediction, which can be used by the optimization algorithm to refine the candidate search [88]. A regression model was used instead of a classification model due to the nature of an aeroelastic system. A regression type of problem produces continuous quantities instead of discrete categories.

Then, using the surrogate model just constructed and knowledge of previously evaluated data points, the optimizer estimates promising candidates. This is also known as solving the auxiliary problem. One challenge is to find an appropriate balance between exploration and exploitation of the design space [88], i.e., candidate points should be well distributed (far from previous points) to avoid local minima and improve the quality of the response surface (exploration), and promptly approximate the minimum of the design space (close to the predicted optimum, exploitation). The main parameter responsible for this balance is the sampling radius, which defines the maxi-

mum random variation around a fixed number of centers. These centers are selected from among the promising candidate points estimated by the surrogate model. Based on the progress of the optimization, an algorithm is applied to dynamically adjust the sampling radius to actively manage the balance between exploration and exploitation. This involves shifting the candidate search towards exploitation at a later stage of the optimization [91].

After selecting the new candidate points, the objective function is evaluated for each of them. Based on the result, the surrogate model is updated and improved with each iteration. This process is repeated until the stopping criterion is reached, and the best solution found during this process is returned [91]. By default, the stopping criterion is either convergence in terms of minimizing the objective function or a maximum number of objective function evaluations equal to 100 times the dimension of the problem.

2.3.2 Multi-Objective Optimization

In this work, several objectives were addressed simultaneously during optimization. While the focus was on power reduction, loads such as pitch-link loads and hub loads were also attempted to be constrained or reduced. In addition, the stall margin of the rotor was to be maintained or increased. Optimization algorithms generally require the result of the objective function to be in scalar form in order to minimize this value. Therefore, when using multiple objectives, a transformation into a scalar must be performed. As suggested in [95], a classical approach for this purpose is the use of the weighted sum method, usually defined as

$$\Pi(\vec{x}) = \sum_{i=1}^{N_o} w_i f_i(\vec{x}). \tag{2.11}$$

In this equation, $\Pi(x)$ is the resulting cost for a combined evaluation of individual objectives f_i (results of the computational rotor analysis) based on an input(vector) $\vec{x}$ (active-camber control inputs). By applying weighting coefficients w_i, an individual importance can be specified for each variable. The following equation had to be satisfied when defining the weighting factors [95]:

$$\sum_{i=1}^{N_o} w_i = 1, \quad w_i \in [0,1] \tag{2.12}$$

However, this sum does not have to be linear. Instead, non-linear, e.g., exponential formulations are also conceivable [95], such as

$$\Pi(\vec{x}) = \sum_{i=1}^{N_o} w_i f_i^e(\vec{x}). \tag{2.13}$$

For the current study, this made it possible to mimic constraints on output parameters while maintaining the continuity of the objective function as required in a regression analysis. This was achieved by the fact that a high exponent e significantly increases the cost function for high values of f_i, and low values of f_i are of vanishing importance for the total cost $\Pi(\vec{x})$.

Finally, as suggested in [95], it is important to carefully select appropriate reference values to normalize the individual results of the aeromechanics computations. This is especially important in the context of using exponents for each term of the objective function. Only with normalization do the weighting factors become a measure of the contribution of a particular variable to the result. When using exponents, the normalization value essentially determines whether the importance of an objective increases or decreases due to the exponent, since it defines the condition under which $f_i / f_{i,\mathrm{ref}}$ becomes greater or less than one. This makes Eq. 2.13 becomes

$$\Pi(\vec{x}) = \sum_{i=1}^{N_o} w_i \left(\frac{f_i(\vec{x})}{f_{i,\mathrm{ref}}} \right)^e . \tag{2.14}$$

The baseline rotor parameters were typically used as a reference. One problem with this definition was that the reference values ($f_{i,\mathrm{ref}}$) for the oscillatory loads converged to zero as the symmetric hover flight state was approached. To avoid dividing by zero when evaluating the objective (see Eq. 2.14), this approach had to be adapted when varying the forward flight speed. The approach taken was to specify minimum values for $f_{i,\mathrm{ref}}$, i.e., 1N for forces and 1Nm for moments. In addition, the weighting of the loads was multiplied by a factor of

$$w_i = \sqrt{\frac{\mu}{0.3}} \cdot w_{i,\mu=0.3} \tag{2.15}$$

to improve the convergence of the optimization problem for small reference values. Thus, the oscillatory forces in hovering flight were not minimized in this study as they were insignificant. On the other hand, they were given higher priority in high-speed flight beyond $\mu = 0.3$.

3 Rotor Performance Improvement Under Different Operating Conditions

This chapter will examine the performance gains achievable with active camber and the underlying physical phenomenon. The first part is based on spanwise uniform active camber actuation in high-speed flight, which involves a variation of the camber deflection along the azimuth position of the rotor blades but a constant deflection along the blade span. The following section includes an investigation of spanwise varying actuation amplitudes, which takes advantage of the inherent flexibility of the blade surface required to construct such a continuous mechanism. This analysis includes a variation of the flight speed of the helicopter. The final section addresses other influences on the prediction of performance gains with active camber. These include further variations of operational aspects as well as modeling aspects.

While performance was the main focus of this work, it was intended to present only solutions that did not degrade the operability of the system. This means that rotor loads and the achievable flight envelope were also considered in the following study. All investigations were carried out with the comprehensive analysis code CAMRAD II. The baseline rotor on which active camber was applied was the Bo 105 main rotor with a NACA23012 airfoil.

3.1 Active Camber Control in High-Speed Flight

While active camber has the potential to improve rotor performance over a wide range of operating conditions, one of its most promising but complex applications is in high-speed flight. This is due to the large variation in aerodynamic conditions over a rotor revolution. The use of an active mechanism is intended to better adapt the rotor blade to each aerodynamic condition experienced. Thus, in this first section, a high-speed flight condition was examined, i.e., an advance ratio of $\mu = 0.3$. This approximates the cruise speed of the Bo 105 helicopter and is also a typical trim state used in other research studies. The exact trim condition is given in Table 2.5. In this section, the focus is on optimal active-camber control inputs based on an appropriate definition of the objective function. It includes an analysis of the underlying aeroelastic phenomenon. Most of this analysis (unless otherwise noted) is based on an implementation of the active-camber section between $r = 0.22$ ($22\%R$, which is the inboard limit of the aerodynamically active part of the rotor blade) and $r = 0.90$. A reassessment of this decision is shown in the last part of this section.

3.1.1 Camber Actuation for Rotor Power Reduction

This section examines trends in power savings based on different types of control inputs, including single-harmonic and multi-harmonic (superimposed) inputs. The different concepts are visualized in Fig. 3.1 based on exemplary specifications. Each harmonic is defined by an amplitude and a phase (relative to the rotor azimuth position). In the following, the control inputs for a specific actuation case are represented by the vector $\vec{x}$. Section 2.1.4 contains the mathematical definition of the actuation inputs.

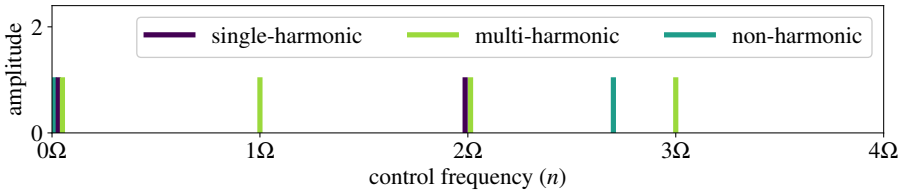

Figure 3.1: Definition of periodic signals in relation to the rotor rotational speed (Ω).

Single-harmonic control inputs help to understand the mechanism of saving rotor power and to evaluate which rotor harmonics are most relevant for this application. In addition, multi-harmonic control based on a superposition of harmonic signals was also investigated. In the following, the term multi-harmonic control was used to describe cases where all terms in the Fourier series that describes $\delta(\psi)$ (see Eq. 2.4) have a non-zero amplitude, and the number of terms is greater than one ($n_{\max} > 1$). That is, a multi-harmonic 3/rev (3Ω) control ($n_{\max} = 3$) also includes 1/rev (1Ω) and 2/rev (2Ω) harmonics. Note that regardless of single or multi-harmonic input, all of the following investigations included an appropriate static deflection (δ_{0P}), as this was essential to capture the full potential of active camber.

Ideally, an infinite number of harmonics (Fourier terms) would be used to identify the optimal control. However, the optimization effort grows exponentially with the number of degrees of freedom. Since each harmonic introduces two degrees of freedom (amplitude and phase), superimposing the first five harmonics results in eleven degrees of freedom (including a static deflection). Therefore, the number of harmonics to sufficiently approximate optimal performance gains was of great interest for the following work in order to limit the computational effort, and was thus investigated up to 5/rev. The corresponding definition of the input vector $\vec{x}$ is as follows:

$$\vec{x} = [\delta_{0P}, \phi_{1P}, \delta_{1P}, \phi_{2P}, \delta_{2P}, \phi_{3P}, \delta_{3P}, \phi_{4P}, \delta_{4P}, \phi_{5P}, \delta_{5P}]. \tag{3.1}$$

Another measure to reduce the optimization effort was to limit these inputs by the following lower (b_{lo}) and upper (b_{up}) bounds:

$$b_{lo} = [-2^\circ, 0^\circ, 0^\circ, 0^\circ, 0^\circ, 0^\circ, 0^\circ, 0^\circ, 0^\circ, 0^\circ, 0^\circ] \tag{3.2}$$

$$b_{up} = [8^\circ, 360^\circ, 6^\circ, 360^\circ, 3^\circ, 360^\circ, 3^\circ, 360^\circ, 3^\circ, 360^\circ, 3^\circ] \tag{3.3}$$

Note that these bounds were only applied when the specific harmonic was part of the optimization. When certain harmonics were excluded (e.g., single-harmonic control), their amplitudes were set to zero. The bounds were defined in such a way that none of the optimizations presented in the following conflicted with them, i.e., the solutions of the optimizations were always sufficiently far away from these specified limits.

Figure 3.2 compares different actuation strategies, including control signals based on a single harmonic and using multiple harmonics. Figure 3.2a shows the amount of power savings possible with each actuation strategy at $\mu = 0.3$. Figures 3.2b to 3.2d give more details about the underlying actuation inputs. For simplicity, this initial study only used rotor power reduction as an objective during optimization. As shown in Fig. 3.2a, the use of a steady (0/rev) control input alone was marginal in terms of improving the rotor efficiency at $\mu = 0.3$. However, in combination with single or multi-harmonic control, it was essential and therefore included in all results that were based on unsteady camber control. As expected, the maximum amount of rotor power savings was achieved by superimposing multiple harmonics, i.e., the rotor efficiency improved by almost 5%. However, beyond 2/rev multi-harmonic control, adding more harmonics (Fourier terms) was irrelevant in terms of additional power savings. This suggests that the potential for rotor power savings was already sufficiently approximated when using up to 2/rev (multi-harmonic) control. Accordingly, the negligible amount of additional power savings from using more than 2/rev control was sacrificed to reduce the computational effort for most of the following investigations. Although most of the power gain was already achieved with single-harmonic 1/rev (1P) actuation (4%), the benefit of adding a 2/rev harmonic to the control signal was considered relevant.

Single-harmonic actuation:
For camber control based on a single (higher-)harmonic signal (1/rev to 5/rev), a decreasing efficiency improvement was found with increasing actuation frequency. At the same time, the required actuation amplitudes for higher-harmonic actuation decreased significantly (see Fig. 3.2c). Especially between 3/rev and 4/rev, a substantial decrease in the efficiency gain was observed. This can be explained by the fact that only an odd harmonic control allowed different amounts of camber deflection at opposite locations on the rotor disk, particularly at $\psi = 90°$ and $\psi = 270°$. Thus, for active camber control based on an even multiple of the rotor frequency, the camber deflection on the retreating side ($\psi = 270°$) is limited by the constraints on the advancing side ($\psi = 90°$). This is also evident by the fact that all different types of control agreed on the (small) amount of camber deflection in the azimuth range between $\psi = 90°$ and $\psi = 120°$ (see Figs. 3.2c and 3.2d).

With 1/rev actuation, rotor power savings were generated by high camber deflections on the retreating side and low camber deflections on the advancing side. In addition, the combination of moderate camber morphing and increased Mach numbers in the fore and aft regions of the rotor disk resulted in additional torsional deformation of the rotor blade (see Fig. 3.3). This resulted in a thrust reduction near the blade tip (see Fig. 3.4a), which in turn implied higher collective pitch control to maintain the trim state. The combination of a higher blade root pitch (see Fig. 3.3b)

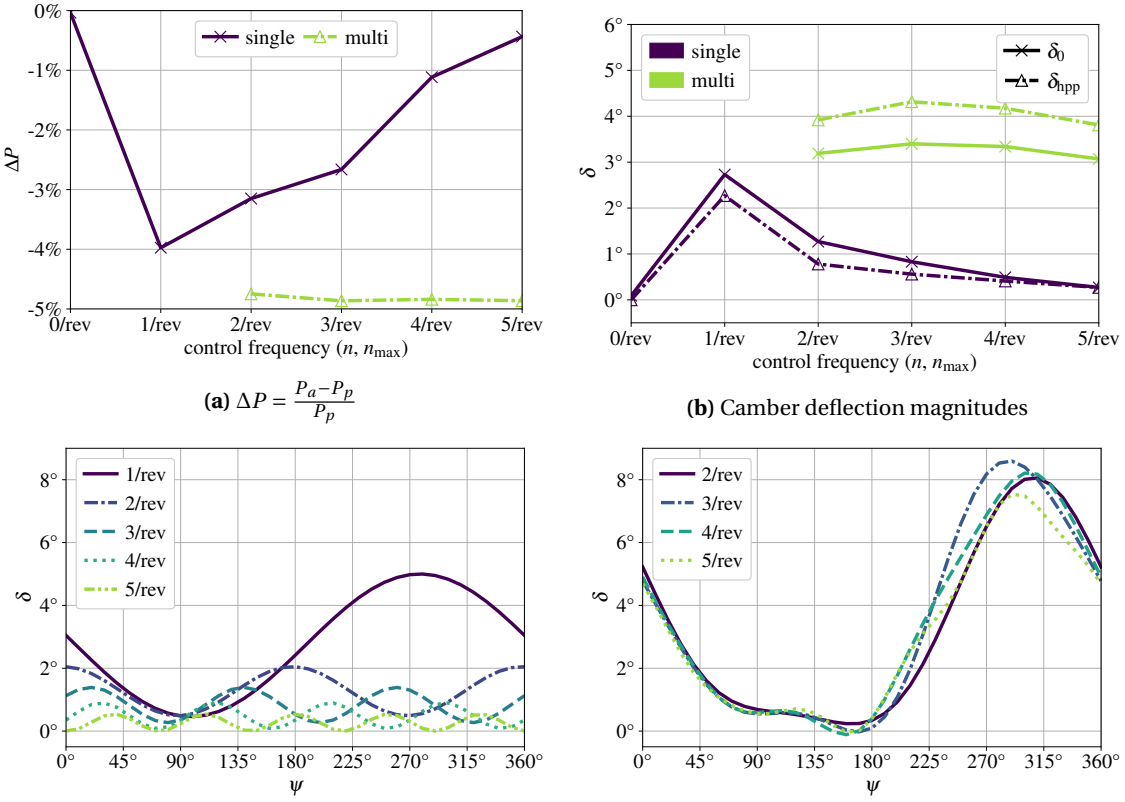

(a) $\Delta P = \frac{P_a - P_p}{P_p}$

(b) Camber deflection magnitudes

(c) Single-harmonic control

(d) Multi-harmonic control

Figure 3.2: Comparison of single and multi-harmonic control inputs. (a) Rotor power savings related to active camber actuation in terms of the relative difference in passive (P_p) and active (P_a) rotor power. (b) Mean deflection and half-peak-to-peak deflection. (c) – (d) Active-camber control signals over one rotor revolution.

and a greater blade camber resulted in an increase in thrust on the lateral sides of the rotor disk (see Fig. 3.4).

In contrast, the 2/rev control required low camber deflections on the retreating side to avoid high camber deflections on the advancing side. Improving the rotor efficiency was therefore only possible by increasing the blade twist in the fore and aft regions of the rotor disk, as already explained for the 1/rev control. The effect of a 3/rev actuation was similar to that of a 1/rev actuation. Accordingly, there was a clear difference in the camber deflection between the advancing and retreating sides. In addition, there was a significant increase in the elastic twisting of the blades in the fore and aft regions of the rotor disk. This efficiently redistributed the thrust to the lateral sides and explains the comparatively small difference between single-harmonic 2/rev and 3/rev actuation, despite the significantly lower amplitudes used for 3/rev actuation. This reduction in amplitude with increasing actuation frequency can be explained by the shift of the camber deflection peaks to the advancing side. Due to the high Mach numbers in this azimuth range, high camber deflections are no longer efficient.

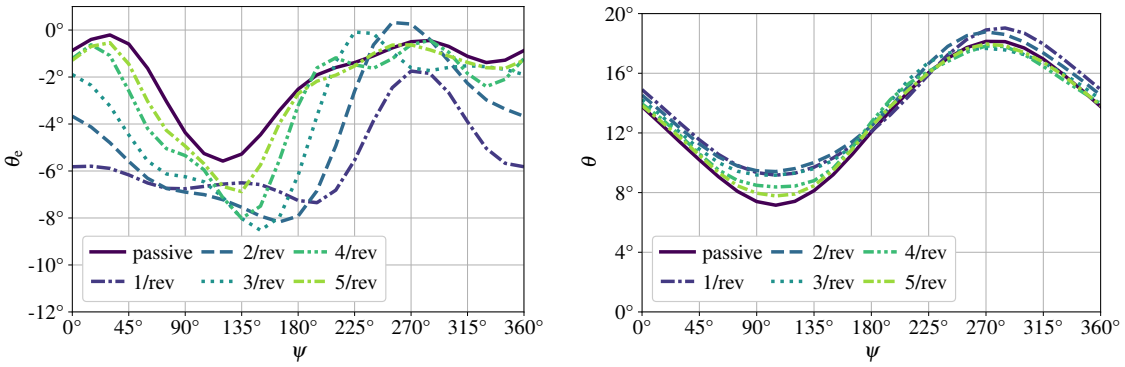

(a) Blade elastic twist

(b) Blade root pitch

Figure 3.3: Effect of active camber on the blade pitch attitude using single-harmonic control.

Comparing the cases in Fig. 3.4, the resulting redistribution of thrust from the fore and aft regions of the rotor to the lateral sides (see Fig. 3.4) was similar for 1/rev to 3/rev, although the underlying camber control was quite different. The main difference was that the areas of load reduction shifted slightly to the advancing side as the actuation frequency increased. This limited the ability to redistribute thrust in a beneficial way.

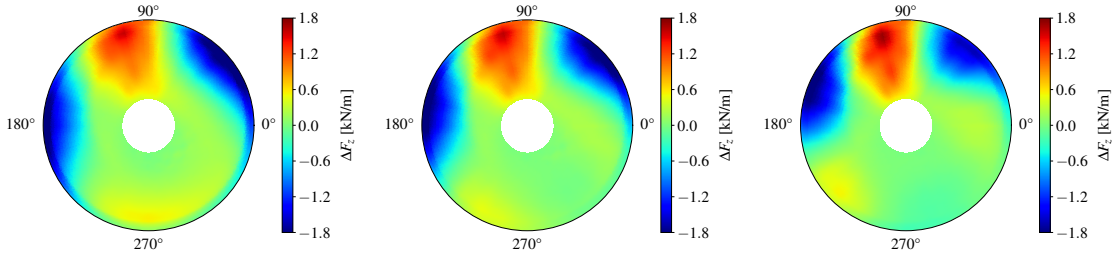

(a) 1P actuation

(b) 2P actuation

(c) 3P actuation

Figure 3.4: Redistribution of rotor thrust using single-harmonic control (1/rev to 3/rev). ΔF_z is defined as the difference in thrust between the passive and active rotors ($\Delta F_z = F_{z,a} - F_{z,p}$). For simplicity, it has been omitted throughout this work to indicate that the dependent variable for any disk plot is a function of the radial location (y) and the azimuth position of the rotor blade (ψ).

Multi-harmonic actuation:

When two or more rotor harmonics were superimposed, the control signals that were most successful in reducing rotor power were quite similar (see Fig. 3.2d). They resembled the characteristic of the 1/rev control signal, but with a narrower and more pronounced peak on the retreating side. The respective peak-to-peak active-camber deflection of about 8° corresponds to a trailing-edge displacement of about 0.01m. For the multi-harmonic actuation, a more detailed aeromechanical analysis is given in the following section, i.e., an evaluation of the 1P+2P (mean deflection, 1/rev and 2/rev harmonics) control.

3.1.2 Active Rotor Aeromechanics Analysis

To better understand the principles of active-camber-related rotor power saving in high-speed flight, it is helpful to understand how power is transmitted through the system, starting at the power source. The power generated by the engine enters the rotor system through the rotor shaft. At the interface between the rotor shaft and the rotor blades, the total power depends on the rotational speed (Ω), the number of blades (N_b), and the averaged moment of each rotor blade about the rotor shaft axis $\overline{M_z(\psi)}$. It is described by

$$P = \Omega \cdot N_b \cdot \overline{M_z(\psi)}. \tag{3.4}$$

For this analysis, the rotational speed (Ω) and the number of blades (N_b) are assumed to be fixed. Therefore, $\overline{M_z(\psi)}$ must be determined to evaluate the required power. Since a periodic state of the rotor is considered, any inertial forces or structural damping forces from rotor blade oscillations do not affect the averaged moment because they cancel out over a full revolution. Consequently, $\overline{M_z(\psi)}$ depends on the aerodynamic forces acting on the rotor blade and is obtained by integration over infinitesimally small elements of the rotor blade:

$$M_z(\psi) = \int_0^R dM_z(\psi, y). \tag{3.5}$$

The moment induced by such blade elements results from the lever arm (y) around the axis of rotation and the in-plane aerodynamic force opposing the rotational motion:

$$dM_z(\psi, y) = y \cdot dF_x(\psi, y) = y \cdot q(\psi, y) \cdot C_x(\psi, y) \cdot c \cdot dy. \tag{3.6}$$

In the context of camber morphing, the aerodynamic coefficients are a function of the Mach number (M), the angle of attack (α), and the camber morphing deflection (δ). Based on the section inflow angle (ϕ), the drag force opposing the rotational motion is composed of a lift and a drag component:

$$C_x = C_d(M, \alpha, \delta)\cos\phi + C_l(M, \alpha, \delta)\sin\phi. \tag{3.7}$$

Assuming a constant chord length c, $\overline{M_z(\psi)}$ is influenced by the local airfoil coefficients ($C_l(M, \alpha, \delta)$ and $C_d(M, \alpha, \delta)$), the section inflow angle (ϕ), the dynamic pressure ($q(\psi, y)$), and the distance to the axis of rotation (y). The inflow angle (ϕ) and the angle of attack (α) both depend on the blade motion and the wake modeling. This is where the structural dynamics modeling, trim calculation, and aerodynamic free-vortex wake modeling come into play. This means that small changes in one of these involved variables, e.g., the camber deflection (δ), affect the whole system through complex interdependencies. This also explains why this system of equations must be solved iteratively.

Although it is not possible to isolate the effect of active camber on rotor power, some ideas can be derived from these equations on how to reduce power consumption. For example, the local efficiency can be improved by a better lift-to-drag ratio (C_l/C_d), e.g., by changing the airfoil geometry

(camber morphing). Also, influencing the lift distribution over the rotor disk is an important feature, especially in high-speed flight. It can be used to shift the lift further inward to reduce the lever arm (y), to regions of lower dynamic pressure (q) to escape the high drag in the transonic regime (as explained below), to regions with negative thrust, or to regions of lower induced inflow angle (ϕ) and thus lower contribution of C_l to the rotor shaft power. Note that due to the non-linear dependence of C_x on ϕ, the latter aspect can become particularly important, i.e., high lift in regions of high induced velocity should be avoided.

Active-rotor-induced rotor power savings:
To evaluate the power gain with active camber, Fig. 3.5 shows how different regions of the rotor disk contribute to the total rotor power required. For the passive rotor (see Fig. 3.5a), a significant amount of power was consumed in the first quadrant of the rotor disk (between $\psi = 0°$ and $\psi = 80°$) near the blade tip. When the blade camber was actively controlled (1P+2P control, as presented in the previous section), this local peak in power consumption was significantly reduced (see Fig. 3.5b). Instead, power consumption increased moderately on both the advancing and retreating sides. Similarly, but less pronounced, was the effect at the front of the rotor disk (about $\psi = 200°$). This variation in rotor power resulted in a total difference between the active and passive rotor of almost 5% (see previous section).

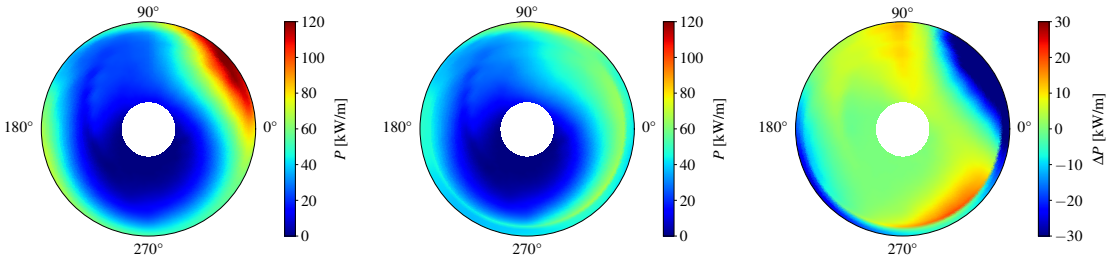

(a) Passive rotor **(b)** Active rotor **(c)** (b) - (a)

Figure 3.5: (a) and (b) Rotor power consumption of the passive (P_p) and active rotor (P_a, multi-harmonic 1P+2P control) at $\mu = 0.3$. (c) Difference in rotor power ($\Delta P = P_a - P_p$).

As explained above, the redistribution of the aerodynamic loads (F_z and F_x) is an important factor influencing the rotor efficiency. According to Eqs. 3.4 to 3.6, the azimuthal distribution of F_x was identical to that of P (see Fig. 3.5) and is therefore not shown here. The distribution of F_z was different from P and thus from F_x and is shown in Fig. 3.6. Instead of a peak in the first quadrant like P and F_x, F_z had two aggregations of thrust, one in the front and one in the rear region of the rotor disk. However, the redistribution induced by active camber morphing was quite similar (Figs. 3.5c and 3.6c). This supports the assumption that there is a strong correlation between power reduction and thrust redistribution. Note that the rotor thrust is purely redistributed, while the variation in rotor power includes the aforementioned difference in rotor power (5%). In addition, Fig. 3.6c shows that regions that experienced unloading were mainly located far outboard. Conversely, regions with increased thrust were generally located further inboard. As a result, the aerodynamic forces that were shifted inward created a smaller moment about the shaft axis due to

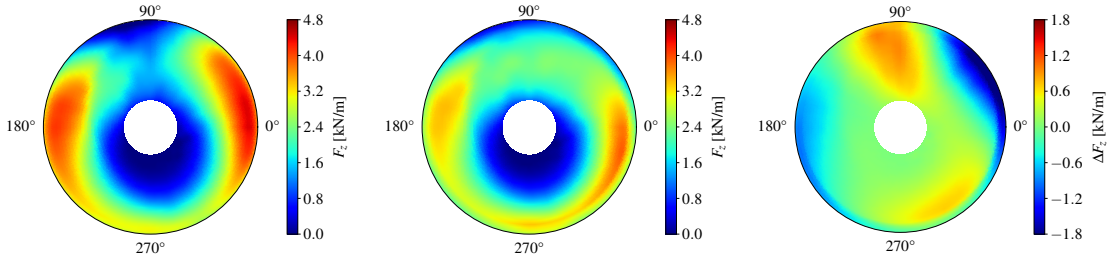

(a) Passive rotor **(b)** Active rotor **(c)** (b) - (a)

Figure 3.6: (a) and (b) Rotor thrust distribution of the passive ($F_{z,p}$) and active rotor ($F_{z,a}$, multi-harmonic 1P+2P control) at $\mu = 0.3$. (c) Difference in thrust ($\Delta F_z = F_{z,a} - F_{z,p}$).

the reduced lever arm. Furthermore, in the area with the highest power consumption, the thrust was redistributed to other parts of the rotor disk, specifically, the advancing and retreating sides. This resulted in a more even distribution of thrust across the rotor disk, which was beneficial in several ways, as described in the following.

On the one hand, the unloaded region was quite inefficient in terms of power generation, since moderate lift coefficients (see Fig. 3.7a) in this region were associated with high drag coefficients (see Fig. 3.7b). This was mainly due to the airfoil characteristics close to the transonic flow regime (see Fig. 3.8a). As shown in Fig. 3.9, a steep increase of the drag coefficient was obtained at high Mach numbers. This was already true for moderate angles of attack. However, the lift coefficient did not show a similar increase, resulting in an unfavorable lift-to-drag ratio (see Fig. 3.7c). In addition, there were high induced velocities and, therefore, high inflow angles ϕ in the same region (see Fig. 3.8b). This resulted in a notable contribution of the lift force to the in-plane (perpendicular to the rotor shaft axis) drag force (see Eq. 3.7).

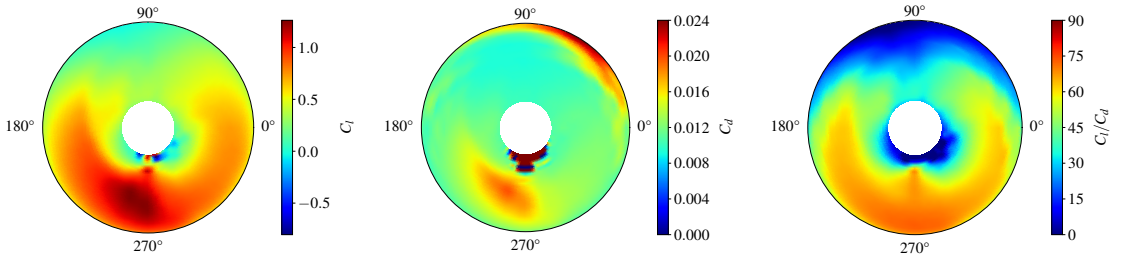

(a) C_l **(b)** C_d **(c)** C_l/C_d

Figure 3.7: Lift and drag coefficients of the passive rotor and the resulting lift-to-drag ratio ($\mu = 0.3$).

On the other hand, loading the regions on the advancing and retreating sides did not result in substantial performance penalties. On the retreating side, lift production was already efficient (see Fig. 3.7c), and it was further improved by increasing the camber of the airfoil in this region (see Fig. 3.10c). This was mainly due to the moderate Mach numbers and angles of attack in this azimuth range [58]. On the advancing side, the negative thrust near the blade tip was reduced. This

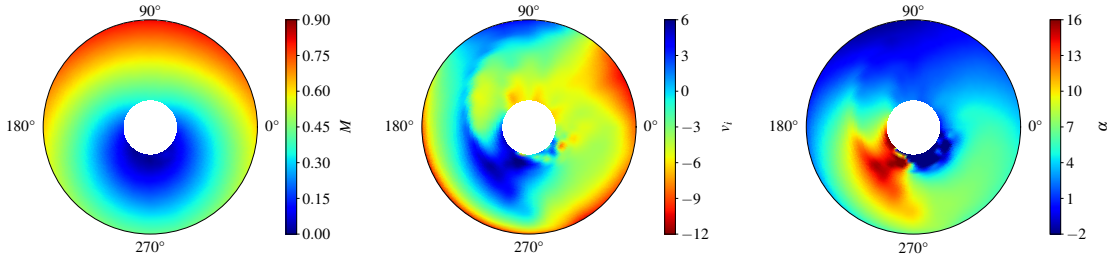

(a) Mach number M **(b)** induced velocity v_i **(c)** angle of attack α

Figure 3.8: Passive rotor parameters that define the oncoming flow velocity vector for each blade section ($\mu = 0.3$).

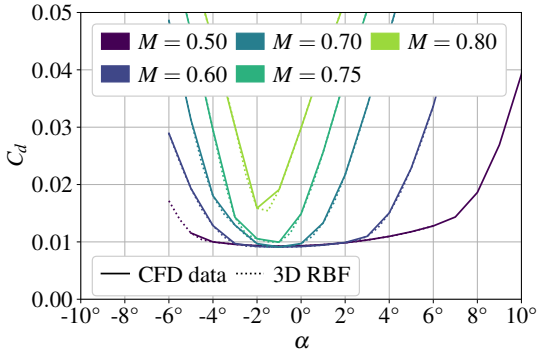

Figure 3.9: Drag coefficient (C_d) over angle of attack (α) for the non-morphed NACA23012 airfoil.

resulted in an increase in performance because this negative thrust no longer had to be compensated by the remaining rotor area. This increase in lift close to $\psi = 90°$ (see Fig. 3.10b) caused only a negligible drag penalty (see Fig. 3.10a). This was attributed to the flat slope of the $C_d - \alpha$ curve in this regime (see Figs. 3.9 and 3.8c). Thus, the lift-to-drag ratio was significantly improved. Also, the induced velocities were generally moderate in the regions that were further loaded by this thrust redistribution. Therefore, the additional lift force did not contribute significantly to the rotor shaft moment.

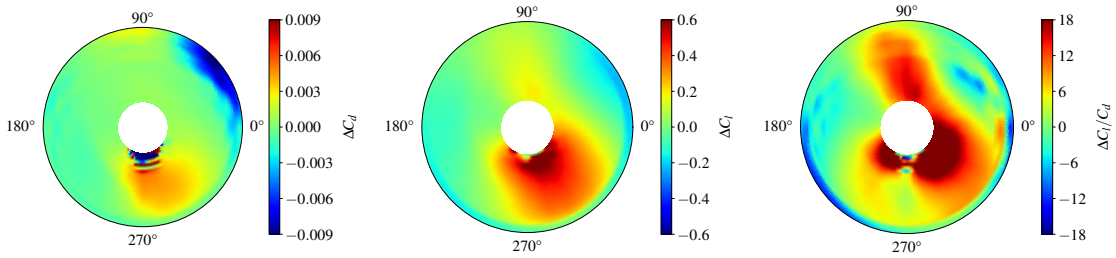

(a) ΔC_d **(b)** ΔC_l **(c)** $\Delta C_l/C_d$

Figure 3.10: Difference in aerodynamic coefficients between the active (multi-harmonic 1P+2P control) and passive rotor ($\Delta() = ()_a - ()_p$) at $\mu = 0.3$.

Local blade pitch angle variation:
As already discussed, the redistribution of loads over the rotor disk was achieved by varying the cross-sectional airfoil polars ($C_l(M,\alpha)$, $C_d(M,\alpha)$, and $C_m(M,\alpha)$) along the rotor azimuth through camber morphing. This also had a significant effect on the aerodynamic moment and induced torsional deformation of the rotor blades. In addition, the primary control had to be adjusted to maintain the original trim condition. All three effects contributed to the resulting redistribution of aerodynamic loads.

Figure 3.11 compares the non-dimensional aerodynamic moment between the passive and active rotors. This moment increased significantly when high camber deflections were applied. Especially in the rear part of the rotor disk, the aerodynamic moment increased substantially. The highest aerodynamic moment occurred after the peak camber deflection (at about $\psi = 300°$, see Fig. 3.2d) because of the dynamic pressure. It depends quadratically on the Mach number, and M increased with distance from $\psi = 270°$ (see Fig. 3.8a). Therefore, as shown in Fig. 3.12, active camber induced a large amount of elastic twist, especially near $\psi = 360°$. Note that the aerodynamic moment in the rear part is substantially high, although the camber deflections and Mach numbers were only moderate. Therefore, an unintentional deployment of overly high camber deflections on the advancing side, where the greatest dynamic pressure occurs, could lead to an overloading of the rotor system.

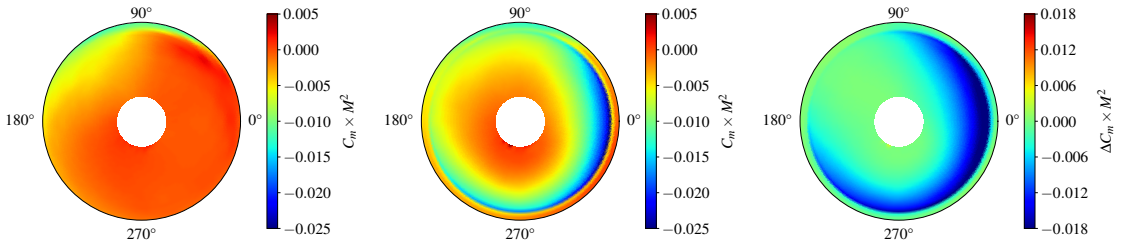

(a) Passive rotor **(b)** Active rotor **(c)** Δ(active − passive)

Figure 3.11: (a) − (b) Aerodynamic moment ($C_m \times M^2$) of the passive and active rotor (multi-harmonic 1P+2P control) at $\mu = 0.3$. (c) Difference between the passive and active rotor ($\Delta C_m \times M^2 = (C_m \times M^2)_a - (C_m \times M^2)_p$).

In Fig. 3.12b, the blade pitch positions at the blade root ($r = 0.22$) and the blade tip ($r = 1$) are shown as a result of the elastic blade deformation, the rotor primary control, and the built-in blade twist. Although the blade root pitch ($r = 0.22$) in the first quadrant of the rotor was increased when camber morphing was applied, the blade pitch angle at the tip was significantly reduced. This reduction was responsible for the observed power reduction in the first quadrant. In general, the blade pitch angle was increased at the root, but mostly decreased at the tip. As a result, thrust was redistributed to more inboard radial stations. However, at $\psi = 90°$, there was a slight increase in the tip pitch angle, which reduced the amount of negative thrust. On the retreating side, the blade pitch angle near the tip decreased. Instead, the greater lift on the retreating side was produced by deforming the airfoil with active camber.

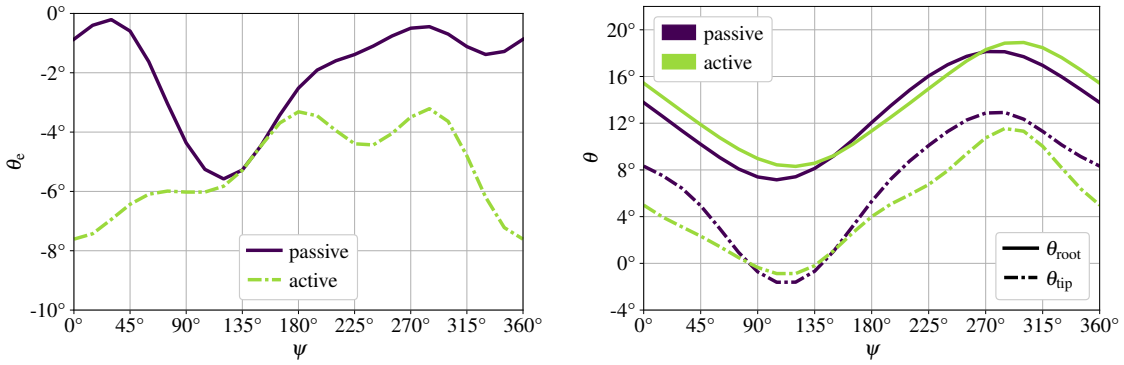

(a) Blade elastic twist θ_e

(b) Blade sectional pitch $\theta(r)$

Figure 3.12: Blade elastic twist and the resulting pitch positions at two specific radial stations, i.e., θ_{root} ($r = 0.22$) and θ_{tip} ($r = 1$). The blade pitch in (b) is based on a superposition of the blade pitch control input, the blade built-in twist θ_{tw}, and the blade elastic twist θ_e.

In-plane and out-of-plane rotor blade deformation:
While the torsional blade deformation actively contributed to the redistribution of the aerodynamic loads, the flap and lag deformations were considered to be mostly a result of the modified aerodynamics. Nevertheless, the resulting blade deformations are of interest and will be examined below. Desirably, the blade deformations should not increase significantly due to the camber actuation, e.g., to keep the oscillatory loads on the rotor hub low.

Figures 3.13 and 3.14 show the deformation of the rotor blades in flap and lag directions. The flap deflection in Figs. 3.13a to 3.13c was evaluated with respect to the reference line defined by the precone angle of 2.5°. The flap motion of the baseline rotor was predominantly influenced by the two thrust peaks in the fore and aft regions of the rotor disk. Due to the proximity of the first flap natural frequency (1.15/rev) to the first rotor harmonic (1/rev), there was a phase shift between the excitation force and the flap displacement of slightly less than $\Delta\psi = 90°$ [73]. Thus, the highest flap deflections were obtained on the lateral sides. The more pronounced flap deflection on the retreating side was explained by the fact that the negative thrust on the advancing side had a damping effect on the flap motion. Instead, on the retreating side, the flapping motion was further facilitated by a continuous thrust force far outboard. With active camber actuation, the thrust at the front and rear of the rotor disk was notably reduced. In addition, the blade tip was generally unloaded. As a result, the overall flap motion was attenuated.

The first lag natural frequency (about 0.65/rev) was below the first rotor harmonic (1/rev). Accordingly, the phase lag between excitation and displacement was between $\Delta\psi = 90°$ and $\Delta\psi = 180°$ [73]. The drag force of the rotor blades $F_x(\psi, y)$ was mainly responsible for the lag motion. In terms of azimuthal distribution, $F_x(\psi, y)$ coincided with the power characteristic in Fig. 3.5a (see mathematical relationship in Eqs. 3.4 to 3.6). Consequently, the peak in $F_x(\psi, y)$ that appeared in the first quadrant of the rotor disk was translated into a lag displacement peak in the fore region of the rotor disk (see Fig. 3.14a). Again, the use of active camber attenuated this lag motion by

reducing the drag peak in the first quadrant and also by reducing the aerodynamic load near the blade tip (see Figs. 3.14b and 3.14c). Overall, active camber control for power reduction did not cause critical blade deformation. Instead, it reduced deformation in the flap and lag directions, which is expected to potentially mitigate rotor oscillatory loads such as rotor hub loads.

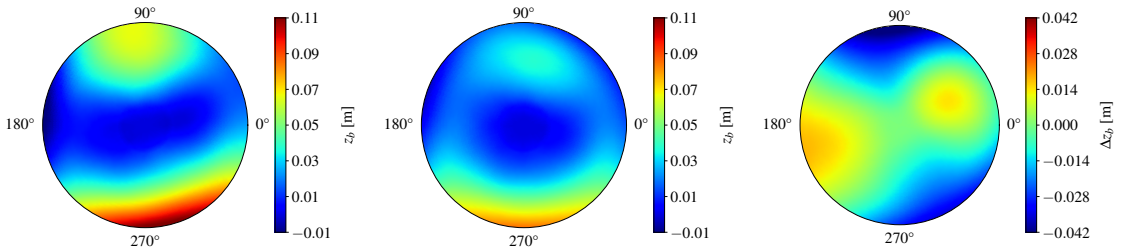

(a) Passive rotor **(b)** Active rotor **(c)** Δ(active − passive)

Figure 3.13: (a) − (b) Blade flap deformation (z_b) of the passive and active rotor (multi-harmonic 1P+2P control) at $\mu = 0.3$. (c) Difference between the passive and active rotor ($\Delta z_b = z_{b,a} - z_{b,p}$).

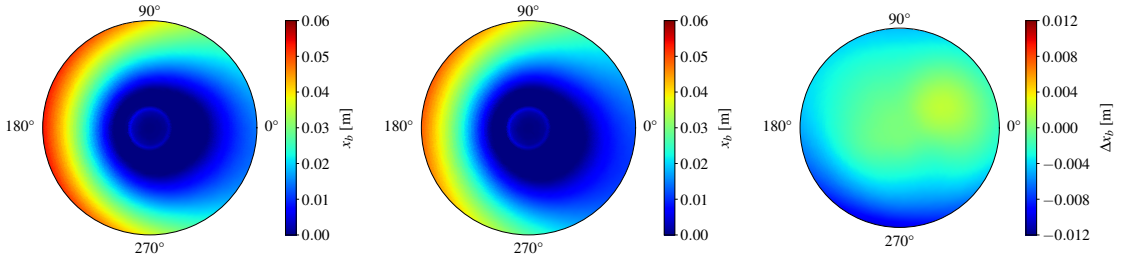

(a) Baseline lag deflection **(b)** Active camber lag deflection **(c)** Δ(active − passive)

Figure 3.14: (a) − (b) Blade lag deformation (x_b) of the passive and active rotor (multi-harmonic 1P+2P control) at $\mu = 0.3$. (c) Difference between the passive and active rotor ($\Delta x_b = x_{b,a} - x_{b,p}$).

So far, only the reduction in rotor power has been considered in the optimization of active-camber control inputs. However, as shown in Fig. 3.12, the actuation also affects other aspects of the rotor system, in particular the blade deformation and the associated loads. In the following, optimization studies will be presented where multiple objectives have been considered, still with the main focus on rotor power optimization.

3.1.3 Multi-Objective Optimization of the Camber Control Signals

While the results presented above were obtained by optimizing the active camber control for rotor power reduction, aspects related to the operability of the rotor system were not considered. However, part of the research question was to determine if active camber could be applied in a way that would not result in operational penalties for the rotorcraft. Therefore, the next step was to investigate whether camber actuation could pursue multiple objectives simultaneously by including them in the cost function. As such, the following analysis also considered peak-to-peak

pitch-link loads, peak-to-peak rotor hub forces and moments, and the retreating-blade stall margin, as these were believed to affect fatigue, comfort, and the flight envelope of the entire system. In particular, the pitch-link loads were expected to have a strong correlation with the active camber actuation due to its effect on the torsional deformation of the rotor blade (see Fig. 3.3a). This is due to the notable increase in the aerodynamic moment as the blade camber increases. However, the rotor hub forces and moments were also considered to interact with active camber actuation due to its influence on the blade motion and the associated displacement imbalances and bending moments. The stall margin SM of the retreating blade (evaluated at $\psi = 270°$ according to Eq. 2.9) was considered important for this study because it is an indication of the feasible flight envelope and maneuverability of the rotorcraft in high-speed flight. By maintaining the original stall margin of the baseline rotor, it was assumed that these operational capabilities would not be compromised.

Several additional aspects may be of interest in the context of active camber control. One example is the emitted rotor noise. However, this topic was beyond the scope of this work. Other aspects, such as rotor blade deformation or fuselage vibrations, were considered to be sufficiently accounted for by evaluating the rotor oscillatory hub loads. The mean loads were not considered because they are less relevant for vibration and fatigue, and some of them were already predefined in the trim targets. Reducing the range of active camber morphing and the movement speed of the mechanism are also valid goals to facilitate the operation of such systems. However, based on the results of Section 3.1.1, the required amplitudes (0.01m trailing-edge deflection) were below the values claimed to be feasible (0.0135m) in the work of [48]. Therefore, it was decided not to reduce the range of camber morphing by including it in the cost function. Instead, amplitude reduction far out at the rotor blades was investigated using spanwise varying camber deflections (see Section 3.2).

Interdependence of active camber and pitch-link loads:
The addition of optimization targets is first discussed in the context of pitch-link loads (see Fig. 3.15). Figure 3.15a shows the same data points as Fig. 3.2, but this time with respect to their effect on pitch-link loads. It can be seen that the maximum power gains resulted in noticeably higher peak-to-peak pitch-link loads. This confirms the importance of considering the oscillatory rotor loads during the optimization process.

Figure 3.15b evaluates the success of simultaneously improving rotor power and pitch-link loads. The line shown in this figure approximates the Pareto front for rotor power and pitch-link loads based on different active-camber control inputs. An important detail in this figure is the broad optimum, which indicates the same amount of power savings for a wide range of different pitch-link loads. This means that not explicitly considering pitch-link loads during optimization most likely resulted in unnecessarily high loads without any benefit. Therefore, defining an appropriate cost function can avoid focusing on irrelevant regimes with respect to real applications. This figure also shows the potential of using active camber for load reduction. Initially, only a small amount of performance gain had to be sacrificed to avoid high pitch-link loads, i.e., maintaining

baseline pitch-link loads was inexpensive. Beyond that, however, load reduction became increasingly expensive in terms of the ability to reduce rotor power. Nevertheless, by changing the priority from power reduction to load reduction, significant load reductions could be achieved with active camber control.

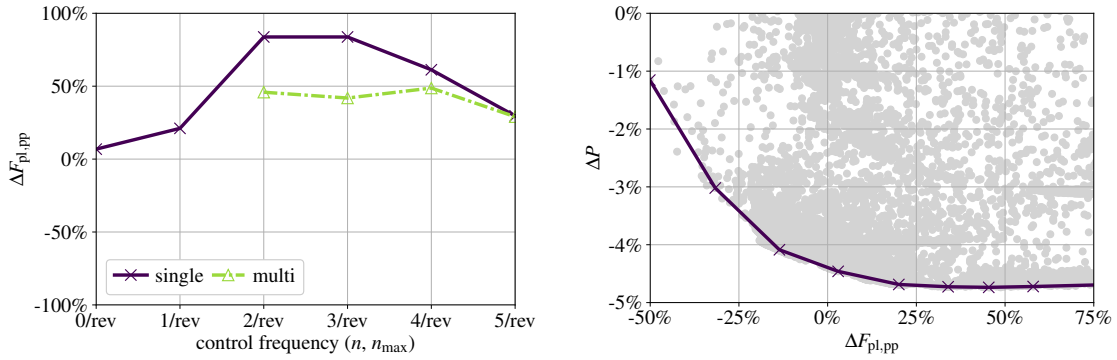

(a) $\Delta F_{\mathrm{pl,pp}} = \frac{F_{\mathrm{pl,pp},a} - F_{\mathrm{pl,pp},p}}{F_{\mathrm{pl,pp},p}}$ **(b)** $\Delta P = \frac{P_a - P_p}{P_p}$, $\Delta F_{\mathrm{pl,pp}} = \frac{F_{\mathrm{pl,pp},a} - F_{\mathrm{pl,pp},p}}{F_{\mathrm{pl,pp},p}}$

Figure 3.15: Effect of active camber on peak-to-peak pitch-link loads $F_{\mathrm{pl,pp}}$. (a) Single-harmonic and multi-harmonic camber control without considering pitch-link loads in the cost function. (b) Pareto front of pitch-link loads and rotor power savings using multi-harmonic 1P+2P control.

Extension of the objective function:

When considering additional objectives during optimization, the previously found rotor power savings should be maintained as much as possible. At the same time, the goal was to avoid any appreciable degradation in the aforementioned aspects compared to the passive baseline rotor. As described in Section 2.3.2, this was achieved by specifically tuning the cost function to drive the optimization in a direction that satisfied these requirements. It involved the use of weighting factors w, exponents e, and normalization with reference values. This allowed mimicking constraints on certain output parameters without sacrificing the continuity of the objective function, which was a requirement of the optimization approach employed. Accordingly, the cost function was defined as

$$\Pi(\vec{x}) = w_P \left(\frac{P(\vec{x})}{P_{\mathrm{ref}}} \right)^e + \sum_{i=1}^{4} w_L \left(\frac{F_i(\vec{x})}{F_{i,\mathrm{ref}}} \right)^e + \sum_{i=1}^{3} w_L \left(\frac{M_i(\vec{x})}{M_{i,\mathrm{ref}}} \right)^e + w_{SM} \left(\frac{SM_o(\vec{x})}{SM_{o,\mathrm{ref}}} \right)^e . \tag{3.8}$$

The forces F_i of a single computation result with control inputs $\vec{x}$ were the peak-to-peak pitch-link loads ($F_{\mathrm{pl,pp}}$) and the peak-to-peak rotor hub loads ($F_{x,\mathrm{pp}}, F_{y,\mathrm{pp}}, F_{z,\mathrm{pp}}$). The moments M_i were the peak-to-peak hub moments ($M_{x,\mathrm{pp}}, M_{y,\mathrm{pp}}, M_{z,\mathrm{pp}}$). The sum of all weighting factors, i.e., for rotor power (w_P), rotor loads (w_L), and stall margin (w_{SM}), should be one:

$$w_P + 7 \cdot w_L + w_{SM} = 1. \tag{3.9}$$

Most of the following analyses were performed with equal weighting factors for loads and stall margin. For these cases, a combined weighting $w_{L,SM} = w_L = w_{SM}$ was defined.

Optimization results based on the extended objective function:
Since appropriate values for w and e were not known prior to the analysis, an iterative approach was used to determine reasonable values. Figure 3.16 shows the influence of these parameters on the optimization results based on three combinations of these parameters. The case with $w_{L,SM} = 0$ represents the results of the previous section, which were based on the optimization of the rotor power only. In addition, two cases with $w_{L,SM} = 0.005$ and thus $w_P = 0.96$ are shown, but one without using an exponent ($e = 1$) and one with a high exponent of $e = 10$. With multi-harmonic control, power savings were only slightly affected when loads and stall margin were considered in the objective function (see Fig. 3.16a). The corresponding loads for these multi-harmonic control cases are shown in Figs. 3.16b to 3.16d. Without optimizing for loads, most of them were significantly increased. Otherwise, especially when using $e = 10$, the loads were efficiently reduced, even though the weighting $w_{L,SM}$ was quite low compared to w_P.

Comparing the effect of different exponents ($e = 1$ and $e = 10$, each with $w_{L,SM} = 0.005$), the results were quite similar for multi-harmonic cases. However, at 1/rev actuation, the passive rotor loads were much closer to the goal of not exceeding the passive baseline rotor loads when using $e = 10$ instead of $e = 1$. This was because the high exponent caused large costs for values exceeding the reference values, even though the weighting factor was quite small. Accordingly, the actual weighting of a particular objective changes dynamically based on its relationship to the reference values. In addition, an exponent of $e = 10$ successfully prevented the generation of a performance penalty with active camber in favor of other objectives. This was favored by the high weighting of the rotor power, w_P. Further increasing the value of e up to $e = 20$ had a marginal effect on the optimization result but worsened the convergence behavior of the optimization process. As a result, using values of $e = 10$ and $w_{L,SM} = 0.005$ was considered successful in terms of emphasizing the improvements in rotor performance while effectively avoiding significant deterioration in other aspects such as rotor loads. Consequently, this setting has been used in the following work unless otherwise noted. Note that this avoidance of exceeding the baseline rotor loads actually improved the loads in the sense that most of the peak-to-peak loads were noticeably reduced.

While the power savings were insignificantly affected by this extension of the objective function when using multi-harmonic actuation, the effect on the power gain was significant when using single-harmonic actuation. Unless a notable penalty in loads and stall margin was allowed, the amount of power gain became negligible. Thus, from an overall assessment, the single-harmonic actuation strategies were considered irrelevant for real-world applications. Instead, in accordance with the previous section, a superposition of 1/rev and 2/rev harmonics was considered to sufficiently approximate the optimal solution. When comparing the resulting rotor power savings and peak-to-peak loads in Fig. 3.16, the benefits of adding more harmonics to the control signal were not in an acceptable ratio to the associated increase in computational effort. Therefore, unless otherwise noted, the following work is based on 2/rev multi-harmonic (1P+2P) control.

Details of the corresponding (multi-harmonic) control inputs are shown in Fig. 3.17. It shows a comparison of the case where only the rotor power was optimized ($w_{L,SM} = 0$) and the case

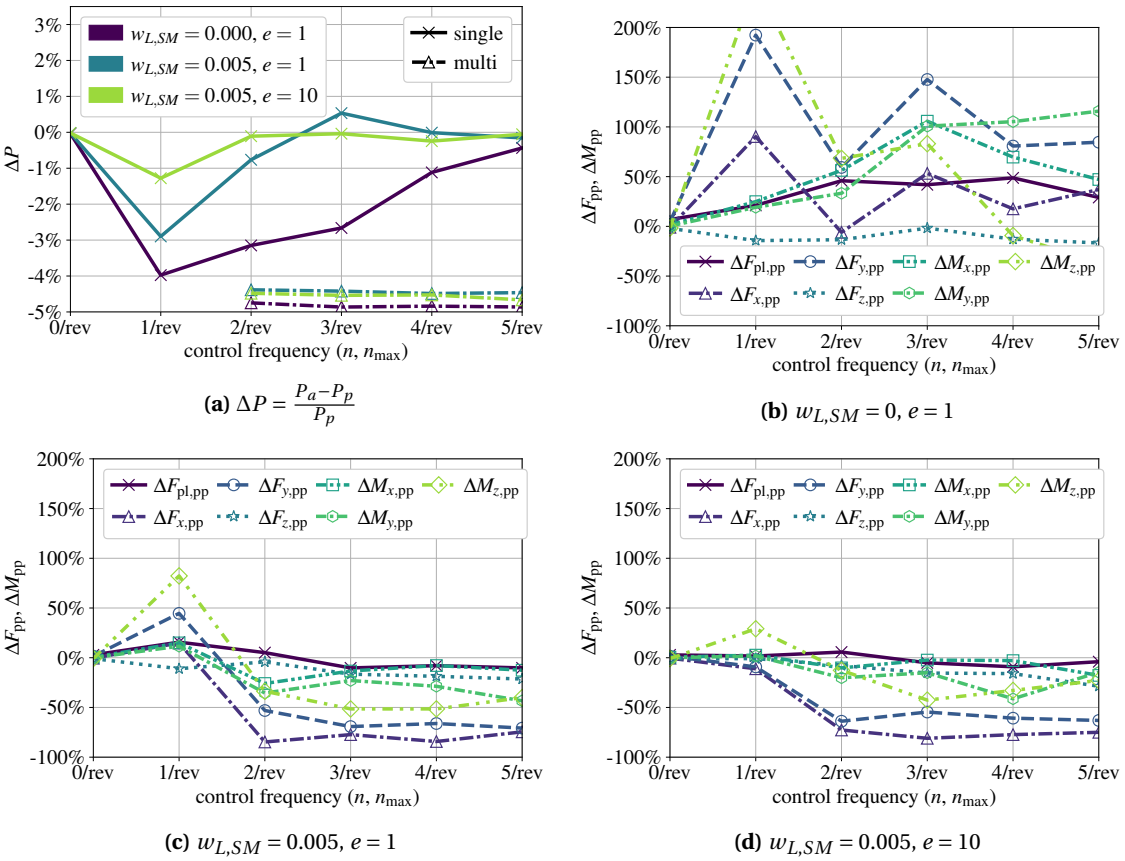

(a) $\Delta P = \frac{P_a - P_p}{P_p}$

(b) $w_{L,SM} = 0$, $e = 1$

(c) $w_{L,SM} = 0.005$, $e = 1$

(d) $w_{L,SM} = 0.005$, $e = 10$

Figure 3.16: Influence of weighting factors (w) and exponents (e) on the optimization result regarding rotor power and rotor loads at $\mu = 0.3$. (b) to (d) Difference in peak-to-peak forces and moments between passive and active rotor ($\Delta() = \frac{0_{pp,a} - 0_{pp,p}}{0_{pp,p}}$). 2/rev to 5/rev are based on multi-harmonic control.

with quasi-constrained loads and stall margin ($w_{L,SM} = 0.005$ and $e = 10$). In terms of mean and peak-to-peak deflections (see Fig. 3.17a), the 1/rev signal had to be reduced significantly to avoid load penalties. The effect on the multi-harmonic control, instead, was quite small. For the 2/rev to 4/rev cases, only a slight reduction in amplitudes was found when considering loads and stall margin in the cost function. For the multi-harmonic 1P+2P control, a comparison of the azimuthal control inputs is shown in Fig. 3.17b for the two different specifications of the objective function. This quasi-constraint of the rotor loads was achieved mainly by a slight phase shift to lower ψ and a small reduction of the peak deflection. Together, this resulted in a reduction in camber deflection mainly in the first and fourth quadrants of the rotor disk. An increase in camber deflection was obtained in the third quadrant.

The azimuthal course of the considered hub loads after subtracting the mean values is shown in Fig. 3.18. Note that the shaft torque M_z is negative when the rotor is absorbing power and therefore negative values indicate high absolute values. Since the pitch-link loads (F_{pl}) are described in the rotating system, there is a clear causal relationship between differences in camber deflection and a reduction in the peak-to-peak pitch-link loads. A reduction in camber morphing

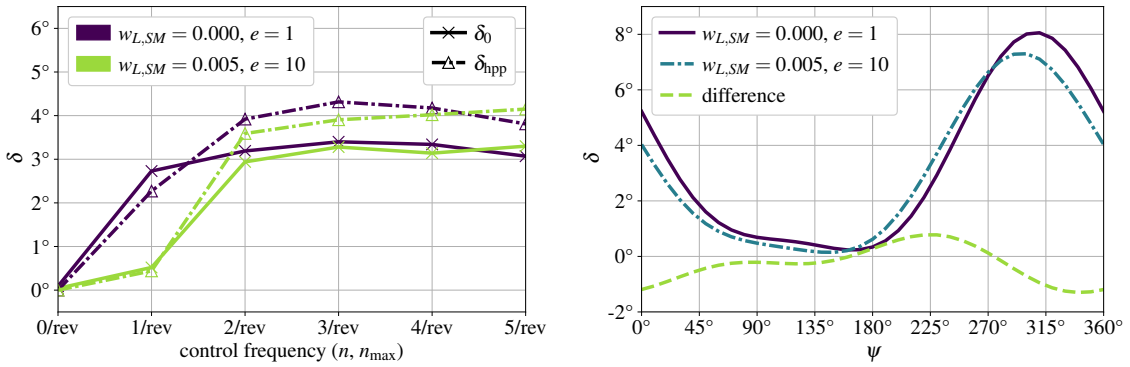

(a) Camber deflection magnitudes

(b) Multi-harmonic 2/rev control (1P+2P)

Figure 3.17: Optimum active-camber control inputs based on different weighting factors (w) and exponents (e) at $\mu = 0.3$. (a) Mean deflection and half-peak-to-peak deflection. 2/rev to 5/rev are based on multi-harmonic control.

around $\psi = 0°$ resulted in a reduction in F_{pl} and, thus, peak-to-peak pitch-link loads ($F_{pl,pp}$), as the highest values of F_{pl} were obtained in this azimuth regime. However, the increase in F_{pl} in the third quadrant of the rotor disk also contributed to a reduction in $F_{pl,pp}$, as F_{pl} was lowest in this azimuth range.

For the non-rotating hub loads, the causal relationship is less obvious. Reducing the peak-to-peak value of a single rotor blade is usually not sufficient because it neglects the compensating effect between the blades. To obtain the effect on the rotor hub, the resulting loads of all four blades must be evaluated together and transferred from the rotating to the non-rotating system. In addition, the phase lag between the aerodynamic excitation force and the blade motion depends on the natural frequencies of the degrees of freedom involved. Most of the non-rotating forces and moments resulted in a 4/rev characteristic. Only the out-of-plane force was described by an 8/rev signal. This was explained by the fact that the third flap natural frequency at nominal rotor speed exactly intersected the 8/rev harmonic (see Campbell diagram of the rotor in Fig. 2.15). Essentially, these loads are related to imbalances and bending stresses resulting from (asymmetric) blade displacements. Subtle differences in local lift and drag forces can affect these displacements and the resulting loads either positively or negatively. Therefore, high precision in phase and amplitude of the actuation mechanism is required when implementing such concepts in order to ensure favorable operation.

While the previous discussion focused on rotor power and rotor loads, the stall margin was also part of the extended cost function. The effect of active camber on the stall margin is shown in Figs. 3.19 and 3.20. The active rotor results are based on the previously presented optimized active-camber control inputs ($w_{L,SM} = 0.005$, $e = 10$, multi-harmonic 1P+2P actuation). For the passive rotor, three regions with only small stall margins were identified. They were centered at approximately $\psi = 30°$, $\psi = 150°$, and $\psi = 270°$ (see Fig. 3.19a). As described in Section 2.1.6, the concept of evaluating $C_{l,max}$ for high Mach numbers is quite limited. However, a qualitative

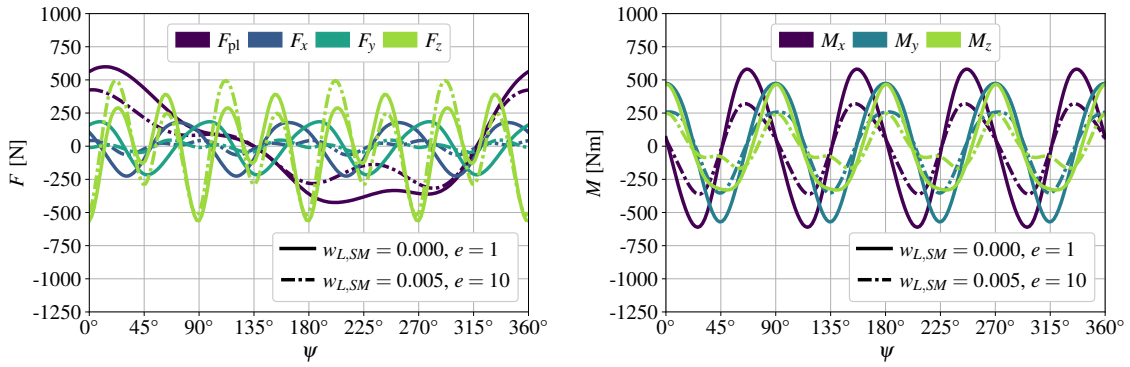

(a) Pitch-link and hub forces

(b) Hub moments

Figure 3.18: Rotor hub loads and pitch-link loads over the rotor azimuth (after mean subtraction) based on different weighting factors (w) and exponents (e). Multi-harmonic 1P+2P camber control, $\mu = 0.3$. Control inputs as described in Fig. 3.17b.

assessment of whether the stall margin is increasing or decreasing is assumed to be valid. As shown in Fig. 3.19c, the total lift capacity and, thus, the stall margin increased in most regions. However, the stall margin also deteriorated in some regions, especially far inboard and where the lift increased due to the active-camber-induced redistribution.

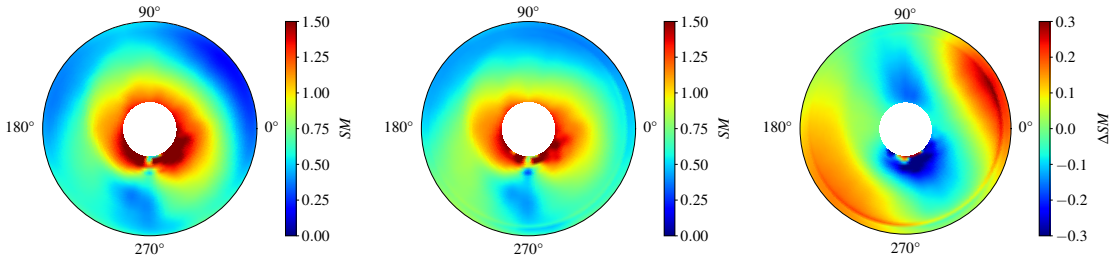

(a) Passive rotor

(b) Active rotor

(c) Δ(active − passive)

Figure 3.19: Effect of multi-harmonic 1P+2P active camber morphing on the stall margin ($SM = C_{l,\max} - C_l$) at $\mu = 0.3$ using $w_{L,SM} = 0.005$, $e = 10$. $\Delta SM = SM_a - SM_p$.

In the following, the focus was on the retreating-blade stall, as it was expected to be more relevant, especially with increasing airspeed [96]. The concept of stall margin calculation was assumed to be fully applicable in this flow regime (low to medium Mach numbers). As already shown, the use of active camber did not provide a clear advantage in the stall margin to the region around $\psi = 270°$. A more detailed description of the stall margin situation at $\psi = 270°$ can be found in Fig. 3.20, especially in Figs. 3.20a and 3.20b, which compare the difference of the local $C_{l,\max}$ and the local C_l for the passive and the active rotor. The effect of camber morphing on the stall margin is double-edged: On the one hand, the lift capacity increases with the camber deflection (higher $C_{l,\max}$). On the other hand, the actual lift also increases, which again reduces the stall margin. As a result, the stall margin was similar between the active and passive rotor (see Fig. 3.20). Only further out on the blade, but within the active-camber section, did the stall margin increase mod-

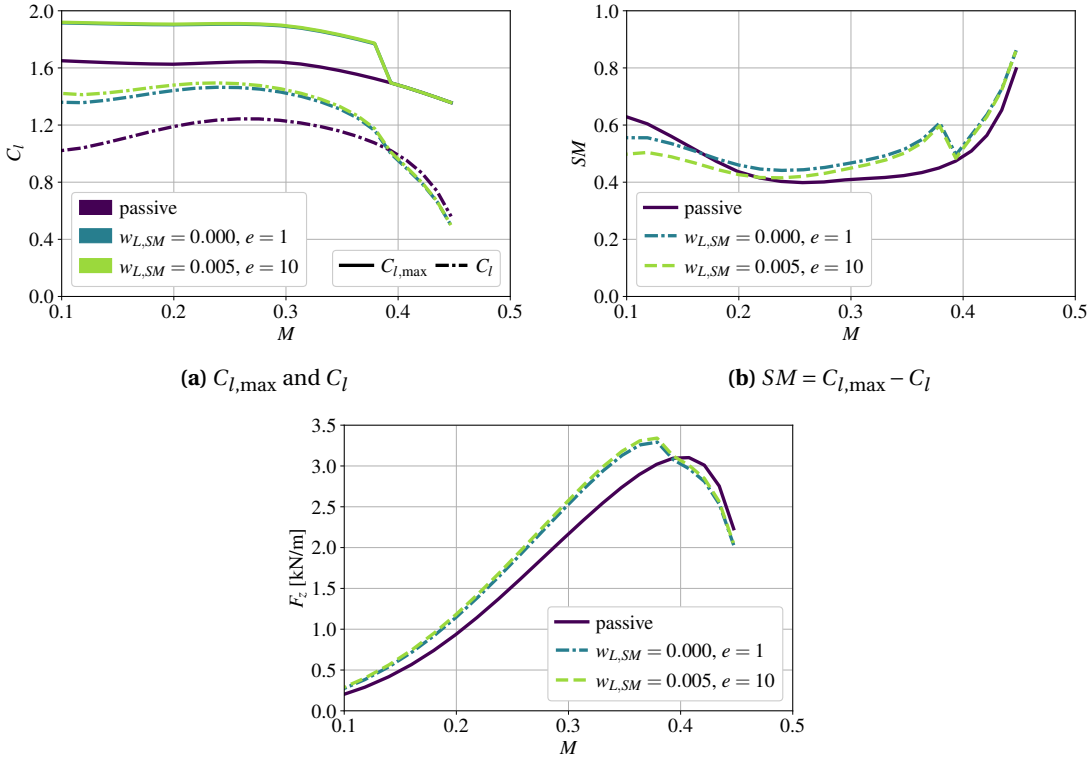

(a) $C_{l,\max}$ and C_l

(b) $SM = C_{l,\max} - C_l$

(c) F_z at $\psi = 270°$

Figure 3.20: Retreating-blade stall margin and lift generation ($\psi = 270°$) at $\mu = 0.3$ using multi-harmonic 1P+2P active camber morphing ($w_{L,SM} = 0.005$, $e = 10$).

erately. Therefore, as shown in Fig. 3.20c, the increase in stall margin covered the most relevant range in terms of lift generation. Accordingly, the effect on stall margin was considered positive for this camber morphing deployment. Another interesting aspect can be seen when comparing the stall margin for cases with $w_{L,SM} = 0$ and $w_{L,SM} = 0.005$. When the stall margin was not part of the objective function, the values of $C_{l,\max} - C_l$ were slightly higher than in the case of $w_{L,SM} = 0.005$. This can be explained by the fact that reducing the rotor loads and increasing the stall margin are competing goals. Since the stall margin was already moderately higher than the reference value from the passive baseline rotor, the optimizer accepted a slight degradation in favor of the rotor loads.

3.1.4 Radial Size and Placement of the Active-Camber Section

So far, all results have been calculated with a large active-camber section covering almost the full range of the blade span, i.e., from the blade root ($r = 0.22$) to $r = 0.9$. A re-evaluation of this decision is presented below, but still under the premise of not exceeding the maximum radial station of $r = 0.9$. Two different scenarios were investigated with respect to the size and placement of the active-camber section. First, a variation of the inner radial station was analyzed while keeping the

outer radial station constant at $r = 0.9$. Second, the size of the section was kept at a comparatively small value of $s = 0.2$ while the radial station was varied with a focus on the aerodynamically most relevant region. Furthermore, both scenarios were investigated for the previously introduced optimization objectives, i.e., rotor power optimization only and rotor power optimization including quasi-constraints for rotor loads and stall margin ($w_{L,SM} = 0.005$ and $e = 10$).

The results are shown in Fig. 3.21. For visualization purposes, both variations were specified in terms of the radial position of the inner edge of the active-camber section. Regardless of the optimization objective, the large section ranging from $r = 0.22$ to $r = 0.9$ yielded the greatest amount of power savings. However, relative to the additional size, e.g., compared to a configuration starting at $r = 0.5$, the added power gain was disproportionately small. Hence, from a manufacturing and operational perspective, a smaller section size may be more appropriate. However, under the current constraints and objectives, the previous decision to use the large active-camber section ($r = 0.22$ to $r = 0.9$) was confirmed to result in the greatest power gains and was therefore retained as the baseline setting in the following work. Furthermore, it is assumed that there is a good transferability of the results to an active-camber section ranging from $r = 0.5$ to $r = 0.9$. This also includes the required actuation inputs, as shown below.

As the size of the active-camber section was further reduced to $s = 0.2$, the amount of performance gain continued to decrease. However, this smaller size was useful to evaluate the effect of varying the radial position and to identify the most relevant range to apply this technique. For both optimization objectives (single or multi-objective optimization), the most important radial station was in the range of $r = 0.7$ to $r = 0.75$ with respect to the center of the active-camber segment. When optimizing for rotor power only, a further outboard radial station was similarly effective. Otherwise, a far-outboard placement became less attractive.

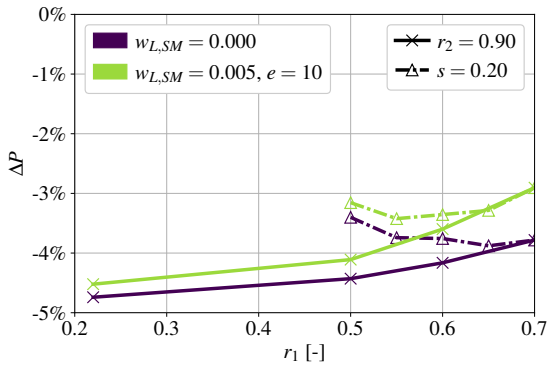

Figure 3.21: Effect of varying the active-camber section placement and size on rotor performance improvements using 1P+2P control ($\mu = 0.3$, $e = 10$). $\Delta P = \frac{P_a - P_p}{P_p}$.

In terms of control inputs (see Fig. 3.22), moving the inner boundary of the active-camber section had no relevant effect. However, changing the radial station of the small section ($s = 0.2$) required a large adjustment of the peak deflection on the retreating side. Thus, the actuation amplitude was dominated by the location of the outer boundary of the active-camber segment. On

the advancing side, the differences in control inputs were still small. Another aspect that follows directly from this result is the potential benefit of varying the control amplitude along the span of the blade. This will be discussed in the next section.

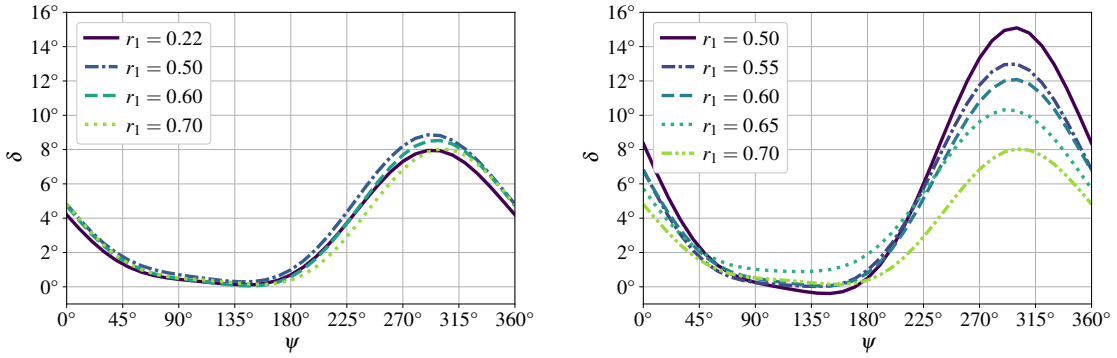

(a) Variation of size s ($r_2 = 0.90$)

(b) Variation of placement r ($s = 0.20$)

Figure 3.22: Relationship between optimum camber control signals and size and placement of the active-camber section based on 1P+2P actuation ($\mu = 0.3$, $w_{L,SM} = 0.005$, $e = 10$).

Interim conclusions:

Based on a computational study, active camber was investigated for its potential to improve rotor performance. In high-speed flight ($\mu = 0.3$), a reduction in main rotor power of almost 5% was obtained compared to the baseline rotor power. The active camber morphing initiated a complex response of the entire aeroelastic system, including blade deformations, primary control adjustments, and induced velocity variations. Essentially, the power savings from active camber were achieved by precisely influencing the aerodynamic load distribution over the rotor disk. This resulted in a redistribution of thrust to regions where it generated less torque about the axis of rotation. This was the case in regions of low induced velocity (minimal lift-induced drag) and low dynamic pressure (more efficient operation in terms of lift-to-drag ratio), further inward on the rotor blade (smaller lever arm), and in regions of negative thrust. Finally, with active camber, it was possible to slightly improve the local efficiency by better adapting the airfoil to the specific flow regime. Thus, by redistributing the thrust to the lateral sides of the rotor disk and relieving the tip regions of the blade, the rotor performance was improved by about 5% at an advance ratio of $\mu = 0.3$.

With active camber, it is possible and necessary to optimize for multiple objectives, i.e. including rotor loads and stall margin in the cost function. Ignoring the effect of active camber on loads resulted in significant load penalties. On the other hand, only a small amount of power savings had to be sacrificed in order not to exceed the loads and stall margin of the baseline rotor. A multi-harmonic control consisting of a mean camber deflection combined with 1/rev and 2/rev (1P+2P) signals provided enough flexibility to sufficiently approximate the optimum with respect to the predefined optimization goals, i.e., represented by the objective function. In high-speed forward flight ($\mu = 0.3$), a large active-camber section ($r_1 = 0.22$ to $r_2 = 0.9$) was only slightly more efficient than a medium-sized active-camber section from $r_1 = 0.5$ to $r_2 = 0.9$.

3.2 Spanwise Varying Camber Morphing at Different Flight Speeds

This section presents an investigation of active camber actuation under varying airspeed, with a particular focus on spanwise varying active camber morphing. As shown in Section 3.1.4, the optimal actuation inputs varied as a function of the radial placement of the active-camber segment. This suggests that individual adjustments of the control inputs along the blade span could be used to further improve the performance gains from active camber. Furthermore, this approach is potentially attractive from an implementation and operational point of view. This is due to the increased difficulty of providing high actuation amplitudes in regimes of high centrifugal and aerodynamic loads. In addition, the strength of the vortex at the outer edge of the active-camber section could be reduced, which could be beneficial in terms of vibration and noise. Last but not least, limiting the magnitude of the outboard camber deflection potentially increases the safety of such systems by reducing the risk of generating unacceptably high loads, e.g., caused by a faulty control deployment. In the first part, the concept of varying the camber morphing along the blade span is discussed for the same representative high-speed flight condition as in the previous section ($\mu = 0.3$). Subsequently, spanwise uniform and spanwise varying camber control are analyzed in a comparative study for a range of flight speeds.

According to Eqs. 2.5 and 2.7 in Section 2.1.4, the spanwise varying camber actuation was modeled with two additional degrees of freedom. The variable ϑ specifies the amount of linear variation over the rotor radius. The variable δ_{ref} defines the reference camber deflection used to define the amount of spanwise variation specified by ϑ. This allowed an inverse behavior of the spanwise variation of camber morphing on the retreating and advancing side of the rotor.

For each combination of ϑ and δ_{ref}, a separate airfoil table had to be generated. In addition, the two additional degrees of freedom significantly increased the optimization effort and the number of computations required. For the sake of computational resources, all subsequent results were based on values for ϑ ranging from 0% (spanwise uniform camber control) to 100% (static camber deflection at the outer edge, twice the mid-span amplitude at the inner edge) in 20% steps. For δ_{ref}, values between 0° and 3° were examined with a step size of 1°. This was considered sufficient to cover the relevant trends. According to the previous section, active camber was applied between $r_1 = 0.22$ and $r_2 = 0.9$ unless otherwise noted, and a 1P+2P multi-harmonic control was used. The optimization was based on the multi-objective cost function with $w_{L,SM} = 0.005$ and $e = 10$.

3.2.1 High-Speed Flight

Figure 3.23 shows the effect of applying spanwise varying camber actuation on rotor power gains ($\mu = 0.3$). A value of $\vartheta = 0$ represents the previously used spanwise uniform camber actuation. When using $\delta_{\text{ref}} = 0$, the additional power gain over spanwise uniform active camber actuation was marginal. However, by introducing a value of $\delta_{\text{ref}} > 0$, the rotor efficiency further increased.

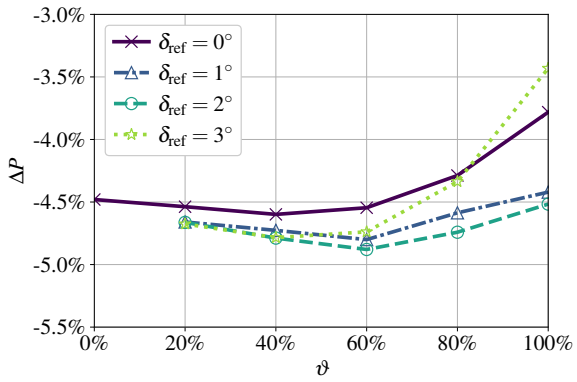

Figure 3.23: Effect of varying the camber deflection along the rotor blade (expressed by ϑ and δ_{ref}) on the high-speed rotor efficiency ($\mu = 0.3$, $w_{L,SM} = 0.005$, $e = 10$, 1P+2P control). $\Delta P = \frac{P_a - P_p}{P_p}$.

Optimal values for ϑ were in the range of 60%. In terms of δ_{ref}, a value of 2° resulted in the highest power gains (about $\Delta P = 0.3\%$).

To analyze the concept of using a non-zero δ_{ref}, Fig. 3.24 shows the azimuth control inputs for a case with $\vartheta = 60\%$ and $\delta_{\text{ref}} = 2°$, and for a case with the same ϑ but $\delta_{\text{ref}} = 0°$. Also shown is the optimal spanwise uniform camber control (dotted line). The main difference between 3.24a and 3.24b was the inverse amplification of the camber deflection between the advancing and retreating side, which only existed for $\delta_{\text{ref}} = 2°$. This was due to the fact that the mid-span camber deflection did not pass a value of $\delta = 0°$, but a value of $\delta = 2°$. Correspondingly, with $\delta_{\text{ref}} = 2°$, the inward amplitude was greater than the outward amplitude only on the retreating side. On the advancing side, slightly positive camber deflections were applied near the blade tip, and slightly negative camber deflections near the blade root. Overall, when considering the analogy between rotor blade twist and spanwise variable camber deflection, this actuation deployment ($\vartheta = 60\%$ and $\delta_{\text{ref}} = 2°$) is comparable to a quasi-untwisting of the blade on the advancing side and a quasi-twisting of the blade on the retreating side.

In terms of actuation amplitudes, both cases resulted in a notable reduction in camber deflection amplitudes near the blade tip. At the outer limit of the active-camber section ($r = 0.9$), the original peak-to-peak amplitude of about 8° (spanwise uniform actuation) was approximately halved. On the other hand, large camber actuation amplitudes were applied close to the blade root. Note that the largest amount of camber deflection occurred in and near the reverse flow region. This was due to the simplification of assuming a linear gradient of camber deflection along the blade span. Thus, the amplitudes far inboard were a result of the demands coming from further outboard radial stations where high aerodynamic forces were experienced. Instead, inboard of $r = 0.5$ on the retreating side, a further increase in the actuation amplitude was assumed to be irrelevant. Therefore, limiting the camber deflection to the maximum value at the center of the active-camber section (δ_c) seems to be a reasonable approach. On the advancing side, also blade regions far inboard operated in an aerodynamically relevant regime. Thus, for this ψ range, it was considered relevant not to deviate from the described actuation deployment.

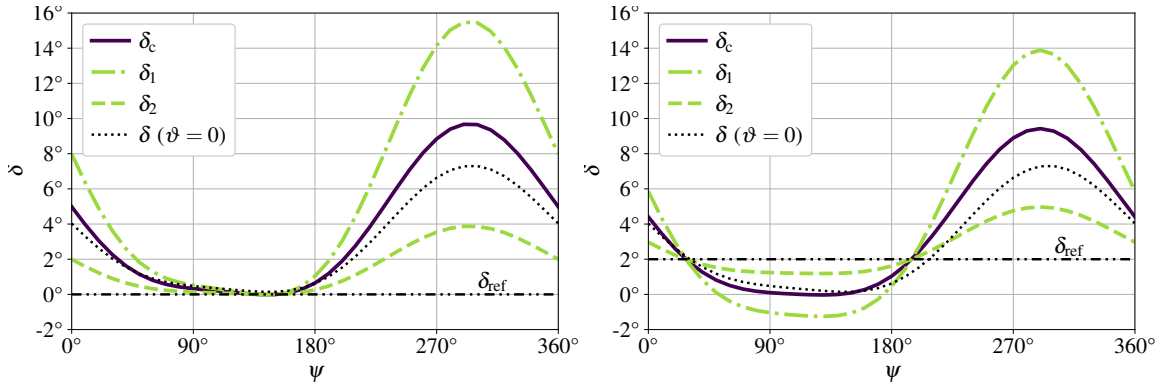

(a) $\delta_{\text{ref}} = 0°$ **(b)** $\delta_{\text{ref}} = 2°$

Figure 3.24: Optimal 1P+2P active-camber control inputs with $\vartheta = 60\%$ using different values of δ_{ref} ($\mu = 0.3$, $w_{L,SM} = 0.005$, $e = 10$).

From an aerodynamic perspective, a comparison of the previously discussed cases (see Fig. 3.24) is shown in Fig. 3.25. The effect of the spanwise variability of the camber morphing is isolated in this figure by subtracting the solution of the optimal spanwise uniform actuation. With $\vartheta = 60\%$ and $\delta_{\text{ref}} = 0°$ (see Figs. 3.25b and 3.25a), it was observed that additional performance gains from varying the camber control along the span came from drag reduction in the outer region on the retreating side. High camber deflections resulted in notable drag values as the Mach number increased toward the blade tip. By reducing the camber morphing in this area, the drag was significantly reduced. However, this was accompanied by a magnitude reduction in the (negative) aerodynamic moment (see Fig. 3.25b), especially in the rear part of the rotor disk. This reduced the amount of induced elastic twisting and, thus, the unloading of the rear part of the rotor disk near the blade tip. Therefore, a power penalty was introduced near the blade tip, which almost eliminated the gains generated on the retreating side.

By using a $\delta_{\text{ref}} > 0$ (see Figs. 3.25d and 3.25c), the magnitude of the (negative) aerodynamic moment in the fore and aft regions of the rotor disk was quite similar to that observed with spanwise uniform actuation. Therefore, the unloading of the blade tip in the rear part of the rotor disk was maintained, while the drag on the retreating side (mainly in the fourth quadrant) was reduced. Overall, this resulted in a net performance gain.

On the advancing side, the positive pitching moments inboard and the negative pitching moments outboard largely compensated each other, ensuring that no negative thrust was introduced by this control scheme. Note that the inner region on the retreating side is not involved in this phenomenon. This confirms the assumption that the high camber deflections in this region are not necessary. With respect to the stall margin, the effect of varying the camber deflection along the blade span was quite negligible (see Fig. 3.26).

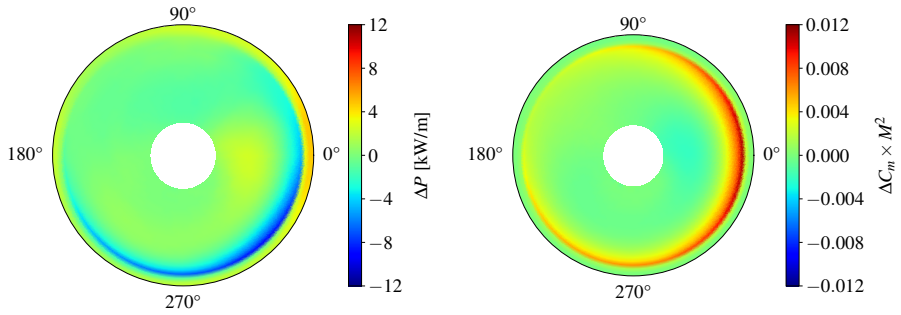

(a) $\delta_{\text{ref}} = 0°$ **(b)** $\delta_{\text{ref}} = 0°$

(c) $\delta_{\text{ref}} = 2°$ **(d)** $\delta_{\text{ref}} = 2°$

Figure 3.25: Difference in rotor power and aerodynamic moment between spanwise varying actuation (ϑ = 60%) and spanwise uniform (ϑ = 0%) actuation at $\mu = 0.3$ (1P+2P control). $\Delta() = ()_{\vartheta=60\%,a} - ()_{\vartheta=0\%,a}$.

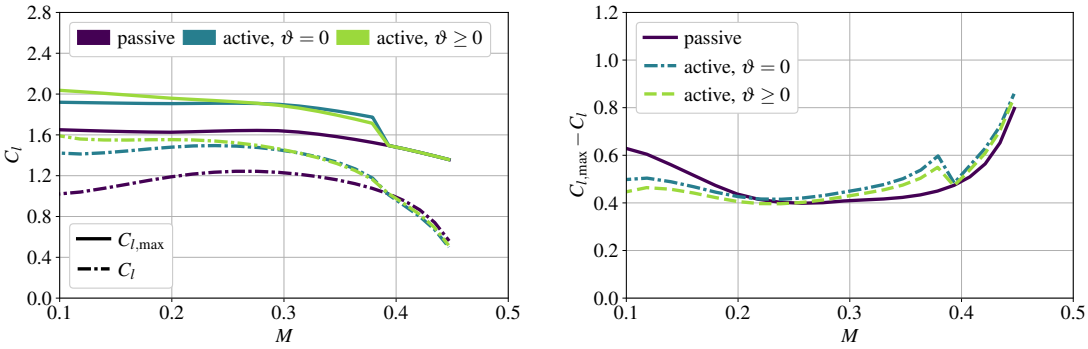

(a) $C_{l,max}$ and C_l **(b)** $C_{l,max} - C_l$

Figure 3.26: Lift coefficient (C_l) and stall margin ($C_{l,\max}$) of the passive rotor, active rotor (1P+2P control) with spanwise uniform actuation (ϑ = 0), and active rotor with spanwise varying actuation ($\vartheta = 60\%$, $\delta_{\text{ref}} = 2°$) at $\mu = 0.3$.

3.2.2 Variation of the Flight Speed

In the previous parts of the work, active camber has been used to improve performance in a specific high-speed flight condition. Another interesting scenario, however, is to use active camber

to better adapt the rotor to different flight conditions, such as different advance ratios μ. This approach is promising because rotor design must be focused on high-speed flight, e.g., to avoid excessive loads, to provide sufficient lift on the retreating side, and to reduce negative thrust on the advancing side. As a result, helicopter rotors are generally not well optimized for low advance ratios, leaving potential for active mechanisms to improve efficiency at low speed. This aspect is also confirmed by Fig. 3.27, which shows the effect on the rotor power when the camber deflection is varied in a quasi-static manner. As expected, this "configuration change" type of camber morphing was able to improve rotor performance in hover and low-speed flight, but not in high-speed flight. That is, the baseline Bo 105 blade airfoil appears to be optimized for high-speed flight, and this approach to improve the efficiency with static camber morphing was not successful for $\mu > 0.25$. Overall, although not efficient for high-speed flight, this quasi-static morphing concept could be a viable starting point for implementing active camber on a real helicopter rotor due to its reduced complexity.

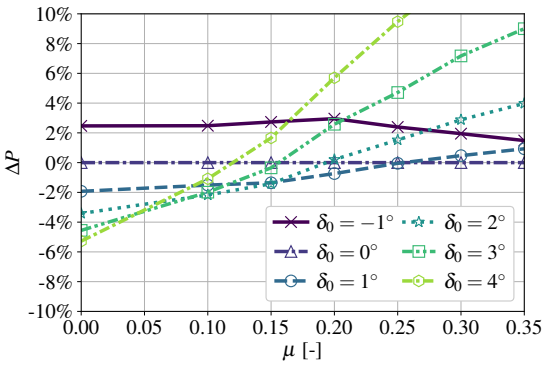

Figure 3.27: Effect of using different amounts of static camber deflection on rotor power over a range of flight speeds. $\Delta P = \frac{P_a - P_p}{P_p}$.

In the following, rotor power savings as a function of the advance ratio are compared for different types of active camber control. This includes the static morphing just discussed, but also a multi-harmonic 1P+2P control, as well as a comparison between spanwise uniform and spanwise varying actuation. The multi-harmonic control was again determined using the previously described multi-objective optimization approach with $w_{L,SM} = 0.005$ and $e = 10$. Furthermore, an adaptation of the cost function to the advance ratio was applied as explained in Section 2.3.2 and Eq. 2.15. In the case of static (0P) camber morphing, it was optimized only for rotor power reduction. This was because there was only one degree of freedom in the input signal, which is insufficient to consider multiple objectives. However, as discussed above, this concept was irrelevant in the high advance ratio regime, which is the most relevant in terms of oscillatory loads. Another exception for static (0P) deflection had to be defined with respect to the spanwise variation of camber deflection. Due to the lack of azimuthal variability, the concept of introducing a non-zero reference δ_{ref} was not only obsolete but also caused redundancy in the exact definition of the control inputs. Therefore, it has been abandoned to use values of $\delta_{\text{ref}} \neq 0$ in this particular case.

As already seen in Fig. 3.27, static camber deflection was quite effective in hovering flight (see Fig. 3.28a). By allowing azimuthal variation of the camber deflection in the form of harmonic or multi-harmonic actuation, it was not possible to further improve the hovering rotor efficiency. However, a further improvement was obtained by varying the camber deflection along the span, e.g., an improvement from about $\Delta P = 5.3\%$ (spanwise uniform) to $\Delta P = 5.9\%$ (spanwise varying). In forward flight, the multi-harmonic (1P+2P) control gave advantages over the static camber deflection. This difference became more important with increasing flight speed. On the other hand, the benefit of varying the camber deflection over the blade span became less significant in terms of power savings towards high-speed flight. Overall, the most power savings were achieved in high-speed flight ($\Delta P = 8\%$ at $\mu = 0.35$), followed by hovering flight ($\Delta P = 5.9\%$ at $\mu = 0$). Since these were the flight regimes with the highest power requirements (see 2.16), it is assumed that these power savings have a direct impact on the maximum engine power to be installed. Note that if the speed range to be covered is reduced and the helicopter is designed accordingly, the design point may shift to a lower advance ratio. This would reduce the performance gains associated with active camber both at (the lower) maximum speed and in hover. On the other hand, it becomes more promising as the advance ratio range (in terms of edgewise flight) of the rotorcraft continues to increase.

Details of the underlying control inputs (1P+2P) are shown in Figs. 3.28b to 3.28d. An almost linear relationship was found between the advance ratio and the optimal amplitudes. The mean deflection was high in hover, decreased at moderate forward speed, and increased again at high speeds to keep the amount of camber deflection on the advancing side under control. The spanwise variability as a function of advance ratio is shown in Figs. 3.28c and 3.28d. The variable ϑ was almost constant over the whole range of advance ratios. Only at hover and high speed ($\mu = 0.35$) was a decrease in spanwise variability more beneficial. At high speed, this was due to the reduction of the dynamic pressure far outboard on the retreating side. Correspondingly, less drag was generated at high camber deflections, resulting in less need for reducing camber deflections. The introduction of a positive value for δ_{ref} was only relevant as the forward speed and azimuthal variability of the rotor aerodynamics increased. The discretization of ϑ and δ_{ref} was suboptimal for this study but was still considered appropriate given its contribution to the overall power savings.

Figure 3.29 shows the control inputs along the rotor azimuth for a selected set of different cases. In Fig. 3.29a, the optimal control inputs of spanwise uniform actuation are compared for advance ratios from $\mu = 0.1$ to $\mu = 0.35$. The previously observed increase in amplitude at higher flight speeds was mostly attributed to higher camber deflections on the retreating side. On the advancing side (especially between $\psi = 45°$ and $\psi = 200°$), the camber deflection converged to a specific control scheme with values around zero deflection. As a result, the peak on the retreating side became narrower at higher flight speeds. The Figs. 3.29b to 3.29d describe the camber deflection when using spanwise varying control. They show the transition from the point ($\mu = 0.1$) where the magnitude of the camber deflection consistently (for all ψ) decreased towards the blade tip, to the point ($\mu = 0.2$) where the opposite trend was observed on the advancing side ($\psi = 0°$ to $180°$).

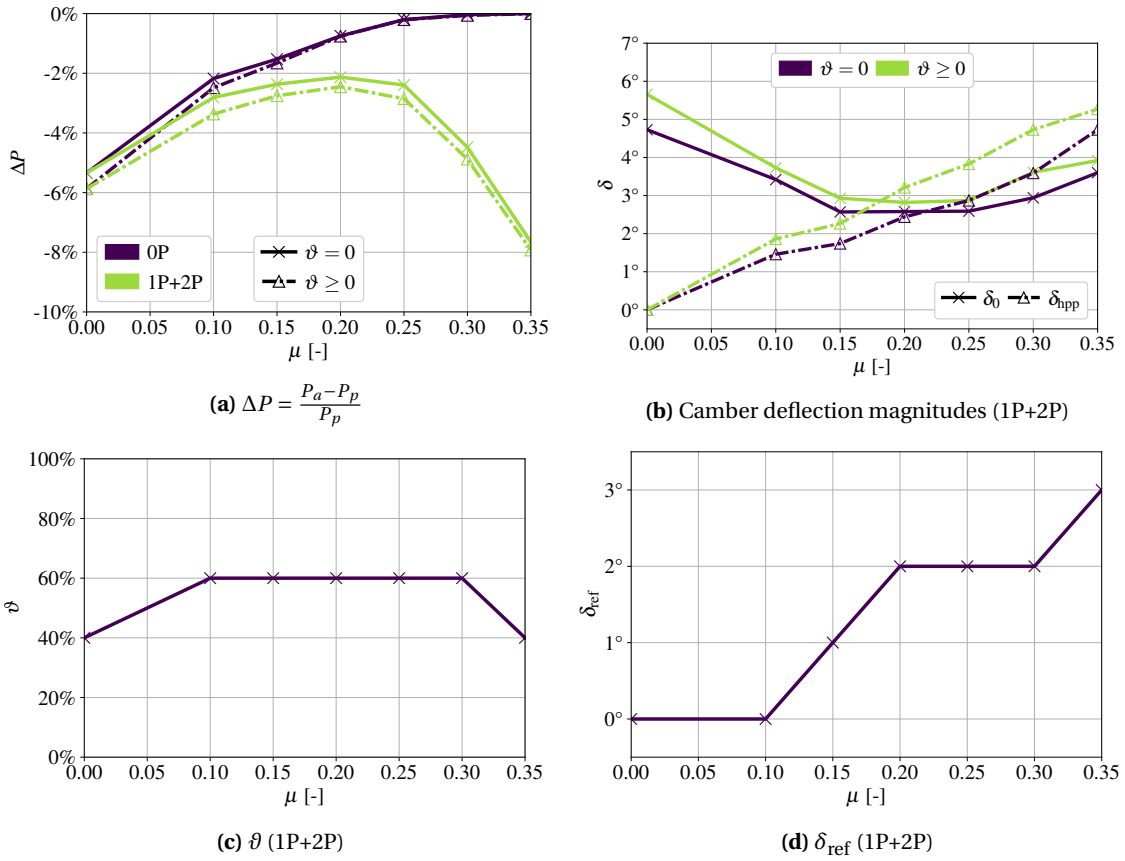

(a) $\Delta P = \frac{P_a - P_p}{P_p}$

(b) Camber deflection magnitudes (1P+2P)

(c) ϑ (1P+2P)

(d) δ_{ref} (1P+2P)

Figure 3.28: Rotor power savings as a function of advance ratio μ. Comparison of static vs. multi-harmonic and spanwise uniform vs. spanwise varying camber control ($w_{L,SM} = 0$ for static camber deflection, $w_{L,SM} = 0.005$, $e = 10$ for multi-harmonic 1P+2P camber control). (b) – (d) Details of the underlying control inputs (multi-harmonic actuation).

Aerodynamics Analysis:
In the following, the dependence of active-camber-related performance gains on the advance ratio is discussed from an aerodynamic point of view. The focus was on the two most promising cases in terms of rotor power savings, i.e., hovering flight ($\mu = 0$) and high-speed flight ($\mu = 0.35$). In addition, the case with the lowest power gain, $\mu = 0.2$, was further examined. The hovering flight was of interest because of its distinctly different aeromechanical state compared to the previously analyzed high-speed flight scenario ($\mu = 0.30$). While the results for $\mu = 0.30$ and $\mu = 0.35$ are expected to be similar, the investigation at $\mu = 0.35$ was aimed at better understanding the relatively steep gradient of performance improvement in this high-speed range (see Fig. 3.28a).

Since the aerodynamics of the hovering rotor can be considered axisymmetric, only one azimuth station, i.e., $\psi = 0°$, was evaluated in Fig. 3.30, which is representative for the entire azimuth range. Figure 3.30a shows the redistribution of thrust along the blade span. In the case of the passive rotor, the blade tip region was heavily loaded. By using (static) active camber morphing, the peak thrust was significantly mitigated and distributed to more inboard radial stations. This resulted in a reduction of the profile drag far outboard and thus a reduction of the rotor profile

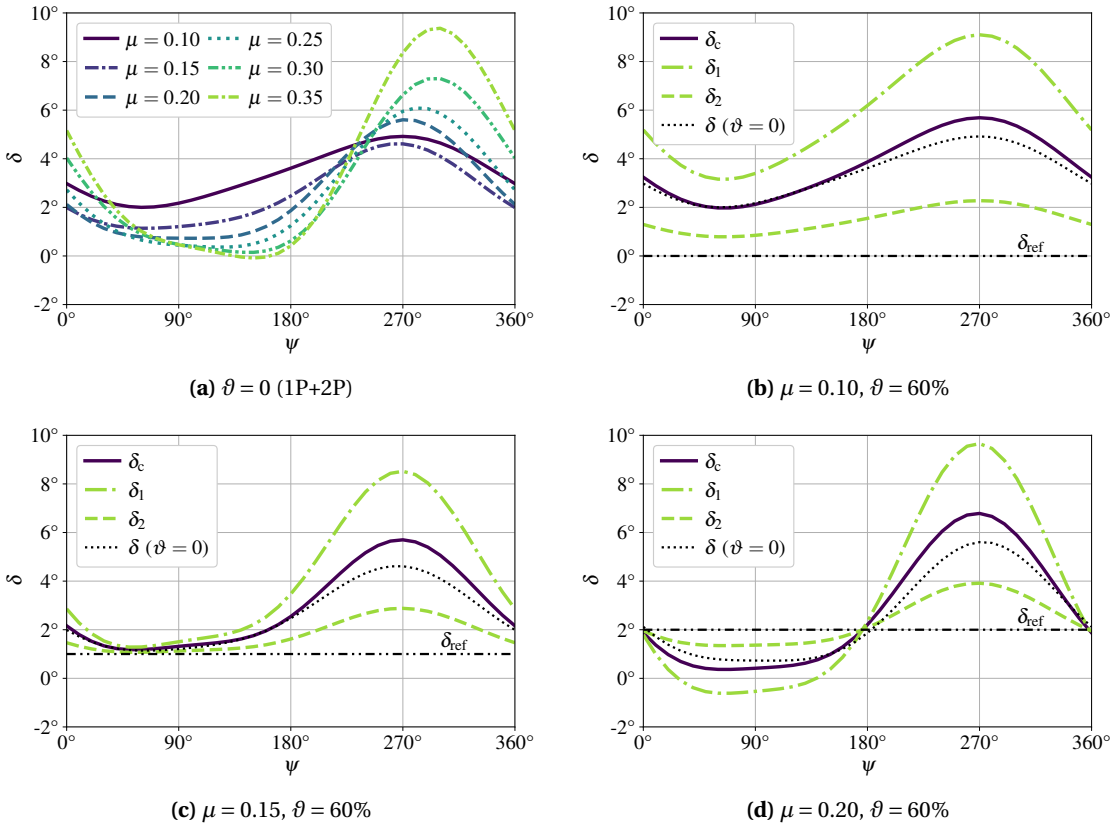

(a) $\vartheta = 0$ (1P+2P)

(b) $\mu = 0.10$, $\vartheta = 60\%$

(c) $\mu = 0.15$, $\vartheta = 60\%$

(d) $\mu = 0.20$, $\vartheta = 60\%$

Figure 3.29: Camber deflection over one rotor revolution (1P+2P). (a) Spanwise uniform actuation for different advance ratios. (b) – (d) Spanwise varying actuation vs. spanwise uniform actuation for specific advance ratios.

power. However, due to the high induced velocity in hovering flight, the more important power savings were achieved with respect to lift-induced drag (as explained by Eq. 3.7). This had a strong effect on rotor performance, especially due to the large lever arm. Thus, these performance gains far outweighed the modest performance penalty induced further inboard ($r < 0.75$) where thrust increased. This unloading of the blade tip also resulted in reduced tip vortex strength. Combined with the increased efficiency of the rotor, this reduced the induced velocity, especially in the outer region of the rotor blade. With spanwise varying actuation ($\vartheta > 0$), the thrust peak was slightly further attenuated.

When transitioning to forward flight, the active-camber-related performance gains decreased to a minimum at about $\mu = 0.2$. To further explain this, Fig. 3.31 shows the corresponding induced velocity for different flight speeds, and Fig. 3.32 shows the thrust and drag variation at $\mu = 0.2$. Due to the larger mass flow, the induced velocity decreases steadily with increasing flight speed. Therefore, the contribution of lift-induced drag to the rotor power was small at $\mu = 0.2$, and only moderate power gains were obtained by redistributing parts of the thrust further inward (see Fig. 3.32a). On the other hand, in the absence of transonic flow, the airfoil drag coefficients were still quite moderate at this flight speed. Correspondingly, the drag coefficients (see Fig. 3.32b) and the resulting profile power were only marginally reduced by relieving the blade tip region.

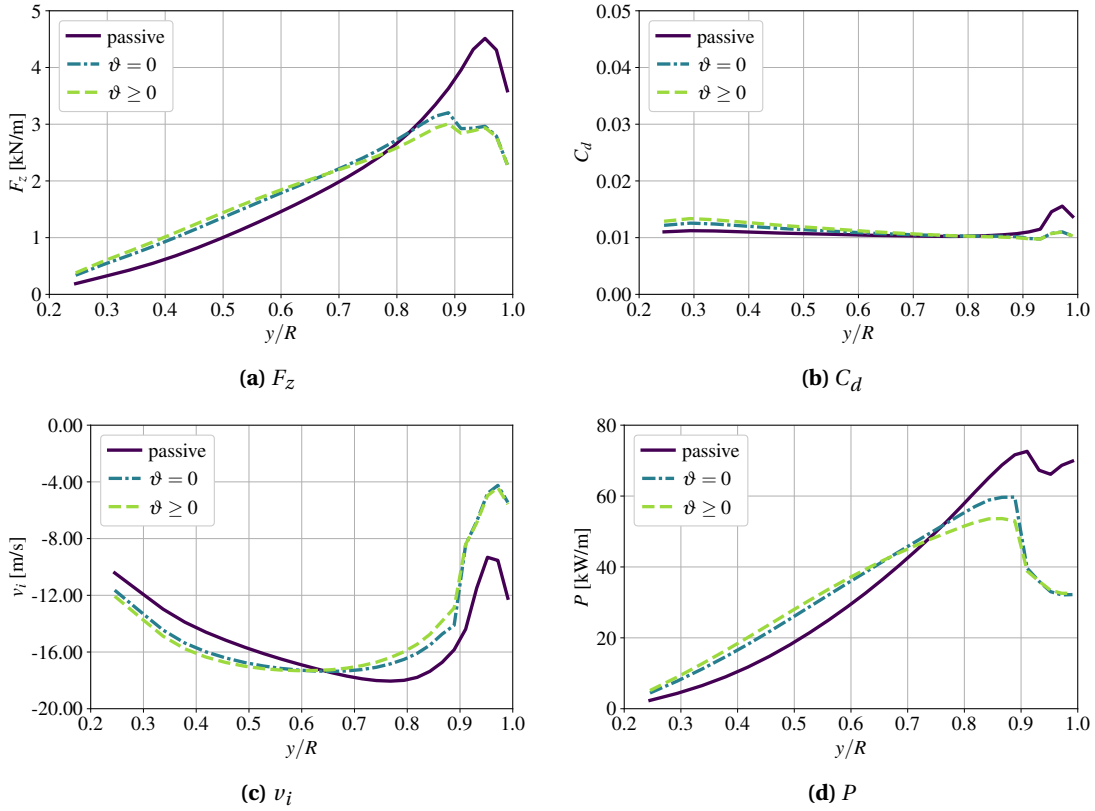

(a) F_z **(b)** C_d

(c) v_i **(d)** P

Figure 3.30: Hovering rotor aerodynamics ($\mu = 0$). Comparison of passive and active rotor, the latter with spanwise uniform (static) and spanwise varying (static) camber morphing.

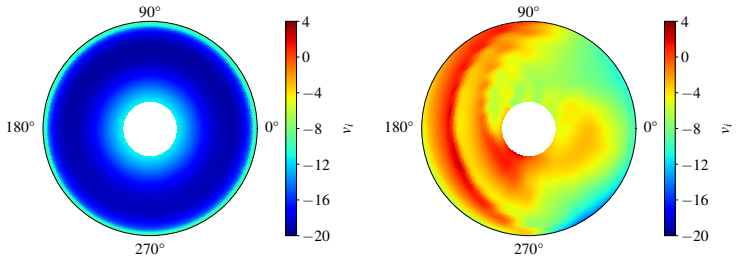

(a) $\mu = 0$ **(b)** $\mu = 0.2$

Figure 3.31: Comparison of the induced velocity v_i for different advance ratios (passive rotor).

As the flight speed continued to increase, the growing asymmetry and transonic effects revived the potential for performance gains with active camber. Comparing the thrust and power of the passive and active rotor at $\mu = 0.35$ in Fig. 3.33, the trends were the same as for $\mu = 0.3$ (see Section 3.1.2). However, the load accumulation in the fore and aft regions and the negative thrust on the advancing side were more pronounced. Since the negative thrust was similarly well compensated as for $\mu = 0.3$ and the load peaks were also well mitigated, greater power savings were achieved with the active-camber system.

While the stall margin was included in the objective function in forward flight, it was removed in

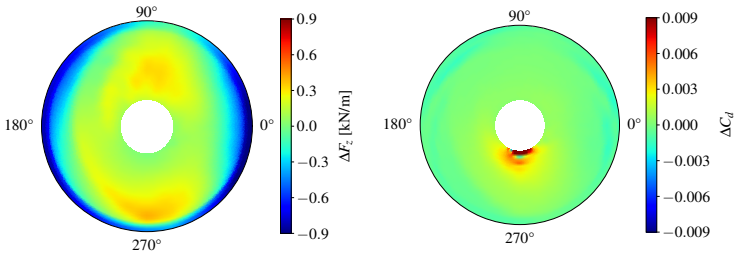

(a) $\Delta F_z = F_{z,a,\vartheta=0} - F_{z,p}$ **(b)** $\Delta C_d = C_{d,a,\vartheta=0} - C_{d,p}$

Figure 3.32: Difference in thrust and drag coefficient between passive and active ($\vartheta = 0$, 1P+2P) rotor at medium speed ($\mu = 0.2$).

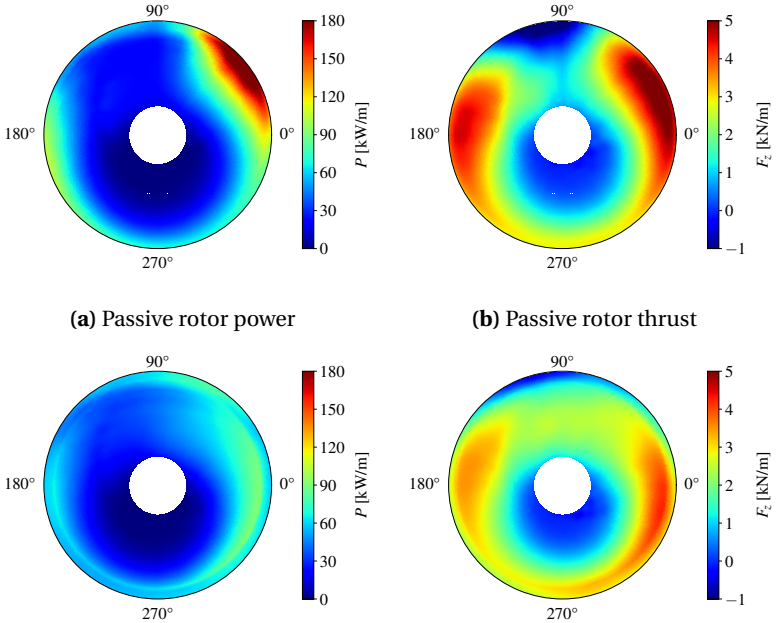

(a) Passive rotor power **(b)** Passive rotor thrust

(c) Active rotor power ($\vartheta = 40\%$) **(d)** Active rotor thrust ($\vartheta = 40\%$)

Figure 3.33: Power and thrust of the passive and the active rotor (1P+2P spanwise varying actuation at $\vartheta = 40\%$) in high-speed forward flight ($\mu = 0.35$).

hovering flight (see Eq. 2.15). Nevertheless, as shown in Fig. 3.34, it was significantly improved by increasing the airfoil camber in this flight condition ($\mu = 0$). Especially in the low stall margin region near the blade tip, most of the enhancements were achieved even though the camber deflection was only applied up to $r = 0.9$. This was because the collective pitch could be reduced as more lift was produced by increasing the airfoil camber. In addition, the elastic twist was increased due to the additional aerodynamic moment created by the camber deflection. Both resulted in a reduction of the pitch angle near the blade tip and thus lower lift coefficients. Thus, active camber morphing is considered particularly useful in hot and high conditions, where engines typically produce less power and rotor blades are more susceptible to stall (reduction of air density ρ). Both problems can be counteracted by using active camber.

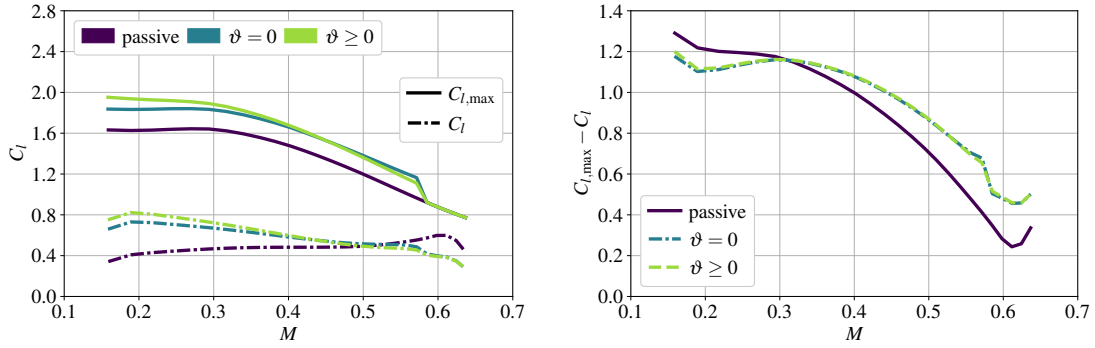

(a) $C_{l,\max}$ and C_l **(b)** SM

Figure 3.34: Lift coefficient (C_l), maximum lift coefficient ($C_{l,\max}$), and stall margin ($SM = C_{l,\max} - C_l$) of the passive rotor and the active rotor (1P+2P control) with spanwise uniform ($\vartheta = 0$) and spanwise varying actuation ($\vartheta = 40\%$) in hovering flight ($\mu = 0$).

Reevaluation of the active-camber section size:

A reduced scope re-evaluation of the required active-camber section size was performed in the context of spanwise varying actuation and different advance ratios from $\mu = 0$ to $\mu = 0.35$. Only a variation of the inboard radial limit was investigated, as it is assumed to leave more potential for reducing the camber section size without noticeably affecting the performance gain than a variation of the outboard limit. Consistent with previous results (Section 3.1.4), the inboard region of the active-camber section from $r = 0.22$ to $r = 0.5$ contributed little to the high-speed performance gains (see Fig. 3.35). Even when the spanwise varying control was applied, the importance of this inboard region of the blade did not increase significantly.

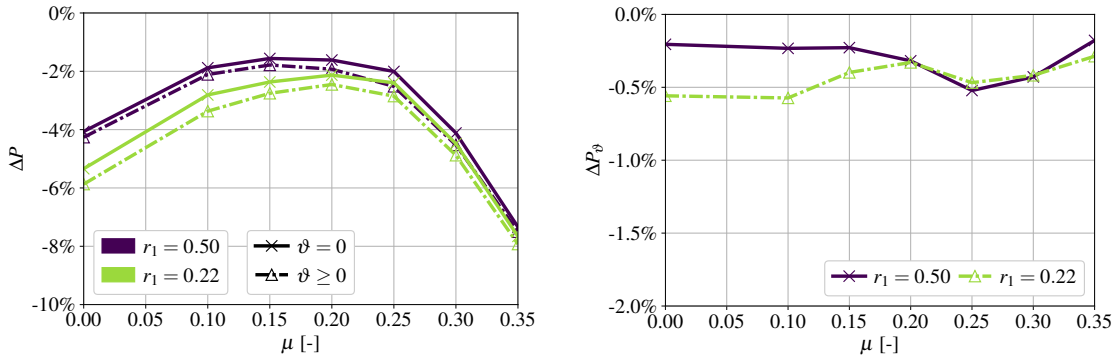

(a) $\Delta P = \frac{P_a - P_p}{P_p}$ **(b)** $\Delta P = \frac{P_{a,\vartheta>0} - P_{a,\vartheta=0}}{P_{a,\vartheta=0}}$

Figure 3.35: Rotor power savings as a function of the advance ratio μ ($w_{L,SM} = 0.005$, $e = 10$, 1P+2P control in forward flight). Comparison of spanwise uniform and spanwise varying camber control using different active-camber section sizes. (b) Relative performance gain achieved by varying the camber deflection along the radius.

Towards low flight speeds, this inboard region of the rotor disk became more important. In hovering flight, almost 2% of the total performance improvement was achieved in the range between $r = 0.22$ and $r = 0.5$ when using spanwise varying camber deflection. However, if only a small portion of a typical mission involves hovering, using active camber between $r = 0.5$ and $r = 0.9$

may be an appropriate approach. The nature of the spanwise variation of the camber deflection was largely independent of the position of the inner edge, as shown in Fig. 3.36.

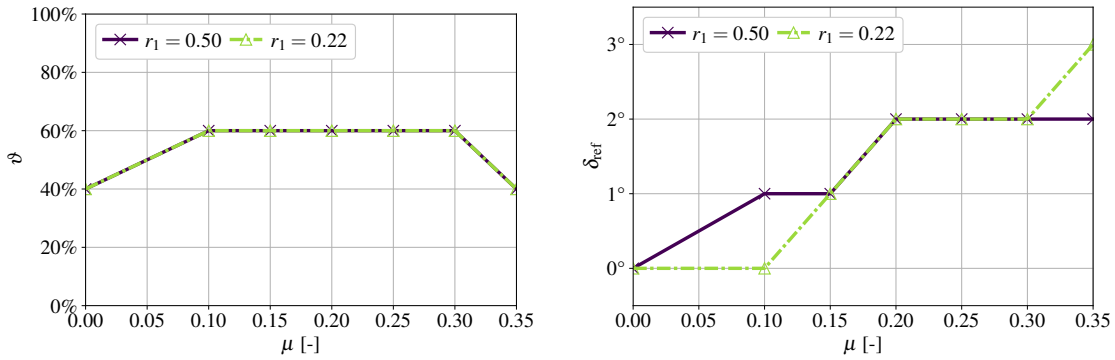

(a) ϑ **(b)** δ_{ref}

Figure 3.36: Details of the spanwise variation of camber morphing for cases shown in Fig. 3.35.

3.2.3 Control Amplitude Minimization at Outer Radial Stations

Varying the actuation amplitude across the span of the rotor blade was done to improve the efficiency of the rotor, but also to reduce the actuation amplitude in the outer region of the rotor blade. This was motivated by the fact that very high forces are obtained in this area of the rotor blade, and it is particularly challenging to design an active-camber mechanism that operates reliably under such conditions. Furthermore, safety considerations encouraged the investigation of this type of actuation, as the potential for generating excessive pitch-link loads increases towards the tip of the blade. Finally, the power required to operate the mechanism and the associated actuator dimensions are also influenced by this aspect. To continue this approach, a borderline case was analyzed (see Fig. 3.37), i.e., the use of spanwise varying control with zero amplitude at the outermost radial station (r_2) of the active-camber section. According to Eq. 2.7, this is the case for $\vartheta = 100\%$. Therefore, the outer actuator could be replaced by a fixed mounting.

Figure 3.37a shows a comparison between optimal spanwise uniform actuation and optimal spanwise varying actuation, first with $\vartheta \geq 0$ and $\delta_{\text{ref}} \geq 0$ (see Figs. 3.28c and 3.28d, respectively) and second with $\vartheta = 100\%$ and $\delta_{\text{ref}} = 2°$. For the latter case, the exact control inputs are shown in Fig. 3.37b for an advance ratio of $\mu = 0.3$. An initial "built-in" camber morphing of 2° was defined at the outer edge of the active-camber section, and the amplitude gradually increased towards the inner radial stations. Finally, this active-camber control mode required large amplitudes far inboard. However, as discussed earlier, the large camber deflections in the reverse flow regime on the retreating side were not considered necessary and could be assimilated with the mid-span camber deflections, δ_c.

With this type of camber morphing, the performance improvements were only slightly less than with the optimum spanwise varying actuation for most of the advance ratios examined. Only at

the highest speed of $\mu = 0.35$ were the differences more pronounced. Correspondingly, the case with $\vartheta = 100\%$ and $\delta_{\text{ref}} = 2°$ was always equal or better in terms of power savings than the case with spanwise uniform actuation, except for $\mu = 0.35$. Overall, for implementation reasons, it may make sense to minimize the actuation amplitude towards the outer edge of the active-camber section, as no major penalty in the ability to save rotor power is expected.

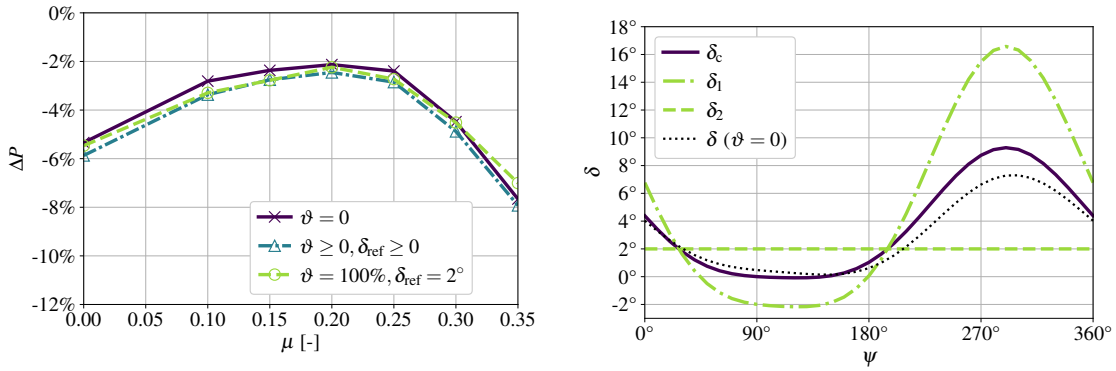

(a) $\Delta P = \frac{P_a - P_p}{P_p}$ **(b)** $\vartheta = 100\%$, $\delta_{\text{ref}} = 2°$, $\mu = 0.3$

Figure 3.37: Effect of minimizing the outer camber morphing amplitude on rotor power savings. Description of the corresponding actuation deployment.

Interim conclusions:
The ability of active camber to improve rotor performance increased towards high-speed flight (in terms of edgewise flight) and resulted in up to 8% power savings at $\mu = 0.35$. However, improving hover performance with static camber deflection is also a promising application (up to 5.9% power gains). At high speed, static camber deflection did not improve rotor efficiency, indicating that the airfoil was already optimized for this flight condition. Overall, the active-camber control scheme required significant adaptation as the advance ratio was varied. The inner range from $r = 0.22$ to $r = 0.5$ improved the power saving in hover, but almost not in high-speed flight. Spanwise varying camber morphing moderately enhanced the performance improvements compared to spanwise uniform control. However, the main advantage of this type of actuation is considered to be the significant reduction of the actuation amplitudes in the outer region of the rotor blade without sacrificing performance gains. A beneficial application of spanwise varying camber actuation required a reverse nature of spanwise camber morphing on the advancing and the retreating sides. The effect of camber morphing on the stall margin was less pronounced at high speeds. A clear benefit was observed in hovering flight, which could be particularly valuable in hot and high conditions.

3.3 Other Influences on Performance Gain Estimation

In this section, other aspects relevant to the evaluation of active-camber-related power savings have been analyzed. In addition to the variation of the flight speed (see previous section), other variations of the trim state are studied. These include variations of the thrust coefficient, the fuse-

lage drag, and the rotor hub moments. The purpose was to evaluate not only the effectiveness of active camber in different operational scenarios but also the generality of the results. This will allow a better assessment of whether this concept might be relevant for certain helicopters or mission tasks. It will also allow conclusions about the sensitivity of the results to the precise definition of the trim conditions derived from the flight test campaign [83]. Beyond operational aspects, the influence of modeling decisions is also addressed. Finally, performance improvements due to active camber are discussed from a more holistic point of view by considering secondary effects. This section is based on 1P+2P spanwise uniform camber morphing using the previously introduced multiple objective optimization approach ($w_{L,SM} = 0.005$, $e = 10$).

3.3.1 Influence of Other Operating Parameters

In addition to the previously studied correlation between active-camber-related power gains and flight speed, the influence of other operating conditions is further analyzed below. This includes a variation of the rotor thrust (e.g., different payload or turning flight with higher g-forces), a variation of the fuselage drag (e.g., due to an external load or equipment), and a variation of the air density (e.g., due to different flight altitudes or weather conditions). In addition, the influence of rotor hub moments was further investigated. From an operational point of view, this type of variation can be caused by a different helicopter center of gravity (CG), e.g., due to passenger placement or payload. Also, changes in the aerodynamic center of the fuselage (e.g. due to external equipment) can cause variations in the rotor pitch moment. The roll moment, on the other hand, also depends on the rotor power demand.

Variation of rotor thrust and air density:
Since rotor thrust and air density are related by the rotor thrust coefficient, C_T, this variable was used to improve comparability. C_T indicates the relationship between the actual rotor thrust and its potential to generate thrust. It is defined as

$$C_T = \frac{T}{\rho A(\Omega R)^2}. \tag{3.10}$$

Assuming a constant rotor geometry and rotational speed, only the rotor thrust (T) and the air density (ρ) remain as independent variables affecting C_T. Both increased takeoff weight and turning flight were assumed to have a negligible effect on the fuselage drag (D). Consequently, D remained constant as C_T was varied as a function of T. Furthermore, since D was small compared to the rotor lift (L), the variation of L was presumed to be equal to the variation of T. Details of the trim conditions studied are summarized in Table 3.1.

In terms of air density (ρ), the International Standard Atmosphere (ISA) conditions have usually been used in this work. However, ρ can vary due to changes in temperature, atmospheric pressure, or altitude. It was assumed that changes in ρ would not affect the required rotor lift. However, fuselage drag is linearly dependent on air density, so it was adjusted proportionally to

Table 3.1: Variation of C_T in terms of L.

Rotor thrust coefficient (C_T)	≈ 90%	≈ 110%
Rotor lift (L)	90%	110%
Fuselage drag (D)	100%	100%
Air density (ρ)	100%	100%

Table 3.2: Variation of C_T in terms of ρ.

Rotor thrust coefficient (C_T)	≈ 110%	≈ 90%
Rotor lift (L)	100%	100%
Fuselage drag (D)	91%	111%
Air density (ρ)	91%	111%

ρ. For the calculation of C_T, changes in fuselage drag were neglected. The variation of the flight state is summarized in Table 3.2.

The additional power required by increasing L was more pronounced in hover and low-speed flight than in high-speed flight (see Fig. 3.38). At the same time, the power gain from active camber also increased slightly, and vice versa in the case of decreasing C_T via L. A similar slope of the curves was obtained when ρ was used to vary C_T (see Fig. 3.39). However, compared to the lift variation, the curves representing different values of C_T were shifted closer together. This resulted in an inverse response of the rotor power to a variation of ρ in low-speed and high-speed flight. Increasing C_T by decreasing ρ resulted in higher hover power and lower high-speed power demand. Regardless of these differences, the effect on performance gains from active camber was largely the same for the two different approaches to varying C_T.

In essence, both an increase in takeoff weight and a higher altitude resulted in moderately enhanced performance gains from active camber. This means that in addition to improving efficiency, active camber has the potential to moderately expand the feasible flight envelope, particularly with respect to maximum takeoff weight and low-density flight conditions. A further reduction of ρ was also realistic, since the existing variation of 10% corresponded to an altitude difference of about 1000 m (assuming ISA conditions). In terms of control inputs (see Fig. 3.40), the variation of C_T moderately affected the required mean deflection, especially at low speeds. Amplitude differences were marginal.

Variation of the fuselage drag:
When changing the rotor drag variation, it was assumed that the rotor thrust was not affected and remained constant. Therefore, C_T was also assumed to be unaffected by the moderate 10% change in D studied. The effect on passive rotor power increased with airspeed (see Fig. 3.41). At $\mu = 0.3$, a 10% increase in helicopter drag resulted in an additional power requirement of about 5%. However, the relative power savings induced by active camber morphing were insignificantly

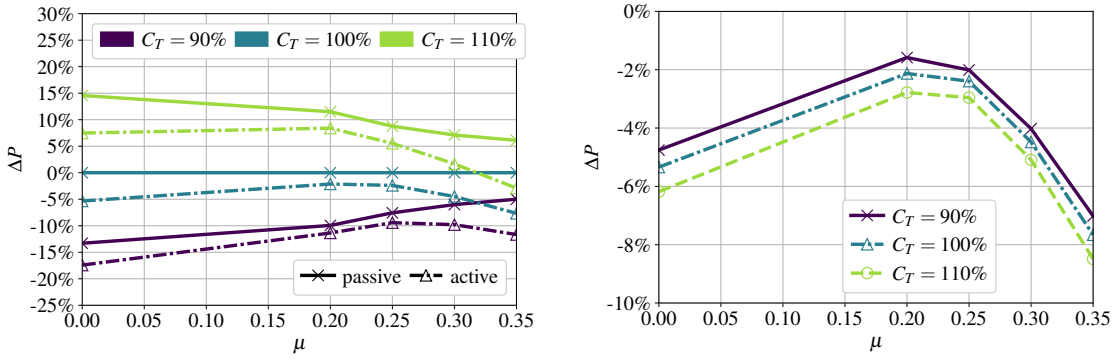

(a) $\Delta P = \frac{P_{C_{T,i}} - P_{p,C_T=100\%}}{P_{p,C_T=100\%}}$ **(b)** $\Delta P = \frac{P_{a,C_{T,i}} - P_{p,C_{T,i}}}{P_{p,C_{T,i}}}$

Figure 3.38: Effect of varying the rotor lift L on (a) the passive and active rotor power and (b) active-camber-related power gains. Variation of the trim condition according to Table 3.1.

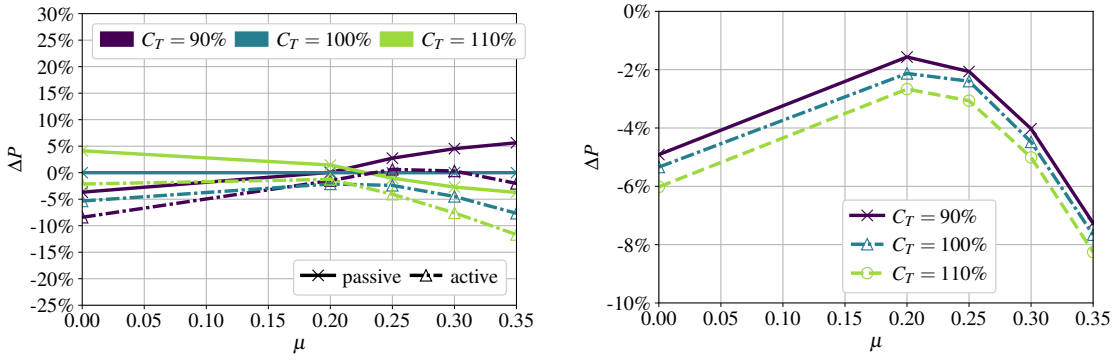

(a) $\Delta P = \frac{P_{C_{T,i}} - P_{p,C_T=100\%}}{P_{p,C_T=100\%}}$ **(b)** $\Delta P = \frac{P_{a,C_{T,i}} - P_{p,C_{T,i}}}{P_{p,C_{T,i}}}$

Figure 3.39: Effect of varying the air density ρ on (a) the passive and active rotor power and (b) active-camber-related power gains. Variation of the trim condition according to Table 3.2).

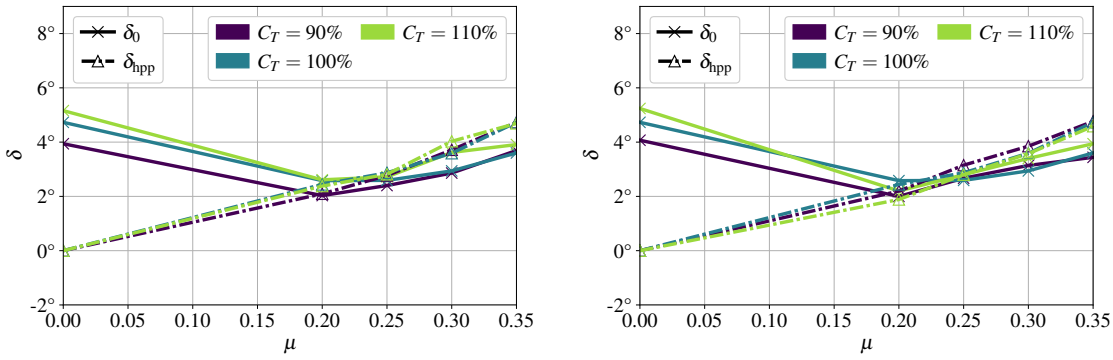

(a) Variation of lift (L) **(b)** Variation of air density (ρ)

Figure 3.40: Mean camber deflections and amplitudes used for cases shown in Figs. 3.38 and 3.39.

affected. A marginal increase in power gain was obtained with greater fuselage drag at high speed. The insignificance of the variation in relative power gains was explained by the fact that two opposing effects contributed to the result. On the one hand, the amount of power required to overcome fuselage drag is fixed and cannot be influenced by active camber. Conversely, due to the higher power requirement, the rotor becomes less efficient in terms of induced and profile power, which results in a greater scope for active camber to save rotor power. Accordingly, the required adjustments to the control inputs were also marginal for the variation of rotor drag.

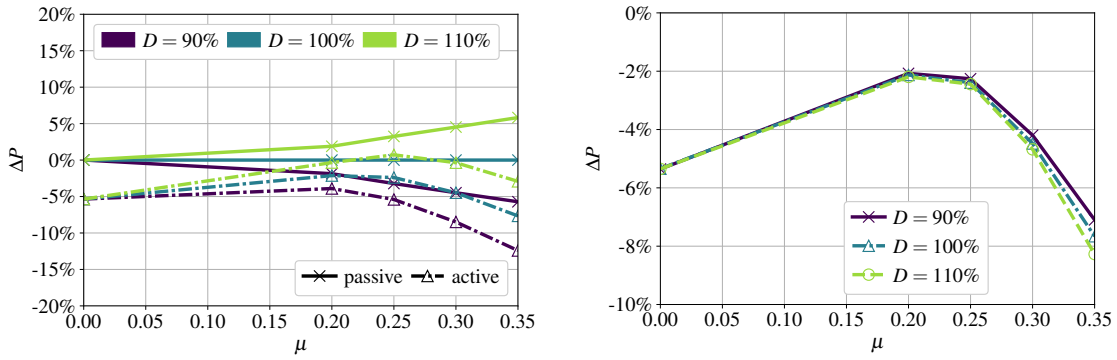

(a) $\Delta P = \frac{P_{D_i} - P_{p,D=100\%}}{P_{p,D=100\%}}$ **(b)** $\Delta P = \frac{P_{a,D_i} - P_{p,D_i}}{P_{p,D_i}}$

Figure 3.41: Effect of varying the fuselage drag D on (a) the passive and active rotor power and (b) active-camber-related power gains.

Variation of the rotor hub moments:

Due to the use of a propulsive trim condition (wind tunnel) to ensure good comparability in terms of rotor power, the rotor hub pitch moment (M_y) was not directly specified but was a result of the rotor shaft tilt (α_S) relative to the free stream. Even small variations in the rotor tilt resulted in significantly different pitch moments. This was due to the hingeless configuration of the baseline Bo105 rotor with a large virtual flap hinge distance ϵ_β [86]. For example, at $\mu = 0.3$, a variation in α_S of $\pm 1^\circ$ resulted in a variation in M_y of ± 3.0 kNm (compared to about $M_y = -0.1$ kNm of the baseline case).

The effect of changing the rotor shaft tilt ($\Delta\alpha_S = \pm 1^\circ$) on the rotor power is shown in Fig. 3.42. Negative numbers of α_S refer to a forward tilt of the rotor. Slight variations in the power of the passive rotor were obtained at high speed. For the active rotor, the effect was more or less negligible. This means that active camber was able to compensate for small performance losses due to suboptimal rotor shaft pitch. Regarding possible uncertainties in the specified trim targets, i.e., the shaft position or the rotor hub pitch moment, they were considered insignificant for the current investigations due to their small impact on the estimation of power savings. As shown in Fig. 3.43, small adjustments to the actuation inputs were required due to the variation in rotor shaft tilt. As the rotor is tilted further backward, a pitch-down moment occurs while the rotor is maintained at constant lift and propulsion. Therefore, the rear region of the rotor is slightly more loaded, and larger camber deflections are required in this azimuth range (around $\psi = 360^\circ$) to relieve the blade tip region. The opposite was obtained for a forward tilt of the rotor shaft, resulting

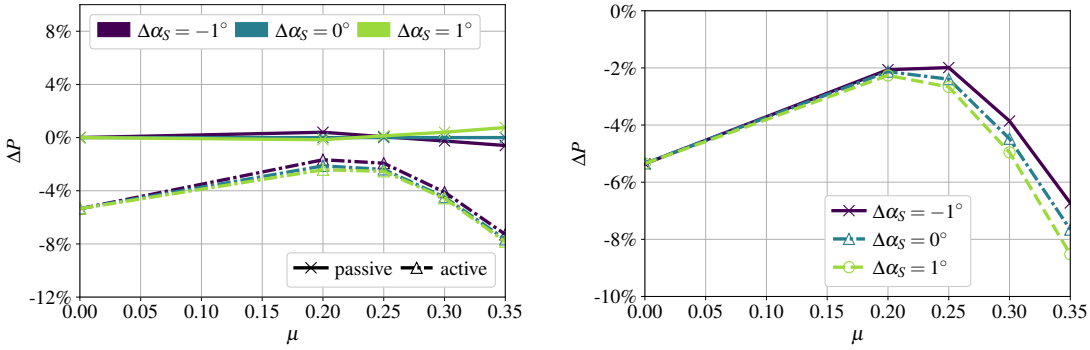

(a) $\Delta P = \frac{P_{\Delta\alpha_{S,i}} - P_{p,\Delta\alpha_S=0°}}{P_{p,\Delta\alpha_S=0°}}$ **(b)** $\Delta P = \frac{P_{a,\Delta\alpha_{S,i}} - P_{p,\Delta\alpha_{S,i}}}{P_{p,\Delta\alpha_{S,i}}}$

Figure 3.42: Effect of varying the shaft angle α_S on (a) the passive and active rotor power and (b) active-camber-related power gains.

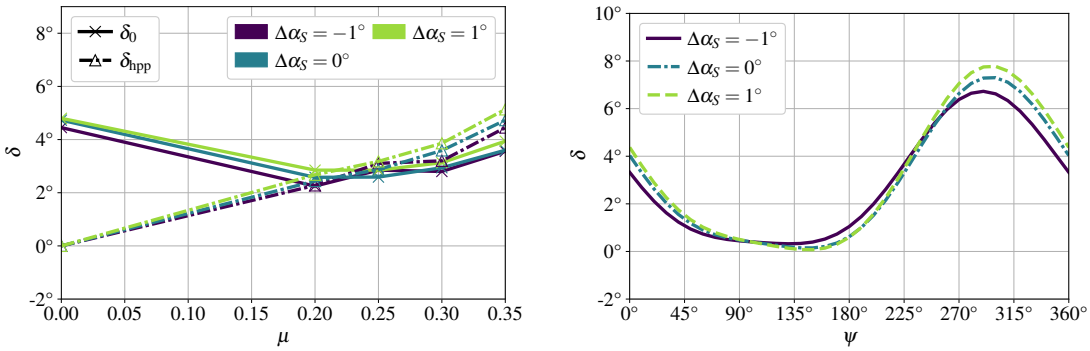

(a) Camber deflection magnitudes **(b)** Azimuthal camber morphing at $\mu = 0.3$

Figure 3.43: Effect of varying the shaft angle α_S on active-camber control inputs. (a) Mean camber deflections and amplitudes used for cases shown in Fig. 3.42. (b) Azimuthal control inputs at $\mu = 0.3$.

in slightly higher camber deflections around $\psi = 180°$.

Figure 3.44 shows that the thrust distribution was indeed moderately different as α_S was varied. Increasing the forward tilt ($\Delta\alpha_S = -1°$) slightly increased the load on the front part of the rotor. With $\Delta\alpha_S = 1°$, the thrust was concentrated a bit more in the rear part of the rotor. However, when comparing the active rotor cases, the success in distributing the loads more evenly across the rotor disk was quite comparable. Thus, with active camber, essentially the same rotor efficiency was obtained for all shaft angles studied, and it did not matter whether more thrust from the front or rear of the rotor disk was distributed to the lateral sides.

With respect to a variation of the rotor hub roll moment (M_x, see Table 2.5), neither the passive nor the active rotor power was affected when M_x was varied in a magnitude of ±20% (see Fig. 3.45). Consequently, any uncertainties in this parameter of the investigated magnitude of 20% were also considered irrelevant.

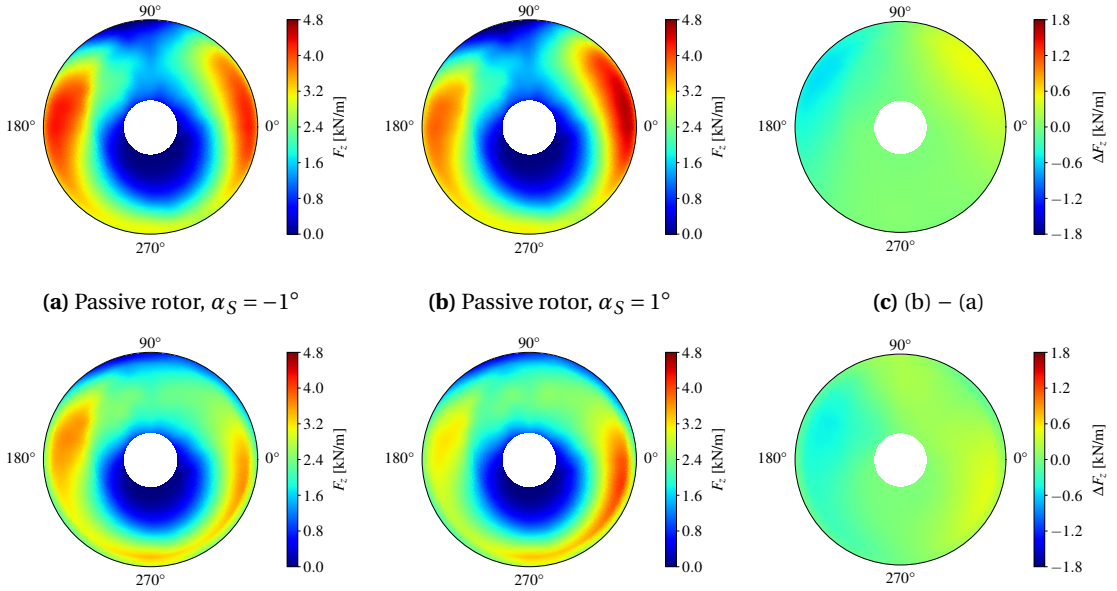

(a) Passive rotor, $\alpha_S = -1°$ **(b)** Passive rotor, $\alpha_S = 1°$ **(c)** (b) − (a)

(d) Active rotor, $\alpha_S = -1°$ **(e)** Active rotor, $\alpha_S = 1°$ **(f)** (e) − (d)

Figure 3.44: Effect of varying the rotor shaft tilt angle α_S on the rotor thrust distribution F_z.

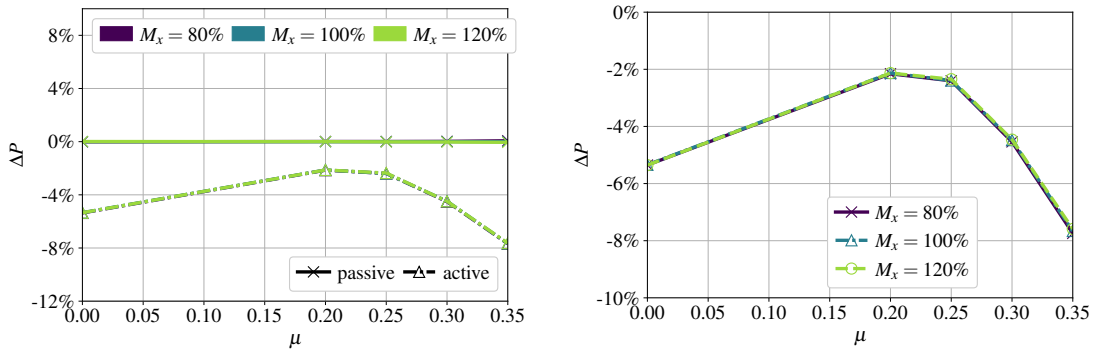

(a) $\Delta P = \frac{P_{M_{x,i}} - P_{p,M_x=100\%}}{P_{p,M_x=100\%}}$ **(b)** $\Delta P = \frac{P_{a,M_{x,i}} - P_{p,M_{x,i}}}{P_{p,M_{x,i}}}$

Figure 3.45: Effect of varying the roll moment M_x on (a) the passive and active rotor power and (b) active-camber-related power gains.

3.3.2 Influence of the Wake Modeling Approach

Accurate modeling of the inflow is quite challenging and, at the same time, very important for analyses where complex aerodynamic phenomena are evaluated. Therefore, a brief discussion and reassessment of some of the most influential modeling decisions are presented here. In Fig. 3.46, the power estimate for calculations based on a free-vortex wake method is compared to a lower fidelity linear inflow approach using the White and Blake model. The linear inflow approach predicted lower power gains at low speeds, while higher power gains were obtained at high speeds. This was attributed to the reduced ability of this modeling approach to adjust the inflow to local

aerodynamic effects. As a result, it was not possible to significantly reduce the induced velocity in the blade tip region by active-camber deflection in hovering flight. In high-speed flight, more extreme angles of attack occurred due to the inability to adjust the local induced velocity in high thrust regions. This increased the potential for active camber to improve rotor efficiency. Therefore, it is assumed, as confirmed in the literature, that the free-vortex wake method provides more reliable results.

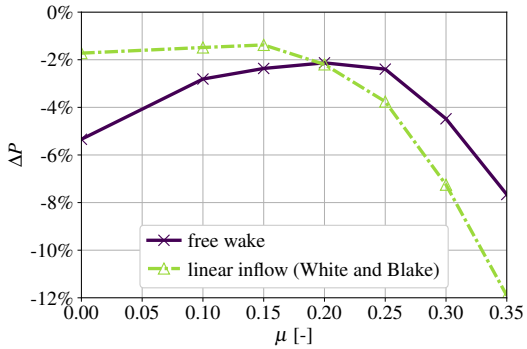

Figure 3.46: Effect of varying the wake modeling (WM) on the prediction of active-camber-induced rotor power savings. Comparison of the free-vortex wake and the linear inflow wake modeling. $\Delta P = \frac{P_{a,\mathrm{WM}_i} - P_{p,\mathrm{WM}_i}}{P_{p,\mathrm{WM}_i}}$.

In free-vortex wake modeling, the number of far wake trailed vorticity panels (N_{panels}) affects the result of the power estimation. There are several known approaches for specifying the number and placement of trailed vorticity panels. While for some problems a single panel has been found to be sufficient, the concept of physical reasoning of far wake vortices is also well established. In the current context, the latter concept corresponds to the addition of vortices at the edges of the active-camber section, since from the physical understanding they are expected to emerge from these locations. Furthermore, the concept of using multiple trailed vorticity panels is widely used. At most, the number of trailed vorticity panels can be equal to the number of aerodynamic panels. However, it should be noted that the computational complexity increases over-proportionally with the number of trailed vortices.

The effect of varying the number of trailed vorticity panels is examined below. The size and distribution of the vorticity panels had to be consistent with the definition of the aerodynamic panels, such that each vorticity panel had to consist of an integer number of aerodynamic panels. In order to distribute the vorticity panels evenly across the rotor blade, an attempt was made to define the vorticity panels so that each contained the same number of aerodynamic panels. When this was not mathematically possible, it was decided that the outer panel would exceed the inner panel by one additional aerodynamic panel. An exception to this approach was only made to also implement the concept of physical reasoning for the vortices. Accordingly, the vortices closest to the edges of the active-camber section were always moved to the exact position of the edges of the active-camber section, prioritizing (in the case of $N_{\mathrm{panels}} = 2$) the outer edge of the active-camber section, since the stronger vortex was expected to occur at this position. The camber control inputs and trim targets were not changed during the variation of N_{panels}.

For the high-speed range, the result of this study is shown in Fig. 3.47. In terms of absolute rotor power, the effect of changing the number of trailing vortices was quite small (see Fig. 3.47a). However, in terms of the relative difference between the passive and active rotor (see Fig. 3.47b), one or two trailed vorticity panels seemed to be insufficient. Instead, a number of $N_{\text{panels}} = 3$ was considered to sufficiently capture the trends in terms of active-camber-induced power savings. In addition, a dual-peak approach was compared to a single-peak approach for the highest advance ratio studied ($\mu = 0.35$). Both results were in excellent agreement.

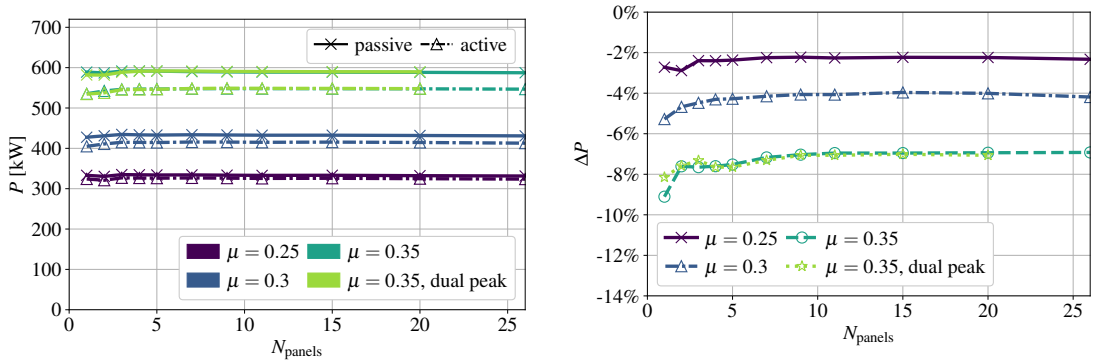

(a) Rotor power

(b) $\Delta P = \frac{P_a - P_p}{P_p}$

Figure 3.47: Rotor power and active-camber-induced power gains for a different number of far-wake trailed vorticity panels (N_{panels}) at high speeds ($\mu = 0.25$ to $\mu = 0.35$).

In the low-speed range (see Fig. 3.48), the results were more dependent on the number of trailed vorticity panels. Especially in hover, a small number of panels led to very ambiguous results and was therefore inappropriate for this study. Instead, a number of $N_{\text{panels}} = 7$ was found to be suitable for $\mu = 0$ and $\mu = 0.1$, as further increasing N_{panels} had no relevant effect on the result. For $\mu = 0.15$, a number of $N_{\text{panels}} \geq 5$ was deemed sufficient based on this convergence study.

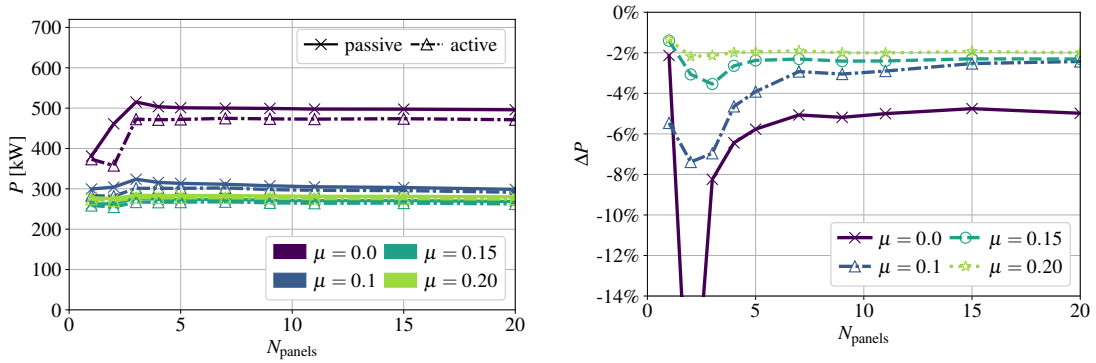

(a) Rotor power

(b) $\Delta P = \frac{P_a - P_p}{P_p}$

Figure 3.48: Rotor power and active-camber-induced power gains for a different number of far wake trailed vorticity panels (N_{panels}) at low speeds ($\mu = 0$ to $\mu = 0.20$).

3.3.3 Secondary Effects on the Helicopter

The previous results were based on isolated rotor calculations. The following is a brief discussion of other aspects that may be relevant in assessing the value of this active-camber mechanism when considering the helicopter as a whole. First, some additional weight is required to implement this mechanism. This concerns the power supply of the system and the mechanical components required to enable the camber morphing. Second, the power required to actuate the mechanism will also negatively affect the efficiency gain of active camber. However, based on a simplified model, only a marginal power requirement was estimated compared to the potential savings with active camber [77]. Therefore, this topic was not pursued further.

On the other hand, there are aspects that could indirectly enhance the performance gains of active camber. First, a reduction in rotorcraft power results in lower fuel consumption. Thus, less fuel is required for the same mission, and the takeoff weight can be reduced accordingly. Since the fuel capacity of a typical helicopter is on the order of 20% of MTOW, this can have a relevant effect. In addition, the power unit and drivetrain can be adequately designed for lower power generation. This includes the helicopter's engine and transmission, as well as the supply structure for these components. It should be noted that most of the power savings have been achieved in the most power consuming flight conditions, i.e., hovering and high-speed flight, especially in hot and high conditions. As a result, the weight of the rotorcraft is expected to continue to decrease. Finally, it is anticipated that weight can be reduced due to the ability of active camber to reduce vibration. This allows for the use of softer support structures and less additional passive or active vibration suppression measures or systems. In this work, it is assumed that the above negative effects are at least compensated by the above positive secondary effects.

Interim conclusions:
The correlation between active-camber-related power savings and C_T was quite independent of the source of variation, i.e., ρ or L. At higher C_T, moderately higher performance gains were obtained, which is particularly interesting in the context of hot and high conditions. The variation of fuselage drag affected the passive rotor power at high speeds but not the relative power savings from active camber. Also, the rotor hub moments had little effect on the power savings from active camber. Therefore, possible uncertainties in the trim targets are expected to have an insignificant effect on the results of this chapter. Moreover, it is expected that for helicopters with different parameters, e.g., fuselage drag or CG, similar results will be obtained as previously presented. As an exception to this, the rotor parameters are treated separately in the following chapter.

Inflow modeling was found to be important in accurately capturing the active-camber-related rotor power savings. Especially in hover and low-speed flight, the results were sensitive to the complexity of the free-vortex wake method. With respect to the secondary effects of implementing active camber, both weight increase and weight reduction are likely to cancel each other out.

4 Correlation Between Rotor Performance Improvements and Rotor Design Parameters

In the previous chapter, performance improvements with active camber were analyzed for a specific helicopter main rotor (Bo 105). In the following, it is examined how design aspects of the base rotor influence these results. One reason for this is to evaluate the transferability of the previous results to other, particularly more efficient rotor systems. This is because future helicopter main rotors are expected to be more aerodynamically efficient than the Bo 105 main rotor. In addition, this variation of the baseline rotor parameters is intended to identify design targets for rotors used in conjunction with an active-camber mechanism. This includes a discussion of the differences in optimal rotor design compared to a purely passive rotor. It is also being investigated whether the effectiveness of such active rotors can be further improved through informed rotor design decisions. Finally, the following study aims to provide further insight into the underlying aeromechanical phenomena by analyzing the effect of various design changes on the achievable power savings.

The rotor design parameters studied were selected based on preliminary investigations and literature review, but also based on the resources available to model and calculate such variations. Accordingly, variations in blade stiffness, built-in twist, chord length (cross-sectional dimension), taper ratio, rotor radius, and tip speed were examined. Blade root cut-out and number of rotor blades had insignificant interdependencies with active camber, so investigations of these parameters were not pursued further. Analysis of complex, small-scale design changes such as blade tip design, blade airfoils, and other complex blade geometries was not feasible in this study. In order not to leave the regime of operable and feasible configurations, only moderate variations in the design parameters were applied to the rotor. This also prevented too much deviation from the validated baseline case and allowed the use of identical numerical settings.

As explained in Section 2.1.1, most of this section is based on the same blade structural properties, even though the blade geometry has been modified. Only Section 4.2.4 presents an analysis where the structural properties of the blade were scaled according to the geometry using the approach described in Section 2.1.1. The multi-objective cost function definition from the previous chapter was used for optimizations, usually with values of $w_{L,SM} = 0.005$ and $e = 10$. In terms of reference values, the loads and stall margin of the modified rotor were used to ensure a fair comparison of the capabilities of active camber. Only a few studies in Section 4.2 included optimizations where the original baseline loads and stall margin were to be maintained, even if the

modified rotor design introduced significant penalties in these properties. Again, active camber was applied between $r = 0.22$ and $r = 0.90$, and a multi-harmonic 1P+2P control scheme was used. In order to keep the optimization problem and the associated computational effort feasible, a spanwise variation of the camber deflection was applied only for some specific investigations, and in those cases it was explicitly stated. While the (dimensionless) advance ratio was usually used to specify the forward speed of the rotor, in some of the following studies the (dimensional) airspeed had to be used to ensure comparability between cases. This was necessary when varying rotor parameters that affect the advance ratio, such as radius or blade tip speed.

4.1 Separate Modification of Rotor Design Aspects

A separate variation of rotor design parameters was used to assess their individual relevance and influence on active-camber-related performance gains. This helped to improve the understanding of how performance improvements were achieved and to identify relevant design variables with respect to active camber morphing. Also, the results of this study were subsequently used to define a study with combined variations of rotor parameters (see next section).

4.1.1 Variation of the Rotor Blade Stiffness

Due to the substantial interaction between rotor elastic deformations and aerodynamic forces, it was considered important to evaluate the effect of changing the blade elastic behavior in the context of active camber actuation. In particular, the torsional stiffness was assumed to be an important parameter, since the morphing of the aft region of the blade notably affected the aerodynamic moment and thus the torsional deformation of the blade. Variations in the blade stiffness were applied separately for the flap, lag, and torsional degrees of freedom. Along the blade span, the original stiffness values were multiplied by a constant factor. However, only torsional stiffness had a noteworthy impact on the power savings induced by active camber. For flap and lag bending stiffness, the correlation with rotor power savings from active camber was negligible when the original mechanical properties were varied by 20%. Therefore, the previous results were considered to remain valid for rotors with reasonably different flap and lag bending stiffness, and only a variation of the torsional stiffness is further discussed below.

When the blade torsional stiffness GJ was increased by 20%, the passive rotor efficiency increased moderately at high speed (see Fig. 4.1). However, with active camber control, the effect on rotor power at high speed was negligible. Accordingly, the power savings associated with active camber were slightly reduced at high speed. Reducing the torsional stiffness of the rotor blades degraded the efficiency of the passive rotor at high speeds. Again, it had little effect on the performance of the active rotor. Especially for vibration reduction, some studies on trailing-edge flaps have suggested reducing the stiffness of the rotor blades [30, 31]. This does not seem to be a reasonable

approach if the goal is to use active camber to improve efficiency. However, if the rotor blade is highly flexible for other reasons (e.g., weight reduction, thinner airfoils, etc.), an active-camber system is expected to have a slightly higher profit margin. In hover, the variation in passive rotor power was marginal when GJ was varied by 20%. When using active camber, the rotor power increased slightly as the torsional stiffness was reduced.

In addition to this moderate variation of GJ, Fig. 4.1 shows a case where the blade was quasi-rigid in the torsional degree of freedom. This indicates the contribution of the induced elastic blade twisting to the total active-camber-induced power gains. Only in medium-speed flight, the blade twisting did not contribute to the power savings. Instead, in hover and at high speeds, a significant portion of the power savings (about 50%) was related to the induced elastic blade twisting.

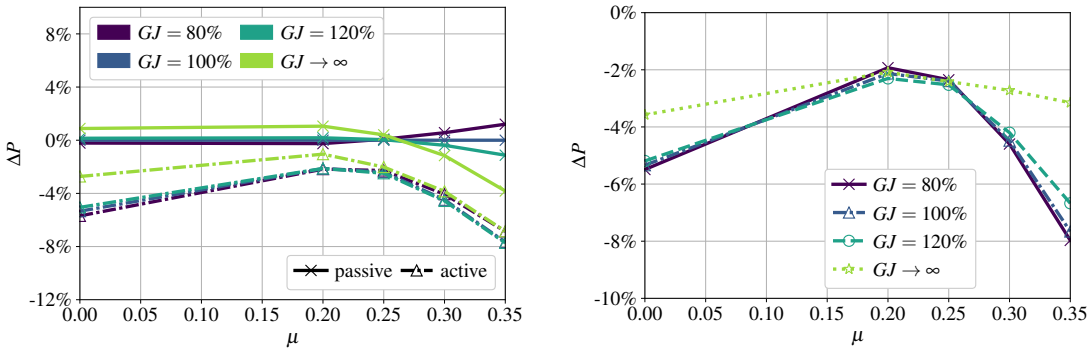

(a) $\Delta P = \frac{P_{GJ_i} - P_{p,GJ=100\%}}{P_{p,GJ=100\%}}$ **(b)** $\Delta P = \frac{P_{a,GJ_i} - P_{p,GJ_i}}{P_{p,GJ_i}}$

Figure 4.1: Influence of torsional stiffness (GJ) on (a) passive (P_p) and active (P_a) rotor power and (b) relative power gain due to active camber (spanwise uniform actuation, i.e., $\vartheta = 0$).

In hover, lower values of GJ resulted in higher blade twisting of the active rotor due to the aerodynamic moment induced by the camber deflection. This better approximated the ideal blade twist and contributed significantly to the power savings. With torsionally stiff rotor blades, this effect was not available and resulted in a reduced ability to improve the hovering rotor efficiency. Instead, a spanwise variation of the camber deflection became more important for cases with high values of GJ (see Fig. 4.2). This is due to the similarity of spanwise varying camber morphing to twisting of the rotor blade.

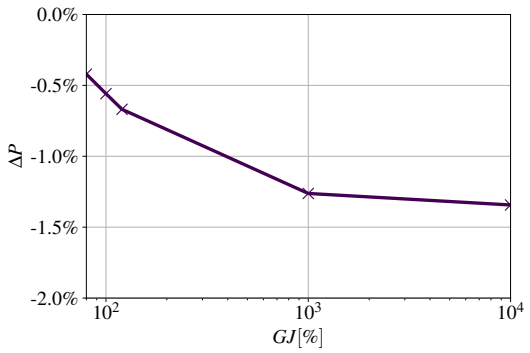

Figure 4.2: Increase in additional power savings from spanwise variation of camber morphing ($\vartheta > 0$) in hover ($\mu = 0$) as the torsional stiffness GJ increases. $\Delta P = \frac{P_{a,GJ_i,\vartheta>0} - P_{a,GJ_i,\vartheta=0}}{P_{a,GJ_i,\vartheta=0}}$.

At high speeds, changes in the active-camber-related power gains as GJ was varied were mainly driven by the variation in passive rotor efficiency, which is therefore further analyzed below (see Figs. 4.3 and 4.4). Most of the torsional deformation in the case of elastic rotor blades (e.g., GJ = 100%) occurred on the advancing side in the second quadrant of the rotor disk (see Fig. 4.3a). Correspondingly, a negative amount of blade pitch was obtained near the blade tip in this azimuth regime (see Fig. 4.3b). Without elastic blade twisting ($GJ \to \infty$), the pitch angles increased in this ψ-range even though the blade root pitch was reduced. As a result, the amount of negative thrust was eliminated at $\mu = 0.3$ (see Fig. 4.4). Furthermore, the reduction of the blade root pitch on the advancing side (allowed by the reduced blade twisting) resulted in less thrust in the first quadrant of the rotor disk where most of the power was induced. Both effects increased the baseline rotor efficiency and reduced the ability of active camber to generate rotor power savings.

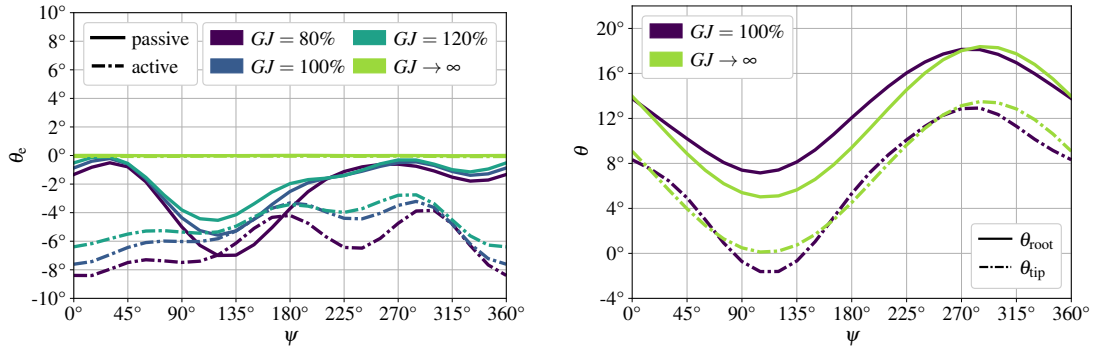

(a) Blade elastic twist θ_e

(b) Blade sectional pitch $\theta(r)$ (passive rotor)

Figure 4.3: Effect of varying GJ on the elastic twist and the blade pitch ($\mu = 0.3$).

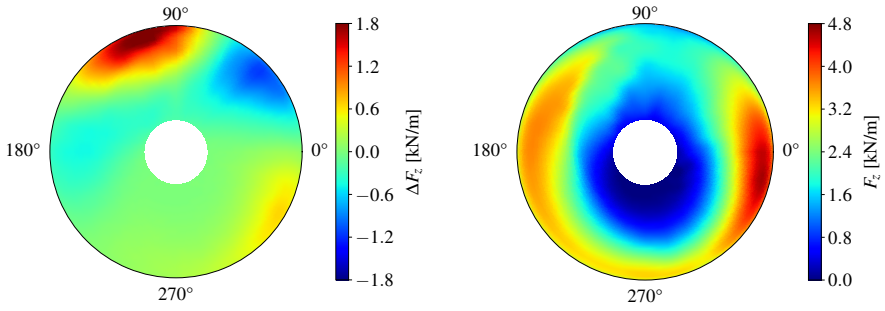

(a) $\Delta F_z = F_{z,p,GJ\to\infty} - F_{z,p,GJ=100\%}$

(b) $F_{z,p,GJ\to\infty}$

Figure 4.4: Effect of increasing GJ on the thrust distribution of the passive rotor ($\mu = 0.3$).

Regardless of how much torsional stiffness is feasible from a constructional perspective, the peak-to-peak rotor hub loads were mostly negatively affected by a large increase in GJ (see Fig. 4.5). As GJ approached infinity, some loads increased notably, such as the oscillatory torque moment (M_z). This was explained by the fact that not only the thrust but also the drag increased near $\psi = 90°$. However, at this azimuth position, the averaged effect of all blades on the rotor torque was already at a peak before increasing GJ. Thus, increasing GJ amplified this oscillation of M_z. With active camber control (see Fig. 4.5b), it was generally possible to reduce the loads compared to the corresponding passive rotor. Note that the optimization target was not to exceed the rotor

loads of the corresponding (modified GJ) passive rotor. However, Fig. 4.5 shows a comparison to the original passive Bo 105 rotor for both the passive and active rotor.

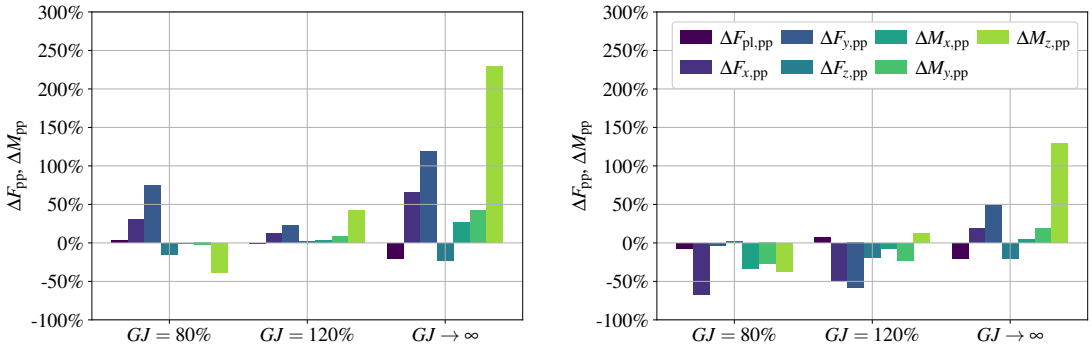

(a) Passive rotor

(b) Active rotor

Figure 4.5: Peak-to-peak forces and moments (rotor hub and pitch links) under variation of GJ. Comparison between (a) the passive and (b) the active rotor at high speed ($\mu = 0.30$). $\Delta() = \frac{0_{pp,GJ_i} - 0_{pp,p,GJ=100\%}}{0_{pp,p,GJ=100\%}}$.

Lower actuation amplitudes have been reported for vibration reduction with torsionally softer rotor blades [28] (trailing-edge flap). The current study confirmed this trend, but only to a secondary extent (see Fig. 4.6). Only when the blade was torsionally rigid, slightly higher amplitudes were required. Conversely, a moderate variation of GJ had little effect on the optimal control inputs. This may change when minimizing the actuation amplitude is included in the objective function.

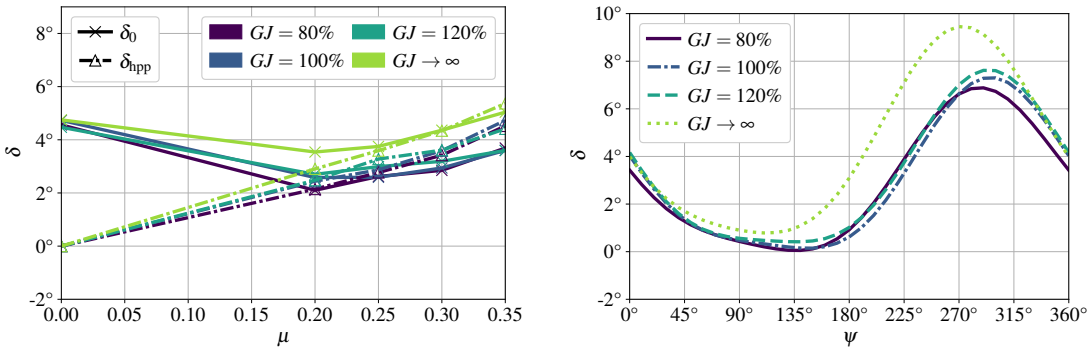

(a) Camber deflection magnitudes

(b) Azimuthal camber morphing at $\mu = 0.3$

Figure 4.6: Active-camber control inputs under variation of GJ. Higher camber deflection magnitudes required for torsionally stiff rotor blades.

4.1.2 Variation of the Rotor Blade Twist

As shown in the evaluation of the influence of GJ, the manipulation of the blade elastic twist over the azimuth is a key feature of this active-camber system and contributes substantially to the performance gains achieved. This suggests a relevant correlation between the active-camber-induced efficiency improvements and the blade twist angle (θ_{tw}), which will be discussed below.

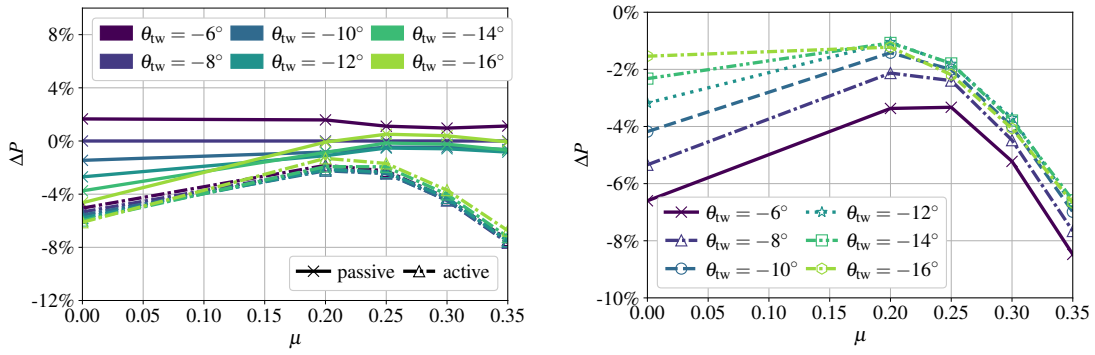

(a) $\Delta P = \frac{P_{\theta_{\mathrm{tw},i}} - P_{p,\theta_{\mathrm{tw}}=-8°}}{P_{p,\theta_{\mathrm{tw}}=-8°}}$ **(b)** $\Delta P = \frac{P_{a,\theta_{\mathrm{tw},i}} - P_{p,\theta_{\mathrm{tw},i}}}{P_{p,\theta_{\mathrm{tw},i}}}$

Figure 4.7: Influence of built-in blade twist (θ_{tw}) on (a) passive (P_p) and active (P_a) rotor power and (b) relative power gain due to active camber (spanwise uniform actuation, i.e., $\vartheta = 0$).

Due to the multiple demands on a helicopter main rotor, the Bo 105 rotor blade has a θ_{tw} that is below the optimum for hovering rotors. From hub to tip it is $\theta_{\mathrm{tw}} = -8°$, which corresponds to a blade twist of $-6.24°$ in the aerodynamically active section.

Figure 4.7 shows the effect of changing θ_{tw} on the rotor power of the active and passive rotors. With more built-in twist (higher negative values), the hovering power of the passive rotor increased significantly (see Fig. 4.7a). At high speed, the passive rotor power was only slightly affected, showing a small performance penalty for less than $\theta_{\mathrm{tw}} = -8°$ and more than $\theta_{\mathrm{tw}} = -14°$ blade twist. This indicates that from a performance perspective, increasing the twist angle of the passive rotor would be beneficial. In terms of active rotor power, the influence of θ_{tw} was much smaller. In high-speed flight, there was a marginal reduction in rotor efficiency at high blade twist rates, resulting in moderately reduced power savings. However, the power savings converged to a certain amount of power savings (about 6.5% at $\mu = 0.35$). In hover, high blade twist improved efficiency only slightly, resulting in significantly less active-camber-induced power savings at higher blade twist. This trend has not yet converged at the highest blade twist of $\theta_{\mathrm{tw}} = -16°$.

Not only the (spanwise uniform) static camber deflection but also the variation of the camber deflection along the blade span steadily lost importance in hovering flight as the built-in twist was increased (see Fig. 4.8). This was attributed to the fact that for moderate angles of attack a variation of the camber along the blade span has a similar effect on the rotor aerodynamics as the addition of blade twist.

Although the effect on rotor power was small, the thrust distribution in high-speed flight was noticeably different for passive rotors with $\theta_{\mathrm{tw}} = -8°$ and $\theta_{\mathrm{tw}} = -16°$ (see Fig. 4.9). Increasing the blade twist resulted in a relief of the heavily loaded fore and aft regions of the rotor disk, which positively affects the rotor performance. At the same time, however, the negative thrust on the advancing side was increased, offsetting the efficiency gain just mentioned. Therefore, at high twist angles, the focus of the active camber control was shifted to better compensate for the negative thrust on the retreating side. This required a negative camber deflection on the advancing

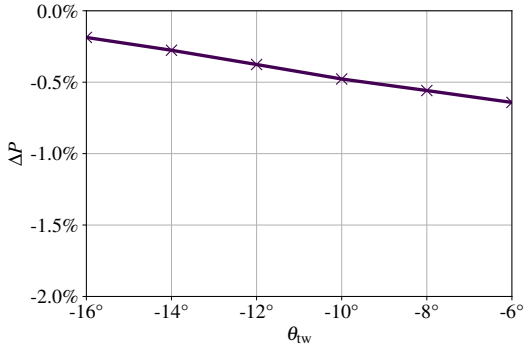

Figure 4.8: Reduction in additional power savings from spanwise variation of camber morphing ($\vartheta > 0$) in hover ($\mu = 0$) as the blade built-in twist θ_{tw} increases. $\Delta P = \frac{P_{a,\theta_{\text{tw},i},\vartheta>0} - P_{a,\theta_{\text{tw},i},\vartheta=0}}{P_{a,\theta_{\text{tw},i},\vartheta=0}}$.

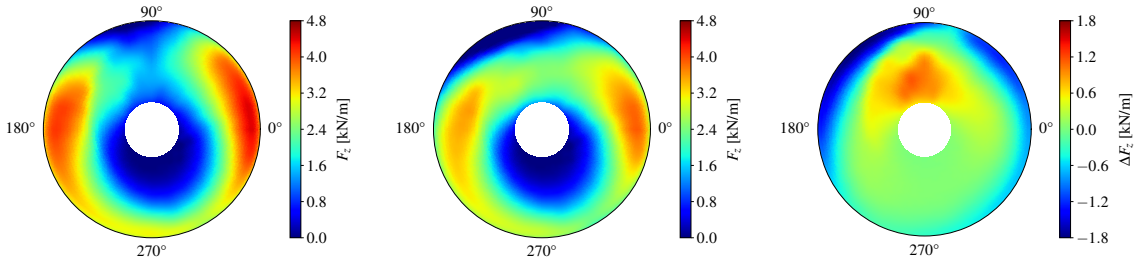

(a) $\theta_{\text{tw}} = -8°$ **(b)** $\theta_{\text{tw}} = -16°$ **(c)** $\Delta F = F_{z,\theta_{\text{tw}}=-16°} - F_{z,\theta_{\text{tw}}=-8°}$

Figure 4.9: Thrust distribution of the passive rotors for different built-in blade twist (θ_{tw}) at $\mu = 0.3$.

side to reduce the blade twist in this region (see Fig. 4.10). This was mainly achieved by reducing the mean camber deflection $\delta_{0\text{P}}$ for larger θ_{tw}. The amplitudes, instead, were only marginally affected. In hover, the required camber deflection was distinctly reduced as the blade built-in twist increased (see Fig. 4.10a). This was expected due to the notable reduction in active-camber-related performance gains in this flight state.

In terms of rotor loads at high speed, an increase in most peak-to-peak hub loads was found at higher blade twist angles, especially the in-plane forces (see Fig. 4.11). This is believed to limit the feasibility of such highly twisted blade designs. Although the loads were weakly considered in the optimization cost function, this substantial increase in blade loads was not observed with active camber actuation.

Regarding the stall margin (see Fig. 4.12), the passive rotor was positively affected in hover by increasing the built-in twist. When using active camber, a variation of the twist angle had negligible effect on the most relevant region near the blade tip. In high-speed flight, the stall margin of the active rotor moderately decreased at $\psi = 270°$ when increasing θ_{tw}. Overall, a possible design target for a rotor equipped with this active-camber system would be a slight increase in blade twist. With respect to the active rotor, this moderately improved the efficiency in hover, while not affecting the high-speed rotor performance and not significantly increasing the rotor loads.

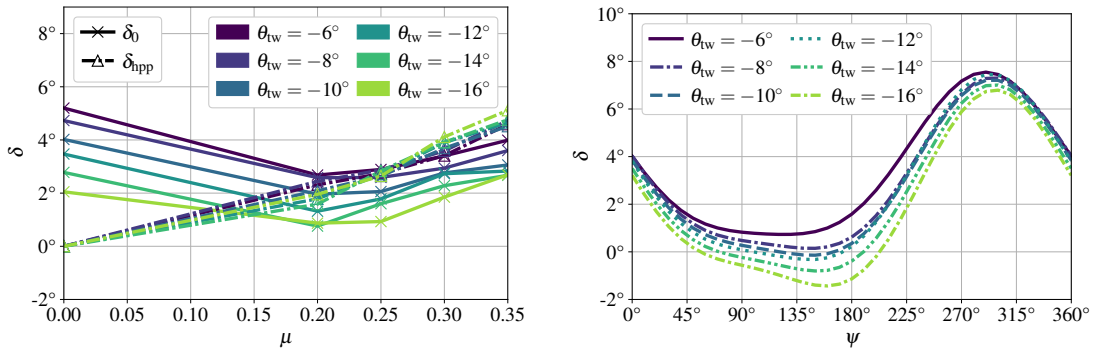

(a) Camber deflection magnitudes

(b) Azimuthal camber morphing at $\mu = 0.3$

Figure 4.10: Active-camber control inputs under variation of θ_{tw}. Decreasing mean camber deflections and thus negative deflections on the advancing side as θ_{tw} increases.

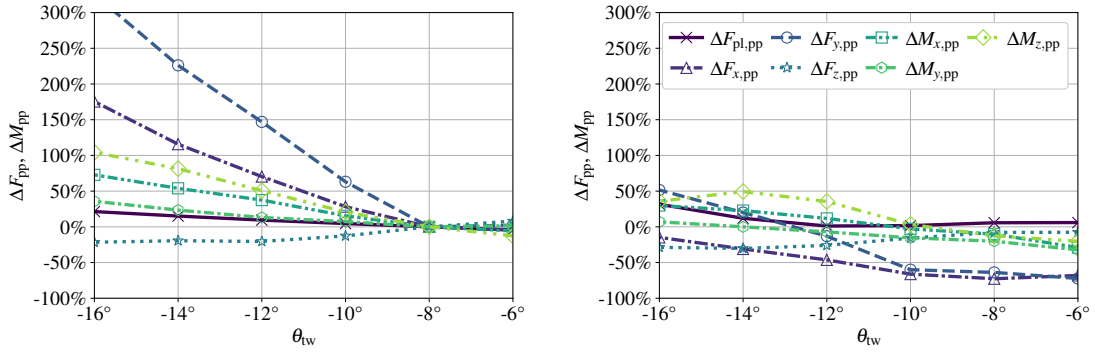

(a) Passive rotor

(b) Active rotor

Figure 4.11: Peak-to-peak forces and moments (rotor hub and pitch links) under variation of θ_{tw}. Comparison between (a) the passive and (b) the active rotor at high speed ($\mu = 0.30$). $\Delta() = \frac{()_{pp,\theta_{tw,i}} - ()_{pp,p,\theta_{tw}=-8°}}{()_{pp,p,\theta_{tw}=-8°}}$.

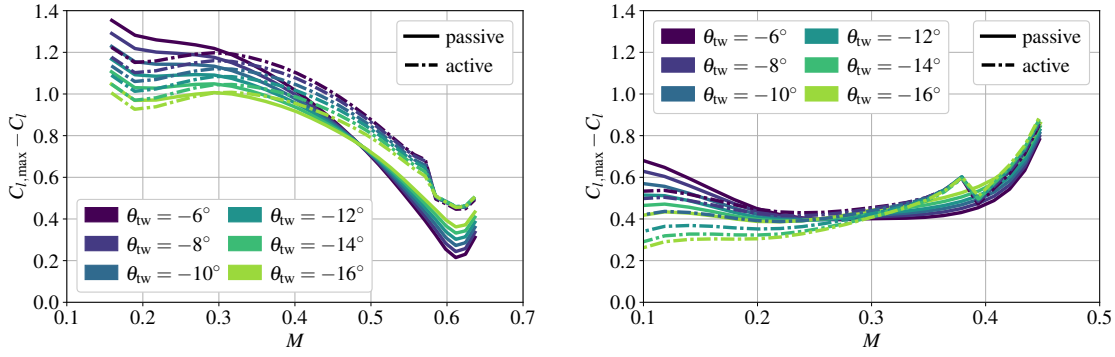

(a) $\mu = 0.0$

(b) $\mu = 0.3$

Figure 4.12: Stall margin ($SM = C_{l,\max} - C_l$) under variation of θ_{tw} in hover and high-speed flight. (b) SM at the retreating blade ($\psi = 270°$).

4.1.3 Variation of the Rotor Blade Chord Length

The Bo 105 baseline rotor blade has a rectangular geometry with a constant chord length of c = 0.27m in the aerodynamically active region between $r = 0.22$ and $r = 1$. Since more lift can be generated by increasing the camber of the airfoil, it may be possible to reduce the cross-sectional area of the blade when using an active-camber system. In this way, the drag of the rotor blade could be reduced while increasing lift only where needed. In the following investigation, the entire airfoil was scaled up and down by a constant factor along the blade span. Thus, the variation of the chord length was performed with the airfoil geometry and relative thickness unchanged. By modifying the rotor chord length, the rotor solidity σ and the blade loading C_T/σ also changed. The blade structural properties were not scaled in this investigation.

For the passive rotor, neither increasing nor decreasing c by ±10% resulted in a relevant performance improvement (see Fig. 4.13). However, for the active rotor, as expected, an improvement in rotor efficiency was obtained by decreasing the size of the airfoil section and vice versa. Correspondingly, the relative efficiency improvement through the use of active camber increased notably for all advance ratios as the chord length was reduced. Regarding the oscillatory rotor loads at $\mu = 0.3$, a variation of the blade chord length had only a moderate effect on the passive rotor and negligible effect on the active rotor (see Fig. 4.14).

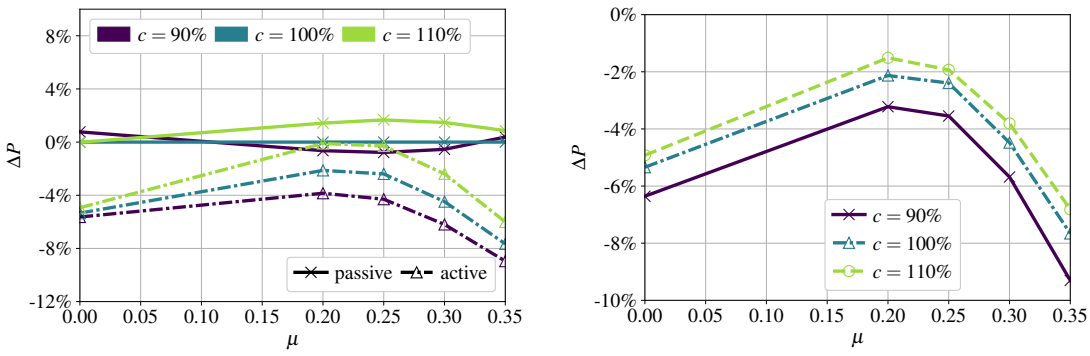

(a) $\Delta P = \frac{P_{c_i} - P_{p,c=100\%}}{P_{p,c=100\%}}$ **(b)** $\Delta P = \frac{P_{a,c_i} - P_{p,c_i}}{P_{p,c_i}}$

Figure 4.13: Influence of chord length (c) on (a) passive (P_p) and active (P_a) rotor power and (b) relative power gain due to active camber (spanwise uniform actuation, i.e., $\vartheta = 0$).

In terms of the control signal (see Fig. 4.15), the mean camber deflections were slightly increased when using smaller c. The stall margin of the passive and active rotor noticeably deteriorated as c was reduced (see Fig. 4.16). Nevertheless, when using an active-camber system, a moderate reduction in blade cross-sectional dimensions is considered beneficial.

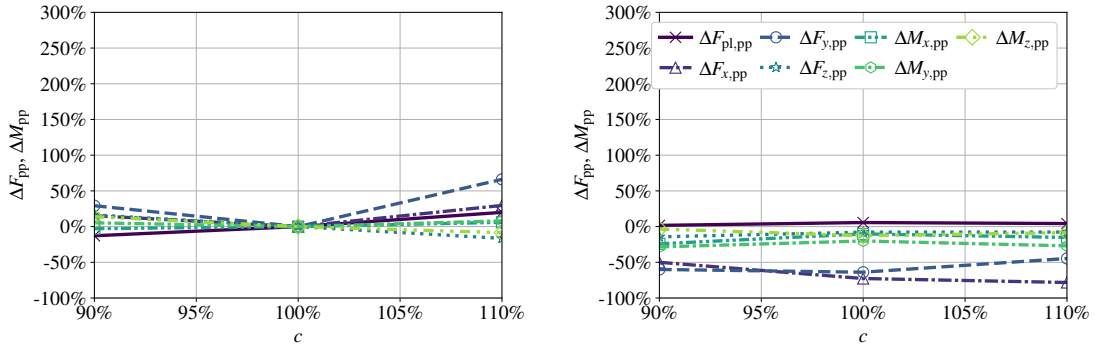

(a) Passive rotor

(b) Active rotor

Figure 4.14: Peak-to-peak forces and moments (rotor hub and pitch links) under variation of c. Comparison between (a) the passive and (b) the active rotor at $\mu = 0.30$. $\Delta() = \frac{()_{pp,c_i} - ()_{pp,p,c=100\%}}{()_{pp,p,c=100\%}}$.

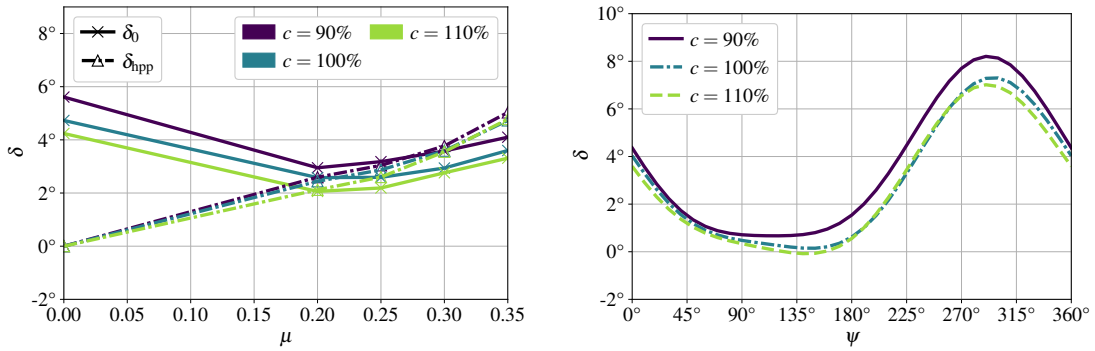

(a) Camber deflection magnitudes

(b) Azimuthal camber morphing at $\mu = 0.3$

Figure 4.15: Active-camber control inputs under variation of c. Higher mean camber deflections as c increases.

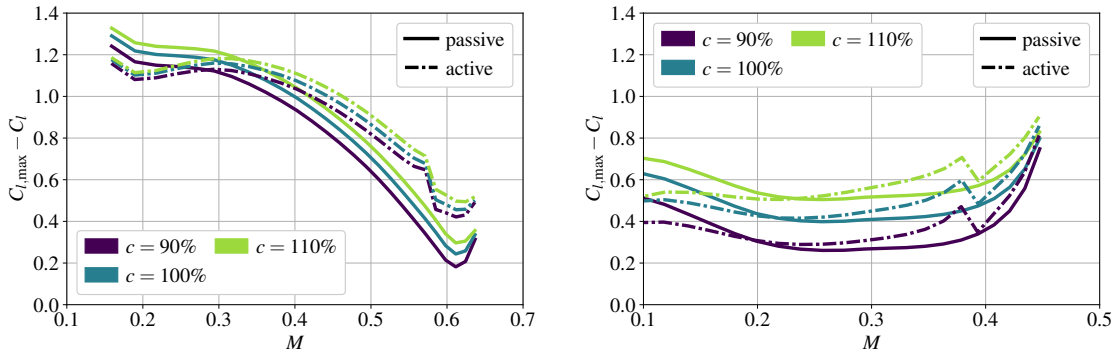

(a) $\mu = 0.0$

(b) $\mu = 0.3$

Figure 4.16: Stall margin ($SM = C_{l,max} - C_l$) under variation of c in hover and high-speed flight. (b) SM at the retreating blade ($\psi = 270°$).

4.1.4 Variation of the Rotor Blade Taper Ratio

In contrast to the previous section where the effect of a spanwise uniform c variation was studied, the following section analyzes the variation of the chord length along the blade span. This was considered promising due to its potential to reduce drag far outboard, where the highest dynamic pressure is experienced. At the same time, the reduction in the ability to generate thrust could be compensated by the active-camber mechanism. The taper ratio is defined as

$$t = \frac{c_{\text{tip}}}{c_{\text{root}}} \cdot 100\% \tag{4.1}$$

This means that the rectangular Bo 105 baseline rotor blade is described by $t = 100\%$. As in the previous section, the blade thickness was simultaneously adjusted to the blade chord length to maintain the same airfoil geometry and relative thickness. A change in the structural properties due to the geometry variation was again neglected. For good comparability in terms of blade loading, the thrust-weighted solidity was kept constant during the variation of t [73], while trimming consistently to the same rotor thrust. Since the variation of c along the span was linear, the chord at $r_{\text{ref}} = 0.75$ had to remain constant at $c_{\text{ref}} = 0.27\text{m}$ to maintain the same thrust-weighted solidity. Correspondingly, the required chord length at the blade tip ($r_{\text{tip}} = 1$) for a given t can be determined by the equation

$$c_{\text{tip}} = c_{\text{ref}} \cdot \frac{r_{\text{tip}} - r_{\text{root}}}{(r_{\text{ref}} - r_{\text{root}}) + (r_{\text{tip}} - r_{\text{ref}})/t}. \tag{4.2}$$

The chord length at $r_{\text{root}} = 0.22$ can then be extrapolated based on the chord length at r_{tip} and r_{ref}.

$$c_{\text{root}} = c_{\text{ref}} + \frac{c_{\text{tip}} - c_{\text{ref}}}{r_{\text{tip}} - r_{\text{ref}}} \cdot (r_{\text{root}} - r_{\text{ref}}) \tag{4.3}$$

Two configurations were compared to the baseline rotor with rectangular blades, i.e., a value of $t = 75\%$ and a value of $t = 50\%$. In both cases, the chord length was reduced towards the blade tip to improve efficiency. As shown in Fig. 4.17, the passive and active rotor performance was notably improved by introducing a taper of $t < 100\%$ for all flight speeds. In terms of active-camber-related power gains, the efficiency gains decreased slightly at medium speeds. However, the hover and high-speed power gains were not affected by this change in blade geometry. The effect of spanwise varying actuation was again evaluated for hovering flight (see Fig. 4.18). Similar to blade twisting, the benefits of spanwise varying actuation decreased when blade taper was introduced.

As shown in Fig. 4.19, the rotor loads generally increased when the rotor blade was tapered. However, with active camber, the load increase was significantly lower. At the same time, the stall margin (see Fig. 4.20) of the passive rotor deteriorated slightly. Also, the active-camber control scheme was hardly affected, only a marginal reduction of the mean deflection was observed at lower values of t (see Fig. 4.21). In terms of deriving a design target for this parameter, the introduction of blade tapering improved the performance of both the passive and active rotors.

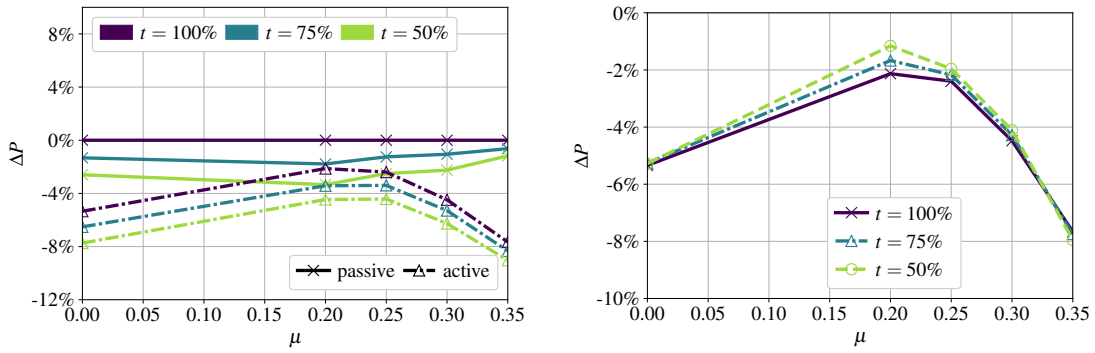

(a) $\Delta P = \frac{P_{t_i} - P_{p,t=100\%}}{P_{p,t=100\%}}$ **(b)** $\Delta P = \frac{P_{a,t_i} - P_{p,t_i}}{P_{p,t_i}}$

Figure 4.17: Influence of the blade taper ratio $t = c_{\text{tip}}/c_{\text{root}}$ on (a) passive (P_p) and active (P_a) rotor power and (b) relative power gain due to active camber (spanwise uniform actuation, i.e., $\vartheta = 0$).

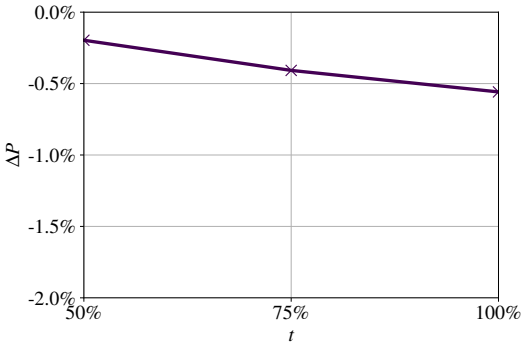

Figure 4.18: Reduction in additional power savings from spanwise variation of camber morphing ($\vartheta > 0$) in hover ($\mu = 0$) as the blade taper ratio (t) increases. $\Delta P = \frac{P_{a,t_i,\vartheta>0} - P_{a,t_i,\vartheta=0}}{P_{a,t_i,\vartheta=0}}$.

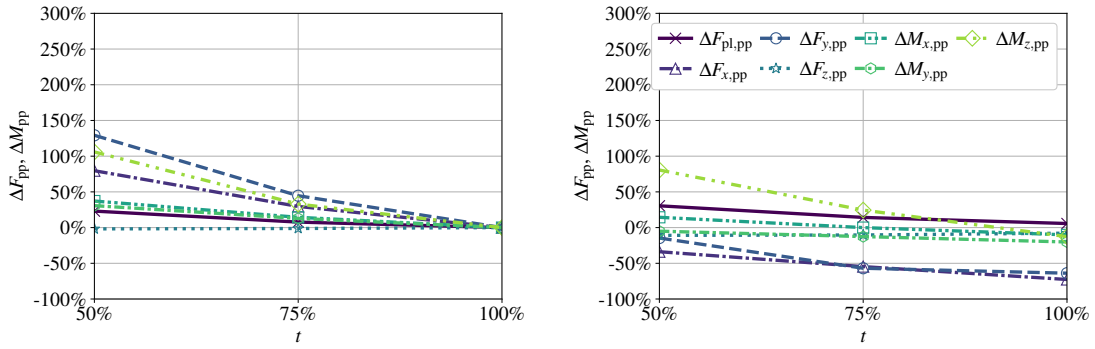

(a) Passive rotor **(b)** Active rotor

Figure 4.19: Peak-to-peak forces and moments (rotor hub and pitch links) under variation of t. Comparison between (a) the passive and (b) the active rotor at high speed ($\mu = 0.30$). $\Delta() = \frac{0_{\text{pp},t_i} - 0_{\text{pp},p,t=100\%}}{0_{\text{pp},p,t=100\%}}$.

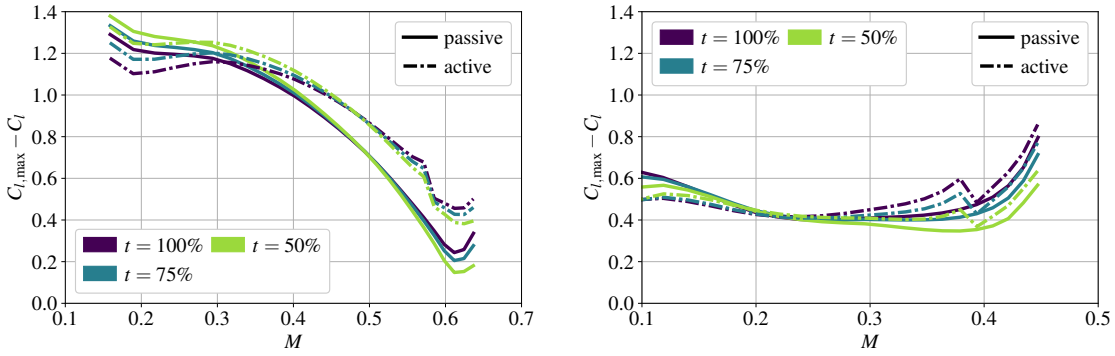

(a) $\mu = 0.0$ **(b)** $\mu = 0.3$

Figure 4.20: Stall margin ($SM = C_{l,\max} - C_l$) under variation of t in hover and high-speed flight. (b) SM at the retreating blade ($\psi = 270°$).

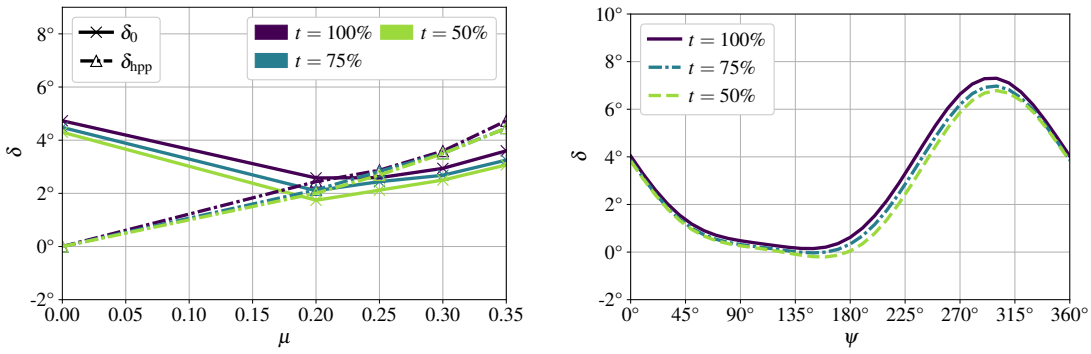

(a) Camber deflection magnitudes **(b)** Azimuthal camber morphing at $\mu = 0.3$

Figure 4.21: Active-camber control inputs under variation of t. Minor adjustments to the camber control inputs required as t changes.

4.1.5 Variation of the Rotor Radius at Constant Rotor Tip Speed

The effect of varying the rotor radius (R) on the active-camber-related power gains is of particular interest due to its influence on the induced velocity and induced rotor power. Varying R involved an adjustment of the rotor rotational speed to maintain a constant blade tip speed. In this way, the effects of changing the rotor radius and changing the rotor tip speed could be studied independently. As a result, for the same trim condition, this variation affected the thrust coefficient (C_T), the blade loading (C_T/σ), the rotor solidity (σ), and the advance ratio (μ). Accordingly, the investigations in this section are compared in terms of flight speed v rather than advance ratio μ to ensure a meaningful comparison. With respect to the unmodified rotor, the same advance ratios were used as in the previous studies in this section ($\mu = 0.3$ corresponds to $v = 65.6$ m/s). Cross-sectional dimensions and structural properties were not adjusted as the rotor radius was varied.

As shown in Fig. 4.22, the rotor power was noticeably affected by changing R. Increasing R was

beneficial for both the passive and active rotor (see Fig. 4.22a). This benefit was more pronounced from hover to medium-speed flight where the induced rotor power is most relevant. In high-speed flight, the effect of changing R gradually diminished as the induced power became less important in this flight regime. Since both the passive and active rotor were equally affected, the effect on the relative power savings induced by active camber was marginal (see Fig. 4.22b).

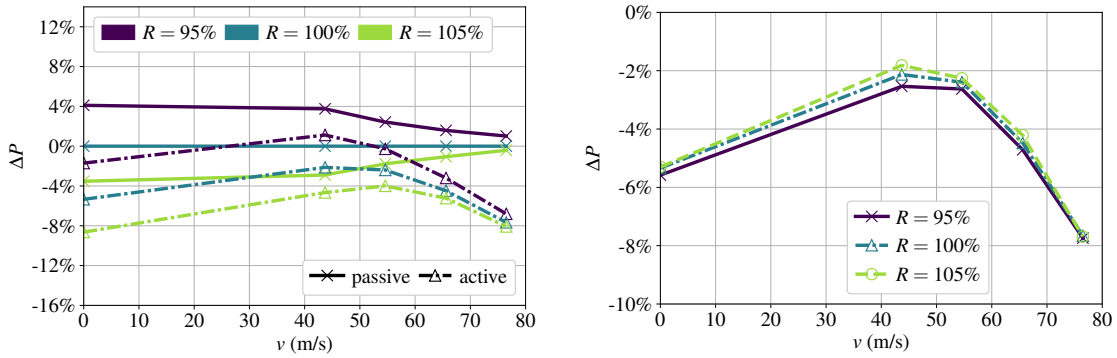

(a) $\Delta P = \frac{P_{R_i} - P_{p,R=100\%}}{P_{p,R=100\%}}$ **(b)** $\Delta P = \frac{P_{a,R_i} - P_{p,R_i}}{P_{p,R_i}}$

Figure 4.22: Influence of the rotor radius R on (a) passive (P_p) and active (P_a) rotor power and (b) relative power gain due to active camber (spanwise uniform actuation, i.e., $\vartheta = 0$).

With respect to the rotor loads at $v = 65.6$ m/s (see Fig. 4.23), a moderate deterioration was obtained for both increased and decreased R. The control inputs (see Fig. 4.24) were only slightly affected by changing R, with a small reduction in the mean deflection (δ_{0P}) as R was increased. The retreating-blade stall margin at high speeds (see Fig. 4.25) was improved by increasing R. Overall, for both active and passive rotors, a moderate increase in radius is beneficial in terms of the aspects studied. However, varying the rotor radius had little effect on the relative power savings induced by active camber. Thus, the decision for a particular rotor radius is largely independent of whether an active-camber system is applied or not.

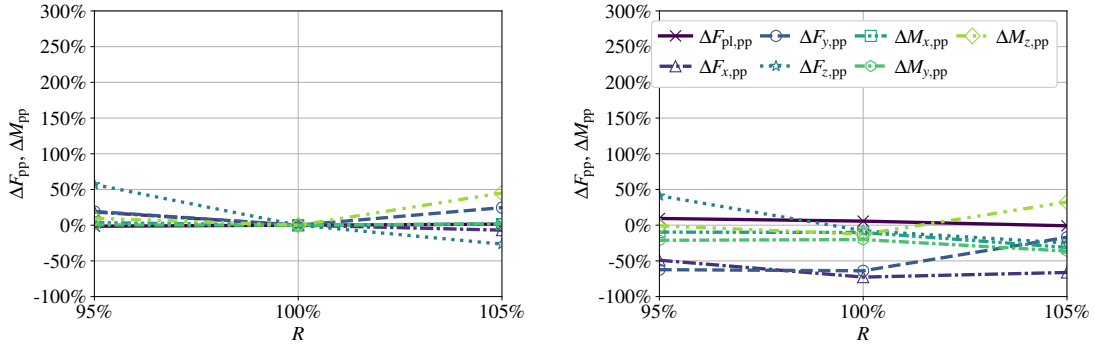

(a) Passive rotor **(b)** Active rotor

Figure 4.23: Peak-to-peak forces and moments (rotor hub and pitch links) under variation of R. Comparison between (a) the passive and (b) the active rotor at high speed ($v = 65.6$ m/s). $\Delta() = \frac{()_{pp,R_i} - ()_{pp,p,R=100\%}}{()_{pp,p,R=100\%}}$.

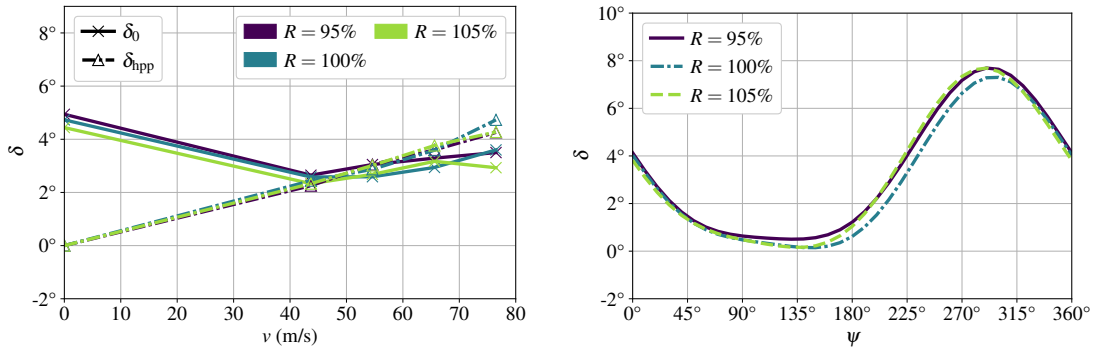

(a) Camber deflection magnitudes

(b) Azimuthal camber morphing at $v = 65.6$ m/s

Figure 4.24: Active-camber control inputs under variation of R. Minor adjustments to the camber control inputs required as R changes.

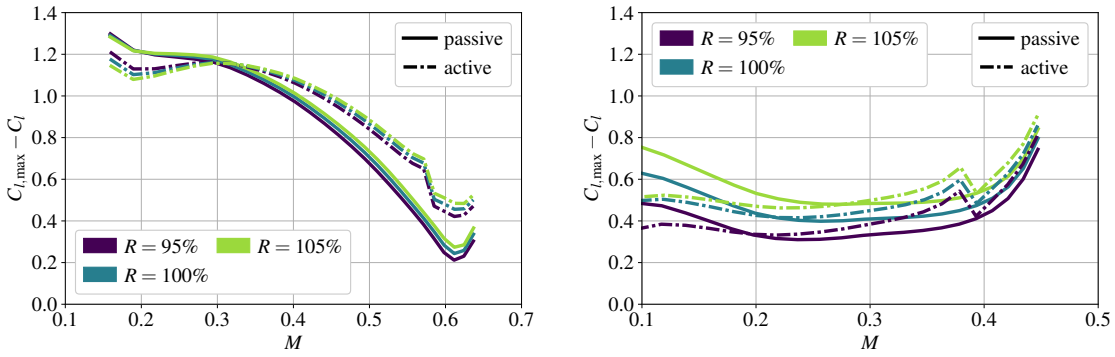

(a) $v = 0$ m/s

(b) $v = 65.6$ m/s

Figure 4.25: Stall margin ($SM = C_{l,\max} - C_l$) under variation of R in hover and high-speed flight. (b) SM at the retreating blade ($\psi = 270°$).

4.1.6 Variation of the Rotor Tip Speed at Constant Rotor Radius

While previous investigations in this chapter dealt with variations of the rotor blade design, i.e., blade structural properties or blade geometry, this analysis was based on the exact same Bo 105 baseline rotor. Instead, a variation of the blade tip velocity (v_{tip}) was investigated by varying the nominal rotor speed (Ω). The blade tip velocity is an important parameter in the design of a helicopter rotor with a substantial impact on the required power, stall margin, vibration, and noise of the rotorcraft. As before, the flight speed (v) was used for this comparison because of the interdependence between v_{tip} and the advance ratio (μ). For the same reason, the investigations were performed based on the same rotor thrust instead of the same rotor thrust coefficient.

The effect of varying v_{tip} on the rotor power is shown in Fig. 4.26. Both the passive and active rotor power improved for all flight speeds examined as v_{tip} was reduced (and vice versa). This was mainly due to the reduction of the dynamic pressure on the advancing side and thus the reduction of drag and aerodynamic moment in this region. This resulted in less potential for

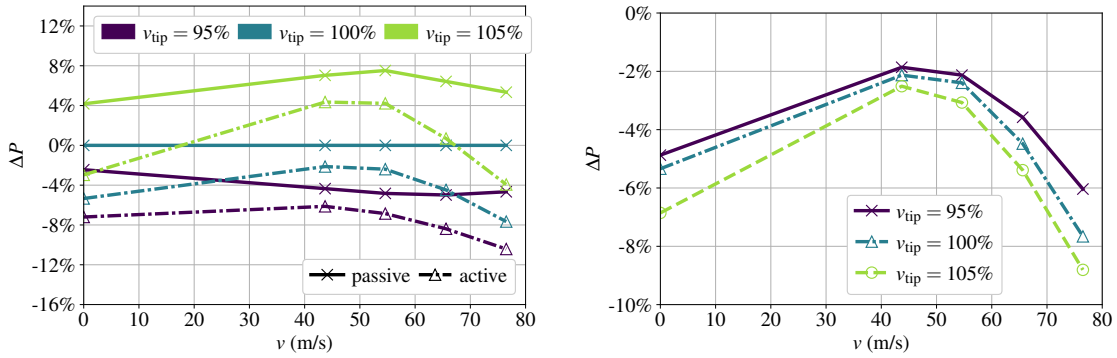

(a) $\Delta P = \frac{P_{v_{tip,i}} - P_{p,v_{tip}=100\%}}{P_{p,v_{tip}=100\%}}$ **(b)** $\Delta P = \frac{P_{a,v_{tip,i}} - P_{p,v_{tip,i}}}{P_{p,v_{tip,i}}}$

Figure 4.26: Influence of the rotor tip speed v_{tip} on (a) passive (P_p) and active (P_a) rotor power and (b) relative power gain due to active camber (spanwise uniform actuation, i.e., $\vartheta = 0$).

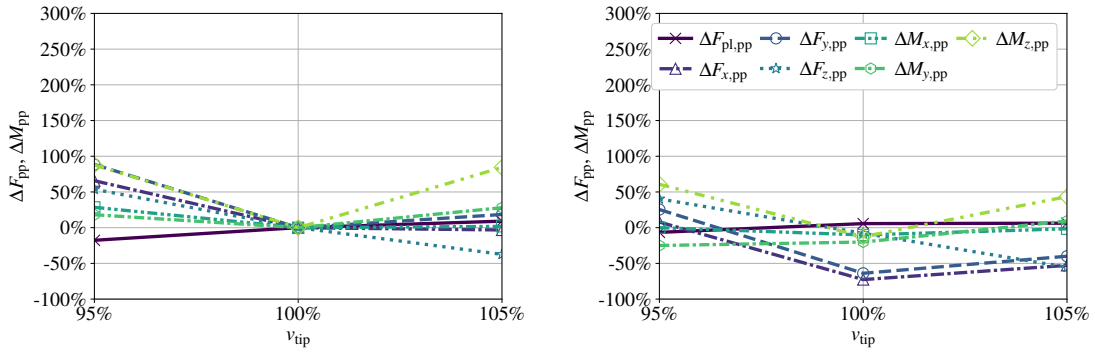

(a) Passive rotor **(b)** Active rotor

Figure 4.27: Peak-to-peak forces and moments (rotor hub and pitch links) under variation of v_{tip}. Comparison between (a) the passive and (b) the active rotor at high speed (v = 65.6 m/s). $\Delta() = \frac{()_{pp,v_{tip,i}} - ()_{pp,p,v_{tip}=100\%}}{()_{pp,p,v_{tip}=100\%}}$.

active camber to improve rotor efficiency and the active-camber-induced performance gains at high speeds were moderately mitigated.

Changing v_{tip} in either direction always increased some of the rotor loads (see Fig. 4.27). Reducing the tip speed increased most of the hub loads because of the greater variation in the oncoming flow velocity perpendicular to the rotor blade. Instead, increasing the tip speed mainly increased the oscillatory torque M_z on the rotor shaft due to the higher compressibility effects that occurred on the advancing side. With active camber control, the loads were generally lower for all tip speeds studied. Regarding the active-camber control inputs, no clear trend was observed by varying v_{tip} (see Fig. 4.28). However, a slight increase in the actuation amplitude seemed to be beneficial at lower v_{tip}.

The effect of tip speed variation on the retreating-blade stall margin is shown in Fig. 4.29. Even

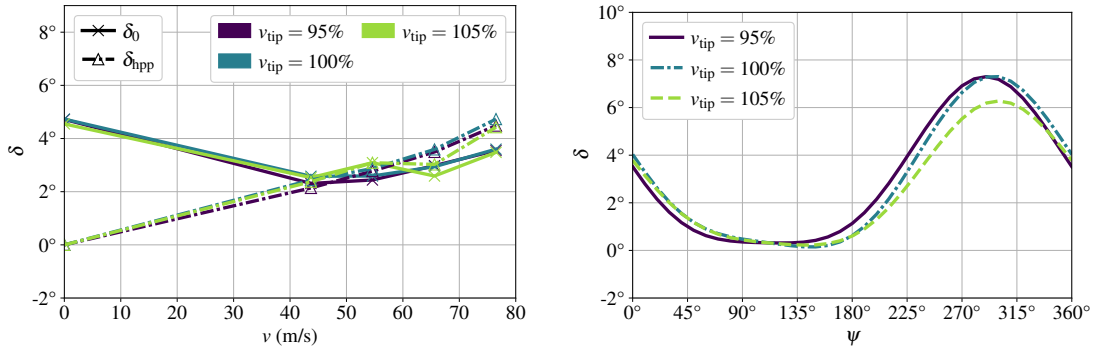

(a) Camber deflection magnitudes

(b) Azimuthal camber morphing at $v = 65.6$ m/s

Figure 4.28: Active-camber control inputs under variation of v_{tip}. Moderately higher peak camber deflections as v_{tip} decreases.

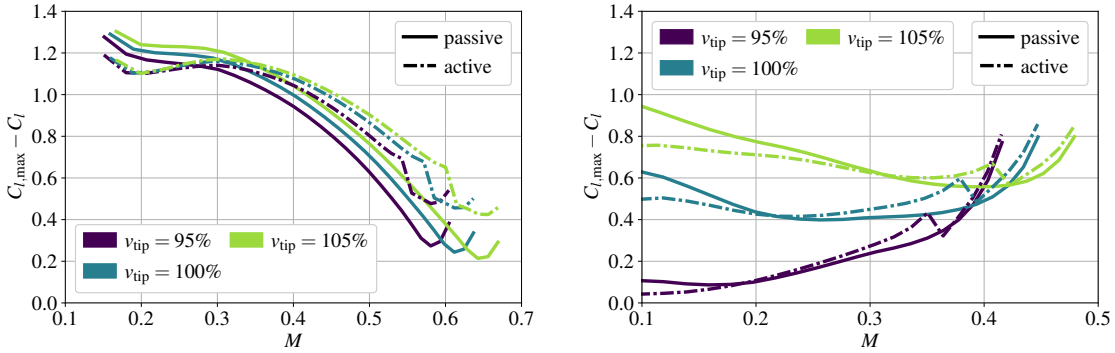

(a) $v = 0$ m/s

(b) $v = 65.6$ m/s

Figure 4.29: Stall margin ($SM = C_{l,\max} - C_l$) under variation of v_{tip} in hover and high-speed flight. (b) SM at the retreating blade ($\psi = 270°$).

a moderate reduction in tip speed of 5% resulted in a significant deterioration of the stall margin and vice versa. In this particular case, however, it is important to note that the stall margin is not the only parameter potentially limiting the flight envelope. Compressibility effects on the advancing side can also be the limiting factor, which can be improved by reducing v_{tip}. Therefore, the effect of tip speed variation on the available speed range of the helicopter cannot be determined unless it is known which is the more critical aspect in the actual case. However, since a performance improvement was obtained by reducing v_{tip}, the conservative approach was to assume that the stall margin is the limiting factor, since the compressibility effects were mitigated by this change.

Thus, from a rotor performance point of view, a reduction of v_{tip} for both the active and the passive rotor would be recommended, as it improved the rotor efficiency over the entire flight envelope. In addition, a reduction in rotor noise is quite likely due to the reduced compressibility effects on the advancing side. However, adverse effects on loads and stall margin are expected. The question of whether active camber can be used to restore some of the stall margin and reduce the rotor loads resulting from such design changes is discussed in Section 4.2.3.

Interim conclusions:
Overall, a moderate interdependence between baseline rotor design aspects and active-camber-induced power gains was observed. As the efficiency of the baseline rotor increased, the power gain from active camber was either indifferent or moderately reduced. Only by introducing a blade taper ratio and increasing the rotor radius was the power gain approximately maintained as the baseline rotor performance improved. A similar trend was observed for the mean chord length c. While the baseline rotor performance was only marginally affected, the power gain from active camber increased as c was reduced. Most of the rotor design modifications had a greater effect on efficiency in hover than in high-speed flight. This supports the hypothesis that the rotor design was selected primarily on the basis of high-speed flight requirements. This is further supported by the fact that any improvements in passive rotor efficiency came at the expense of rotor hub loads at high speeds. In terms of structural properties, blade torsional elasticity contributed substantially to the active-camber-induced power savings. However, this was mainly due to the inefficiency of the passive rotor at low torsional stiffness. Therefore, reducing the torsional stiffness was not suitable to increase the overall efficiency of the active rotor. With respect to active-camber control inputs, the main characteristic of optimal inputs was always the same. Only the mean camber deflection was a bit more sensitive to changes in the baseline rotor design.

In terms of possible rotor design targets, most changes had a similar effect on both active and passive rotor efficiency. Only the relative power gains from active camber were often adversely affected. Small differences in design targets between passive and active rotors were obtained for chord length (i.e., a scaling of the entire airfoil cross section) and blade twist, which should be considered when designing a rotor for use with active camber. However, when rotor loads are considered, the design targets for passive and active rotors are expected to diverge further. This is because passive rotors are more limited with respect to oscillatory loads, while active camber has the potential to actively reduce these loads if an appropriate control scheme is used. This aspect will be further discussed in the following section by taking these loads more into account in the objective function.

4.2 Combined Modification of Multiple Rotor Design Aspects

In this section, the relationship between passive rotor efficiency and active-camber-induced power gains is further investigated. This includes an assessment of the applicability of previous results to more efficient rotor systems. In addition, the ability of active camber to produce indirect gains, i.e., gains that cannot be directly attributed to active camber but are made possible by offsetting the negative side effects of modifying the rotor design, was investigated. For this study, the results of the previous section were used to estimate a more efficient rotor configuration. This approach was based on the assumption that a superposition of multiple beneficial modifications would result in an even more efficient configuration. To evaluate the success of this approach, the target configuration was approached using intermediate steps as described in more detail below. Since

variations in rotor radius and rotor tip speed are involved, the entire section compares different configurations based on flight speed v instead of the advance ratio μ.

4.2.1 Selection of Suitable Rotor Design Modifications

In order to derive the most efficient rotor based on the results presented in the last section, modifications were selected solely based on their impact on rotor performance. Since the active rotor was always more efficient than the corresponding passive rotor, the decision for design modifications was based on the active rotor cases. Of all baseline rotor variations presented in Section 4.1, only torsional stiffness was neglected for the following study. This is because it was not considered an appropriate design parameter due to its irrelevant effect on the active rotor efficiency. For most of the remaining modifications, a clear statement could be made about their effect on the overall efficiency. Only the built-in blade twist showed an opposite behavior for different flight speeds. Eventually, a blade twist of $\theta_{tw} = -12°$ was considered to be a good compromise, as it resulted in near-optimal performance improvements at hover and high speeds. The resulting rotor modifications, which were found to enhance rotor performance, are listed in Table 4.1.

Table 4.1: Baseline rotor modifications.

Variable	Symbol	New value	Δ to baseline
Rotor blade built-in twist	θ_{tw}	-12°	-4°
Rotor blade chord	c	90%	-10%
Rotor blade taper	t	50%	-50%
Rotor tip speed	v_{tip}	95%	-5%
Rotor radius	R	105%	+5%

Their effect on the rotor power is summarized in Fig. 4.30 for both the passive (Fig. 4.30a) and active (Fig. 4.30b) cases. It shows that although the selection was mainly based on the active rotor power, the passive rotor power also generally improved. Only the variation of the chord length was quite insignificant in terms of passive rotor power. On the other hand, the increase in the built-in twist was only beneficial for the passive rotor, i.e., it had a negligible effect on the active rotor. As a result, the same rotor modifications could be used to approximate the most efficient passive and active configurations within the predefined scope of modifications.

Since only the resulting total rotor power was considered in this selection process, the relative power gains from active camber were not correspondingly improved by these rotor design changes. In fact, as shown in Fig. 4.30c, all rotor modifications that improved the passive rotor efficiency had a (moderately) negative or neutral effect on relative power gains. Only a reduction in chord length, which was essentially indifferent in terms of the passive rotor power, resulted in a greater relative improvement from the active camber mechanism.

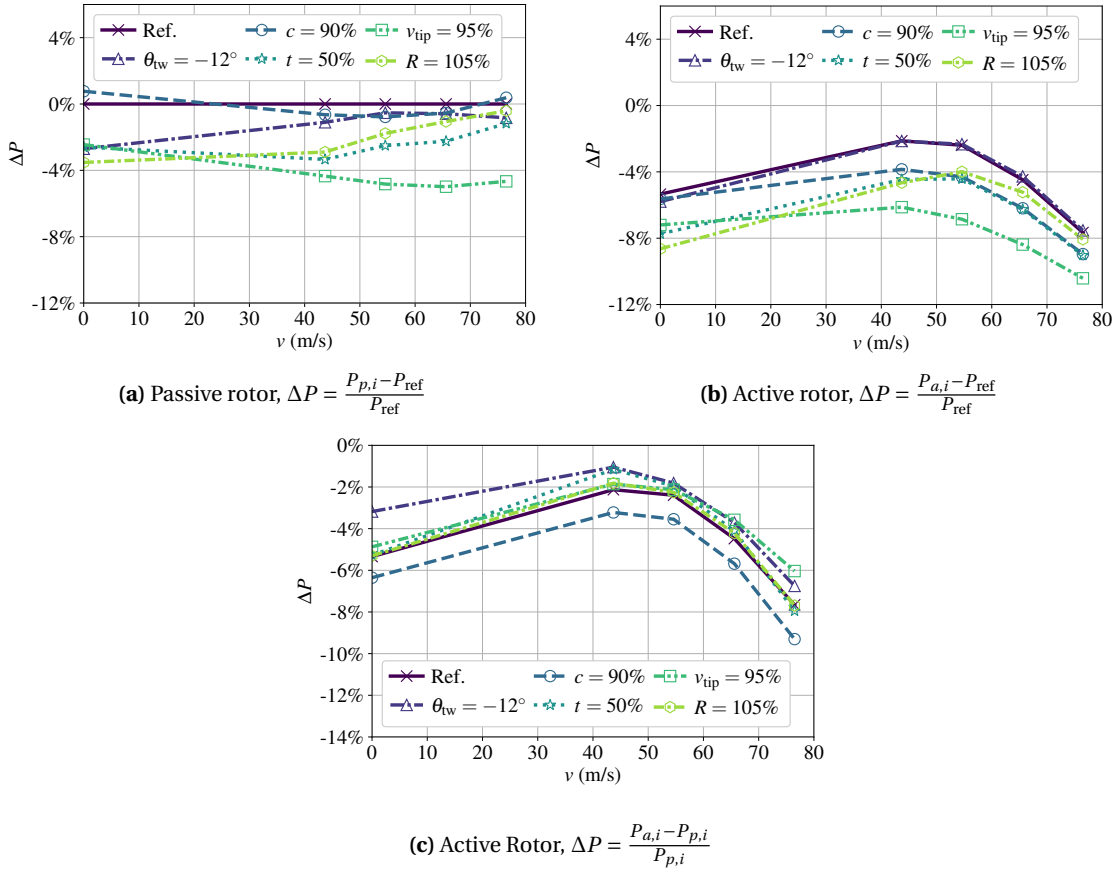

(a) Passive rotor, $\Delta P = \frac{P_{p,i} - P_{ref}}{P_{ref}}$

(b) Active rotor, $\Delta P = \frac{P_{a,i} - P_{ref}}{P_{ref}}$

(c) Active Rotor, $\Delta P = \frac{P_{a,i} - P_{p,i}}{P_{p,i}}$

Figure 4.30: Summary of the previously investigated separate variation of rotor design parameters. Comparison of the required rotor power for specific modifications (P_i) and the original passive Bo 105 reference (Ref.) rotor power (P_{ref}).

As shown in Fig. 4.31, the passive rotor loads at $v = 65.6$ m/s increased due to the rotor modifications. This was because only the rotor efficiency was considered when selecting the rotor modifications presented However, when active camber was applied, most of the loads were attenuated compared to the corresponding (modified) passive case. Only the pitch-link loads increased slightly for some of the baseline modifications.

With respect to the stall margin of the hovering rotor (see Fig. 4.32), the rotor modifications did not have a significant effect. However, as shown previously, the stall margin was notably higher when active camber was applied. In high-speed flight ($v = 65.6$ m/s, see Fig. 4.33), a major effect on the stall margin was observed. In particular, a reduction of the rotor tip speed resulted in a significantly lower stall margin at $\psi = 270°$. In general, most of the modifications had a negative effect on the stall margin, with the exception of the rotor radius.

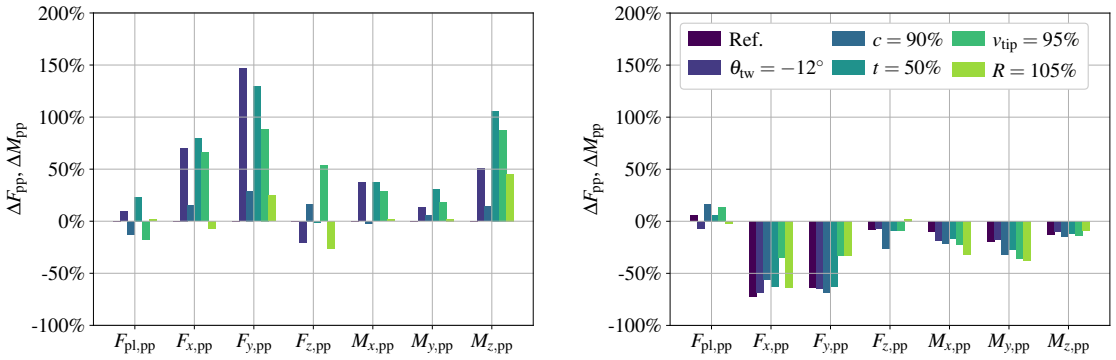

(a) Passive rotor, $\Delta() = \frac{()_{pp,i} - ()_{pp,ref}}{()_{pp,ref}}$

(b) Active rotor, $\Delta() = \frac{()_{pp,a,i} - ()_{pp,p,i}}{()_{pp,p,i}}$

Figure 4.31: Peak-to-peak forces and moments (rotor hub and pitch links) resulting from the previously presented rotor design modifications at high speed ($v = 65.6$ m/s). (a) Passive rotor loads in comparison to the original Bo 105 rotor (Ref.). (b) Difference in rotor loads between the active and passive modified rotors.

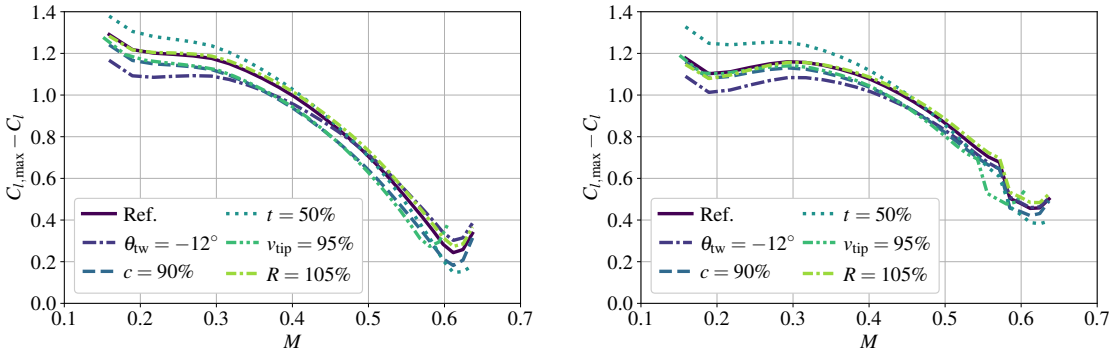

(a) Passive rotor

(b) Active rotor

Figure 4.32: Stall margin ($SM = C_{l,max} - C_l$) resulting from the previously presented rotor design modifications in hover ($v = 0$ m/s).

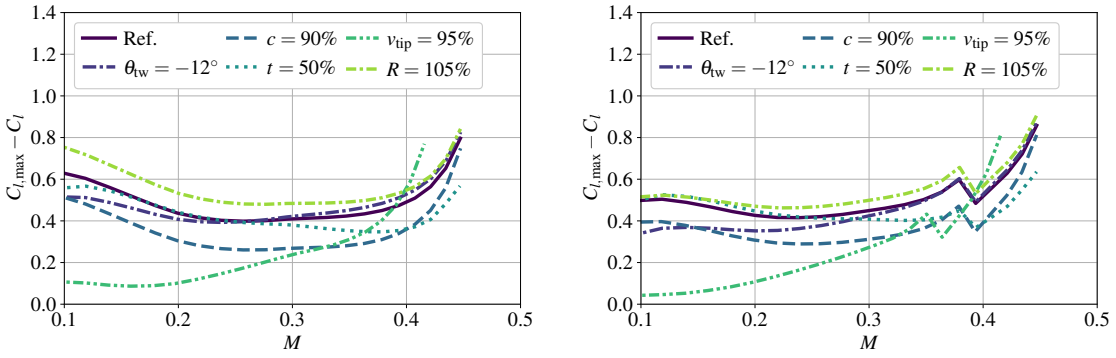

(a) Passive rotor

(b) Active rotor

Figure 4.33: Stall margin ($SM = C_{l,max} - C_l$) resulting from the previously presented rotor design modifications in high-speed flight ($v = 65.6$ m/s). (b) SM at the retreating blade ($\psi = 270°$).

4.2.2 Simultaneous Variation of Rotor Parameters

In the following, the previously identified modifications that improved the efficiency of the baseline rotor (see Table 4.1) were superimposed, assuming that the benefits would largely add up. The purpose was to assess whether this active-camber concept is relevant also for modern rotors that are more efficient than the Bo 105 rotor used in previous parts of this study. The parameter changes were applied in a stepwise manner towards the determined rotor design target (denoted as τ_R), i.e., in 20% steps. This was done mainly to avoid overshooting a possible optimum by superimposing all the previously discussed design variations. It was also intended to provide insight into the existing trends. The resulting rotor parameters of this stepwise variation are listed in Table 4.2. In terms of chord variation, the entire airfoil was always scaled, maintaining the original NACA23012 airfoil with a thickness-to-chord ratio of 12%.

Table 4.2: Simultaneous modification of multiple baseline rotor design parameters.

Variable	Unit	$\tau_R = 0\%$	$\tau_R = 20\%$	$\tau_R = 40\%$	$\tau_R = 60\%$	$\tau_R = 80\%$	$\tau_R = 100\%$
θ_{tw}	deg	-8	-8.8	-9.6	-10.4	-11.2	-12
c_{root}	m	0.27	0.2839	0.3000	0.3188	0.3411	0.3680
c_{tip}	m	0.27	0.2556	0.2400	0.2231	0.2047	0.1840
v_{tip}	m/s	218.61	216.42	214.24	212.05	209.87	207.68
R	m	4.912	4.961	5.010	5.059	5.108	5.158
Ω	RPM	425.0	420.75	416.5	412.25	408	384.524

c_{root} is the chord length at $r = 0.22$.

Figure 4.34 compares the separate modification of the rotor design parameters and the combined modification of the parameters for the passive and active rotors. It shows that the approach taken was successful, as the efficiency gains of the isolated modifications added up quite well when combined. Thus, for both the passive and active rotors, the superposition of the baseline rotor modifications resulted in a substantially more efficient rotor.

In Fig. 4.35, the intermediate steps towards the defined design target of the rotor ($\tau_R = 100\%$) are shown. The efficiency of both the passive and active rotors increased continuously as the final rotor design was approached. Thus, there was no performance optimum before $\tau_R = 100\%$ was reached, and overshooting of the optimal configuration was ruled out. Instead, it is expected that further development in the same direction will continue to improve rotor performance. However, this would lead to an increasingly unrealistic scenario, as discussed below. The available power gains induced by active camber are shown in Fig. 4.35b. In hover, the power gain from active camber was almost halved by this change in rotor design. However, even in the most efficient configuration, active camber reduced the power of the hovering rotor by about 3% compared to the total power consumption. As the flight speed increased above 50 m/s, the performance gains from active camber were only marginally reduced by the rotor design changes. This indicates that performance gains at high speeds are largely independent of the underlying rotor aerody-

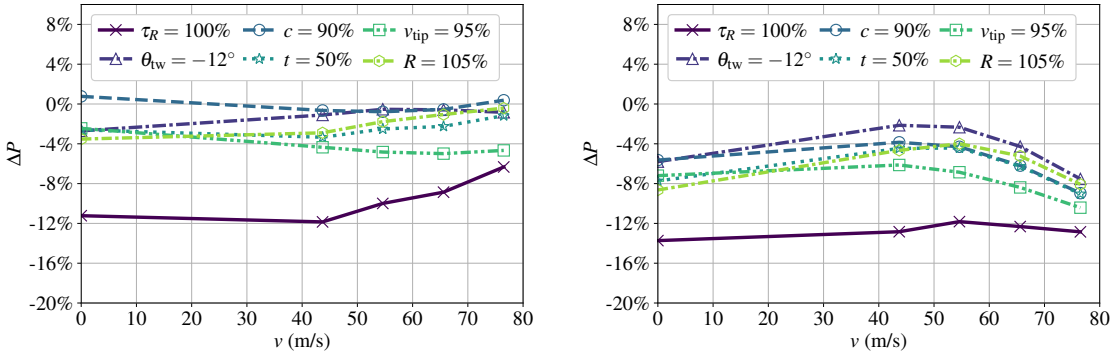

(a) Passive rotor

(b) Active rotor

Figure 4.34: Comparison of separate and combined ($\tau_R = 100\%$) modification of rotor design parameters in terms of rotor efficiency improvements. $\Delta P = \frac{P_i - P_{\text{ref}}}{P_{\text{ref}}}$.

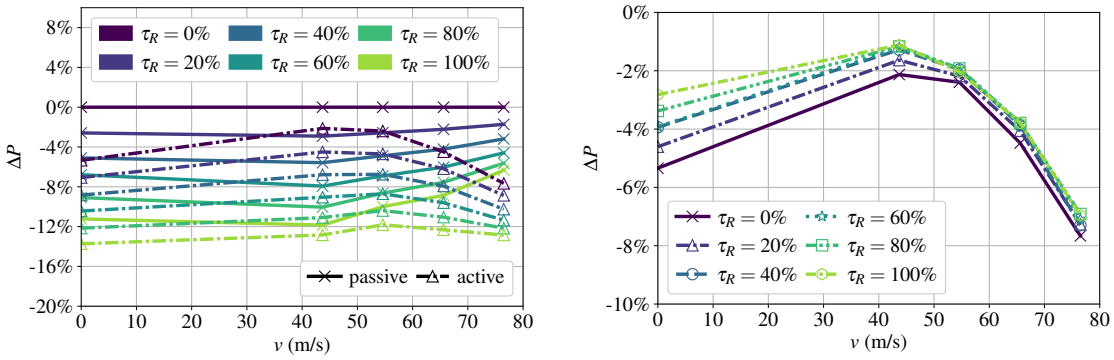

(a) $\Delta P = \frac{P_{\tau_{R,i}} - P_{p,\tau_R=0\%}}{P_{p,\tau_R=0\%}}$

(b) $\Delta P = \frac{P_{a,\tau_{R,i}} - P_{p,\tau_{R,i}}}{P_{p,\tau_{R,i}}}$

Figure 4.35: Gradual modification ($\Delta\tau_R = 20\%$) of multiple rotor parameters. (a) Passive (P_p) and active (P_a) rotor power. (b) Relative power gain due to active camber.

namic efficiency. Thus, even for efficient rotor systems, active camber can improve rotor power consumption in hover and especially in high-speed flight ($4\% < \Delta P < 7\%$ at $v \geq 65.6$ m/s).

While Fig. 4.35 was based on spanwise uniform actuation, Fig. 4.36 shows the additional benefits of using spanwise varying active camber actuation. Two cases are shown, a hovering case and a high-speed flight case at $v = 65.58$ m/s (which corresponds to $v = 65.6$ m/s in terms of the unmodified Bo 105 rotor). In hover, the additional power gains decreased continuously with increasing τ_R. In high-speed flight, the amount of power saved by the spanwise varying actuation remained approximately constant. Overall, at $\tau_R = 100\%$, both flight states yielded additional power savings of about 0.3% by varying the control inputs in the spanwise direction. Although these values were not very impressive, the additional benefit in terms of feasibility must be considered when evaluating the merits of this actuation mode.

In terms of the required camber control inputs, the mean camber deflection in particular was af-

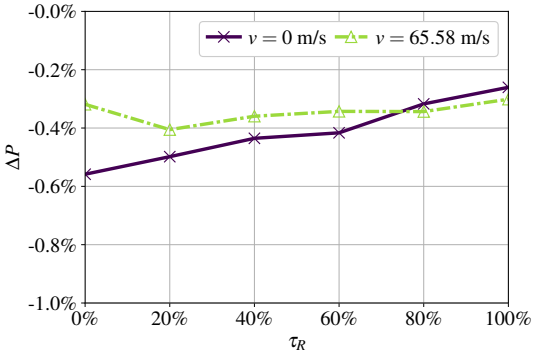

Figure 4.36: Moderate reduction in additional power savings from spanwise variation of camber morphing ($\vartheta = 40\%$) towards $\tau_R \to \infty$. $\Delta P = \frac{P_{a,\tau_{R,i},\vartheta=40\%} - P_{a,\tau_{R,i},\vartheta=0}}{P_{a,\tau_{R,i},\vartheta=0}}$.

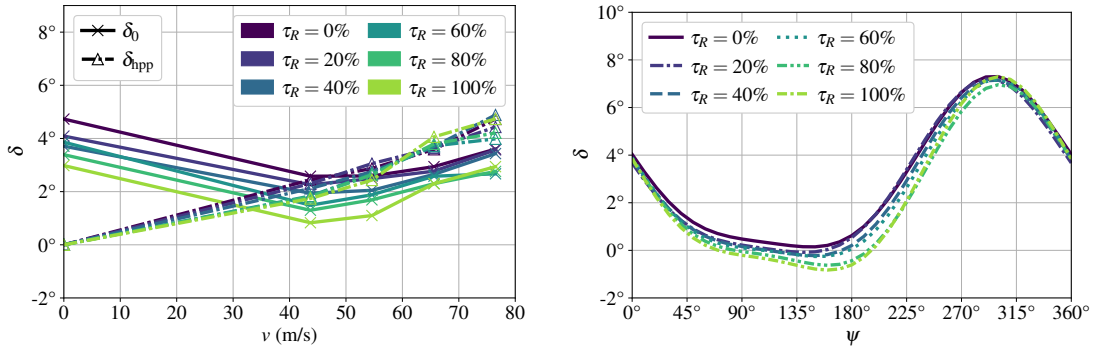

(a) Camber deflection magnitudes

(b) Azimuthal camber morphing at $v = 65.58$ m/s

Figure 4.37: Active-camber control inputs under variation of τ_R. Decreasing mean camber deflections and thus negative deflections on the advancing side as τ_R increases.

fected by the variation of the baseline rotor, as shown in Fig. 4.37. As the efficiency of the baseline rotor increased, lower mean camber deflections were required (see Fig. 4.37a). The actuation amplitudes and the resulting control signals were only marginally affected, as shown for high-speed flight in Fig. 4.37b.

Therefore, it was concluded that the transferability of the results to other, especially more efficient rotor systems is quite good for high-speed flight cases. This applies to both the power savings that can be achieved and to the control inputs (except for the static part of the control signal) required to produce them. For low-speed flight, the results were more dependent on the baseline rotor characteristics. Nevertheless, it is assumed that even with well-optimized rotors there is still relevant potential for optimization of the hovering performance.

Figures 4.38 and 4.39 compare the effect of changing the baseline rotor characteristics on the power and thrust distribution of both the passive and active rotors. The passive rotor modifications resulted mainly in a reduction of the power consumption in the outer region of the rotor (see Figs. 4.38c and 4.38f), while the power consumption in the inner region increased slightly. Hence,

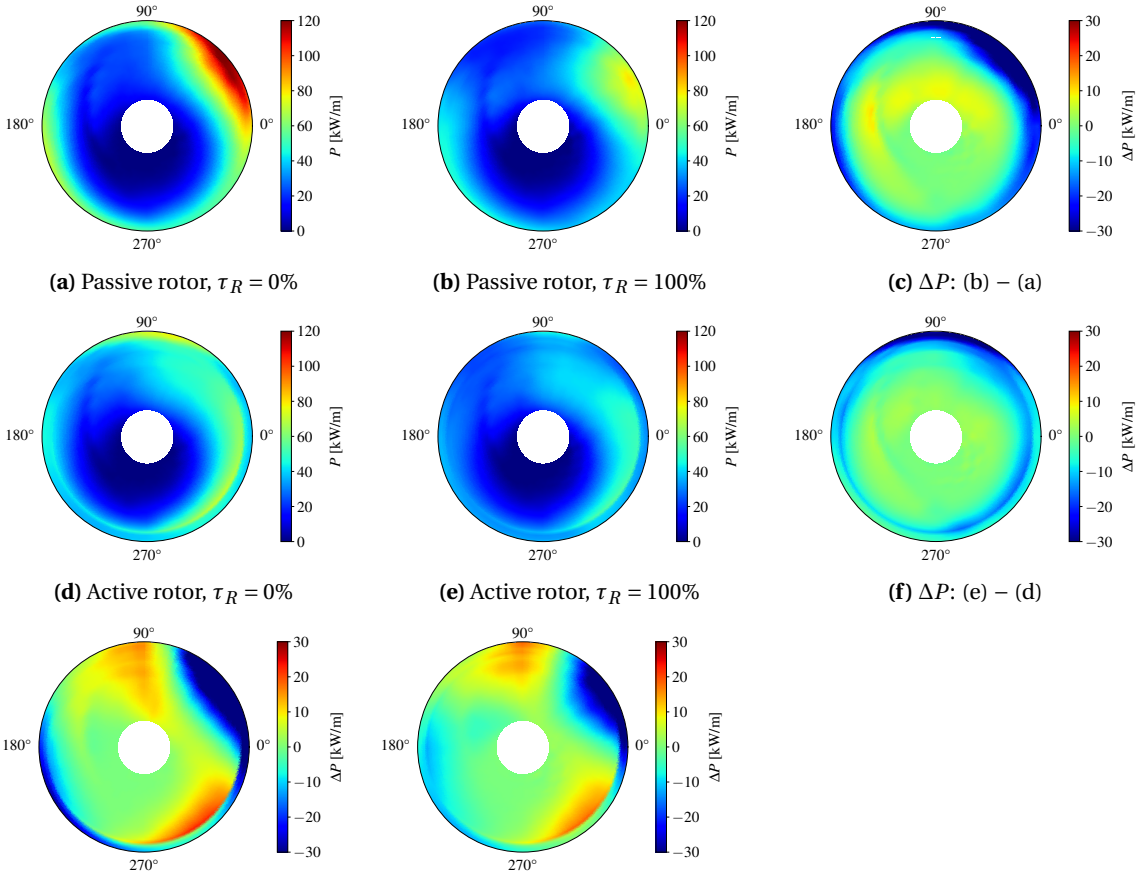

(a) Passive rotor, $\tau_R = 0\%$ **(b)** Passive rotor, $\tau_R = 100\%$ **(c)** ΔP: (b) − (a)

(d) Active rotor, $\tau_R = 0\%$ **(e)** Active rotor, $\tau_R = 100\%$ **(f)** ΔP: (e) − (d)

(g) ΔP: (d) − (a) **(h)** ΔP: (e) − (b)

Figure 4.38: Rotor power distribution in high-speed flight ($v = 65.58$ m/s) under variation of τ_R. (c) and (f) Difference in rotor power due to rotor design modifications. (g) and (h) Difference in rotor power due to active camber morphing.

any azimuthal variation due to the design change was small and was attributed to the nonlinear response of the aerodynamic forces to these design changes. With active camber control (see Figs. 4.38g and 4.38h), a more complex redistribution of power consumption was obtained, mainly along the rotor azimuth. Interestingly, it was almost independent of the baseline rotor characteristics. While the high-power regions were considerably relieved, the power consumption on both the retreating and advancing sides was increased. Therefore, this primary ability of active camber to influence the azimuthal distribution of aerodynamic forces and the resulting power demand was not noticeably degraded by modifications to the baseline rotor.

Another reason why the improvement of the baseline rotor efficiency did not significantly affect the active rotor performance is shown in Figure 4.39. The relief of the blade tip loading due to the design changes resulted in a further reduction of the thrust on the advancing blade side. This further reduced the low or even negative thrust in this region and opened up additional potential for active camber to beneficially redistribute thrust along the rotor azimuth. Note that the total thrust of all cases compared was the same, but the rotor disk area increased due to the modifications. Therefore, the same amount of thrust was distributed over a (slightly) larger area.

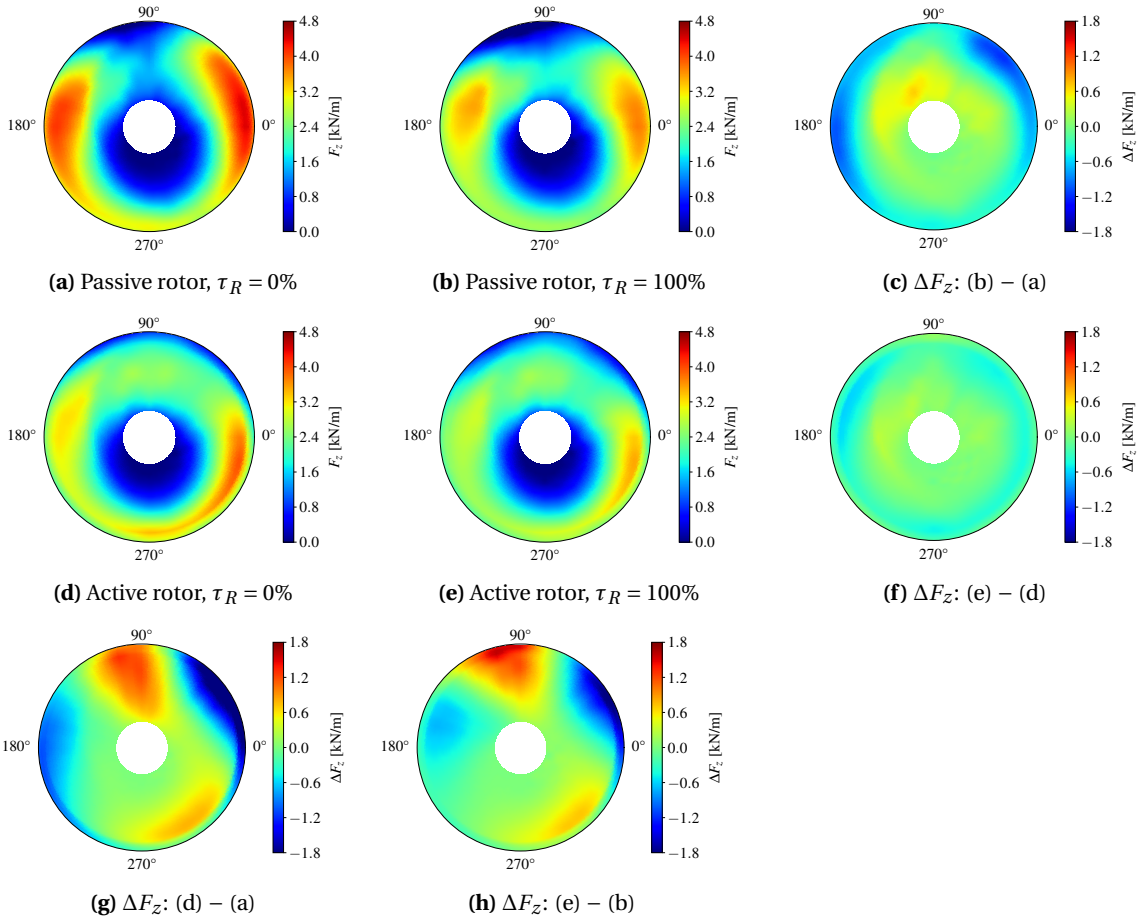

(a) Passive rotor, $\tau_R = 0\%$ **(b)** Passive rotor, $\tau_R = 100\%$ **(c)** ΔF_z: (b) − (a)

(d) Active rotor, $\tau_R = 0\%$ **(e)** Active rotor, $\tau_R = 100\%$ **(f)** ΔF_z: (e) − (d)

(g) ΔF_z: (d) − (a) **(h)** ΔF_z: (e) − (b)

Figure 4.39: Rotor thrust F_z in high-speed flight ($v = 65.58$ m/s) under variation of τ_R. (c) and (f) Difference in rotor thrust due to rotor design modifications. (g) and (h) Difference in rotor thrust due to active camber morphing.

As expected from the individual application of design modifications to the rotor (see Section 4.1), most of the peak-to-peak rotor hub loads deteriorated considerably when the rotor design modifications were combined (see Fig. 4.40). In particular, the peak-to-peak rotor shaft torque ($M_{z,\mathrm{pp}}$) and the in-plane hub forces increased significantly due to the above-presented rotor modifications (see Fig. 4.40a). Therefore, these passive rotor modifications would not be feasible if the rotor loads were not to exceed the baseline Bo 105 rotor loads. According to the definition of the cost function, the active rotor loads were lower than the passive rotor loads but often higher than the passive rotor loads before modification (see Fig. 4.40b).

Regarding the stall margin (see Fig. 4.41), no major effect was obtained at hover by modifying the rotor towards $\tau_R = 100\%$ for both the passive and active rotors. The benefit of camber morphing was largely maintained when the rotor design was changed. In high-speed flight ($v = 65.6$ m/s), the stall margin evaluated at $\psi = 270°$ was significantly reduced towards $\tau_R = 100\%$. This was true for both the passive and the active rotor. Thus, the efficiency gains due to these rotor modifications were most likely accompanied by a reduction of the feasible flight envelope and the ability to provide sufficient lift near the high-speed limit of the flight envelope, especially with respect to

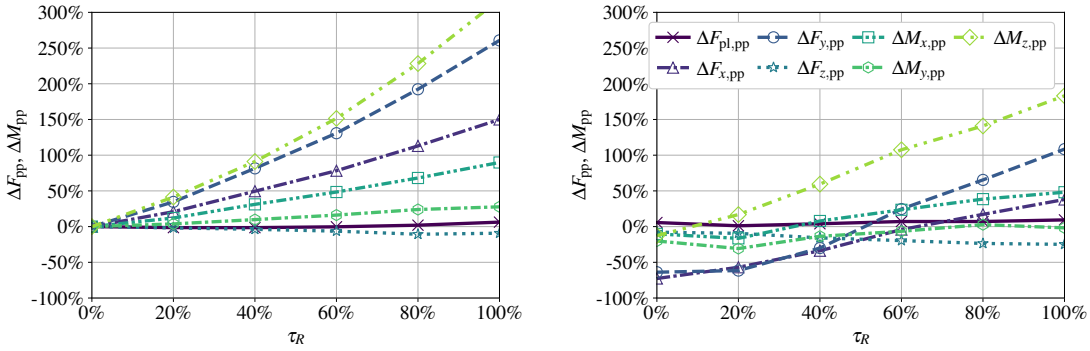

(a) Passive rotor

(b) Active rotor

Figure 4.40: Peak-to-peak forces and moments (rotor hub and pitch links) under variation of τ_R. Comparison between (a) the passive and (b) the active rotor at high speed (v = 65.6 m/s). $\Delta() = \frac{()_{pp,\tau_{R,i}} - ()_{pp,p,\tau_R=0\%}}{()_{pp,p,\tau_R=0\%}}$.

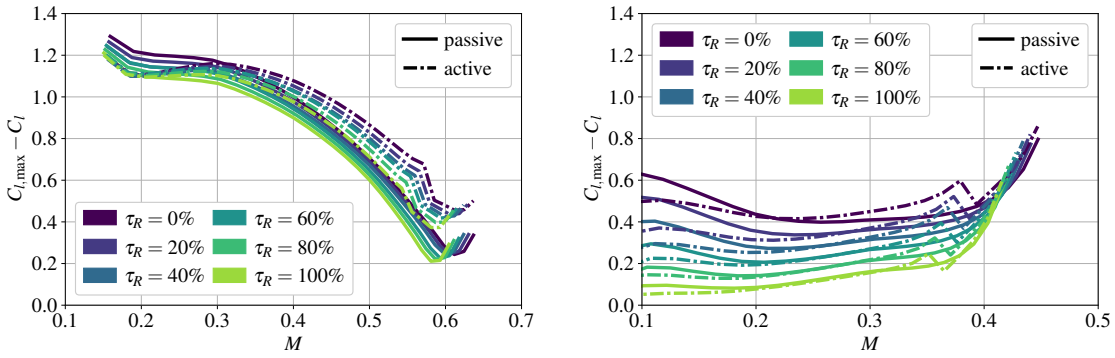

(a) $v = 0$ m/s

(b) $v = 65.6$ m/s

Figure 4.41: Stall margin ($SM = C_{l,\max} - C_l$) under variation of τ_R in hover and high-speed flight. (b) Reduction in retreating-blade SM ($\psi = 270°$) as τ_R increases.

flight maneuvers. Overall, considering the penalties in terms of rotor loads and stall margin, it is assumed that the optimization of the helicopter rotor efficiency is limited due to the requirements of other disciplines. This makes it unlikely to realize the most efficient configuration presented in this work ($\tau_R = 100\%$), at least in terms of a passive design.

4.2.3 Potential for Indirect Active-Camber-Induced Power Savings

As discussed above, the previously introduced rotor design changes have improved rotor performance, but the rotor hub loads and stall margin have been adversely affected. This section discusses the extent to which active camber actuation can compensate for these drawbacks while still improving rotor efficiency. None of the gains from passive rotor modifications were possible without compromising loads and stall margin. Consequently, for any step towards τ_R = 100% where it is possible to offset these penalties by using an appropriate active-camber control scheme, the resulting power savings could be attributed to the active camber as an indirect gain.

Although a real-world design may shift the focus further towards load reduction, this can also be understood as an approach to measure the benefits of this mechanism, which are generated in different disciplines, in a single value. This approach is based on the assumption that there is no passive measure available to neutralize the penalties resulting from the rotor design change. While it is likely that solutions exist to mitigate some of the adverse effects, it is assumed that the majority of the penalties will remain or the problem will simply be moved to a different starting point.

For this study, the parameters of the cost function, i.e., normalization, weights, and exponents, had to be modified in order to achieve the objective just described. First of all, the unmodified passive Bo 105 rotor had to be used as the reference instead of the modified passive rotor as before (to penalize exceeding the original Bo 105 conditions). In addition, the weighting of the loads and the stall margin had to be increased. Finally, a higher exponent was needed to ensure that the value of the cost function increased more rapidly when exceeding the value of the reference case. In the following, the variable o_A describes the objective definition used earlier in this chapter, while o_B describes the objective definition now introduced. The exact parameters used in the cost function (Eq. 2.13) are given in Table 4.3.

Table 4.3: Objective function parameters o_A, o_B, and o_C.

	o_A			o_B			o_C		
Objectives	w	e	Ref.	w	e	Ref.	w	e	Ref.
P	0.96	10	τ_R	0.83	20	$\tau_R = 0\%$	0.84	20	$\tau_R = 0\%$
F_{pl}	0.005	10	τ_R	0.01	20	$\tau_R = 0\%$	0.01	20	$\tau_R = 0\%$
F_x	0.005	10	τ_R	0.01	20	$\tau_R = 0\%$	0.01	20	$\tau_R = 0\%$
F_y	0.005	10	τ_R	0.01	20	$\tau_R = 0\%$	0.01	20	$\tau_R = 0\%$
F_z	0.005	10	τ_R	0.01	20	$\tau_R = 0\%$	0.01	20	$\tau_R = 0\%$
M_x	0.005	10	τ_R	0.01	20	$\tau_R = 0\%$	0.01	20	$\tau_R = 0\%$
M_y	0.005	10	τ_R	0.01	20	$\tau_R = 0\%$	0.01	20	$\tau_R = 0\%$
M_z	0.005	10	τ_R	0.01	20	$\tau_R = 0\%$	0.01	20	$\tau_R = 0\%$
SM	0.005	10	τ_R	0.10	20	$\tau_R = 0\%$	0	-	-

A high-speed flight case of v = 65.6 m/s (with respect to the original Bo 105 rotor) was investigated, as this flight state is the most relevant in terms of oscillating loads and retreating-blade stall. The result is shown in Fig. 4.42. Figure 4.42a shows the relationship between rotor performance and modification of the rotor design (τ_R), for both the passive and active (o_A and o_B) rotor cases. The variation of the rotor power of the passive and active rotor (o_A) had almost the same gradient with respect to τ_R. Thus, as discussed in the previous section, the relative gains from active camber were almost constant. When the cost function was redefined according to o_B, the gradient between power savings and τ_R was reduced. At the same time, it was successfully prevented from exceeding the peak-to-peak loads of the original Bo 105 rotor, but only up to a value of about τ_R = 40% (see Figs. 4.42b to 4.42d). Accordingly, when utilizing the power savings

at $\tau_R = 0\%$ (approximately $\Delta P = 4\%$) as a reference, additional (indirect) power savings of over 2% (indicated by the red area in Fig. 4.42a) were achieved, resulting in a total of over 6%. Beyond $\tau_R = 40\%$, it was no longer possible to meet the predefined target in terms of loads and stall margin (see Figs. 4.42b to 4.42f). That is, for $\tau_R = 60\%$ or greater, no active-camber control inputs were found where loads did not exceed the baseline level and at the same time the stall margin was not reduced. Therefore, cases with $\tau_R > 40\%$ were considered irrelevant in the given context.

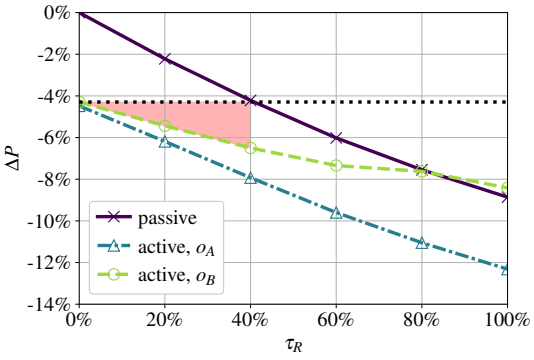

(a) $\Delta P = \frac{P - P_{p,\tau_R=0}}{P_{p,\tau_R=0}}$

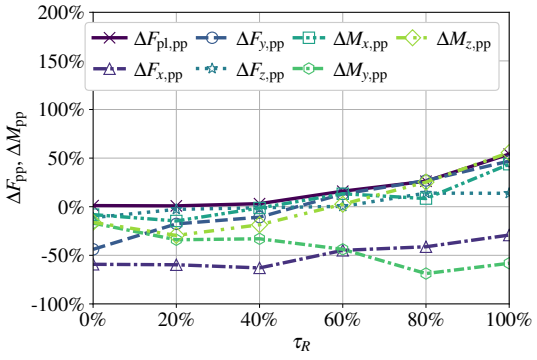

(b) $\Delta() = \frac{()_{pp,a} - ()_{pp,p,\tau_R=0}}{()_{pp,p,\tau_R=0}}$, o_B

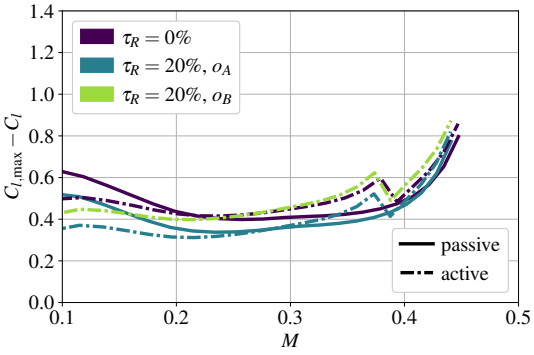

(c) SM at $\psi = 270°$, $\tau_R = 20\%$

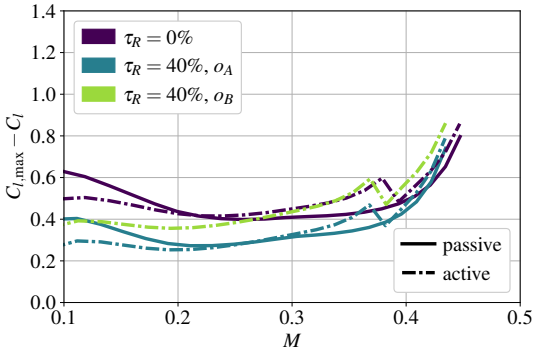

(d) SM at $\psi = 270°$, $\tau_R = 40\%$

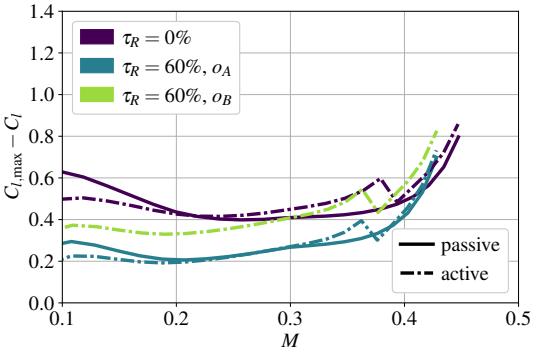

(e) SM at $\psi = 270°$, $\tau_R = 60\%$

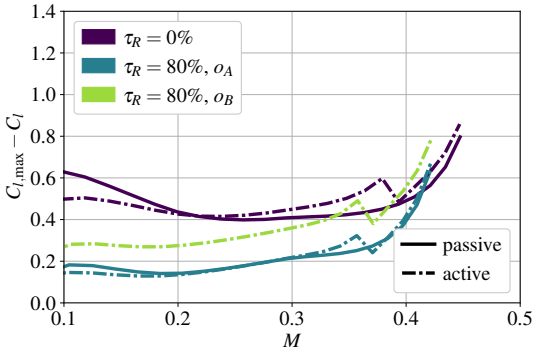

(f) SM at $\psi = 270°$, $\tau_R = 80\%$

Figure 4.42: Rotor power, rotor loads, and retreating-blade stall margin for different degrees of baseline rotor modifications (τ_R) and different cost function parameters ($v = 65.6$ m/s). The red area in (a) indicates the additional indirect power gains from active camber.

In Fig. 4.43, the camber control inputs are shown based on the different optimization targets, o_A and o_B, for a modification of the baseline rotor in the most relevant range from $\tau_R = 20\%$ to $\tau_R = 60\%$. In the case of o_B, slightly higher deflections were required, and the peak deflection was slightly shifted to smaller azimuth positions (towards $\psi = 270°$). This is probably due to the higher stall margin required near $\psi = 270°$. Apart from that, the most pronounced offset in the control signal was obtained at $\psi = 90°$. This was assumed to smooth M_z, which gave the most penalty in the o_A scenario (see Fig. 4.40b). The reason why this resulted in an improvement of M_z is the low amount of torque at this rotor position compared to other azimuth positions (see Fig. 3.18b).

It should also be noted that this modification to the baseline rotor also improved efficiency at other advance ratios including hovering and medium-speed flight. For instance, in hover, additional gains of about 3% were obtained when comparing the active rotor power with $\tau_R = 0\%$ and $\tau_R = 40\%$. Hence, the indirect improvements added by the rotor design modifications were in the order of 50% of the direct power savings and resulted in a total improvement of more than 8% in hover. Furthermore, with $\tau_R = 40\%$, the tip Mach number was reduced by 2%, which could be beneficial in terms of noise.

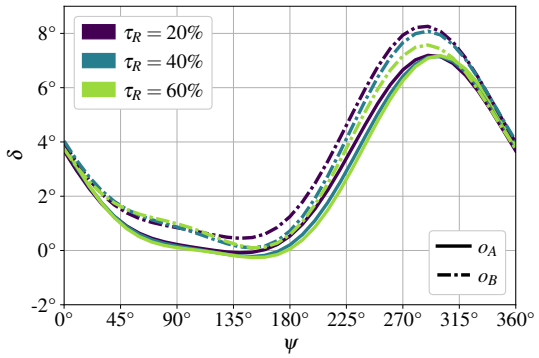

Figure 4.43: Azimuthal camber morphing for different degrees of baseline rotor modifications (τ_R) and different cost function parameters ($v = 65.6$ m/s).

Another aspect worth mentioning is the fact that indirect performance gains with active camber could also be achieved if the hover stall margin in hot and high conditions is a limiting factor for the blade design. That is, a significant improvement in the stall margin was achieved in hover. Similar to the previous approach regarding oscillatory loads and retreating-blade stall margin at high speeds, active camber could allow the use of reduced blade chord, blade thickness, rotational speed, or increased blade taper without running into blade stall when hovering under hot and high conditions.

4.2.4 Adjustment of Blade Structural Properties

The previous studies in this chapter considered rotor design changes only from an aerodynamic perspective. As described in Section 2.1.1, it was assumed that the blade design techniques offer sufficient flexibility to maintain the same mechanical properties even if the blade geometry changes. Up to a certain degree of variation in the blade geometry, this approach is justified and

represents the typical approach in the blade design process, where the structural properties of the blades are frozen as early as possible. However, if major changes are made to the cross-sectional dimensions, this assumption may no longer be valid. Since the applicability of this assumption could not be evaluated conclusively, the previous results are compared in the following with an analysis where the structural properties of the blade were scaled together with the external dimensions of the rotor blade cross-section. Details of this scaling are given in Section 2.1.1. The scaling factor λ is the ratio of the actual chord length to the chord length of the Bo 105 rotor blade (c = 0.27 m). For the blade root and tip positions, the values for c are given in Table 4.2. A real rotor design would probably be a mixture of the previous approach (no scaling of the structural properties, hereafter referred to as S_{Bo105}) and the present approach (proportional scaling of all involved thicknesses and dimensions of the blade structure, hereafter referred to as S_{mod}). Only the aerodynamically active region from r = 0.22 to r = 1 was modified in terms of geometry and thus also in terms of structural properties.

Influence of rotor blade structural properties during rotor design modifications:
A comparison of different strategies regarding the definition of rotor blade structural properties (S_{Bo105}, S_{mod}) during a gradual modification of the rotor blade geometry (represented by τ_R) is shown in Fig. 4.44. It shows that the described adjustment of the blade structural properties (S_{mod}) significantly improved the performance of the passive rotor at high speeds (see Fig. 4.44a). The active rotor power, on the other hand, was hardly affected (see Fig. 4.44b). As a result, the ability of active camber to improve rotor performance at high speeds was considerably reduced (see Fig. 4.44c). The previously found convergence to a value of 7% power saving at v = 76.5 m/s (see Section 4.2.2) was approximately halved when the structural properties of the blade were adjusted as described. In hover, the active-camber-related rotor power savings were not affected by this variation of the structural parameters and therefore the previous conclusions were still valid.

The following analysis focuses on the change in the passive rotor efficiency at high speeds, as this was essential for the reduction of the active-camber-induced power gains. Figure 4.44d shows for a high-speed flight condition (v = 76.51 m/s) the differences in the elastic twist with and without the described variation of the structural properties when changing the rotor design. It shows that the elastic blade twist on the advancing side was noticeably reduced when the mechanical parameter modification (S_{mod}) was applied in addition to the aerodynamic parameter modification. As a result, the negative thrust on the advancing side was relevantly reduced (see Fig. 4.45). Since the compensation of the negative thrust of the advancing blade was an important mechanism to generate rotor power with active camber, the effectiveness of the active camber was significantly reduced.

However, this enhancement of the passive rotor efficiency was accompanied by a massive deterioration in the oscillatory rotor hub loads, as shown in Fig. 4.46 for v = 65.6 m/s. Already the previous investigation of the pure modification of the blade aerodynamic parameters (S_{Bo105}) caused a notable increase of the peak-to-peak hub loads. While this trend was approximately in

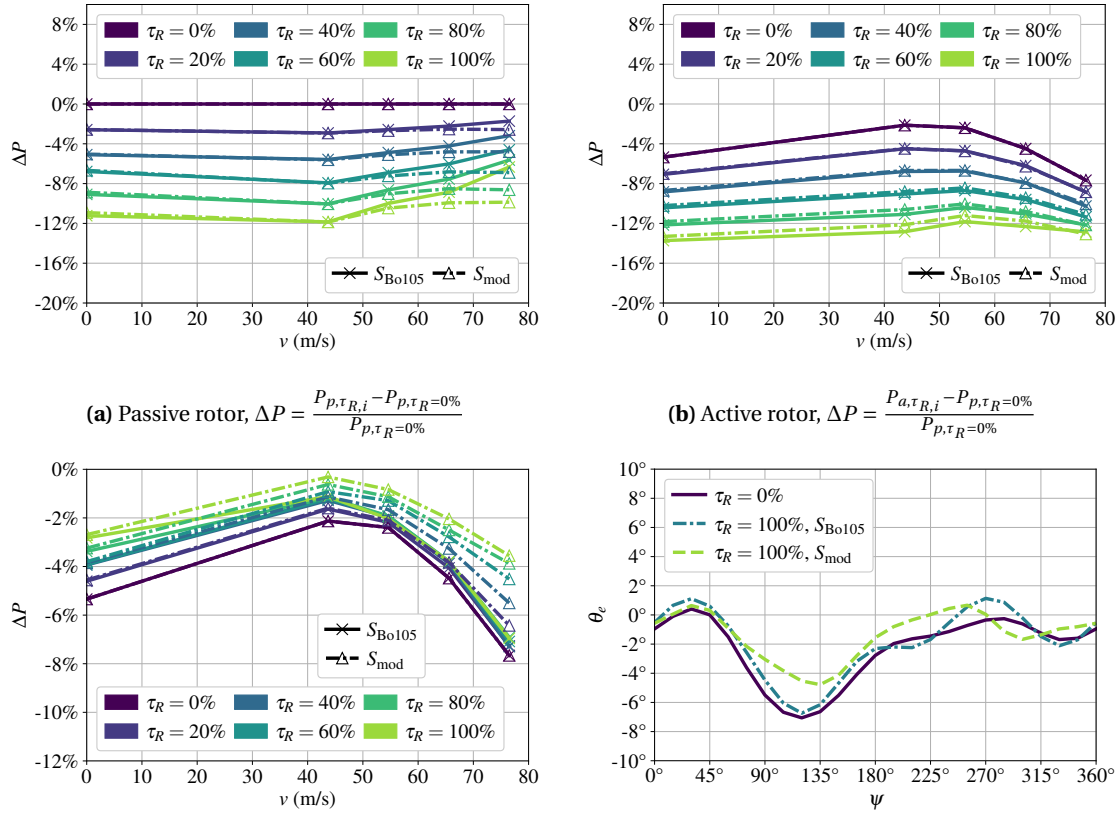

(a) Passive rotor, $\Delta P = \frac{P_{p,\tau_{R,i}} - P_{p,\tau_R=0\%}}{P_{p,\tau_R=0\%}}$

(b) Active rotor, $\Delta P = \frac{P_{a,\tau_{R,i}} - P_{p,\tau_R=0\%}}{P_{p,\tau_R=0\%}}$

(c) Power gains, $\Delta P = \frac{P_{a,\tau_{R,i}} - P_{p,\tau_{R,i},S_i}}{P_{p,\tau_{R,i},S_i}}$

(d) Passive rotor, $v = 76.5$ m/s

Figure 4.44: Comparison of different strategies in terms of defining the rotor blade structural properties ($S_{\text{Bo105}}, S_{\text{mod}}$) while gradually modifying multiple rotor parameters ($\Delta\tau_R = 20\%$). (a) Passive (P_p) and (b) active (P_a) rotor power. (c) Relative power gain due to active camber. (d) Torsional deformation of the rotor blades.

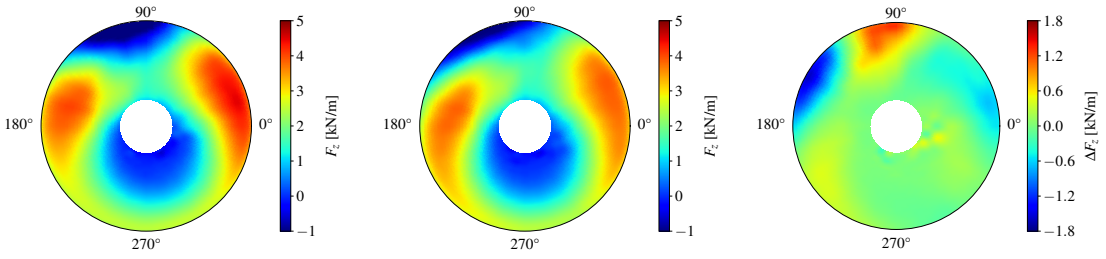

(a) S_{Bo105}

(b) S_{mod}

(c) ΔF_z: (b) − (a)

Figure 4.45: Comparison of the passive rotor thrust F_z for different rotor blade structural properties ($S_{\text{Bo105}}, S_{\text{mod}}$, each with $\tau_R = 100\%$) at high speed ($v = 76.5$ m/s). (c) Differences in rotor thrust due to changes in structural parameters.

linear relation to τ_R, the loads grew in a non-linear manner as the blade structural properties were included in this modification (see Fig. 4.46a). Only the peak-to-peak pitch-link force ($F_{\text{pl,pp}}$) and vertical hub force ($F_{z,\text{pp}}$) were reduced by such rotor modifications. The reduction in $F_{z,\text{pp}}$ was assumed to be at least partly related to the additional thrust in the region of $\psi = 90°$, as this resulted

in a better approximation of a uniform thrust distribution. The reduction in $F_{\mathrm{pl,pp}}$ was a direct result of the reduction in elastic twist. Note that this reduction in $F_{\mathrm{pl,pp}}$ made it a bit more difficult for the active-camber mechanism to produce power gains, since the goal was not to exceed the passive rotor loads.

The largest increase in loads was observed in the oscillatory in-plane forces ($F_{x,\mathrm{pp}}$ and $F_{y,\mathrm{pp}}$), but the oscillatory shaft torque ($M_{z,\mathrm{pp}}$) also underwent significant amplification. This was primarily attributed to the noticeable increase in the flap and lag motion of the rotor blades (see Fig. 4.47), which favors the development of an imbalance in the rotor system. Such displacements were caused by the reduction of mass near the blade tip. In fact, the associated reduction of the counteracting centrifugal force and the reduction of inertia resulted in an increased responsiveness of the blade tip displacement to (unsteady) aerodynamic forces. This outweighed the predominant increase in blade bending stiffness from $r = 0.22$ to $r = 0.64$ as a result of the blade taper ratio ($r_{\mathrm{ref}} = 0.75$) and chord length reduction.

In contrast to the bending motion of the rotor blades, the twisting of the rotor blades was not facilitated by the mass reduction in the outer area of the blade, since the torsional stiffness is much less dependent on centrifugal forces. As a result, the effect on the elastic twisting of the rotor blades was dominated by the overall higher torsional stiffness. This was supported by the use of a taper ratio that reduced the amount of aerodynamic moment generated near the blade tip. Altogether, the effect was similar to a pure increase of the rotor blade GJ (see Section 4.1.1).

When active camber was applied, the increase in loads was much less pronounced. Due to subtle redistribution of aerodynamic loads, active camber was able to efficiently eliminate most of the additional hub loads without sacrificing a relevant amount of power gains. An exception was observed for the rotor shaft torque $M_{z,\mathrm{pp}}$ (see Fig. 4.46b). This could be related to a reduced ability of active-camber mechanisms to precisely influence the lag motion of the blade compared to the flap and torsional motion. However, as discussed below, it was quite possible to absorb these high values of $M_{z,\mathrm{pp}}$ when the requirement to not exceed the retreating-blade stall margin of the passive rotor was dropped.

In summary, if significant portions of the negative thrust on the advancing side of the rotor blade are eliminated by static blade design measures, the potential for performance improvement with active camber is likely to decrease. A sophisticated tailoring of the torsional stiffness, bending-torsion coupling, and mass distribution of the rotor blades seems to be the most promising for this application. However, it is essential that such a rotor design does not exceed acceptable loads, does not lead to retreating-blade stall, and does not significantly degrade the hover performance of the rotor. In the current study, this was not achieved by the passive rotor design modifications. Therefore, the current reductions in active-camber-related performance gains were considered to be the result of an unrealistic scenario. Instead, similar to the purely aerodynamic modification of the rotor, such multidisciplinary design problems open the potential for active-camber systems to produce indirect power gains.

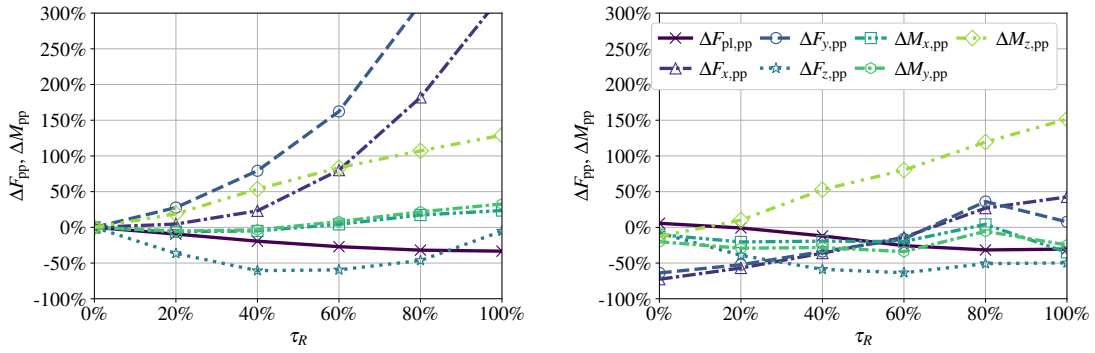

(a) Passive rotor **(b)** Active rotor

Figure 4.46: Peak-to-peak forces and moments (rotor hub and pitch links) under variation of τ_R including a modification of the blade structural properties (S_{mod}). Comparison between (a) the passive and (b) the active rotor at high speed ($v = 65.6$ m/s). $\Delta() = \frac{()_{\text{pp},\tau_{R,i}} - ()_{\text{pp},p,\tau_R=0\%}}{()_{\text{pp},p,\tau_R=0\%}}$.

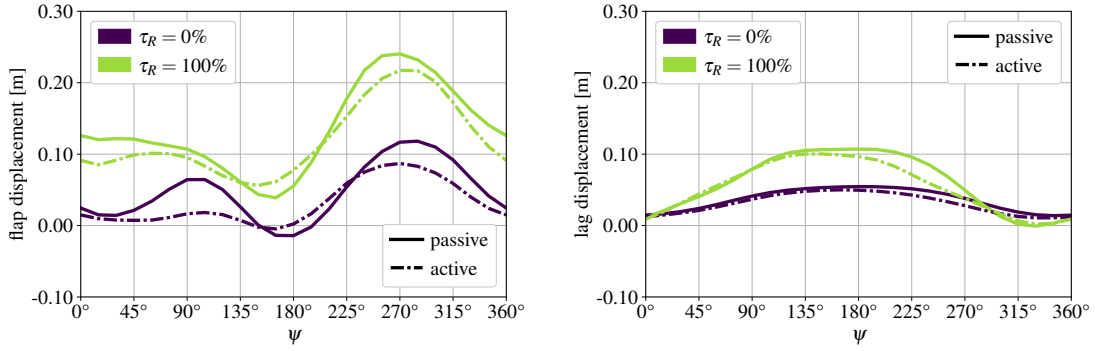

(a) Blade tip displacement (flap) **(b)** Blade tip displacement (lag)

Figure 4.47: Blade displacements and deformations based on different rotor designs (τ_R) under adjustment of the blade structural properties (S_{mod}). Comparison of the active and passive rotor ($v = 65.6$ m/s).

Indirect active-camber-induced performance gains:

Again, it was investigated if the penalties in rotor loads and stall margin due to rotor design modifications could be compensated by active camber, this time under the presented adjustments of the blade mechanical properties. The relationship between rotor power and τ_R is shown in Fig. 4.48 for the passive rotor and, based on the previously introduced cost function definitions (o_A and o_B), for the active rotor. As discussed earlier, the active rotor results based on o_A were quite identical to those obtained by purely aerodynamic modifications (see Fig. 4.42a). The gradient of the passive rotor was slightly steeper, resulting in the previously shown reduction in the relative improvement achieved with active camber. In terms of indirect performance gains, the result was quite similar to the case where the structural properties were kept constant (see Section 4.2.3). That is, it was possible to neutralize the negative effects (peak-to-peak loads and stall margin) almost up to $\tau_R = 40\%$ while still achieving a significant amount of performance gain. Compared to the purely aerodynamic modification of the rotor, even less power had to be sacrificed to maintain the original loads and stall margin. This resulted in a total active-camber-related improvement of about 7% when combining the indirect and direct power gains at $v = 65.6$ m/s. For $\tau_R > 40\%$,

neither the original peak-to-peak loads nor the original stall margin could be restored.

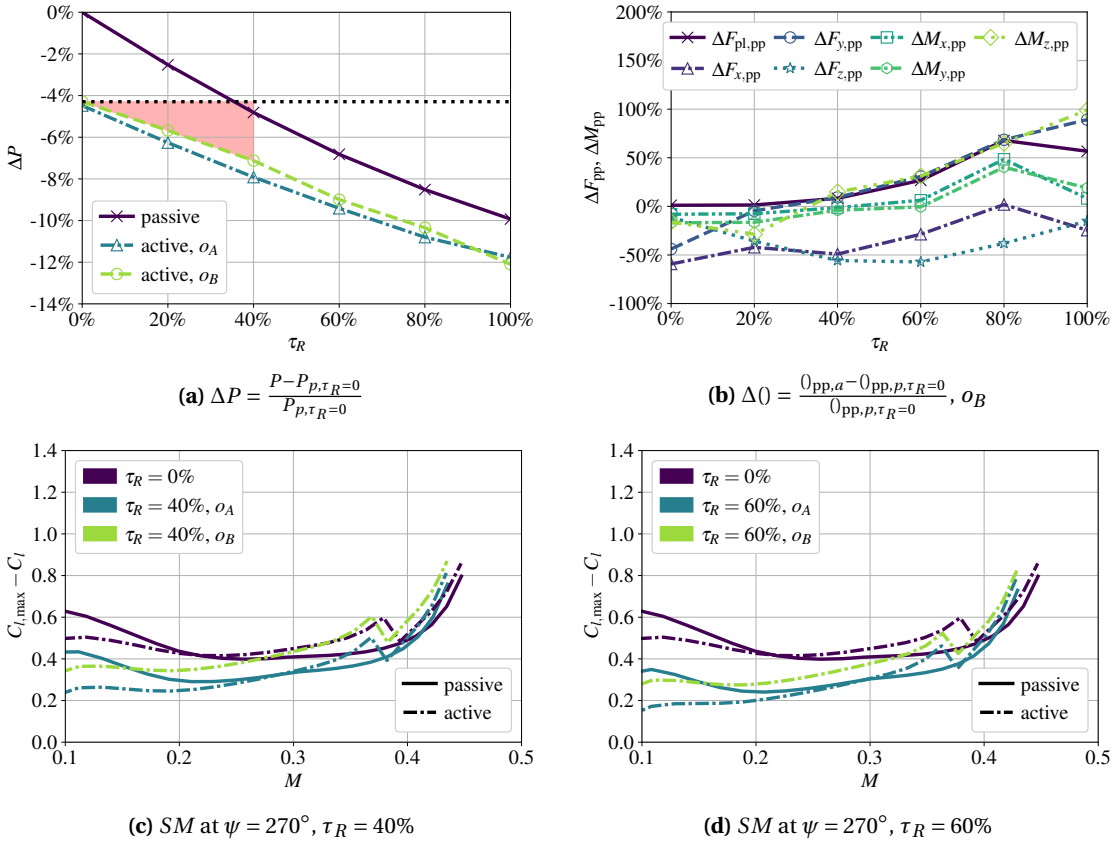

(a) $\Delta P = \frac{P - P_{p,\tau_R=0}}{P_{p,\tau_R=0}}$ **(b)** $\Delta() = \frac{()_{pp,a} - ()_{pp,p,\tau_R=0}}{()_{pp,p,\tau_R=0}}$, o_B

(c) SM at $\psi = 270°$, $\tau_R = 40\%$ **(d)** SM at $\psi = 270°$, $\tau_R = 60\%$

Figure 4.48: Rotor power, rotor loads, and retreating-blade stall margin for different degrees of baseline rotor modifications (τ_R) under adjustment of the blade structural properties (S_{mod}) at $v = 65.6$ m/s. Comparison of using different cost function parameters. The red area in (a) indicates the additional indirect power gains from active camber.

In addition to the aforementioned investigation, a further case was examined where the retreating-blade stall margin was removed from the cost function (o_C, see Table 4.3). Consequently, no attempt was made to restore the original Bo 105 rotor stall margin. This scenario may be relevant in instances where some of the retreating-blade stall margin is dispensable. This may be the case if the aircraft is not operating at or near the speed limit, or if the retreating-blade stall margin is not the limiting factor for the required speed range. With regard to rotor design choices, only the latter case is relevant, and it may occur, for example, if the general level of oscillatory loads and vibrations, stability problems, or available power are limiting the flight speed. Another relevant scenario in this context is a change in the mix of blade design variables so that the stall margin is less degraded, i.e., by using less chord length reduction and less rotational speed reduction. The result in Fig. 4.49 shows that in this case it was possible to restore the baseline rotor peak-to-peak loads up to $\tau_R = 60\%$ (see Fig. 4.49b), and only a marginal amount of the direct power savings had to be sacrificed to maintain the original hub and pitch-link loads (see Fig. 4.49a). As expected, the stall margin of the retreating blade deteriorated, but was comparable to the corresponding ($\tau_R = 60\%$) passive rotor stall margin (see Fig. 4.49c). This resulted in an additional indirect power saving of more than 2% and added up to a total rotor power reduction of more than 9% at $v = 65.6$ m/s.

Again, the indirect benefits apply to other flight conditions as well, since the rotor design change improved efficiency across the entire flight envelope (see Fig. 4.44b for $\tau_R = 60\%$). In hover, this would be a total power reduction of about 10%. Even at medium flight speeds, more than 7% power savings would be possible. At the highest flight speed investigated ($\nu = 76.5$ m/s), power gains of about 11% could be possible, assuming that additional loads continue to be compensated up to $\tau_R = 60\%$. This investigation also shows how sensitive the predictions of performance gains are to the exact definition of the boundary conditions of the optimization problem. Furthermore, it is shown that the implementation of an active-camber system should be based on a holistic approach using all available degrees of freedom instead of retrofitting it to an existing rotor concept.

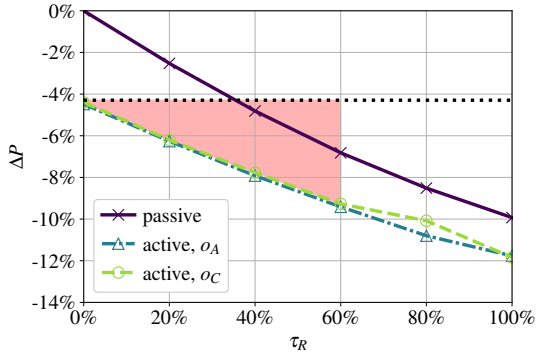

(a) $\Delta P = \frac{P - P_{p,\tau_R=0}}{P_{p,\tau_R=0}}$

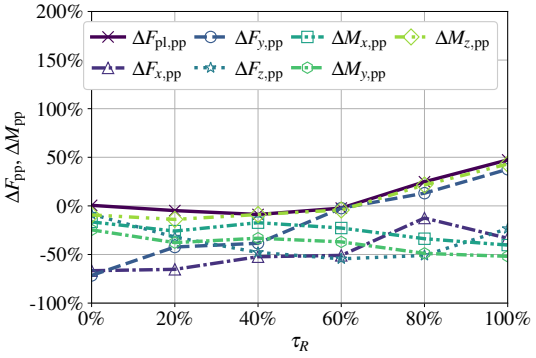

(b) $\Delta() = \frac{()_{pp,a} - ()_{pp,p,\tau_R=0}}{()_{pp,p,\tau_R=0}}$, o_C

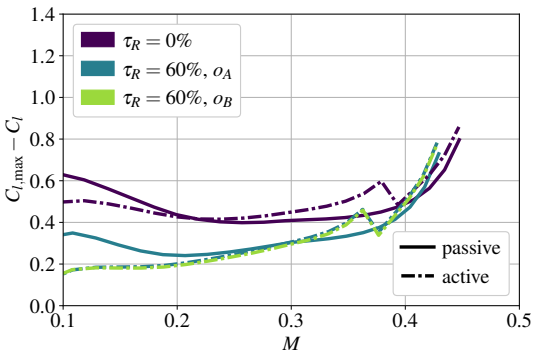

(c) SM at $\psi = 270°$, $\tau_R = 60\%$

Figure 4.49: Rotor power, rotor loads, and retreating-blade stall margin for different degrees of baseline rotor modifications (τ_R) under adjustment of the blade structural properties (S_{mod}) at $\nu = 65.6$ m/s. Comparison of using different cost function parameters. The red area in (a) indicates the additional indirect power gains from active camber.

Interim conclusions:

Based on the conclusions of Section 4.1, the baseline Bo 105 rotor was successfully modified to significantly improve both passive and active rotor efficiency. At high speeds, the effect of this modification on the direct power gains from active camber depended on the modeling decision regarding the structural properties of the rotor blade. When the structural properties were scaled based on the cross-sectional dimension of the rotor blade, the direct power gains from active camber decreased noticeably as more efficient rotor designs were approached. When the blade

structural properties were assumed to be constant, the effect on power gains was negligible. For real helicopter rotors, results are expected to lie between these two approaches. In hovering flight, the results were quite independent of this approach, and the gains from camber morphing were reduced up to 50% of the original value when the most efficient configuration was used as the baseline rotor.

For both modeling concepts, the modifications made to the baseline rotor increased the efficiency of the rotor at the expense of higher rotor loads and reduced blade stall margin. Therefore, it is assumed that the passive rotor design is tightly constrained with respect to such modifications. Accordingly, the results obtained with the Bo 105 rotor are expected to be reasonably transferable to modern, more efficient rotor systems. Apart from that, an indication of this transferability was found in the amount of negative thrust on the advancing blade side. If this phenomenon is not very pronounced, the power gains achievable with active camber at high speeds are substantially reduced.

This deterioration in other disciplines introduced the opportunity to indirectly generate rotor power gains. That is, power gains were achieved through design changes to the passive rotor, but any resulting penalties were offset by the active-camber system. With this approach, it was possible to measure the merit of an active-camber system in a single value, even though the benefits were obtained in different disciplines. Overall, the combination of direct and indirect active-camber-induced power savings resulted in more than 6% performance improvements at $v = 65.6$ m/s ($\mu = 0.3$ with respect to the original Bo 105 rotor), regardless of whether the blade structural characteristics were retained or scaled. Up to 9% power savings were achievable for the same flight condition when no attempt was made to restore the original stall margin. The indirect power gains were available throughout the flight envelope due to the nature of these rotor modifications and could result in even higher total power gains (over 10%) in hover and for $v > 65.6$ m/s.

5 Summary, Conclusions, and Outlook

5.1 Summary

In this work, a computational framework was used to investigate active camber control for helicopter main rotors. The focus of this research was to improve the rotor efficiency in terms of rotor power reduction. At the same time, the goal was to maintain good operability of the rotor system, particularly with regard to peak-to-peak rotor hub loads as well as the stall margin of the retreating blade. Accordingly, a more comprehensive understanding of such systems was sought in order to fully realize the potential of this technology. This included a detailed analysis of the aeroelastic phenomenon, along with an investigation into its interdependence with operational and rotor design aspects. Ultimately, this should facilitate the assessment of the technical and economic viability of such systems, as well as the guidance of a multidisciplinary rotor design and development process in the case of implementing such an active-camber control system.

The CAMRAD II comprehensive analysis code was used to develop a full-scale aeromechanical model of the Bo 105 main rotor, which served as the baseline for the present investigation. Aerodynamic forces were calculated using lifting-line theory based on CFD-generated lookup tables. The rotor inflow was calculated using a free-vortex wake analysis. To model the complex interaction between such aerodynamic forces and the elastic deformation of the rotor in a coupled manner, the Euler-Bernoulli beam theory was applied to solve the elastic motion of the rotor blades. The same propulsive trim targets with a blade loading of $C_T/\sigma = 0.089$ were employed for the active and passive rotor in order to ensure comparability in terms of rotor performance. The model was validated through wind tunnel and flight tests. The exact layout of the active-camber control system has been derived from the FishBAC concept [45], but it is assumed that the results of this study are mostly applicable to similar systems, i.e., other mechanisms to actively morph the rear part of the blade cross section in a continuous way.

First, a number of parameters related to active camber control were analyzed. These included the control inputs in terms of spanwise uniform and spanwise varying camber morphing, as well as the radial size and placement of the active-camber system. The chordwise range of active camber was kept constant and covered the aft 25% of the airfoil. In the spanwise direction, active camber was only applied up to 90% radius due to implementation constraints. Regarding the azimuthal control signal, different strategies were applied, including static deflection, single-harmonic actuation, and multi-harmonic actuation up to a superposition of the first five rotor harmonics.

The optimal control schemes were selected based on a surrogate optimization approach using a multi-objective cost function. In order to meet the predefined requirements, different weights, exponents, and scaling strategies were employed.

Investigations were carried out for different operating conditions with a focus on the variation of the flight speed, i.e., from hover to high-speed flight ($\mu = 0.35$ or $v = 76.5$ m/s). However, other variations of the rotor trim state, such as hub forces and moments and air density, and the influence of specific modeling decisions were also investigated. In addition, the relationship between rotor design parameters and active-camber-induced performance improvements was investigated with the objective of evaluating the transferability of the results to more efficient rotor systems, and identifying potential design targets when implementing active camber control on a helicopter main rotor. This included a separate and a combined modification of specific rotor parameters such as blade geometry, rotor tip speed, and blade torsional stiffness. Two different approaches were employed to define the blade structural parameters during the modification of the blade cross-sectional geometry. Finally, this investigation encompassed an analysis of the potential for indirect generation of rotor power savings through the use of active camber.

5.2 Conclusions

The following specific conclusions were drawn during this study using the aforementioned computational aeromechanics model of a full-scale Bo 105 main rotor:

1. **Performance improvements**
   The efficiency of a helicopter main rotor can be improved by active camber morphing, especially during high-speed flight conditions in terms of edgewise operation (about 8% at $\mu = 0.35$ or $v = 76.5$ m/s), but also in hovering flight (about 5%). In these flight states, the rotor power consumption is generally the highest. Therefore, the maximum power to be supplied by the engines could be reduced accordingly. In addition, by applying appropriate control signals, this improvement in rotor efficiency had no detrimental effect on rotor hub loads, pitch-link loads, or the stall margin of the retreating blade.

2. **Principle of saving rotor power in high-speed flight**
   In high-speed flight, the power savings from active camber were primarily achieved by the ability to redistribute aerodynamic loads across the rotor disk. Improving the local efficiency by adapting the airfoil to the specific flow regime was of secondary importance. The first aspect allowed thrust to be redistributed to regions where it could be produced more efficiently. This involved compensating for negative thrust on the advancing side and reducing lift-induced drag by avoiding high thrust concentrations in regions of high local induced velocities. In addition, thrust could be reduced in regions of high dynamic pressure where it caused disproportionately high profile drag, and distributed to more inboard radial stations to reduce the impact on rotor shaft torque. The morphing of the blade airfoil not

only directly affected the local aerodynamic coefficients, but also implied an adjustment of the primary control to maintain the predefined trim state. In combination, this triggered a complex response of the whole rotor system, including elastic blade deformations (especially of a torsional nature) and variations in the induced velocity.

3. **Principle of saving rotor power in hover**
   In hover, power savings were primarily achieved through distributing the lift to further inboard radial stations. By reducing the lever arm, the associated lift-induced drag generated less torque on the rotor shaft. This effect was most prominent in hover, as a high induced velocity is required to compensate for the comparatively low mass flow. Furthermore, it was found that the scope for improving the hovering rotor performance with active camber is highly dependent on the requirement to orient the rotor design towards high-speed flight. Accordingly, the blade twist, blade taper ratio, and airfoil camber are kept below the optimum for hovering flight to prevent issues at high advance ratios, such as excessive negative thrust, airfoil drag, and pitching moment on the advancing side, as well as insufficient thrust on the retreating side. With regard to camber control, a static deflection was found to adequately realize the available potential for power savings in this symmetrical flight condition. Without further adjustments, such camber deflections were also found to positively affect the stall margin in hovering flight.

4. **Indirect power gains from active camber**
   Modifying the passive rotor design to enhance efficiency had a detrimental effect on the peak-to-peak hub loads and the retreating-blade stall margin. This introduced the opportunity for indirect improvement of the rotor efficiency through enabling a more efficient rotor design by actively equalizing the emerging penalties. This application exploits the mechanism's capacity to optimize for multiple objectives simultaneously, while expressing the benefits in a single value. The performance gains were enhanced by approximately 50% in comparison to the performance gains directly obtained without modifying the rotor design, and they were observed across the entire range of advance ratios. In particular, medium-speed rotor performance benefited from this concept disproportionately. The sum of direct and indirect gains continuously exceeded 5% (more than 8% at hover and more than 6% at $\mu = 0.3$). Even further enhancements in power were achieved (exceeding 7% for all μ and exceeding 10% at hover and high speed) when refraining from restoring the full retreating-blade stall margin. However, the aforementioned indirect power gains depend on the assumption that no passive measures exist to counteract the increase in oscillatory hub loads. Nevertheless, this demonstrates the necessity to optimize the active rotor in a comprehensive manner, including both passive and active (design) parameters, rather than retrofitting such mechanisms to an existing rotor.

5. **Active-rotor design targets**
   When rotor efficiency is the only criterion, beneficial rotor design modifications are largely independent of the intended application, whether as a passive rotor or a rotor utilizing ac-

tive camber control. Only for the blade built-in twist and the chord length were minor differences found with respect to the optimal value. Consequently, an optimized passive rotor is considered a suitable starting point for optimizing a rotor to be used in conjunction with an active-camber system. However, in order to successfully exploit the aforementioned indirect power gains, it seems promising to slightly over-optimize for (low-speed) power efficiency, mainly by reducing the lift capacity in the outer range of the rotor blades.

6. **Transferability of results to modern, more efficient rotors**
   The modification of the baseline rotor design towards higher efficiency generally resulted in a reduction of the potential active-camber-induced power savings, as the active-rotor efficiency did not increase equally. At high speeds, this was mainly due to the mitigation of negative thrust on the advancing side of the passive rotor. However, due to the increase in oscillatory rotor hub loads and reduction in the blade stall margin, it is unlikely that a large portion of the passive rotor adjustments investigated is feasible. It is therefore probable that the majority of the reported power savings can be achieved with more efficient rotors.

7. **Influence of torsional stiffness in high-speed flight**
   Torsional deformation contributed essentially to the total amount of active-camber-related rotor power savings. At high speed, more than 50% of the performance gains depended on the torsional flexibility of the rotor blade. Influencing the torsional deformation of the rotor blades was possible due to the notable effect of camber morphing on the aerodynamic moment. However, reducing the torsional stiffness (GJ) is not deemed an appropriate design goal. This is because any additional gains from active camber were based on compensating for the degradation in passive rotor efficiency associated with lower torsional stiffness. In fact, higher torsional stiffness mitigated the negative thrust on the advancing side by preventing pitch-down twisting of the rotor blades. However, if other circumstances, such as weight reduction or thinner airfoils, resulted in greater torsional flexibility of the blade, the positive effect of active camber on rotor performance could be increased.

8. **Active-camber control inputs in high-speed flight**
   In terms of actuation control signals, the superposition of a static deflection, a 1/rev (1P), and a 2/rev (2P) harmonic signal was necessary but also sufficient to successfully optimize for multiple objectives, such as rotor power, peak-to-peak loads, and stall margin. The optimal phases and amplitudes of the contributing harmonics depended on several factors, including the operating condition, the precise definition of the objective function, the baseline rotor design, and the dimensions of the active-camber section. However, the typical characteristic of the control signal remained constant. On the advancing side, camber deflections close to $\delta = 0^\circ$ were required, while on the retreating side (close to $\psi = 270^\circ$), a prominent peak in the camber deflection was most beneficial.

9. **Spanwise varying camber morphing**
   Varying the active camber morphing along the blade span resulted in additional power gains (approximately 0.4%) for all flight speeds studied. However, this result was depen-

dent on the amount of built-in twist (θ_{tw}), taper ratio (t), and torsional stiffness of the rotor blades. For $\mu = 0$, the positive effect of varying the amount of camber deflection along the span diminished when further twisting or tapering the blade. Conversely, it increased (up to 1.3%) towards infinite torsional stiffness GJ. However, the main advantage of this type of actuation was considered to be the reduction of the actuation amplitudes at outer radial stations.

10. **Spanwise location of the active-camber mechanism**
For all advance ratios investigated ($\mu = 0$ to $\mu = 0.35$), the greatest performance gains were achieved with the largest investigated active-camber section from $r = 0.22$ to $r = 0.9$. However, in high-speed flight, the inner part from $r = 0.22$ to $r = 0.5$ was less relevant. The most important spanwise region was identified to be between $r = 0.6$ and $r = 0.8$ at this flight condition. This range was of particular importance for generating lift on the retreating side. Conversely, in hovering flight, the range between $r = 0.22$ and $r = 0.5$ also contributed a notable portion of rotor power savings.

11. **Influence of the operating condition**
The flight speed had a substantial impact on the capacity to achieve power gains through the use of active camber. Other variations in operating conditions exhibited a low correlation with rotor power gains, such as fuselage drag due to external load or equipment, or rotor hub moments due to variation in the center of gravity. This also suggests that possible uncertainties in the trim targets had a negligible impact on the previously presented results. Only a significant variation in blade loading (C_T/σ) could have a perceptible impact on the benefits of active camber.

12. **Influence of the aerodynamics modeling**
The determination of the induced velocity had a significant impact on the prediction of performance gains. At high-speed flight, linear inflow modeling was found to overpredict the performance gains (compared to free-vortex wake modeling) due to its inability to adjust the induced velocity to the exact distribution of rotor thrust. At hover, the predictions were found to be highly sensitive to the resolution of the free-vortex wake modeling. To enhance the reliability of the rotor power estimation, it was necessary to employ a more complex wake model.

13. **Secondary effects on the helicopter**
The implementation of an active-camber system increases the complexity and weight of a rotorcraft due to the mechanical integration of the system, which includes a power supply unit. Furthermore, a moderate amount of power is required to operate the mechanism. Conversely, weight benefits are expected in other parts of the helicopter, such as a reduction in fuel that needs to be carried for the same mission. Furthermore, the weight of the engine and drive train can be reduced by designing them for lower peak power. Finally, the use of active camber is expected to reduce the necessity for vibration suppression systems and measures.

5.3 Outlook

Based on the results of this work, active camber control is considered a promising technology for improving the efficiency of helicopter main rotors. Although recent progress in improving the performance of passive rotors is expected to reduce the potential of active camber control, it is likely to produce a noteworthy amount of power savings, especially if a holistic approach is taken where integration is performed from a multidisciplinary perspective and with adaptation of the overall rotor design. This is not least due to the potential for indirect improvement in rotor performance, which also brings the savings in the low-speed range more into focus.

In general, high-speed flight applications are of particular interest for this technology. Considering a scenario where the helicopter is designed to achieve flight speeds of $\mu \geq 0.35$, the performance gains from active camber could be even higher. However, under such flight conditions, helicopters are expected to increasingly compete with tiltrotors or lift-plus-cruise vehicles. Active camber is not considered to be a promising technology for these aircraft, as there is typically little edgewise operation of a lifting rotor. However, where both hovering and high-speed flight (up to helicopter-typical values) are essential parts of typical missions, a conventional helicopter is likely to remain the most efficient and capable solution, especially when utilizing active camber control. In addition, this technology offers advantages when it is necessary to reach high altitudes or when a significant amount of maneuvering is involved, which increases the average blade loading of the main rotor. Finally, active camber is considered to be well suited for use in conjunction with variable rotor speed. This is because the camber control can be adapted to different rotor speeds and counteract the individual problems of the respective operating conditions, such as certain vibration modes or blade stall.

To realize the full potential of active-camber control systems, it is necessary to exploit the ability of active camber to improve rotor performance in multiple disciplines. One way of doing this is to indirectly improve efficiency, as was done in the current work. The disciplines considered were rotor power demand, peak-to-peak hub and pitch-link loads, and retreating-blade stall margin. In the future, this approach could be extended to other aspects such as vibration suppression at a more detailed level and rotor stability. Potentially, active camber could also be used to reduce noise emission. The agility and maneuverability of a helicopter are also expected to be improved with active camber. Another area of interest could be the compensation of unexpected or outside-the-sphere-of-influence lying problems resulting from an insufficient predictive capability, late design changes, or manufacturing inaccuracies. For example, rotor track and balance could be partially taken over by active camber control. Finally, it is expected that active camber can mitigate the consequences of dynamic stall. This represents a separate field of research that has not been addressed in the present work, which instead sought to avoid dynamic stall by ensuring sufficient stall margin.

In addition to the expansion of disciplines tackled with active camber, the variables related to rotor design can be expanded for the purpose of improving the synergy with active camber. While

the majority of the global aspects were evaluated in the present work, some additional degrees of freedom remain on a more detailed level. The most important of these are probably the blade tip design, a complex spanwise distribution of the blade chord length, and the blade airfoil. For instance, a variation of the airfoil along the blade span is assumed to contribute to the optimization problem. A thin, flat airfoil geometry may exhibit particularly favorable synergy with active camber. However, it is also a matter of feasibility whether a thin airfoil is a suitable platform for such a mechanism. In addition to the external geometry of the rotor blades, this work has also demonstrated the importance of structural properties on the rotor performance. The use of anisotropic beam properties could also be exploited.

Finally, a cost function must be defined that encompasses all objectives and assigns appropriate weights to them. In addition, each objective must be normalized with respect to suitable target values. In the present work, such target values were based on the Bo 105 reference rotor, which was useful in terms of comparability and benchmarking. For the development of a real active rotor system, the optimization targets should be based more closely on the actual requirements (e.g., on the desired level and characteristic of vibration). In addition, the boundary conditions must be precisely defined. This includes ensuring that the rotorcraft is capable of performing all required missions and tasks. Where possible, such requirements should be addressed by constraining the input parameters. Alternatively, they can be represented by additional objectives, such as the retreating-blade stall margin to represent the available flight speed. Moreover, technical feasibility must be ensured. A challenge in this respect is to precisely define the implementation constraints in terms of a general metric, such as feasible bounds on the mechanical properties for an arbitrary blade geometry.

Once the optimization problem has been thoroughly defined, one of the remaining challenges is to solve it. This is because of the large number of independent variables combined with an objective function based on a complex aeromechanics simulation. The independent variables comprise the parameters of the active-camber system and the baseline rotor design. A particular challenge is that the number of degrees of freedom increases as the level of detail increases. Concurrently, both higher levels of detail and the consideration of complex phenomena necessitate the use of increasingly sophisticated modeling techniques, which may result in significantly greater computational effort. Consequently, the utilization of prior knowledge and the narrowing of the problem may prove to be essential to successfully accomplish this task. At this point, the present work is intended to provide assistance, for example, in the identification of appropriate starting points and the determination of which degrees of freedom should be prioritized.

Having identified an optimal active-rotor design, the next step is to integrate an active-camber mechanism into a real helicopter. This study did not further analyze solutions for the mechanical integration of such systems. However, several other research studies have addressed this topic [45, 50–54, 56]. Thus far, the level of readiness, robustness, and reliability is not yet satisfactory, and further development efforts are required. In addition to implementation aspects, the operation and control of active camber during flight also pose challenges. A sophisticated control

law in conjunction with a thorough application of sensors is necessary to ensure beneficial use under real-world conditions, including continuously changing flight states and atmospheric turbulence. Additionally, a robust lower-order model that appropriately represents the system's behavior is essential for real-time guidance towards a more optimal actuation. It is noteworthy that the previously presented results were highly sensitive to the precise control inputs. Moreover, this technology must also be considered from a safety perspective, as a misalignment of the active-camber deployment could result in exceedingly high loads. This could result in the pilot being unable to control the helicopter or in the mechanical system of the rotor being overloaded. One potential solution for mitigating the risk when applying this technology to a real helicopter is the previously suggested spanwise varying actuation with constructional restriction of the amplitude far outboard.

6 Previous Related Publications by the Author

- Komp, D., Hajek, M., Yavrucuk, I., and Rauleder, J., "Rotor Power Savings and Pitch-Link Load Reductions with Spanwise-Varying Active CamberMorphing," *Journal of Aircraft,* 2024. https://doi.org/10.2514/1.C037505

- Abdelmoula, A., Yurt, M. K., Komp, D., Hajek,M., and Rauleder, J., "CFD/CSD Coupling for Camber Morphed Rotor Blades," *AIAA Aviation Forum,* 2022. https://doi.org/10.2514/6.2022-3751

- Kumar, S., Komp, D., Hajek, M., and Rauleder, J., "Effect of Active Camber on Rotor Noise, Power and Hub Vibration," *AIAA Scitech Forum,* 2021. https://doi.org/10.2514/6.2021-1927

- Komp, D., Hajek, M., and Rauleder, J., "Rotor Performance Enhancements With Spanwise Varying Active Camber Morphing," *AIAA Scitech Forum,* 2021. https://doi.org/10.2514/6.2021-0200

- Komp, D., Hajek, M., and Rauleder, J., "Rotor Power Savings with Active Camber Actuation Varying Baseline Rotor Properties and Operating Conditions," *47th European Rotorcraft Forum,* 2021

- Komp, D., Kumar, S., Hajek, M., and Rauleder, J., "Effect of Active Camber Morphing on Rotor Performance and Control Loads," *Aerospace Science and Technology,* 2021, p. 106311. https://doi.org/10.1016/j.ast.2020.106311

- Komp, D., Kumar, S., Abdelmoula, A., Hajek,M., and Rauleder, J., "Investigation of Active Rotor Design and Control for Performance Improvement," *Vertical Flight Society 75th Annual Forum,* 2019. https://doi.org/10.4050/F-0075-2019-14530

- Kumar, S., Komp, D., Hajek, M., and Rauleder, J., "Integrated Rotor Performance Improvement and Vibration Reduction Using Active Camber Morphing," *ASME Conference on Smart Materials, Adaptive Structures and Intelligent Systems,* 2019. https://doi.org/10.1115/SMASIS2019-5588

- Rauleder, J., van der Wall, B. G., Abdelmoula, A., Komp, D., Kumar, S., Ondra, V., Titurus, B., and Woods, B. K. S., "Aerodynamic Performance of Morphing Blades and Rotor Systems," *American Helicopter Society 74th Annual Forum,* 2018

Bibliography

[1] Jacklin, S. A., Blass, A., Swanson, S. M., and Teves, D., "Second Test of a Helicopter Individual Blade Control System in the NASA Ames 40- By 80-Foot Wind Tunnel," American Helicopter Society 2nd International Aeromechanics Specialists' Conference, Bridgeport, CT, 1995.

[2] Nguyen, K., and Chopra, I., "Effects of Higher Harmonic Control on Rotor Performance and Control Loads," *Journal of Aircraft*, Vol. 29, No. 3, 1992, pp. 336–342. https://doi.org/10.2514/6.1990-1158.

[3] Nguyen, K., "Active Control of Helicopter Blade Stall," *Journal of Aircraft*, Vol. 35, No. 1, 1996, pp. 91–98. https://doi.org/10.2514/2.2264.

[4] Arnold, U. T., "Recent IBC Flight Test Results From the CH-53G Helicopter," *29th European Rotorcraft Forum*, 2003.

[5] Arnold, U., and Fürst, D., "Closed Loop IBC Results From CH-53G Flight Tests," *Aerospace Science and Technology*, Vol. 9, No. 5, 2005, pp. 421–435. https://doi.org/10.1016/j.ast.2005.01.014.

[6] Norman, T. R., Theodore, C., Shinoda, P., Fuerst, D., Arnold, U. T., Makinen, S., Lorber, P., and O'Neill, J., "Full-Scale Wind Tunnel Test of a UH-60 Individual Blade Control System for Performance Improvement and Vibration, Loads, and Noise Control," *American Helicopter Society 65th Annual Forum, Grapevine, TX*, 2009.

[7] Yeo, H., Romander, E. A., and Norman, T. R., "Investigation of Rotor Performance and Loads of a UH-60A Individual Blade Control System," *Journal of the American Helicopter Society*, Vol. 56, No. 4, 2011, pp. 1–18. https://doi.org/10.4050/JAHS.56.042006.

[8] Yeo, H., Jain, R., and Jayaraman, B., "Investigation of Rotor Vibratory Loads of a UH-60A Individual Blade Control System," *Journal of the American Helicopter Society*, Vol. 61, No. 3, 2016, pp. 1–16. https://doi.org/10.4050/jahs.61.032009.

[9] Küfmann, P., Bartels, R., van der Wall, B. G., Schneider, O., Holthusen, H., and Postma, J., "The Second Wind-Tunnel Test of DLR's Multiple Swashplate System: IBC on a Five-Bladed Rotor With Fuselage-Mounted (Fixed Frame) Actuators," *CEAS Aeronautical Journal*, Vol. 10, 2019, pp. 385–402. https://doi.org/10.1007/s13272-018-0323-2.

[10] Kessler, C., "Active Rotor Control for Helicopters: Motivation and Survey on Higher Harmonic Control," *CEAS Aeronautical Journal*, Vol. 1, No. 1-4, 2011, pp. 3–22. https://doi.org/10.1007/s13272-011-0005-9.

[11] Ham, N. D., "Helicopter Stall Alleviation Using Individual-Blade Control," *10th European Rotorcraft Forum, Netherlands*, 1984.

[12] Wilbur, M. L., Mirick, P. H., Yeager, W. T., Langston, C. W., Cesnik, C. E. S., and Shin, S., "Vibratory Loads Reduction Testing of the NASA/Army/MIT Active Twist Rotor," *Journal of the American Helicopter Society*, Vol. 47, No. 2, 2002, pp. 123–133. https://doi.org/10.4050/jahs.47.123.

[13] Sekula, M. K., Wilbur, M. L., and Yeager Jr, W. T., "Aerodynamic Design Study of an Advanced Active Twist Rotor," *American Helicopter Society 4th Decennial Specialist's Conference on Aeromechanics, San Francisco, CA*, 2003.

[14] Sekula, M. K., and Wilbur, M. L., "Optimization of an Active Twist Rotor Blade Planform for Improved Active Response and Forward Flight Performance," *Journal of the American Helicopter Society*, Vol. 62, No. 3, 2017, pp. 1–12. https://doi.org/10.4050/JAHS.62.032002.

[15] Ward, E., Chopra, I., and Datta, A., "Rotation-Frequency-Driven Extension-Torsion Coupled Self-Twisting Rotor Blades," *Journal of Aircraft*, Vol. 55, No. 5, 2018, pp. 1929–1941. https://doi.org/10.2514/1.C034617.

[16] Ameduri, S., and Concilio, A., "A Shape Memory Alloy Torsion Actuator for Static Blade Twist," *Journal of Intelligent Material Systems and Structures*, Vol. 30, No. 17, 2019, pp. 2605–2626. https://doi.org/10.1177/1045389X19873396.

[17] Shin, S. J., and Cesnik, C. E. S., "Helicopter Vibration Reduction in Forward Flight Using Blade Integral Twist Actuation," *Journal of Mechanical Science and Technology*, Vol. 21, No. 2, 2007, pp. 251–263. https://doi.org/10.1007/bf02916286.

[18] Kreshock, A., Thornburgh, R., Wilbur, M., and Langston, C., "Experimental Bench Testing of an Active-Twist Rotor Blade," *53rd AIAA/ASME/ASCE/AHS/ASC Structures, Structural Dynamics and Materials Conference, Honolulu, Hawaii*, 2012, p. 1478. https://doi.org/10.2514/6.2012-1478.

[19] Yeo, H., "Assessment of Active Controls for Rotor Performance Enhancement," *Journal of the American Helicopter Society*, Vol. 53, No. 2, 2007, pp. 152–163. https://doi.org/10.4050/JAHS.53.152.

[20] Shen, J., "Comprehensive Aeroelastic Analysis of Helicopter Rotor With Trailing-Edge Flap

for Primary Control and Vibration Control," Ph.D. thesis, University of Maryland, College Park, 2004.

[21] Shen, J., Chopra, I., and Johnson, W., "Performance of Swashplateless Helicopter Rotor With Trailing-Edge Flaps for Primary Flight Control," *Journal of the American Helicopter Society*, Vol. 55, No. 4, 2010, pp. 42005–42005. https://doi.org/10.4050/jahs.55.042005.

[22] Enenkl, B., Klöppel, V., Preißler, D., and Jänker, P., "Full Scale Rotor With Piezoelectric Actuated Blade Flaps," *28th European Rotorcraft Forum*, Royal Aeronautical Society London, 2002.

[23] Roth, D., Enenkl, B., and Dieterich, O., "Active Rotor Control by Flaps for Vibration Reduction-Full Scale Demonstrator and First Flight Test Results," *32nd European Rotorcraft Forum, Maastrich*, 2006.

[24] Dieterich, O., Konstanzer, P., Roth, D., Ayadi, W., Reber, D., and Well, K. H., "Model Based H.. Control for Helicopter Vibration Reduction-Flight Tests With Active Trailing Edge Flaps," *33rd European Rotorcraft Forum, Kazan*, 2007.

[25] Stacey, S., Connolly, N., Court, P., Allen, J., Monteggia, C., and Oliveros, J., "Leonardo Helicopters Active Rotor Programmes to Improve Helicopter Comfort and Performance," *American Helicopter Society 74th Annual Forum, Phoenix, AZ, USA*, 2018.

[26] Dawson, S., "Wind Tunnel Test of an Active Flap Rotor: BVI Noise and Vibration Reduction," *51st Annual Forum of the American Helicopter Society, Fort Worth, TX*, 1995.

[27] Straub, F. K., Anand, V. R., Lau, B. H., and Birchette, T. S., "Wind Tunnel Test of the SMART Active Flap Rotor," *Journal of the American Helicopter Society*, Vol. 63, No. 1, 2018, pp. 1–16. https://doi.org/10.4050/JAHS.63.012002.

[28] Zhang, J., Smith, E. C., and Wang, K. W., "Active-Passive Hybrid Optimization of Rotor Blades With Trailing Edge Flaps," *Journal of the American Helicopter Society*, Vol. 49, No. 1, 2004, pp. 54–65. https://doi.org/10.4050/JAHS.49.54.

[29] Jones, M. P., and Newman, S. J., "Vibration Reduction of a Lynx Aircraft via Actively Controlled Trailing Edge Flaps," *32nd European Rotorcraft Forum, Maastricht*, 2006.

[30] Liu, L., Friedmann, P. P., Kim, I., and Bernstein, D. S., "Rotor Performance Enhancement and Vibration Reduction in Presence of Dynamic Stall Using Actively Controlled Flaps," *Journal of the American Helicopter Society*, Vol. 53, No. 4, 2008, pp. 338–350. https://doi.org/10.4050/JAHS.53.338.

[31] Jain, R., and Yeo, H., "Effects of Torsion Frequencies on Rotor Performance and Structural

Loads With Trailing Edge Flap," *Smart Materials and Structures*, Vol. 21, No. 8, 2012, p. 085026. https://doi.org/10.1088/0964-1726/21/8/085026.

[32] Jain, R., Yeo, H., and Chopra, I., "Investigation of Trailing-Edge Flap Gap Effects on Rotor Performance Using High Fidelity Analysis," *Journal of Aircraft*, Vol. 50, No. 1, 2013, pp. 140–151. https://doi.org/10.2514/1.C031837.

[33] Ravichandran, K., Chopra, I., Wake, B. E., and Hein, B., "Trailing-Edge Flaps for Rotor Performance Enhancement and Vibration Reduction," *Journal of the American Helicopter Society*, Vol. 58, No. 2, 2013. https://doi.org/10.4050/JAHS.58.022006.

[34] Kody, F., Corle, E., Maughmer, M. D., and Schmitz, S., "Higher-Harmonic Deployment of Trailing-Edge Flaps for Rotor-Performance Enhancement and Vibration Reduction," *Journal of Aircraft*, Vol. 53, No. 2, 2015, pp. 333–342. https://doi.org/10.2514/1.c033335.

[35] Jain, R., Yeo, H., and Chopra, I., "Computational Fluid Dynamics - Computational Structural Dynamics Analysis of Active Control of Helicopter Rotor for Performance Improvement," *Journal of the American Helicopter Society*, Vol. 55, No. 4, 2010. https://doi.org/10.4050/JAHS.55.042004.

[36] Kinzel, M. P., Maughmer, M. D., and Lesieutre, G. A., "Miniature Trailing-Edge Effectors for Rotorcraft Performance Enhancement," *Journal of the American Helicopter Society*, Vol. 52, No. 2, 2007, pp. 146–158. https://doi.org/10.4050/JAHS.52.146.

[37] Bae, E., and Gandhi, F., "Optimally Actuated Spanwise-Segmented Aerodynamic Effectors for Rotorcraft Power Reduction," *American Helicopter Society 66th Annual Forum*, 2010.

[38] Kinzel, M. P., Maughmer, M. D., and N. Duque, E. P., "Numerical Investigation on the Aerodynamics of Oscillating Airfoils With Deployable Gurney Flaps," *AIAA Journal*, Vol. 48, No. 7, 2010, pp. 1457–1469. https://doi.org/10.2514/1.J050070.

[39] Palacios, J., Kinzel, M., Overmeyer, A., and Szefi, J., "Active Gurney Flaps: Their Application in a Rotor Blade Centrifugal Field," *Journal of Aircraft*, Vol. 51, No. 2, 2014, pp. 473–489. https://doi.org/10.2514/1.C032082.

[40] Matalanis, C. G., Wake, B. E., Opoku, D., Min, B.-Y., Yeshala, N., and Sankar, L., "Aerodynamic Evaluation of Miniature Trailing-Edge Effectors for Active Rotor Control," *Journal of Aircraft*, Vol. 48, No. 3, 2011, pp. 995–1004. https://doi.org/10.2514/1.C031191.

[41] Liu, L., Padthe, A. K., and Friedmann, P. P., "Computational Study of Microflaps With Application to Vibration Reduction in Helicopter Rotors," *AIAA Journal*, Vol. 49, No. 7, 2011, pp. 1450–1465. https://doi.org/10.2514/1.J050829.

[42] Mishra, A., Ananthan, S., Baeder, J. D., Opoku, D. G., Wake, B. E., and Lin, R. S., "Coupled

CFD/CSD Prediction of the Effects of Leading Edge Slat on Rotor Performance," *65th Annual Forum and Technology Display of the American Helicopter Society International, Dallas, TX*, 2009.

[43] Jain, R., Yeo, H., and Chopra, I., "Examination of Rotor Loads Due to on-Blade Active Controls for Performance Enhancement," *Journal of Aircraft*, Vol. 47, No. 6, 2010, pp. 2049–2066. https://doi.org/10.2514/1.C000306.

[44] Ravichandran, K., and Chopra, I., "Open-Loop Control of Performance and Vibratory Loads Using Leading-Edge Slats," *Journal of the American Helicopter Society*, Vol. 61, No. 3, 2016, pp. 1–9. https://doi.org/10.4050/jahs.61.032003.

[45] Woods, B. K., Bilgen, O., and Friswell, M. I., "Wind Tunnel Testing of the Fish Bone Active Camber Morphing Concept," *Journal of Intelligent Material Systems and Structures*, Vol. 25, No. 7, 2014, pp. 772–785. https://doi.org/10.1177/1045389X14521700.

[46] Fournier, S., and Woods, B. K., "Surrogate Modelling of the Steady Aeroelastic Performance of the Fish Bone Active Camber Concept," *AIAA Scitech 2019 Forum*, 2019, p. 1859.

[47] Rivero, A. E., Fournier, S., Manolesos, M., Cooper, J. E., and Woods, B. K., "Experimental Aerodynamic Comparison of Active Camber Morphing and Trailing-Edge Flaps," *AIAA Journal*, 2021, pp. 1–14. https://doi.org/10.2514/1.j059606.

[48] Rivero, A. E., Fournier, S., Heeb, R. M., and Woods, B. K., "Design, Manufacture and Wind Tunnel Test of a Modular FishBAC Wing With Novel 3D Printed Skins," *Applied Sciences*, Vol. 12, No. 2, 2022, p. 652. https://doi.org/10.3390/app12020652.

[49] Kumar, D., Glaz, B., Mok, J., Friedmann, P. P., and Cesnik, C. E. S., "Determination of Optimum Camber Distribution in Rotating Wings With Deformable Airfoils for Vibration Reduction and Performance Enhancement Using Surrogate Modeling," *36th European Rotorcraft Forum, France*, 2010.

[50] Kumar, D., and Cesnik, C. E., "Performance Enhancement in Dynamic Stall Condition Using Active Camber Deformation," *Journal of the American Helicopter Society*, Vol. 60, No. 2, 2015, pp. 1–12. https://doi.org/10.4050/JAHS.60.022001.

[51] Mistry, M., and Gandhi, F., "Design, Fabrication, and Benchtop Testing of a Helicopter Rotor Blade Section With Warp-Induced Spanwise Camber Variation," *Journal of Intelligent Material Systems and Structures*, Vol. 26, No. 10, 2015, pp. 1272–1289. https://doi.org/10.1177/1045389X14541491.

[52] Ferede, E., and Gandhi, F., "Design, Fabrication, and Testing of an Active Camber Rotor Blade

Tip," *Journal of Intelligent Material Systems and Structures*, Vol. 33, No. 13, 2022, pp. 1663–1677. https://doi.org/10.1177/1045389X211063940.

[53] Zahoor, Y., De Breuker, R., and Voskuijl, M., "Preliminary Design of a TE Morphing Surface for Rotorcraft," *AIAA Scitech 2020 Forum*, 2020. https://doi.org/10.2514/6.2020-1301.

[54] Mkhoyan, T., Thakrar, N. R., De Breuker, R., and Sodja, J., "Design and Development of a Seamless Smart Morphing Wing Using Distributed Trailing Edge Camber Morphing for Active Control," *AIAA Scitech 2021 Forum*, 2021. https://doi.org/10.2514/6.2021-0477.

[55] Zahoor, Y., Sodja, J., De Breuker, R., and Voskuijl, M., "Design and Validation of a Passive Camber Morphing Concept for Rotorcraft," *AIAA Scitech 2022 Forum*, 2022. https://doi.org/10.2514/6.2022-0173.

[56] Thornburgh, R. P., Kreshock, A. R., Wilbur, M. L., Sekula, M. K., and Shen, J., "Continuous Trailing-Edge Flaps for Primary Flight Control of a Helicopter Main Rotor," *American Helicopter Society (AHS) 70th Annual Forum*, 2014.

[57] Thornburgh, R. P., Kreshock, A. R., and Wilbur, M. L., "Experimental Measurement of a Blade Section With a Continuous Trailing-Edge Flap," *American Helicopter Society (AHS) 72nd Annual Forum*, 2016.

[58] Abdelmoula, A., and Rauleder, J., "Aerodynamic Performance of Morphed Camber Rotor Airfoils," *AIAA Scitech 2019 Forum*, 2019, p. 1101. https://doi.org/10.2514/6.2019-1101.

[59] Woods, B. K., Fincham, J. H., and Friswell, M. I., "Aerodynamic Modelling of the Fish Bone Active Camber Morphing Concept," *Proceedings of the RAeS Applied Aerodynamics Conference, Bristol, UK*, Vol. 2224, 2014.

[60] Barbarino, S., Gandhi, F., and Webster, S. D., "Design of Extendable Chord Sections for Morphing Helicopter Rotor Blades," *Journal of Intelligent Material Systems and Structures*, Vol. 22, No. 9, 2011, pp. 891–905. https://doi.org/10.1177/1045389X11414077.

[61] Khoshlahjeh, M., and Gandhi, F., "Extendable Chord Rotors for Helicopter Envelope Expansion and Performance Improvement," *Journal of the American Helicopter Society*, Vol. 59, No. 1, 2014, pp. 1–10. https://doi.org/10.4050/JAHS.59.012007.

[62] Balzarek, C., Kalow, S., Riemenschneider, J., and Rivero, A., "Manufacturing and Testing of a Variable Chord Extension for Helicopter Rotor Blades," *Actuators*, Vol. 11, MDPI, 2022, p. 53. https://doi.org/10.3390/act11020053.

[63] Floros, M. W., and Johnson, W., "Performance Analysis of the Slowed-Rotor Compound Helicopter Configuration," *Journal of the American Helicopter Society*, Vol. 54, No. 2, 2009, pp. 1–12. https://doi.org/10.4050/JAHS.54.022002.

[64] Goulos, I., and Bonesso, M., "Variable Rotor Speed and Active Blade Twist for Civil Rotorcraft: Optimum Scheduling, Mission Analysis, and Environmental Impact," *Aerospace Science and Technology*, Vol. 88, 2019, pp. 444–456. https://doi.org/10.1016/j.ast.2019.03.040.

[65] Grohmann, B., Maucher, C., and Jänker, P., "Actuation Concepts for Morphing Helicopter Rotor Blades," *25th International Congress of the Aeronautical sciences*, 2006.

[66] Braun, D., and Humpert, A., "BO105 CBS-5: BO105 Upgrade Through New Rotor Blades," *19th European Rotorcraft Forum, Italy*, 1993.

[67] Brocklehurst, A., and Barakos, G. N., "A Review of Helicopter Rotor Blade Tip Shapes," *Progress in Aerospace Sciences*, Vol. 56, 2013, pp. 35–74. https://doi.org/10.1016/j.paerosci.2012.06.003.

[68] Bailly, J., Ortun, B., and Delrieux, Y., "Recent Advances in Rotor Aerodynamic Optimization, Including Structural Data Update," *Journal of the American Helicopter Society*, Vol. 62, No. 2, 2017. https://doi.org/10.4050/JAHS.62.022009.

[69] Bousman, W. G., "Airfoil Design and Rotorcraft Performance," *58th Annual Forum of the American Helicopter Society, Montrèal, Canada*, 2002.

[70] Glaz, B., Goel, T., Liu, L., Friedmann, P. P., and Haftka, R. T., "Multiple-Surrogate Approach to Helicopter Rotor Blade Vibration Reduction," *AIAA Journal*, Vol. 47, No. 1, 2009, pp. 271–282. https://doi.org/10.2514/1.40291.

[71] Glaz, B., Friedmann, P. P., and Liu, L., "Helicopter Vibration Reduction Throughout the Entire Flight Envelope Using Surrogate-Based Optimization," *Journal of the American Helicopter Society*, Vol. 54, No. 1, 2009, pp. 12007–12007. https://doi.org/10.4050/JAHS.54.012007.

[72] "Shape Adaptive Blades for Rotorcraft Efficiency (SABRE)," *EU Funded Project 723491*, 2021. https://doi.org/10.3030/723491.

[73] Johnson, W., *Rotorcraft Aeromechanics*, Cambridge University Press, 2013.

[74] Pflumm, T., "Numerical and Experimental Structural Beam Analysis for the Development of Helicopter Rotor Blades," Ph.D. thesis, Technische Universität München, 2022.

[75] Johnson, W., "Rotorcraft Aerodynamics Models for a Comprehensive Analysis," *54th Annual Forum of the American Helicopter Society, Washington, DC*, 1998.

[76] Komp, D., Kumar, S., Abdelmoula, A., Hajek, M., and Rauleder, J., "Investigation of Active Rotor Design and Control for Performance Improvement," *Vertical Flight Society 75th Annual Forum*, 2019. https://doi.org/10.4050/F-0075-2019-14530.

[77] Komp, D., Kumar, S., Hajek, M., and Rauleder, J., "Effect of active camber morphing on rotor performance and control loads," *Aerospace Science and Technology*, Vol. 108, 2021, p. 106311. https://doi.org/10.1016/j.ast.2020.106311.

[78] Virtanen, P., Gommers, R., and Oliphant, T. E. e. a., "SciPy 1.0: Fundamental Algorithms for Scientific Computing in Python," *Nature Methods*, Vol. 17, 2020, pp. 261–272. https://doi.org/10.1038/s41592-019-0686-2.

[79] Leishman, G. J., *Principles of Helicopter Aerodynamics*, Cambridge University Press, 2006.

[80] Hoadley, A. W., and VanderBok, R. S., "Stall Margin Indication," *Journal of Aircraft*, Vol. 25, No. 4, 1988, pp. 380–383. https://doi.org/10.2514/3.45574.

[81] Jacklin, S. A., Swanson, S., Blaas, A., Richter, P., Teves, D., Niesl, G., Kube, R., Key, D. L., and Gmelin, B., "Investigation of a Helicopter Individual Blade Control (IBC) System in Two Full-Scale Wind Tunnel Tests: Volume I," NASA/TP-20205003457 Vol I, 2020.

[82] Jacklin, S. A., Swanson, S., Blaas, A., Richter, P., Teves, D., Niesl, G., Kube, R., Gmelin, B., and Key, D. L., "Investigation of a Helicopter Individual Blade Control (IBC) System in Two Full-Scale Wind Tunnel Tests: Volume II—Tabulated Data," NASA/TP-20205003457 Vol II, 2020.

[83] Langer, H. J., and Tränapp, N., "BO 105 Flight Test Data for a Wind Tunnel Test Program," DLR IB 111–93/58, 1993.

[84] Peterson, R. L., Maier, T. H., Langer, H. J., and Tränapp, N., "Correlation of Wind Tunnel and Flight Test Results of a Full-Scale Hingeless Rotor," *American Helicopter Society Aeromechanics Specialist Conference*, 1994.

[85] van der Wall, B. G., "Selection of the Baseline Rotor," 2017.

[86] Götz, J., "Bo105: Configuration Data," GARTEUR HC AG16 Technical Report, DLR, Institute of Flight Systems, 2006.

[87] Rios, L. M., and Sahinidis, N. V., "Derivative-Free Optimization: A Review of Algorithms and Comparison of Software Implementations," *Journal of Global Optimization*, Vol. 56, 2013, pp. 1247–1293. https://doi.org/10.1007/s10898-012-9951-y.

[88] Eriksson, D., Bindel, D., and Shoemaker, C. A., "pySOT and POAP: An Event-Driven Asynchronous Framework for Surrogate Optimization," *arXiv*, 2019. https://doi.org/10.48550/arXiv.1908.00420.

[89] Queipo, N. V., Haftka, R. T., Shyy, W., Goel, T., Vaidyanathan, R., and Tucker, P. K., "Surrogate-Based Analysis and Optimization," *Progress in Aerospace Sciences*, Vol. 41, No. 1, 2005, pp. 1–28. https://doi.org/10.1016/j.paerosci.2005.02.001.

[90] Forrester, A. I., and Keane, A. J., "Recent Advances in Surrogate-Based Optimization," *Progress in Aerospace Sciences*, Vol. 45, No. 1-3, 2009, pp. 50–79. https://doi.org/10.1016/j.paerosci.2008.11.001.

[91] Krityakierne, T., Akhtar, T., and Shoemaker, C. A., "SOP: Parallel Surrogate Global Optimization With Pareto Center Selection for Computationally Expensive Single Objective Problems," *Journal of Global Optimization*, Vol. 66, 2016, pp. 417–437. https://doi.org/10.1007/s10898-016-0407-7.

[92] Kenny, Q. Y., Li, W., and Sudjianto, A., "Algorithmic Construction of Optimal Symmetric Latin Hypercube Designs," *Journal of Statistical Planning and Inference*, Vol. 90, No. 1, 2000, pp. 145–159. https://doi.org/10.1016/S0378-3758(00)00105-1.

[93] Pedregosa, F., Varoquaux, G., Gramfort, A., Michel, V., and et al., T., "Scikit-Learn: Machine Learning in Python," *Journal of Machine Learning Research*, Vol. 12, 2011, pp. 2825–2830. https://doi.org/10.48550/arXiv.1201.0490.

[94] Williams, C. K., and Rasmussen, C. E., *Gaussian Processes for Machine Learning*, Vol. 2, MIT press Cambridge, MA, 2006.

[95] Yang, X.-S., "Nature-Inspired Optimization Algorithms (Second Edition)," Academic Press, 2021, pp. 221–237. https://doi.org/https://doi.org/10.1016/B978-0-12-821986-7.00022-6.

[96] Bousman, W. G., "A Qualitative Examination of Dynamic Stall From Flight Test Data," *Journal of the American Helicopter Society*, Vol. 43, No. 4, 1998, pp. 279–295. https://doi.org/10.4050/JAHS.43.279.